UNIVERSIDADE
LUSÓFONA

AGE OF INFORMATION IN WIRELESS COMMUNICATION SYSTEMS

Wijerathna Basnayaka Mudiyanselage Chathuranga Madhushan Basnayaka

Thesis to obtain the Degree of Doctor of Philosophy in
Computer Science

Adviser: Prof. Dr. Jayakody Arachchilage Dushantha Nalin Kumara
Professor, Universidade Lusófona

Co-adviser: Prof. Dr. Marko Beko
Professor, Universidade Lusófona

October, 2024

**WIJERATHNA BASNAYAKA MUDIYANSELAGE CHATHURANGA
MADHUSHAN BASNAYAKA**

AGE OF INFORMATION IN WIRELESS COMMUNICATION SYSTEMS

Tese defendida em provas públicas na Universidade Lusófona, Centro Universitário de Lisboa no dia 14/11 2024, nomeada pela ordem de Nomeação Nº.: 1049/2024, de 12 de Novembro de 2024, para obtenção do grau de Doutor em Informática perante o júri, com a seguinte composição:

Presidente:

Prof. Dr. Paulo Jorge Tavares Guedes, Professor, Universidade Lusófona

Vogais:

Prof. Dr. Rui Dinis, Full Professor, Universidade Nova de Lisboa

Prof. Dr. João Carlos Marques Silva, Professor, Instituto Universitário de Lisboa

Prof. Dr. Slavisa Tomic, Professor, Universidade Lusófona

Prof. Dr. João Canto, Professor, Universidade Lusófona

Prof. Dr. João Pedro Matos Carvalho, Professor, Universidade Lusófona

Orientadora:

Prof. Dr. Jayakody Arachchilage Dushantha Nalin Kumara, Professor, Universidade Lusófona

Co-orientador:

Prof. Dr. Marko Beko, Professor, Universidade Lusófona

Universidade Lusófona – Centro Universitário de Lisboa

Escola de Comunicação, Arquitectura, Artes e Tecnologias da Informação (ECATI)

Lisboa

2024

AGE OF INFORMATION IN WIRELESS COMMUNICATION SYSTEMS

Acknowledgements

Last but not least, I want to express my heartfelt gratitude to my family. To my parents, grandparents, and siblings: Your unwavering love, support, and faith in me have been the cornerstone of my academic journey and success. Your sacrifices and unconditional love have not gone unnoticed, and I am profoundly grateful for everything you have done to support me throughout this endeavor.

Abstract

The rapid evolution of wireless communication technologies has paved the way for an era of data-driven applications that heavily rely on the exchange of time-critical information for monitoring and control purposes. This shift is evident across various domains: autonomous vehicles exchanging safety-related information, remote surgery systems requiring ultra-reliable and low-latency communication, and high-frequency automated trading platforms demanding real-time data updates. In these emerging application scenarios, the freshness of information is of paramount importance, as outdated data not only loses its value but can also lead to system failures and potentially catastrophic safety risks. Traditional timeliness performance metrics such as latency and inter-delivery time have proven inadequate to capture the timeliness requirements of these mission-critical applications. To address this limitation, the concept of Age of Information (AoI) has emerged as a reliable metric for quantifying information freshness in communication networks.

This thesis investigates AoI analysis and optimization across diverse wireless communication systems, including ultra-reliable low-latency communication (URLLC), simultaneous wireless information and power transfer (SWIPT), unmanned aerial vehicle (UAV) assisted networks, and deep joint source-channel coding (DJSCC)-based semantic communication. Mathematical models are employed to analyse average AoI (AAoI) in URLLC-enabled UAV-assisted communication systems and UAV-assisted wireless sensor networks (WSNs). Closed-form expressions for AAoI are derived using stochastic hybrid systems models, and the effect of system parameters such as UAV altitude, block length, and update generation rate on information freshness is investigated. For analysis of short packet systems, finite blocklength information theory is employed to accurately model the performance of URLLC systems. Simulation results demonstrate that UAV-assisted relay communication maintains lower AoI compared to traditional direct transmission.

The thesis also examines the AAoI in SWIPT-enabled cooperative relay networks under different scheduling policies, namely, transmit without waiting and wait until charged. Moreover, it introduces a novel DJSCC-based semantic communication approach to minimize AoI for image transmission and proposes a new content-based AoI metric, the age of misclassified information (AoMI), for DJSCC-based systems. These concepts are applied to a UAV-based wildfire detection system, enhancing accuracy and timeliness of information delivery. Simulation results show the DJSCC-based approach achieves lower AoMI than traditional methods, especially at low signal-to-noise ratios and bandwidth.

In summary, this thesis emphasises AoI as a critical metric for mission-critical applications, offering insights into optimising wireless communication systems for information freshness. It

enhances understanding of AoI in UAV-assisted networks, WSNs, and semantic communication systems, paving the way for future research on improving information freshness.

Resumo

A rápida evolução das tecnologias de comunicação sem fio abriu caminho para uma era de aplicações baseadas em dados que dependem fortemente da troca de informações críticas em tempo real para fins de monitoramento e controle. Essa mudança é evidente em vários domínios: veículos autônomos trocando informações relacionadas à segurança, sistemas de cirurgia remota que requerem comunicação ultra-confiável e de baixa latência, e plataformas de negociação automatizada de alta frequência que exigem atualizações de dados em tempo real. Nesses cenários de aplicação emergentes, a atualidade da informação é de suma importância, pois dados desatualizados não apenas perdem seu valor, mas também podem levar a falhas no sistema e potencialmente a riscos catastróficos de segurança. As métricas tradicionais de desempenho de pontualidade, como latência e tempo entre entregas, provaram ser inadequadas para capturar os requisitos de pontualidade dessas aplicações críticas. Para abordar essa limitação, o conceito de Idade da Informação (Age of Information - AoI) surgiu como uma métrica confiável para quantificar a atualidade da informação em redes de comunicação.

Esta tese investiga a análise e otimização de AoI em diversos sistemas de comunicação sem fio, incluindo comunicação ultra-confiável de baixa latência (URLLC), transferência simultânea de informação e energia sem fio (SWIPT), redes assistidas por veículos aéreos não tripulados (UAV) e comunicação semântica baseada em codificação conjunta de fonte e canal profunda (DJSCC).

Modelos matemáticos são empregados para analisar a AoI média (AAoI) em sistemas de comunicação assistidos por UAV habilitados para URLLC e redes de sensores sem fio (WSNs) assistidas por UAV. Expressões de forma fechada para AAoI são derivadas usando modelos de sistemas híbridos estocásticos, e o efeito de parâmetros do sistema, como altitude do UAV, comprimento do bloco e taxa de geração de atualizações na atualidade da informação, é investigado. Para análise de sistemas de pacotes curtos, a teoria da informação de comprimento de bloco finito é empregada para modelar com precisão o desempenho dos sistemas URLLC. Resultados de simulação demonstram que a comunicação por retransmissão assistida por UAV mantém menor AoI em comparação com a transmissão direta tradicional.

A tese também examina a AAoI em redes de retransmissão cooperativas habilitadas para SWIPT sob diferentes políticas de agendamento, nomeadamente, transmitir sem esperar e esperar até carregar. Além disso, introduz uma nova abordagem de comunicação semântica baseada em DJSCC para minimizar a AoI na transmissão de imagens e propõe uma nova métrica de AoI baseada em conteúdo, a idade da informação classificada erroneamente (age of misclassified information - AoMI), para sistemas baseados em DJSCC. Esses conceitos são aplicados a um sistema de detecção

de incêndios florestais baseado em UAV, melhorando a precisão e a pontualidade da entrega de informações. Resultados de simulação mostram que a abordagem baseada em DJSCC alcança menor AoMI do que os métodos tradicionais, especialmente em baixas relações sinal-ruído e largura de banda.

Em resumo, esta tese enfatiza a AoI como uma métrica crítica para aplicações críticas, oferecendo insights para otimizar sistemas de comunicação sem fio para a atualidade da informação. Ela melhora a compreensão da AoI em redes assistidas por UAV, WSNs e sistemas de comunicação semântica, abrindo caminho para pesquisas futuras sobre a melhoria da atualidade da informação.

Palavras-chave: Comunicação semântica, Comunicação ultra-confiável de baixa latência, Idade da Informação (Age of Information), Transferência simultânea de informação e energia sem fio, Veículos aéreos não tripulados.

Contents

List of Figures

xv

List of Tables

Acronyms

3GPP   3rd generation partnership project *(p. 15)*

AAoI   average age of information *(pp. 3, 5, 6, 11, 13, 14, 22, 25, 26, 31, 32, 34–36, 38–40, 43, 44, 52, 53, 55–64, 67, 72–76, 106, 107, 113, 114, 116, 117)*

AAoMI   average AoMI *(pp. 79, 80, 82, 85–92, 97, 100–102, 105–107, 109–111)*

AoI   age of information *(pp. 1–6, 9–13, 15, 16, 19, 21, 23–25, 31–34, 43, 44, 46, 52, 53, 64, 67, 76, 79, 80, 83, 88, 89, 91, 92, 97, 113–118)*

AoMI   age of misclassified information *(pp. 2, 6, 79, 80, 82–84, 90–92, 97, 98, 111, 115, 117)*

AWGN   additive white Gaussian noise *(pp. 17, 18, 27, 48)*

BLER   block error rate *(pp. 44, 46, 47, 49, 56–62, 67, 113, 114, 116)*

BPG   better portable graphics *(pp. 80, 86, 88, 115)*

BTS   base transceiver station *(pp. 67, 75, 76)*

CDF   cumulative distribution function *(pp. 30, 49–51, 54, 69)*

CNN   convolutional neural network *(pp. 81, 96)*

CSI   channel state information *(pp. 19, 48, 71, 116)*

DF   decode-and-forward *(pp. 26, 27, 31, 46, 68)*

DJSCC   deep joint source-channel coding *(pp. xvii, 2–4, 6, 22, 79, 80, 82, 86–93, 104, 107, 108, 113, 115, 117, 118)*

DNN   deep neural network *(pp. 79, 80, 90, 93)*

EH   energy harvesting *(pp. 1–5, 13, 19–21, 44, 47, 56, 57, 64, 114, 116)*

eMBB   enhanced mobile broadband *(p. 16)*

FCFS   first-come first-served *(p. 12)*

FDMA   frequency-division multiple access *(p. 20)*

GCQ   Gaussian-Chebyshev-quadrature *(pp. 50, 51, 70)*

GCS   ground control station *(pp. xiv, 92–95, 97, 103, 106)*

Symbols

$\mathbf{A}_l$	Binary transition reset matrix for transition l in the SHS model *(pp. 13, 84, 98)*
α_{ij}	Large scale channel gain between transmitter i and receiver j *(pp. 28, 46, 69)*
α	General notation for Large-scale channel gain *(p. 95)*
b_1	Expected number of buildings passed per km *(p. 27)*
β	Distance dividing factor *(p. 26)*
$\mathbf{b}_q$	Growth rate vector for discrete state q in the SHS model *(pp. 13, 84)*
b_r	Number of buildings crossed by the ray *(pp. 27, 28)*
C	General notation for channel capacity *(pp. 17, 18)*
c	Speed of light *(pp. 28, 46, 56, 69, 73, 95, 103)*
C_ϵ	Outage capacity *(p. 17)*
$C(\gamma_j^t)$	Channel capacity of complex AWGN channel for transmission from node t to node j *(p. 48)*
c_i	Time stamp when image i is captured by the source *(p. 83)*
$\mathcal{CN}$	Complex Normal (Gaussian) distribution *(pp. 46, 81, 94)*
$\mathbb{C}^{x \times y}$	Space of $x \times y$ complex-valued matrices *(p. 81)*
Δ_0	Initial Age of Information *(p. 52)*
Δ^{AAoI}	Average Age of Information *(pp. 11, 14, 32)*
$\Delta(t)$	Age of Information as time-dependent function *(pp. 10, 53)*
Δ	Average age of misclassified information (AAoMI) *(pp. 84–86, 101)*
$\delta(X)$	Dirac impulse (Dirac delta function) *(p. 55)*
Δ_i^{AAoI}	AAoI at source S_i, $i \in (A, B)$ in two-way relay system *(pp. 11, 53, 56)*
$\delta_{\hat{q}, q(t)}$	Kronecker delta function used in SHS model to limit occurrence of transitions to specific states *(pp. 13, 98)*
Δ_{net}^{AAOI}	Network average age of information in the UAV-assisted Wireless Sensor Network *(p. 72)*
$\hat{\Delta}_{net}^{AAOI}$	Lower bound of the network average age of information in the UAV-assisted Wireless Sensor Network *(p. 72)*
Δ_{Sum}^{AAoI}	Expected weighted sum AAoI of the two-way relay system *(p. 53)*

Δ_{T_c}	Time average age	*(pp. 10, 11, 32, 84, 98)*
D_{G_c}	Coordinates of Ground Control Station (GCS)	*(p. 92)*
d_{ij}	Distance between node i and node j	*(p. 46)*
$d_{S,D}$	Distance between source (S) and destination (D)	*(pp. 26, 35)*
D_U	Coordinates of the UAV	*(p. 92)*
d_{U,G_c}	Horizontal distance between UAV and GCS	*(p. 92)*
E'_{harv}	Required harvested energy for transmission	*(p. 51)*
E_{max}	Maximum energy limit for harvesting	*(pp. 47, 56)*
E_{min}	Minimum energy required for transmission	*(p. 47)*
$\mathbb{E}[\cdot]$	Expectation operator	*(pp. 11, 29, 48, 71, 81)*
E_{PS}	Harvested energy in power-splitting SWIPT	*(p. 20)*
ϵ	Packet error probability	*(pp. 17, 18)*
ε_D	Block error probability at the destination	*(p. 31)*
$\varepsilon_{ovr,k}$	Overall decoding error probability for node k	*(p. 71)*
ε_j^t	Decoding error probability at receiving node $j \in \{i, R\}$ for block received from node $t \in \{i', R\}$ in SWIPT-enabled two-way relay system	*(pp. 48, 49)*
ε_i^R	Decoding error probability at node i for block received from node relay in SWIPT-enabled two-way relay system	*(pp. 49, 137)*
$\varepsilon_R^{i'}$	Decoding error probability at relay for block received from node i' in SWIPT-enabled two-way relay system	*(pp. 49, 137)*
ε_{UAV}	Block error probability at the UAV	*(p. 31)*
E_R	Total energy harvested by the relay within the first transmission slot	*(p. 47)*
E_R^T	Available energy harvested by the relay for transmission	*(p. 47)*
η	Energy harvesting efficiency in the SWIPT-enabled system	*(pp. 20, 47, 56)*
η_{LoS}	Additional environment-dependent excessive path loss for LoS	*(pp. 28, 35, 69, 73, 103)*
η_{NLoS}	Additional environment-dependent excessive path loss for NLoS	*(pp. 28, 35, 69, 73, 95, 103)*
E_{TS}	Harvested energy in time-switching SWIPT	*(p. 20)*
$f(\cdot, \boldsymbol{\vartheta})$	DJSCC encoder function	*(pp. 80, 87, 93, 102)*
f_c	Carrier frequency	*(pp. 28, 35, 46, 56, 95)*
$F(\cdot)$	General notation for the cumulative distribution function (CDF) of a random variable	*(p. 50)*
$f_{c_{i,j}}$	Carrier frequency between nodes i and j	*(p. 69)*
F_{γ_j}	CDF of the instantaneous SNR at node j	*(p. 30)*
$f_{\gamma_j}(z)$	PDF of the instantaneous SNR at node j	*(p. 29)*
$F_{\gamma_{k,U}}(z \mid l_{k,U})$	Conditional CDF of the SNR at the UAV given the horizontal distance between sensor node k and UAV	*(p. 70)*

$f_{\gamma_{k,U}}(z \mid l_{k,U})$	Conditional PDF of the SNR at the UAV given the horizontal distance between sensor node k and UAV *(p. 70)*
$F_{\gamma_j^t}(z)$	Cumulative Distribution Function (CDF) of the SNR γ_j^t in SWIPT-enabled two-way relay system *(pp. 49, 51)*
$f_{\gamma_j^t}(z)$	PDF of the SNR γ_j^t in SWIPT-enabled two-way relay system *(p. 48)*
$f(\cdot)$	General notation for the PDF of a random variable *(p. 50)*
$F_X(x)$	Cumulative Distribution Function (CDF) of an arbitrary random variable X *(p. 69)*
$f_X(x)$	Probability Density Function (PDF) of an arbitrary random variable X *(p. 69)*

G	Channel gain *(pp. 94, 95)*
g_{ij}	Small scale channel gain *(pp. 29, 46, 69)*
g	General notation for Small-scale channel gain *(p. 95)*
γ	General notation for instantaneous SNR *(p. 19)*
$\bar{\gamma}$	General notation for Expectation of SNR *(pp. 18, 81, 101)*
$\bar{\gamma}_j$	Expectation of SNR at node j *(p. 30)*
$\bar{\gamma}_j(l_{i,j})$	Expectation of SNR at node j as a function of distance *(p. 69)*
γ_i	Received SNR at source node i from the relay *(p. 47)*
$\gamma_R^{i'}$	Received SNR at the relay from source node i' *(p. 47)*
γ_j	Instantaneous SNR at node j *(pp. 29, 30, 69)*
γ_{PS}	SNR for power-splitting SWIPT *(p. 20)*
$\bar{\gamma}_{train}$	Fixed average SNR used during the training phase *(pp. 87, 88, 107)*
γ_{TS}	SNR for time-switching SWIPT *(p. 20)*
$\bar{g}_{ij}$	Expectation of small scale channel gain *(pp. 29, 69)*
G_c	Ground Control Station (GCS) *(pp. 92, 97–99, 101)*
g_i	Generation time of updates at the Source *(pp. 10, 31)*
G_{ij}	Channel gain between node *i* and node *j* *(p. 46)*
$g(t)$	Generation time of the freshest update received at time t *(pp. 10, 31, 52, 82, 97)*

H	Altitude of UAV *(pp. 26, 68, 73, 92)*
h	Structure height *(p. 27)*
h_d	Scale parameter describing buildings' heights distribution *(p. 28)*
H_{ij}	Channel coefficient *(pp. 27, 29, 46, 69)*
H_k	General notation channel coefficient *(pp. 17, 20)*

I	Input image *(p. 93)*
$I_0(\cdot)$	Zero-order modified Bessel function of the first kind *(pp. 29, 69, 95)*
I_C	Number of color channels in the input image *(pp. 80, 93)*
I_H	Height of the input image *(pp. 80, 93)*
$\hat{I}$	Estimated reconstruction of the original transmitted image at the receiver *(p. 95)*
I_n	Identity matrix of size n *(pp. 81, 94)*

I_W	Width of the input image *(pp. 80, 93)*	
K	Total number of sensor nodes in the UAV-assisted WSN *(pp. 68, 72, 73)*	
k	Number of bits in a packet *(p. 17)*	
k_b	Number of information bits in a block *(pp. 29, 35, 71, 73)*	
K_f	Rician fading factor *(pp. 29, 69, 95)*	
k_i	Number of information bits in a packet *(p. 17)*	
k_o	Number of additional bits for metadata in a packet *(p. 17)*	
k_P	Total number of pixels in the image *(pp. 80, 93, 96, 107)*	
k_j^t	Number of bits per block for transmission from node t to node j *(p. 48)*	
$\mathcal{L}$	Set of transitions in Stochastic Hybrid System model *(pp. 13, 33, 84, 85, 100)*	
λ_a	Mean update generation rate at source *(pp. 31, 35)*	
λ_I	Average image capture rate *(pp. 82, 87, 89, 97, 102, 105)*	
L_D	Location of destination node *(p. 68)*	
$l_{i,j}$	Horizontal distance between nodes i and j *(pp. 68, 69)*	
L_k	Location of sensor node k *(p. 68)*	
l_{ob}	Distance from transmitter to the obstacle *(p. 27)*	
$\mathcal{L}_q'$	Set of incoming transitions for state q in the SHS model *(p. 13)*	
$\mathcal{L}_q$	Set of outgoing transitions for state q in the SHS model *(p. 13)*	
L_U	Location of UAV *(p. 68)*	
M	Complexity-accuracy trade-off factor in GCQ method *(pp. 51, 70)*	
MAX	Maximum potential value of image pixels *(p. 96)*	
M_B	Average number of buildings per unit area *(p. 28)*	
$M(\cdot, \tau)$	Classifier function *(pp. 81, 87, 95, 102)*	
μ	Update transmission rate *(pp. 31, 82, 87, 97, 102, 105)*	
m_w	Number of time slots in waiting time *(pp. 53, 139, 140)*	
n	Total block length *(pp. 17, 18, 31, 35)*	
n_{con}	Depth parameter of the final encoder layer *(pp. 82, 96, 103)*	
n_e	Number of encoded symbols in a packet *(p. 17)*	
n_f	Number of failures until next successful update *(p. 55)*	
$n_{i,j}$	Length of the block in bits for transmission from node i to node j *(pp. 29, 71)*	
n_o	Number of symbols for packet detection, synchronization, and channel state estimation *(p. 17)*	
$\|\cdot\|$	Euclidean norm of a complex-valued vector *(p. 81)*	
n_T	Channel bandwidth in a DJSCC-based wireless system *(pp. 80, 82, 93, 95, 97)*	
$N(T_c)$	Number of updates by time T_c *(p. 10)*	

n_j^t	Block-length for transmission from node t to node j in SWIPT-enabled two-way relay system *(p. 48)*
ω_i	Weighting coefficient for AAoI at source S_i *(p. 53)*
P	General notation for transmission power of the source *(pp. 81, 94, 103)*
P_0	Area of initial polygon in AoI calculation *(p. 10)*
P_1	Area of final triangle in AoI calculation *(p. 10)*
$P_{a,j}$	Sensor activation probability *(p. 68)*
$P_{a,k}^*$	Optimal active probability of sensor k *(p. 72)*
P_i	Transmission power at node i *(pp. 29, 69)*
$\bar{\pi}$	Stationary probability vector *(pp. 14, 34, 85, 100)*
$P_{i'}$	Transmit power at source $S_{i'}$ in SWIPT system *(p. 47)*
$\pi_{\hat{q}}(t)$	Discrete state probability for state $\hat{q}$ in the SHS model *(p. 13)*
$\pi(t)$	State probability vector in the SHS model *(p. 14)*
P_{LoS}	Probability of Line of Sight *(pp. 27, 69, 94)*
P_{min}	Minimum required power for transmission *(pp. 47, 56, 63)*
P_R	Transmit power of relay *(p. 47)*
P_{req}	Required power at relay for transmission *(pp. 51, 56, 62–64)*
P_S	Transmission power at source *(p. 35)*
$\Xi(\cdot, \cdot)$	Semi-linear approximation function of $1 - Q_1(\cdot, \cdot)$ *(pp. 30, 71)*
P_{UAV}	Transmission power at UAV *(p. 35)*
$P_w(m)$	Probability mass function of waiting time slots *(pp. 53, 54)*
Q	Set of discrete states in Stochastic Hybrid System model *(pp. 13, 33)*
$Q_1(\cdot, \cdot)$	First order Marcum Q-function *(pp. 30, 70, 71)*
$q(\cdot, \tilde{\tau})$	Decoder function in the DJSCC-based communication system *(p. 95)*
$Q(\cdot)$	Q-function *(pp. 29, 48)*
Q_i	Trapezoidal areas in AoI calculation *(p. 10)*
q	Discrete state in the Stochastic Hybrid System (SHS) model *(pp. 13, 84, 85, 99, 100)*
$q(t)$	Discrete states in the SHS model of the AoI process *(pp. 13, 14, 32, 84, 85, 100)*
r	Coverage radius of UAV *(pp. 68, 73)*
ρ	Power splitting factor in SWIPT system *(pp. 20, 47, 56)*
ρ_{ac}	Probability of correct image classification *(pp. 82, 87, 102)*
r_{ij}	Horizontal distance between transmitter i and receiver j *(p. 28)*
R_M	Error term associated with the GCQ method, negligible for high M values *(pp. 51, 70)*
$R_t^*(n, \epsilon)$	Maximum coding rate *(pp. 17, 18)*

W_{ij}	Additive White Gaussian Noise (AWGN) *(p. 27)*
W_k	Additive Gaussian noise *(p. 17)*
$\boldsymbol{W_n}$	Complex Gaussian noise vector *(pp. 81, 94)*
X	Inter-departure time between successful updates *(pp. 11, 55, 56)*
X_0	Initial AoMI *(p. 83)*
$x_0(t)$	Age of Information / age of misclassified information as a random process *(pp. 31, 83, 84, 98, 100)*
X_1	Transmitted signal between source and UAV *(p. 27)*
X_2	Transmitted signal between UAV and destination *(p. 27)*
$\dot{\mathbf{x}}(t)$	Growth rate of the continuous state in the SHS model *(p. 13)*
X_i	Inter-departure time between two consecutive successfully received status updates at source S_i *(p. 53)*
X_k	Channel input *(p. 17)*
^dX_k	Inter-departure time between two consecutive successfully received status updates from sensor node k at the destination D *(p. 72)*
$\mathbf{x}(t)$	Continuous states in the SHS model of the AoI process *(pp. 13, 32, 84)*
Y	Time incurred to traverse through the network (System time) *(pp. 11, 55)*
Y_1	Received signal between source and UAV *(p. 27)*
Y_2	Received signal between UAV and destination *(p. 27)*
Y_k	Channel output *(p. 17)*
Z	Random variable representing the sum of energy harvested in previous time slots *(p. 54)*
z	Received signal in a DJSCC-based wireless system *(pp. 81, 87, 95, 102)*
Z_B	Ratio of land area covered by buildings to total land area *(p. 28)*
ζ_T	Time allocation ratio for information decoding in TS-SWIPT *(p. 20)*
$\hat{z}$	Reshaped signal formed from the real and imaginary components of the received signal z *(pp. 81, 95)*
z_i	Time stamps when updates are received *(pp. 10, 31)*

Chapter 1

Introduction

1.1 Scope and Motivation

The rapid advancement of wireless communication technologies has triggered the era of the internet of things (IoT), cyber-physical systems and robotic networks, offering unprecedented opportunities to enhance efficiency across various aspects of our daily lives [1–3]. These technologies enable the collection and transmission of massive quantities of data through wireless networks, facilitating communication amongst numerous nodes, including sensors, actuators, machines, autonomous vehicles, unmanned aerial vehicle (UAV)s and a wide array of smart devices.

In this context, timely delivery of information has become crucial, particularly for mission-critical applications where outdated data can lead to severe consequences. However, traditional performance metrics such as latency and delay have proven inadequate in capturing the essence of information freshness. To address this limitation, researchers have introduced a novel performance metric called the age of information (AoI) [4–6].

AoI measures the time elapsed since the generation of the most recent update successfully received at the destination, providing a comprehensive understanding of information freshness by considering both the generation and the successful delivery of updates. This metric is particularly crucial for applications such as autonomous vehicles, UAV networks and real-time monitoring systems, where outdated information can have severe consequences.

The scope of this thesis encompasses the investigation of AoI in diverse wireless communication scenarios, including short packet communication systems [7], simultaneous wireless information and power transfer (SWIPT)-enabled cooperative relay networks [8–10], multi-source UAV-assisted wireless sensor network (WSN)s [11–13] and deep learning-based semantic communication systems.

This research was motivated by the need to analyse and optimise AoI under various constraints such as short packet transmissions, energy harvesting (EH) and multiple information sources. It aimed to explore the impact of system parameters including transmission policies, block length and update generation rate on information freshness.

By addressing these critical aspects of AoI in wireless communication systems, this thesis sought to provide valuable insights for the design and optimisation of future wireless networks that prioritise information freshness. The findings contribute to the understanding of how various

1

system parameters impact AoI and guide the development of strategies to maintain timely and relevant information delivery in mission-critical applications.

Furthermore, this thesis extends its scope to include semantic communication, a paradigm that focuses on conveying the meaning of information rather than just bits. This approach is particularly relevant in modern wireless networks, where sending all raw bits is often impossible or a waste of limited resources. By integrating semantic communication principles with AoI analysis, this research aims to enhance the efficiency and relevance of information transmission in wireless networks. This combined approach is especially valuable in scenarios where the semantic content of the information is crucial, such as in image classification for surveillance systems, where transmitting and processing only the most relevant semantic information can significantly reduce bandwidth usage and improve system responsiveness.

The ultimate goal of this research was to enhance the reliability and efficiency of time-sensitive communication systems, paving the way for more effective and responsive IoT applications and cyber-physical systems. By developing a comprehensive framework for analysing and optimising AoI in next-generation wireless networks, including semantic communication aspects, this thesis aims to contribute significantly to the evolving landscape of wireless communications and its wide-ranging applications in our increasingly connected world.

1.2   Problem Statement

The rapid advancement of IoT and mission-critical wireless applications has underscored the necessity for the timely delivery of fresh information. Traditional metrics such as latency and delay have proven inadequate in capturing the essence of information freshness. Consequently, AoI has emerged as a novel performance metric, measuring the time elapsed since the generation of the most recently delivered update at the destination [5].

AoI offers a comprehensive view of information freshness by considering both the generation and delivery times of updates, making it particularly crucial for applications such as autonomous vehicles, UAV networks and real-time monitoring systems, where outdated information can lead to severe consequences [4].

This thesis investigates AoI in diverse wireless communication scenarios, including short packet communication, SWIPT enabled cooperative relay networks, multi-source UAV-assisted WSNs and DJSCC-based image transmission systems. The research aims to analyse and optimise AoI under constraints such as short packet transmissions, EH and multiple information sources whilst exploring the impact of system parameters including transmission policies, block length and network topology on information freshness.

Furthermore, this thesis introduces a novel metric called age of misclassified information (AoMI) to address the limitations of traditional AoI in capturing the impact of information content on usefulness, particularly in applications such as image classification in surveillance systems.

1.3 Research Questions and Hypotheses

This thesis addressed the following research questions and corresponding hypotheses:

1. **Research Question 1:** *How does short packet communication affect the AoI in wireless networks?*

   Hypothesis 1: Short packet communication is expected to introduce a trade-off involving transmission errors and latency that affects AoI. An optimal block length is hypothesised to exist that minimises AoI by balancing these competing effects. This optimal block length is likely to depend on channel conditions, particularly the signal-to-noise ratio (SNR).

2. **Research Question 2:** *How does SWIPT affect the AoI in wireless networks?*

   Hypothesis 2: The integration of SWIPT is expected to significantly impact the AoI in wireless systems. The interplay between EH and data transmission in SWIPT systems may introduce new trade-offs that affect information freshness. This research aims to develop a framework for analyzing AoI in SWIPT-enabled networks, providing insights into the performance of time-sensitive applications in these systems.

3. **Research Question 3:** *How can AoI be optimised in multi-source UAV-assisted WSNs, considering the unique challenges of aerial communication?*

   Hypothesis 3: Incorporating UAVs into WSNs will significantly enhance the freshness of information, as measured by the average age of information (AAoI). By optimizing UAV altitude, block length and sensor activation probability, the system can achieve low latency and high data reliability across diverse environmental conditions, thus improving the overall performance and timeliness of data delivery compared to traditional communication systems.

4. **Research Question 4:** *How can we effectively measure information freshness in semantic wireless communication?*

   Hypothesis 4: Novel content-based AoI metrics that incorporate semantic relevance are expected to more accurately capture information freshness in semantic wireless communication systems compared to traditional AoI metrics. Techniques such as DJSCC, when applied to semantic communication, are anticipated to improve freshness of the semantic information across various channel conditions. This approach is expected to lead to more efficient information transmission and better performance in next-generation wireless systems that prioritise semantic content.

By addressing these research questions and testing these hypotheses, this thesis aims to contribute to the growing body of knowledge on AoI and its applications in next-generation wireless networks, including the emerging field of semantic communications, ultimately enhancing the reliability and efficiency of time-sensitive communication systems.

1.4 Outline and Contributions

This thesis addresses critical research gaps in the understanding of AoI in wireless communication systems. It consists of an introductory chapter and four technical chapters, each focusing on a specific aspect of AoI in modern wireless networks. These chapters are interconnected, building upon each other to provide a comprehensive analysis of AoI across various wireless communication scenarios. The concept of AoI has emerged as a crucial metric for quantifying the freshness of information in communication networks, particularly in mission-critical applications. As wireless communication systems evolve towards 5G and beyond, maintaining the timeliness of information becomes increasingly important. However, several critical research gaps exist in the current understanding of AoI in modern wireless networks. This dissertation addresses these gaps through comprehensive theoretical analysis and practical applications.

The research presented in this thesis addresses four key gaps. Firstly, it tackles the lack of comprehensive AoI analysis in ultra-reliable low latency communications (URLLC)-enabled UAV communication systems. While UAVs offer promising solutions for enhancing wireless coverage and capacity, their impact on information freshness, especially in the context of URLLC, remains understudied. Secondly, it explores the limited understanding of AoI dynamics in SWIPT-enabled cooperative relay networks. The interplay between EH and information freshness in resource-constrained networks presents unique challenges that have not been fully explored. Thirdly, it addresses the insufficient theoretical frameworks for analysing AoI in multi-source UAV-assisted WSNs. The complexity of these systems, involving multiple sensors and mobile aerial relays, necessitates a more robust analytical approach to optimise information freshness. Lastly, it tackles the absence of AoI metrics that account for semantic accuracy in DJSCC-based image transmission and classification systems. As wireless networks increasingly support artificial intelligence-driven applications, there is a pressing need for AoI based metrics that consider both the timeliness and semantic correctness of transmitted information. The following provides a summary of the contributions of each chapter and their interconnections with the objectives of this dissertation.

1.4.1 Chapter 2: Background and Analysis of AoI

Chapter 2 presents a comprehensive literature review and background analysis on AoI in wireless communication systems. The current body of knowledge related to AoI and its applications has been critically analysed in this chapter to provide a strong foundation for the technical work presented in subsequent chapters. The review begins with a deep understanding of the AoI concept, its mathematical formulation and its importance in quantifying information freshness compared to traditional timeliness metrics. The chapter proceeds with an assessment of different analytical approaches to the study of AoI, contrasting the traditional graphical method with the more recent stochastic hybrid system (SHS) approach. The chapter reviews AoI applications across various wireless communication scenarios. First, it provides a critical review of the AoI literature in UAV-enabled communications. This review focuses on how AoI has been used to optimise UAV deployment and communication strategies while maintaining information freshness. It also

examines studies on AoI in short packet communication systems, which address the impact of finite blocklength. Another area that this chapter focuses on is AoI in SWIPT systems; more specifically, it assesses the existing body of literature on the trade-offs between EH and information freshness. Finally, an overview of the emerging AoI area in semantic wireless communication systems is provided, along with indications of how AoI concepts are used for adaptation in content-aware communications. This chapter identifies important research gaps and emerging trends in AoI research, thus providing context and motivation for the original contributions described in the following chapters of the thesis.

1.4.2 Chapter 3: AoI in URLLC-enabled UAV Wireless Communications

This chapter makes significant contributions to the analysis of AoI in URLLC-enabled UAV communication systems. A theoretical model is developed to analyse AoI in these systems and closed-form expressions for AAoI in UAV relay networks are derived. The work determines optimal UAV altitude, block length, transmission power and update generation rate to minimise AAoI. Notably, the chapter extends SHS analysis for wireless systems with transmission errors, providing a robust method for AoI analysis in complex scenarios. The research demonstrates the advantages of UAV-assisted communication in maintaining information freshness compared to direct transmission, offering valuable insights for the design of UAV-based communication networks. This chapter lays the foundation for the subsequent chapters by introducing the concept of AoI in UAV-assisted networks and SHS-based analysis for the AoI, which is further explored and expanded upon in later sections.

1.4.3 Chapter 4 : AoI in SWIPT-Driven Wireless Communications

Building upon the AoI analysis framework established in the previous chapter, this section contributes to the understanding of AoI in SWIPT-enabled cooperative relay networks using finite blocklength theory. It derives expressions for block error rate and AAoI under two different transmission policies: *transmit without waiting (TWW)* and *wait until charged (WUC)*. The work evaluates the impact of various factors on AAoI, including transmission power, packet size and block length. By comparing AoI performance between TWW and WUC policies across different network scenarios, the chapter provides valuable insights into the trade-offs between EH and timely information transmission in resource-constrained networks. This analysis is crucial for optimising the performance of SWIPT-enabled systems in terms of information freshness.

1.4.4 Chapter 5 : AoI-Inspired UAV-Assisted Wireless Sensor Networks

Expanding on the UAV-assisted communication concepts introduced in the third chapter, the contributions of this chapter lie in the development of a theoretical framework for analysing AoI in multi-source UAV-assisted WSNs. Closed-form expressions for network AAoI and block error rate are derived, enabling a comprehensive understanding of information freshness in these complex systems. The work determines optimal UAV altitude, block length and sensor activation probability

to minimise network AAoI. A key contribution is the formulation of a lemma specifying the optimal sensor activation probability for maintaining optimal AoI, which is particularly valuable for the design and optimisation of large-scale sensor networks. The chapter demonstrates the superior performance of UAV-assisted WSNs over traditional fixed base station systems in maintaining information freshness, providing strong support for the adoption of UAV technology in WSNs. This chapter synthesises the concepts from the third chapter, applying them to a more complex multi-source network scenario, thus bridging the gap between theoretical AoI analysis and practical network deployments.

1.4.5 Chapter 6 : AoI in Semantic Communications

Building on the comprehensive AoI analysis developed in the previous chapters, this final chapter makes novel contributions to the field of semantic communications by introducing the concept of AoMI for measuring information freshness in image classification systems. It proposes a DJSCC approach to minimise AoI for image transmission, bridging the gap between semantic communication and information freshness. The chapter develops an expression for average AoMI using the stochastic hybrid systems approach, providing a robust analytical framework for these systems. The application of the proposed framework to a UAV-based wildfire detection system demonstrates its effectiveness in maintaining information freshness for critical applications, whilst also incorporating the UAV communication aspects explored in earlier chapters. This work opens new avenues for research in semantic-aware communication systems that prioritise both the meaning and timeliness of information. This chapter represents the culmination of the thesis, integrating the AoI concepts and UAV-assisted communication developed throughout the dissertation to address the emerging field of semantic communications.

1.4.6 Publications Related to This Thesis

The results of this thesis work were published in 10 publications, including 4 Quartile-1 peer-reviewed journal papers, 1 Quartile-2 peer-reviewed journal paper and 5 international conference papers. The list of publications produced during the Doctor of Philosophy in Informatics programme is as follows:

Journal articles

1. [14] **Basnayaka, C. M. W.**, Jayakody, D. N. K., & Chang, Z. (2021). Age of information-based URLLC-enabled UAV wireless communications system. IEEE Internet of Things Journal, 9(12), 10212-10223.

2. [15] **Basnayaka, C. M. W.**, Jayakody, D. N. K., Perera, T. D. P., & Beko, M. (2024). DataAge: Age of Information in SWIPT-Driven Short Packet IoT Wireless Communications. IEEE Internet of Things Journal, 11(16), 26984-26999.

3. [6] **Basnayaka, C. M. W.**, Jayakody, D. N. K., & Beko, M. (2024). Freshness-in-air: An AoI-inspired UAV-assisted wireless sensor networks. ICT Express,10(5), 1103-1109.

4. [16] Sharma, A.[†], Vanjani, P.[†], Paliwal [†], N., **Basnayaka, C. M. W.**[†], Jayakody, D. N. K., Wang, H. C., & Muthuchidambaranathan, P. (2020). Communication and networking technologies for UAVs: A survey. Journal of Network and Computer Applications, 168, 102739.

5. [17] Sharma, A.[†], Sharma, V.[†], Jaiswal, M., Wang, H. C.[†], Jayakody, D. N. K., **Basnayaka, C. M. W.**[†], & Muthanna, A. (2022). Recent trends in AI-based intelligent sensing. Electronics, 11(10), 1661.

6. **Basnayaka, C. M. W.**, Jayakody, D. N. K., & Beko, M. (2024). Sky Sentinels: UAV-Powered Semantics Wireless Communications for Dynamic Wildfire Detection. (Revision stage).

Conference papers

1. [18] **Basnayaka, C. M. W.**, Jayakody, D. N. K., Perera, T. D. P., & Ribeiro, M. V. (2021, April). Age of information in an URLLC-enabled decode-and-forward wireless communication system. In 2021 IEEE 93rd Vehicular Technology Conference (VTC2021-Spring) (pp. 1-6). IEEE.

2. [19] **Basnayaka, C. M. W.**, Jayakody, D. N. K., & Beko, M. (2023, November). Semantics-Empowered UAV-assisted Wireless Communication System for Wildfire Detection. In 2023 IEEE 28th International Workshop on Computer Aided Modeling and Design of Communication Links and Networks (CAMAD) (pp. 152-157). IEEE.

3. [20] **Basnayaka, C. M. W.**, Jayakody, D. N. K., Perera, T. D. P., Hämäläinen, T. T., & Da Silva, M. M. (2022, December). Age of Information in a SWIPT and URLLC enabled Wireless Communications System. In 2022 IEEE International Conference on Advanced Networks and Telecommunications Systems (ANTS) (pp. 302-307). IEEE.

4. **Basnayaka, C. M. W.**, Jayakody, D. N. K., & Beko, M. (2024, December). Optimizing Real-Time Freshness: Deep Joint Source–Channel Coding Based AoI in Wireless Networks. In 2024 IEEE Global Communications Conference (GLOBECOM). IEEE. (Accepted)

5. [21] Payagalage, P. M. P., **Basnayaka, C. M. W.**, Jayakody, D. N. K., & Kumar, A. (2023, March). Network virtualization and slicing in uav-enabled future networks. In 2023 6th Conference on Cloud and Internet of Things (CIoT) (pp. 98-103). IEEE.

---

[1] [†] These authors contributed equally to this work.

Chapter 2

Background and Analysis of AoI

2.1 Introduction to AoI

The evolution of wireless communication has catalysed a new age of interconnectivity, giving rise to transformative technologies such as the IoT and cyber-physical systems. These innovations promise to revolutionise and optimise numerous aspects of our daily existence [1–3]. In this emerging landscape, a large array of data-gathering devices continuously collect enormous volumes of information, which is then disseminated through extensive wireless networks. While the low-latency transmission of data is critical for time-sensitive applications, maintaining data freshness is equally crucial in ensuring the relevance and utility of the information being communicated [1–3].

To address this pressing need for information freshness, the concept of AoI has emerged as a pivotal performance metric. AoI is defined as the time elapsed since the generation of the last successfully received update at the destination. This metric captures the timeliness and relevance of the data by considering both the generation and successful delivery of updates [5, 15, 20, 22]. This approach, originally employed in the 1990s to determine time consistency in real-time databases, AoI has recently gained significant attention from the wireless communication community, especially for studying status update systems and mission-critical applications [23–26].

The AoI metric deviates from traditional timeliness measures such as latency, offering a more comprehensive approach to quantifying the freshness of received information [4, 5, 20]. It evaluates information freshness from the perspective of the destination as an alternative to well-established performance metrics such as packet delay and round-trip latency [14]. AoI measures the time interval between the generation and delivery of the most recently delivered packet, while packet delay measures the time interval between packet creation and delivery [27].

As a timeliness metric, AoI outperforms delay in effectively capturing the freshness of updates. For instance, even when the transmission delay is minimal, received data may not always be considered fresh if the packet generation rate is low. Conversely, if the update generation rate is high, the received data may still lack freshness if packets experience substantial queuing delays during transmission. Therefore, AoI is recognised as a valuable and pivotal performance metric for mission-critical IoT applications [28].

The importance of AoI becomes particularly crucial in scenarios where the status of sensors

or devices must be known as quickly as possible to make critical decisions. For example, in autonomous vehicles, even a few milliseconds of outdated sensor data could potentially lead to accidents [4]. In IoT networks, maintaining up-to-date status information at the receiver is essential, as most IoT applications are mission-critical and outdated information could result in significant consequences.

2.1.1   The AoI Metric

Consider a simple communication system containing a source-destination pair as illustrated in Figure 2.1. The source sends fresh updates to a network and the network subsequently delivers
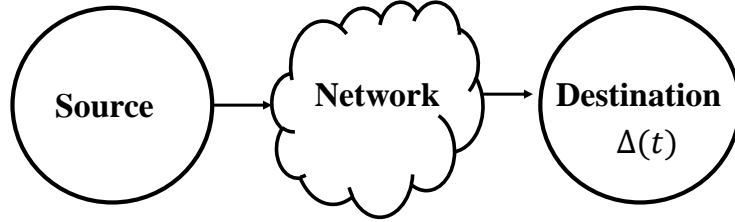
Figure 2.1: Simple communication system containing a source-destination pair

those updates to the destination. The generation time of the most recent update received by the destination at timestamp t denotes as $g(t)$. Then, the AoI $\Delta(t)$ can be described as a random process as follows:

$$\Delta(t) = t - g(t). \tag{2.1}$$

As illustrated in Figure 2.2, it is assumed that at $t = 0$, the measurement of AoI starts. The AoI at the opposite source is set to $\Delta(0) = \Delta_0$. The source generates updates at instants $g_0, g_1, g_2, ..., g_n$. These updates pass through the network and the destination receives them at instants $z_0, z_1, z_2, ..., z_n$. As illustrated in Figure 2.2, data update i is transmitted from the source at time instant $t = g_i$ and it is successfully delivered to the opposite source at time instant $z_i = g_i + Y_i$. Therefore, the AoI at the destination can be calculated as $\Delta(z_i) = z_i - g_i$. The AoI grows at a unit rate until the next update is delivered to the destination. Similarly, AoI just before the $i + 1$ update is successfully delivered can be written as $\Delta(z_{i+1}^-) = Y_i + X_i$. Then, after the update is delivered, the AoI drops as $\Delta\left(z_{i+1}^+\right) = Y_{i+1}$. Hence, the age process $\Delta(t)$ exhibits the saw-tooth pattern as illustrated in Figure 2.2. For a given time period, time average AoI can be computed using the area under $\Delta(t)$. For this system, the observation time interval considered as $[0, T_c]$ and $N(T_c) = \max\{n \mid g_n \leq T_c\}$ denotes the number of updates by time T_c. The area under the curve can be treated as a sum of the polygon area P_0, the trapezoidal areas Q_i for $1 \leq i \leq N(T_c)$ (Q_1 and Q_n are highlighted in the figure) and the triangular area P_1 of width Y_n over the time interval (g_n, z_n) as shown in Figure 2.2. Then, the time average age Δ_{T_c} can be calculated by applying graphical methods to the saw-tooth
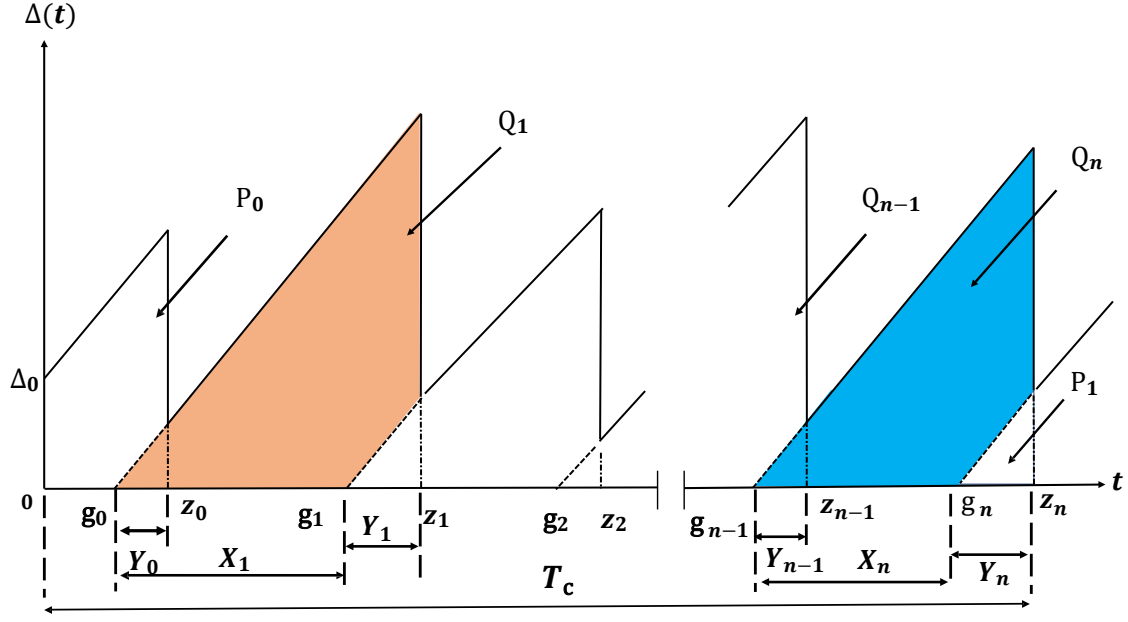
Figure 2.2: Evolution of AoI $\Delta(t)$ with the time at the destination in a simple commutation system containing a source and destination pair: Each source generates updates at time stamps $g_0, g_1, g_2, ..., g_n$ and the opposite source receive these updates at time stamps $z_0, z_1, z_2, ..., z_n$.

age waveform as follows:

$$
\begin{aligned}
\Delta_{T_c} &= \frac{1}{T_c} \int_0^{T_c} \Delta(t) dt \\
&= \frac{P_0 + P_1 + \sum_{i=1}^{N(T_c)} Q_i}{T_c}, \\
&= \frac{P_0 + P_1}{T_c} + \frac{N(T_c)}{T_c} \frac{1}{N(T_c)} \sum_{i=1}^{N(T_c)} Q_i,
\end{aligned}
\tag{2.2}
$$

where

$$
Q_i = \frac{1}{2}(X_i + Y_{i+1})^2 - \frac{1}{2}Y_{i+1}^2 = Y_{i+1}X_i + \frac{1}{2}X_i^2,
$$

where X is the inter-arrival time between delivered updates and Y is the system time of such an update. In here, it is assumed that the system is stationary and ergodic [29] and time average age Δ_{T_c} tends to ensemble-average age Δ_i^{AAoI} when $T_c \to \infty$, i.e.

$$
\Delta^{AAOI} = \lim_{T_c \to \infty} \Delta_{T_c}.
\tag{2.3}
$$

When $T_c \to \infty$, $\frac{N(T_c)}{T_c} \to \frac{1}{\mathbb{E}[X]}$, $\frac{1}{N(T_c)} \sum_{i=1}^{N(T_c)} Q_i \to \mathbb{E}[Q]$ and the $\frac{P_0+P_1}{T_c}$ term goes to zero, where $\mathbb{E}[\cdot]$ is the expectation operator. Thus, the AAoI (Δ^{AAoI}) can be written as

$$
\Delta^{AAOI} = \frac{\frac{\mathbb{E}[X^2]}{2} + \mathbb{E}[XY]}{\mathbb{E}[X]}.
\tag{2.4}
$$

In general, $\mathbb{E}[XY]$ is difficult to estimate since X and Y are dependent random variables for most of the wireless systems. Hence, despite its simplicity, calculating the AoI in complex wireless

11

systems using this type of graphical analysis is challenging. However, the SHS analysis has been introduced as a new tool to analyse AoI replacing traditional graphical-based AoI analysis [30].

The AoI is widely regarded as a destination-centric metric since it measures the time difference between the current time and the generation time of the most recent update received by the destination. It only takes into consideration packets that are correctly sent to the destination. Moreover, the AoI is strongly affected by the system delay and the update generation rate at the source. In contrast to AoI, the delay is a traditional timeliness metric that measures the latency of a packet and is considered a packet-centric metric. On the other hand, the update (or packet) generation rate at the source does not affect the delay [31].

2.2 Analytical Approaches for AoI

AoI has emerged as a critical metric in real-time systems, prompting extensive research across diverse queueing models. The initial work by Kaul et al. [32, 33] analysed AoI in queues M / M / 1, M / D / 1 and D / M / 1 first-come first-served (FCFS), establishing a foundation for future studies. This research aimed to characterise and minimise AoI, focusing on two key AoI-based metrics: time-average age and average peak age.

As the field progressed, the scope expanded to more complex queue types, including M/G/1, G/M/1 and G/G/1 [4, 34–39]. Alternative service policies, such as last-come first-served (LCFS) and various packet management strategies, were analysed under different arrival and service time distributions [40, 41]. System modifications, including reduced buffer sizes and packet deadlines [42], demonstrated the potential to improve AoI in FCFS systems. Significant findings in AoI research include the establishment of LCFS and last-generated first-served (LGFS) policy optimality [35, 43, 44], the benefits of parallel servers in AoI improvement [44, 45] and the impact of packet errors or drops on AoI [46, 47]. Some studies challenged conventional approach, questioning whether deterministic update generation and service times always minimise AoI [48]. The literature also identified trade-offs between AoI metrics and packet delay [31, 49] and analysed age performance for sources with varying priorities [50].

Two primary analytical methods have emerged in AoI studies: the graphical area decomposition method [32, 45, 51] and the SHS method [30, 52–58]. These tools have advanced the understanding of AoI across various scenarios and system configurations. The conventional graphical analysis, which calculates the area under the instantaneous AoI curve, provides a visual representation of AoI evolution over time. Although this approach is well-suited for simple systems, it becomes progressively more complex when applied to systems with multiple data sources or complex update patterns. On the other hand, the SHS method treats instantaneous AoI as a stochastic process with both discrete and continuous characteristics [59, 60]. The SHS model combines continuous state variables (representing age) with discrete state variables (representing system states such as idle or busy). This method is particularly effective for analysing systems with random arrivals, service times and multiple servers or sources.

The SHS model offers advantages over the graphical method for complex wireless communication systems with transmission errors. It enables the derivation of closed-form expressions for

AAoI and related metrics, even in systems with complex dynamics. The SHS approach has been successfully applied to various scenarios, including multi-source systems, prioritised systems and networks with EH nodes.

2.2.1 Stochastic Hybrid System for AoI

Generally, in SHS techniques, the AoI process is modeled as a combination of continuous states x(t) and discrete states $q(t)$. Moreover, discrete states $q(t) \in Q = \{0, 1, \cdots, m\}$ capture status of the communication network that can be represented using Markov chain. The evaluation of the age process of the wireless network is represented using continuous vector x(t) = $[x_0(t), x_1(t), \cdots, x_n(t)] \in \mathbb{R}^{1 \times n+1}$. Then, the SHS model can be described using a directed graph $(Q, \mathcal{L})$, where Q is the set of discrete states and $\mathcal{L}$ is the set of transitions, with each state as a node and each transition as a directed edge. The transaction rate from node q_l to node q_l' is $\lambda^{(l)} \delta_{q_l, q_{(t)}}$, where Kronecker delta function $\delta_{\hat{q}, q(t)}$ limit occurrence of transition only for the state q_l. For each transition l, most of the time, there is a discontinuous jump in the continuous state and it can be represented using linear transition reset mapping as follows:

$$\text{x}' = \text{x}\mathbf{A}_l, \tag{2.5}$$

where $\mathbf{A}_l \in \{0, 1\}^{(n+1) \times (n+1)}$ is a binary transition reset map matrix. The growth rate of the continuous state ($\dot{\text{x}}(t)$)) at each discrete $q(t) = q$ where $q \in Q$ given by

$$\dot{\text{x}}(t) = \frac{\partial \text{x}(t)}{\partial t} = \text{b}_q, \tag{2.6}$$

where $\text{b}_q = [\text{b}_{q,0}\, \text{b}_{q,1}, \cdots, \text{b}_{q,n}]$ is a vector that contains only binary elements. When $\text{x}_j(t)$ grows at a unit rate as a normal age process in the state q, $\text{b}_{q,j} = 1$ and when it is irrelevant to the ageing process or does not need to be tracked in the state q, $\text{b}_{q,j} = 0$. Let $\pi_{\hat{q}}(t)$ denote the discrete state probabilities for all $\hat{q} \in Q$ and $\text{v}_{\hat{q}}(t)$ denote the the conditional expectation of the age process, given that $q(t) = \hat{q}$, weighed by the probability of being in $\hat{q}$. Accordingly, the following is obtained:

$$\pi_{\hat{q}}(t) = \mathbb{E}\left[\delta_{\hat{q}, q(t)}\right], \tag{2.7}$$

and the correlation vector function

$$\text{v}_{\hat{q}}(t) = \left[v_{\hat{q}0}(t), \cdots, v_{\hat{q}n}(t)\right], \tag{2.8}$$

where $v_{\hat{q}j}(t)$ can be defined as

$$v_{\hat{q}j}(t) = \mathbb{E}\left[x_j(t)\,\delta_{\hat{q}, q(t)}\right], 0 \leq j \leq n. \tag{2.9}$$

All transactions $\mathcal{L}$ can be divided into two categories: incoming transitions ($\mathcal{L}_q'$) and outbound transitions ($\mathcal{L}_q$). Then, for each state q, all incoming transitions are labelled as

$$\mathcal{L}_q' = \left\{l \in \mathcal{L} : q_l' = q\right\} \tag{2.10}$$

and all outgoing transitions are labelled as

$$\mathcal{L}_q = \{l \in \mathcal{L} : q_l = q\} . \tag{2.11}$$

To compute the time average age, it is assumed that the Markov chain $q(t)$ is ergodic. Hence, the state probability vector $\pi(t) = [\pi_0 (t) , \cdots , \pi_m (t)]$ always converges to unique stationary vector $\bar{\pi} = [\bar{\pi}_0, \cdots, \bar{\pi}_m]$ satisfying

$$\bar{\pi}_{\bar{q}} \sum_{l \in \mathcal{L}_{\bar{q}}} \lambda^{(l)} = \sum_{l \in \mathcal{L}'_{\bar{q}}} \lambda^{(l)} \bar{\pi}_{q_l}, \bar{q} \in Q, \tag{2.12}$$

$$\sum_{\bar{q} \in Q} \bar{\pi}_{\bar{q}} = 1. \tag{2.13}$$

As it has been shown in [55], when $\pi (t) = \bar{\pi}, \mathrm{v} (t) = [\mathrm{v}_0 (t) , \cdots , \mathrm{v}_m (t)]$, the system follows first-order differential equations for all $\bar{q} \in Q$ as follows:

$$\dot{\mathrm{v}}_{\bar{q}} (t) = \mathrm{b}_{\bar{q}} \bar{\pi}_{\bar{q}} + \sum_{l \in \mathcal{L}'_{\bar{q}}} \lambda^{(l)} \mathrm{v}_{q_l} (t) \mathbf{A}_l - \mathrm{v}_{\bar{q}} (t) \sum_{l \in \mathcal{L}_{\bar{q}}} \lambda^{(l)}. \tag{2.14}$$

Under the ergodicity assumption, the differential equation (2.14) is stable and each $\mathrm{v}_{\bar{q}} (t) = \mathbb{E} \left[\mathrm{x} (t) \delta_{\bar{q}, q(t)} \right]$ converge to a non-negative limit $\bar{\mathrm{v}}_{\bar{q}}$ as $t \rightarrow \infty$. Accordingly, the following is obtained:

$$\mathbb{E} [\mathrm{x}] = \lim_{t \rightarrow \infty} \mathbb{E} [\mathrm{x} (t)] = \lim_{t \rightarrow \infty} \mathbb{E} \left[\mathrm{x} (t) \delta_{\bar{q}, q(t)} \right] = \sum_{\bar{q} \in Q} \bar{\mathrm{v}}_{\bar{\mathrm{q}}}, \tag{2.15}$$

$$\bar{\mathrm{v}}_{\bar{q}} \sum_{l \in \mathcal{L}_{\bar{q}}} \lambda^{(l)} = \mathrm{b}_{\bar{q}} \bar{\pi}_{\bar{q}} + \sum_{l \in \mathcal{L}'_{\bar{q}}} \lambda^{(l)} \bar{\mathrm{v}}_{q_l} \mathbf{A}_l, \bar{q} \in Q. \tag{2.16}$$

Here, $x_0 (t)$ is the age at the destination and AAoI at the destination (Δ^{AAoI}) is calculated as follows [61]:

$$\Delta^{AAoI} = \mathbb{E} [x_0] = \lim_{t \rightarrow \infty} \mathbb{E} [x_0 (t)] = \sum_{\bar{q} \in Q} \bar{v}_{\bar{q}0}. \tag{2.17}$$

2.3 AoI in Various Wireless Communication Scenarios

2.3.1 AoI in UAV-Enabled Communications

In recent years, significant interest has been observed in the integration of UAV communication systems into existing and future cellular networks [21, 62–64]. This concept can be traced back to the early 2000s, with early prototypes such as the one developed by Wzorek et al. in 2006, which demonstrated a network between two UAVs and a ground operator using General packet radio service technology [65]. However, due to technological limitations at the time, immediate commercialization of this idea was not feasible.

A significant advancement was made in 2016 when China Mobile Research Institute and Ericsson presented field results from a prototype long-term evolution (LTE)-UAV integrated network. This prototype elucidated the potential benefits of mobile technologies for the drone ecosystem and analysed the service requirements of mobile networks [66–68]. Subsequent research

led to several proposals by the 3rd generation partnership project (3GPP) that investigated the capability of aerial vehicles to serve using LTE networks [69]. These studies concluded in 2017 and resulted in a comprehensive 3GPP technical report documenting analysis, evaluation and field measurement results.

In the context of UAV-assisted communication networks, the concept of the AoI has been identified as a critical factor. UAVs have gained prominence in mobile networks such as 5G and beyond, owing to their potential as mobile relays to enhance the reliability and timeliness of information. This capability is deemed crucial for the advancement of IoT applications [11–13, 16, 70–72].

Recent studies have focused on applying the AoI concept to various wireless communication scenarios, with UAV-enabled communication systems emerging as a significant area of research. Investigations have been conducted on the average peak AoI for UAV-enabled mobile relays, involving the optimisation of flight trajectories, energy consumption and service time to reduce AoI [73]. These studies have demonstrated that careful planning of UAV paths and energy usage can significantly reduce AoI compared to static relay systems.

The deployment of multiple UAVs has also been explored as a solution to address the challenges of limited energy storage in single UAV operations [74]. Multi-UAV systems have shown potential for further AoI reduction by enabling more efficient coverage of sensor networks and providing redundancy in case of UAV failures or energy depletion. Additional studies have examined AoI-optimal data collection in WSNs [75, 76], addressing the challenges of maintaining information freshness during data collection operations.

Beyond AoI optimisation, researchers have investigated various aspects of UAV-assisted communication networks. Short packet communication has received considerable attention for addressing challenging problems in these networks [77]. Studies have explored the feasibility of employing UAVs to support URLLC using short packet communication [78, 79]. These works have addressed various aspects, including the optimisation of transmit power and block length, the evaluation of latency and reliability and the combination of passive beamforming with resource allocation and UAV positioning. Furthermore, investigations have been conducted on the average packet error probability and effective throughput of the control link in UAV communications [80]. UAV-enabled relay communication systems have been proposed for transmitting latency-critical messages with ultra-high reliability [81]. As UAV-assisted communication networks continue to evolve, addressing the aforementioned challenges and optimising performance metrics such as AoI and latency will be crucial for their successful integration into future wireless communication systems and IoT applications. The ongoing research in this domain is expected to yield significant advancements in the field of UAV-assisted communications, paving the way for more efficient and reliable aerial communication networks.

2.3.1.1 AoI in UAV-Assisted Wireless Sensor Networks

The rapid growth of the IoT, cyber-physical systems and UAV-assisted communication networks has unlocked unprecedented opportunities to enhance efficiency across countless domains of our

daily lives. Among these, UAV-assisted WSNs have garnered substantial interest and attention for their potential applications spanning agriculture, disaster relief operations, military endeavours and beyond [11–13]. The decisive advantage of employing a UAV-based station in WSNs lies in its ability to establish reliable line-of-sight (LoS) communication links with ground nodes, thereby mitigating the adverse effects of obstacles and non-line-of-sight (NLoS) conditions that plague traditional terrestrial base stations. By acting as an aerial relay, the UAV can effectively bypass physical obstructions and maintain strong communication links, ensuring timely and reliable data collection from the distributed sensor nodes. This is particularly crucial in urban environments, disaster zones, or terrains where terrestrial infrastructure may be compromised or inaccessible. Moreover, the mobility and flexibility of UAVs enable dynamic adaptation to changing network conditions, allowing for optimal positioning to minimise communication delays [82].

In time-critical WSN applications where prompt and accurate information is of the essence, maintaining the freshness and reliability of data is paramount importance, as outdated or stale information can precipitate severe and far-reaching consequences. The AoI metric furnishes valuable insights into the effectiveness of time-sensitive UAV-assisted WSNs, serving as a potent tool for evaluating their performance [25, 83, 84]. While existing works have analysed AoI for single-source or grant-based protocols in URLLC-enabled UAV networks [14, 82, 85], they have largely overlooked the challenges posed by multi-source scenarios that are prevalent in practical WSN deployments. Notably, in real-world WSN environments, multiple sensing nodes often coexist and transmit data simultaneously, leading to potential collisions, interference and degradation of information freshness. Failing to account for these multi-source dynamics can result in inaccurate estimates of system performance and suboptimal resource allocation, ultimately compromising the effectiveness of the WSN in time-critical applications [86].

2.3.2 AoI in Short Packet Communication Systems

The integration of AoI analysis with short packet communication has become a crucial area of research for future wireless networks, particularly in the context of 5G and beyond. 5G mobile networks are designed to address three key use cases: enhanced mobile broadband (eMBB), massive machine-type communication (mMTC) and URLLC. Currently, the application areas of eMBB and mMTC have achieved a satisfactory level [7, 87, 88]. However, achieving the latency and reliability requirements set by the URLLC standard is more challenging than the other two use cases.

Traditionally, long codewords have been used to maintain reliable wireless communication. On the other hand, short packet communication is considered an essential feature to support low latency [89]. However, short-packet communication has a higher transmission error rate than traditional long-packet transmission, making it challenging to maintain reliability requirements. As a result, more resources are needed for retransmissions and redundancy to improve reliability, but these induce high latency. Hence, it is necessary to carefully navigate these two constraints to meet the requirements of URLLC.

Thus, it is inappropriate to use conventional asymptotic information-theoretical results deployed for long-packet communication to calculate the block error probability in short-packet

communication. To address these challenges, researchers have been developing new techniques and theoretical frameworks. A significant breakthrough came from Polyanskiy, Poor and Verdú (PPV) [90], who derived an accurate approximation of the achievable coding rate for Additive white Gaussian noise (AWGN) channels within the finite block-length regime. This work has since been expanded to investigate coding rates in various situations, including block-fading [89], multiple-input and multiple-output [91], relaying [92] and multi-access communication [93]. As a result, finite block-length information theory has become a valuable theoretical tool for analysing short-packet communication in wireless systems [7, 16, 94–96].

In wireless systems, packet structure plays a crucial role in information transmission. Each packet contains information bits and additional redundancy bits for error correction. The payload consists of k bits, including k_i information bits and k_o additional bits for metadata. This payload is typically encoded into n_e symbols, with n_o symbols added for packet detection, synchronisation and channel state estimation. The total packet length n is thus given by $n = n_e + n_o$. The efficiency of a communication system is often measured by its net transmission rate, R_t, defined as $R_t = k_i/n$. This ratio represents the number of information bits per complex symbol or, equivalently, the number of transmitted payload bits per second per unit bandwidth. In most current wireless systems, $k_i \gg k_o$ and $n_e \gg n_o$, making R_t approximately equal to k/n_e. A communication channel model can be expressed as:

$$Y_k = H_k X_k + W_k, \quad k \in \mathbb{N}, \tag{2.18}$$

where Y_k is the channel output, X_k is the transmitted complex symbol, H_k is the channel coefficient and W_k is the additive Gaussian noise. This model forms the basis for analysing different channel types in wireless communications. Two main channel types are considered: the AWGN channel and the non-ergodic channel. In the AWGN channel, H_k is a constant known to both the transmitter and receiver. For such ergodic channels, the relevant performance metric is the capacity C. In contrast, for non-ergodic channels, where H_k is random but constant over time, the outage capacity C_ϵ becomes a more relevant metric due to the inability to make the error probability arbitrarily small by increasing n_e. For short-packet communications, the concept of maximum coding rate $R_t^*(n, \epsilon)$ is introduced. It represents the largest rate k/n for which there exists an encoder/decoder pair with a packet error probability not exceeding ϵ. The relationship between $R_t^*(n, \epsilon)$ and traditional metrics is expressed as:

$$C_\epsilon = \lim_{n \to \infty} R^*(n, \epsilon), \tag{2.19}$$

$$C = \lim_{\epsilon \to 0} \lim_{n \to \infty} R^*(n, \epsilon). \tag{2.20}$$

In the non-asymptotic regime of communication systems, there exists no exact formula to determine the $R_t^*(n, \epsilon)$ as a function of blocklength and error probability. However, significant progress has been made through the development of tight achievability and converse bounds that effectively characterise the fundamental limits, even for blocklengths as short as 100 symbols. These bounds, along with normal approximations, have revealed that the necessary backoff from channel capacity in the finite blocklength regime can be accurately and succinctly characterised by a single parameter known as channel dispersion. This parameter quantifies the stochastic variability of the channel relative to a deterministic channel with the same capacity, providing a fundamental measure of

17

how channel uncertainty affects achievable rates. The channel dispersion directly controls the size of the rate penalty term, determining the required reduction in transmission rate below capacity. A larger channel dispersion requires more backoff from capacity for a given blocklength and error probability, whilst a channel with zero dispersion achieves capacity exactly even with finite blocklengths. This provides a precise, quantitative way to understand the fundamental limits of short-packet communication. Thus, for various channels with positive capacity C, $R_t^*(n, \epsilon)$ can be approximated as [90]:

$$R^*(n, \epsilon) \approx C - \sqrt{\frac{V}{n}} Q^{-1}(\epsilon) + O\left(\frac{\log n}{n}\right), \tag{2.21}$$

where V is the channel dispersion and Q^{-1} is the inverse of the Gaussian Q function. This expression shows how the penalty term $\sqrt{\frac{V}{n}} Q^{-1}(\epsilon)$ quantifies the necessary rate reduction in finite blocklength communications. The scaling with $\frac{1}{\sqrt{n}}$ demonstrates how this penalty diminishes with increasing blocklength, though at a relatively slow rate. The presence of $Q^{-1}(\epsilon)$ captures how the required rate reduction grows as stricter reliability requirements are imposed. The remainder term $O\left(\frac{\log n}{n}\right)$ becomes negligible for moderate blocklengths, allowing the first two terms to provide an accurate approximation in most practical scenarios. For the average-power constrained AWGN channel, where $H_k = 1$, the model simplifies to:

$$Y_k = X_k + W_k. \tag{2.22}$$

The capacity and channel dispersion for this channel are given by [95]:

$$C(\bar{\gamma}) = \log(1 + \bar{\gamma}), \tag{2.23}$$

$$V(\bar{\gamma}) = \frac{\bar{\gamma}(2 + \bar{\gamma})}{(1 + \bar{\gamma})^2} (\log e)^2, \tag{2.24}$$

where $\bar{\gamma}$ is the SNR. A good approximation for $R_t^*(n, \epsilon)$, known as the normal approximation, can be obtained by ignoring the $O(\frac{\log n}{n})$ term, resulting in:

$$R^*(n, \epsilon) \approx C - \sqrt{\frac{V}{n}} Q^{-1}(\epsilon). \tag{2.25}$$

The approximation in (2.25) provides a simpler way to characterise the maximum coding rate by omitting the remainder term $O\left(\frac{\log n}{n}\right)$, as this term becomes negligible for practical blocklengths. The expression clearly shows how the achievable rate relates to capacity C, blocklength n, error probability ϵ, and channel dispersion V. This approximation is termed the normal approximation due to its relation to the Gaussian (or normal) distribution. However, whilst this approximation is accurate for many practical scenarios, it may lose precision for very short block lengths (e.g., $n < 100$) or when extremely low error probabilities are required (e.g., $\epsilon < 10^{-5}$) [97]. Finally, given R_t, the packet error probability ϵ (block error probability) can be approximated as:

$$\epsilon \approx Q\left(\frac{nC - k}{\sqrt{nV}}\right). \tag{2.26}$$

Furthermore, Yang et al. extended the normal approximation (2.25) to estimate finite-length code performance across fading channels as follows [97, 98]:

$$\epsilon \approx \mathbb{E}\left[Q\left(\frac{n\left(\log_2(1+\gamma)\right)-k}{\sqrt{n\left(\frac{\log_2^2 e}{2}(1-\frac{1}{(1+\gamma)^2})\right)}}\right)\right],\qquad(2.27)$$

where the expectation is taken for the distribution of the instantaneous (random) SNR, γ. This approach assumes perfect channel state information (CSI) at the receiver. The extension aims to predict code performance more accurately in realistic wireless environments with fluctuating channel conditions. In contrast to previous approximations that considered only static channels, this formulation explicitly accounts for the random nature of wireless fading channels. By incorporating fading effects through expectation over the SNR distribution, this method provides a valuable tool for analysing communication system performance under practical conditions, particularly in scenarios where channel conditions vary significantly over time.

Furthermore, while substantial research has focused on AoI and delay analysis under the traditional assumption of infinite block length, considerably less attention has been devoted to AoI analysis and optimisation in the context of finite block length. Addressing this gap, the AoI metric for short packet communication was investigated in [99–103]. This research specifically addressed monitoring and automation systems that transmit short packet status updates, where finite block length is particularly relevant. Conventional Shannon-based systems can achieve arbitrarily low error rates by maintaining coding rates below channel capacity. In contrast, short packet systems exhibit persistent errors, with error rates strongly dependent on packet length, as described in equations (2.26) and (2.27). Recognising this fundamental difference, the authors of [99–103] examined the critical question: What is the impact of packet length on AoI performance in short packet systems transmitting status updates? Their findings revealed the existence of an optimal packet length that minimises AoI metrics, providing valuable insights for the design of systems where AoI is a key performance indicator.

2.4 AoI in SWIPT systems

SWIPT is a key enabling technology for future wireless communication systems, offering improved spectral efficiency and addressing energy constraints in IoT devices. This technique allows receivers to simultaneously harvest energy and decode information using various strategies and receiver architectures. Traditionally, SWIPT systems are classified into four types based on receiver architectures: separate antenna architecture, time switching-based SWIPT (TS-SWIPT), power splitting-based SWIPT (PS-SWIPT) and antenna switching-based SWIPT [8–10, 104, 105].

The separate antenna architecture uses distinct antennas for EH and information decoding (ID), providing a simple approach that does not affect ID performance. However, its main drawback is that it is not suitable for single-antenna sensor devices. Antenna switching architecture, similar to the separate antenna approach, uses sets of antennas for EH and ID, allowing allocation based

on energy needs. It can be adapted with PS-SWIPT for optimised power allocation but shares the limitation of being unsuitable for single-antenna devices [106].

PS-SWIPT shares the same antenna for EH and ID, using a special circuit to divide received signal power between the two processes. This allows for the adjustment of the energy resources between EH and ID [107]. The harvested energy in PS-SWIPT, denoted as E_{PS}, is expressed as:

$$E_{PS} = \frac{\eta P(1 - \rho)|H_k|^2 T}{d^\kappa},$$
(2.28)

where η is the EH efficiency, P is the transmitted power, ρ is the power splitting ratio, H_k is the channel coefficient, T is the transmission time, d is the distance and κ is the path loss exponent. The SNR for PS-SWIPT, γ_{PS}, is given by:

$$\gamma_{PS} = \frac{P\rho|H_k|^2 d^{-\kappa}}{N_0},$$
(2.29)

where N_0 is the noise power. TS-SWIPT also shares the same antenna for EH and ID but uses a special circuit to periodically switch between the two processes. The harvested energy in TS-SWIPT, E_{TS}, is expressed as:

$$E_{TS} = \frac{\eta T_t(1 - \zeta_T)P|H_k|^2}{d^\kappa},$$
(2.30)

where ζ_T is the time allocation ratio for ID and T_t is the total transmission time. The SNR for TS-SWIPT, γ_{TS}, is given by:

$$\gamma_{TS} = \frac{T_t(1 - \zeta_T)P|H_k|^2 d^{-\kappa}}{N_0}.$$
(2.31)

All existing SWIPT techniques suffer performance degradation due to resource allocation for EH purposes. To address these limitations, novel approaches have been proposed, including Modulation-based SWIPT and Frame-based SWIPT. These techniques explore unique ways to allocate specific sets of symbols for EH and ID, potentially improving system performance [108].

M-SWIPT adopts a symbol-wise EH technique and can be used with both time-division multiple access and frequency-division multiple access (FDMA) signal transmission techniques. Frame-based SWIPT allocates specific symbols for EH and the remaining symbols for ID but can only be adopted with FDMA. Both techniques offer the additional benefit of exploiting symbols allocated for EH for other signal processing applications [109].

Furthermore, SWIPT-enabled two-way communication systems were investigated in [10, 110, 111]. In the real world, these types of SWIPT-enabled two-way relays can be employed as roadside units in vehicular communication networks and as UAV relays in UAV-assisted wireless networks. However, the incorporation of EH into wireless networks introduces additional complexity [112, 113]. In shared environments, devices contend for both data transmission and EH opportunities. This heightened competition can give rise to conflicts over resource allocation, consequently affecting the reliability and timeliness of information [25, 114]. Fluctuations in energy availability for devices relying on harvesting further exacerbate the issue, potentially resulting in increased data packet loss and diminished overall communication reliability [20].

Prioritising EH over immediate information transmission introduces trade-offs, which may lead to delays. The storage of data until sufficient energy is harvested can also take up limited buffer space, causing further delays and potentially impacting the freshness of information. Thus, SWIPT enabled cooperative communication systems should be investigated by integrating finite block-length information theory and AoI to analyse how resource sharing will affect information freshness and reliability. However, the AoI analysis for EH relay networks is relatively novel. Most of the existing research was conducted on simple one-way relay networks or long-block-length transmission [115–118].

Few studies have investigated the timeliness of SWIPT systems using conventional timeliness metrics. For example, in [119], the authors discussed a latency-aware multiantenna SWIPT system with battery-constrained receivers. In their work, the authors jointly considered the interdependence of latency and battery dynamics in SWIPT-enabled systems. They proposed radio resource allocation schemes that enable the system to meet latency and EH requirements at the user equipment while preventing excessive battery depletion. However, these works on SWIPT have mainly focused on improving energy efficiency and latency, with less emphasis on the freshness and reliability of the information.

The AoI has been widely used as a performance metric to quantify the freshness of information over time. In recent times, few attempts have been made to apply AoI as a performance metric in SWIPT-enabled wireless communication systems. In [25], the performance of the AoI is examined in a SWIPT-enabled cooperative wireless communication system. The authors have calculated the AoI performance of the relay node for both the time switching and power splitting protocols. However, it is important to note that in [25] authors did not pay significant attention to transmission errors and the specific policies employed for packet transmission.

In [120], the AoI was employed to measure the freshness of the information in a SWIPT-enabled re-configurable intelligent surfaces (RIS)-assisted communication network. The authors of [121] discussed the AoI as a performance metric for a sensor network equipped with wireless power transfer. However, both of these works have given little attention to the reliability of the transmissions and the transmission policies that are considered to reduce AoI. In addition, the authors of [122] investigated information freshness in a SWIPT-enabled real-time monitoring system where several source nodes are responsible for delivering update packets to a single destination node. This work further examined the optimal online sampling policy for the proposed system configuration, aiming to minimise the average weighted sum of AoI values for various physical processes at the destination node. However, the vast majority of the existing literature related to the AoI and SWIPT regards asymptotic, in terms of block-length, analysis.

On the other hand, Ref. [123–125] analysed the performance of SWIPT-enabled EH cooperative communication systems using finite block-length information theory. However, these existing works related to finite block-length information theory and SWIPT also do not analyse the freshness of the information using AoI. Alternatively, simple communication scenarios were considered in these works. Current literature appears to lack a comprehensive analysis of information freshness in SWIPT-based cooperative wireless networks using finite block-length theory and AoI.

2.5 AoI in Semantic Wireless Communication Systems

In recent years, the field of wireless communication has undergone a substantial transformation due to the emergence of semantic communication principles, which have outperformed traditional techniques [19, 126–131]. Instead of focusing primarily on the accurate transmission of individual symbols or bits, semantic communication prioritises the conveying of intended meaning and context from the information source.

As early as 1949, Weaver [132] introduced the notion of transmitting messages with meaningful intent, expanding Shannon's communication theory by introducing semantic and effective-based communication systems. While the semantic communication system aims to convey semantic information, an effective system focuses on efficient and goal-oriented design. Initially, semantic communication and goal-oriented communication did not receive significant attention, largely due to the urgent need for Shannon's reliable and high-rate communication methods and the limited computational power to develop semantic-aware communication systems [133–136].

Today's wireless mobile communication systems, such as 5G have significantly improved their data transmission speeds, surpassing previous generations. Current progress in wireless communication research brings the achievable rate of current wireless communications systems closer to the theoretical limits defined by Shannon's theorem using more efficient channel coding schemes such as Polar codes and low-density parity-check code (LDPC) codes [137–139]. Additionally, various innovative applications have emerged in wireless communications, including IoT applications, industrial automation, smart agriculture, environmental and healthcare monitoring and smart sensor networks [16, 140]. However, integrating these applications into wireless communication networks results in a surge of data, potentially reaching zettabyte scales [141]. Semantic-based communication approaches offer a potential solution by focusing on the meaning of the transmitted information. This involves extracting semantic meanings from data whilst filtering out unnecessary information. This process allows efficient data compression whilst retaining essential semantic content. Notably, this communication approach is particularly robust, even in challenging conditions with weak signals compared to background noise (low SNRs), making it well-suited for applications demanding high reliability.

One of the strategies for developing a semantic communication system is treating it as a joint source-channel coding (JSCC) problem [142–144]. JSCC has been a long-standing challenge in communication and coding theory. Recent breakthroughs have demonstrated significant performance improvements over traditional systems that treat source and channel coding separately. This improvement is especially pronounced in scenarios where low latency and low power consumption are critical. Recent advances in JSCC are mainly due to the integration of deep learning techniques. Deep learning-based JSCC schemes have been shown to outperform traditional JSCC methods. Several studies have investigated the application of deep learning-based JSCC, particularly DJSCC, for image transmission [145–148]. This approach has shown promising results in enhancing the efficiency and robustness of semantic communication systems.

Applying the AAoI metric has demonstrated substantial improvements in data freshness in various applications [25, 149]. However, it is important to acknowledge the inherent limitations

associated with this metric. Specifically, the AoI metric relies solely on temporal timestamps to quantify the freshness of data, disregarding the actual information content in the transmitted packets. This limitation gives rise to scenarios in which the AoI metric may not adequately capture the real-world significance of transmitted data. It is especially relevant in contexts where the content itself carries more weight than its temporal arrival.

After recognising the limitations of the AoI concept, researchers introduced several alternative interpretations of the age concept. For example, a new performance metric called the "age of incorrect information" is introduced in [150]. This extended version of the AoI metric addresses the limitations of both the AoI and established error penalty methods by broadening the concept of timely updates to encompass updates that are not only recent yet also considered "informative". In this context, "informative" refers to updates that deliver fresh and accurate information to the receiver. In [29], another metric termed the Value of Information of Update is presented. This metric effectively measures the reduction in the cost of update delay that occurs when an update is received.

Another context-based AoI measurement called the "Urgency of Information" was introduced in [151] to assess the promptness of status updates. Unlike AoI, this metric takes into account the changing contextual details and the evolving nature of status changes. This enhanced approach allows the investigation of adaptive status update strategies based on contextual information. Additionally, it facilitates better remote monitoring and control. Furthermore, most context-based AoI metrics often depend on the specific application in which they are used.

Conventional approaches to measuring timeliness of the information often overlook the semantic meaning of data, potentially leading to poor performance. Thus, in semantics-based communication paradigms, the AoI has emerged as a crucial performance metric for quantifying the timeliness of information in wireless communication systems [152]. The AoI was first introduced for semantic communication in [152], which highlighted the importance of data significance in achieving communication objectives. In addition, the authors of [152] addressed the challenges associated with minimising AoI in simple semantic-based wireless communication networks. They offer valuable insights into an optimal transmission strategy employing a randomised threshold policy. Furthermore, this work presents a robust method for determining the optimal parameters.

In [153], the authors investigated the dynamics of AoI in task-oriented wireless communication. Their aim is to efficiently execute tasks by using the transmitting data at the receiver. Through a jointly trained encoder-decoder pair that takes into account channel effects, data samples are transformed into compact feature vectors, which reduces the need for lengthy transmission blocks while reducing latency. The decoder, in this context, performs tasks such as classification rather than reconstructing the transmitted content at the receiver. The study demonstrates a trade-off: increased channel usage improves classifier accuracy, however, extends transmission time. The concept of the "peak age of task information (PAoTI)" provides insights into this accuracy-latency relationship. Design guidelines for task-oriented communications are derived, including a dynamic update mechanism to adapt channel usage based on prevailing conditions, thus reducing PAoTI.

As semantic wireless communication systems continue to evolve, addressing the challenges of maintaining data freshness whilst optimising for semantic content will be crucial. The integration

of AoI metrics with semantic communication principles offers a promising direction for future research in this field, particularly for IoT applications, autonomous vehicles, UAV communication and smart sensor networks, where the rapid exchange of time-sensitive information is critical [87].

Chapter 3

AoI in URLLC-enabled UAV Wireless Communications

3.1 Introduction

This chapter considers an UAV communication network, where UAV operate as an aerial mobile relay between a source and a destination of the network. To capture the freshness of the information at the destination node, AoI is considered. In addition, a short-packet communication scheme maintains low latency in the proposed UAV wireless communication system. The finite block-length theory investigates the performances of short-packet communications schemes in the UAV-assisted wireless communications system. In this chapter, the AAoI is estimated by applying the SHS model. The SHS model comprises discrete states, which represent events that reset the AoI process and continuous dynamics that represent linearly growing age processes. Finally, a closed-form expression for the AAoI of the proposed UAV wireless communication system is derived and it can be used to estimate the optimal altitude, block length and other parameters.

3.1.1 Contributions

As per the best of the author's knowledge, this is the first study that investigates the AoI of an URLLC-enabled UAV wireless network. In this chapter, a closed-form expression for the AoI in a UAV relay communication network is derived. Furthermore, our study enables us to determine the optimal altitude, block-length, transmission power and update generation rate that guarantee the freshness of the received information at the destination. Moreover, the SHS analysis in [55] has been further extended for wireless systems with transmission errors. Additionally, this work builds upon previous research on URLLC-enabled decode and forward relay [18] by analysing UAV communication networks, which have different channel statistics compared to terrestrial wireless channels. Due to erroneous transmission in the relay system, it is not easy to use a graphical method in this analysis. Hence, the SHS approach is adopted and the AoI process is modeled as a stochastic hybrid process that considers both continuous and discrete behaviours of the AoI process.

25
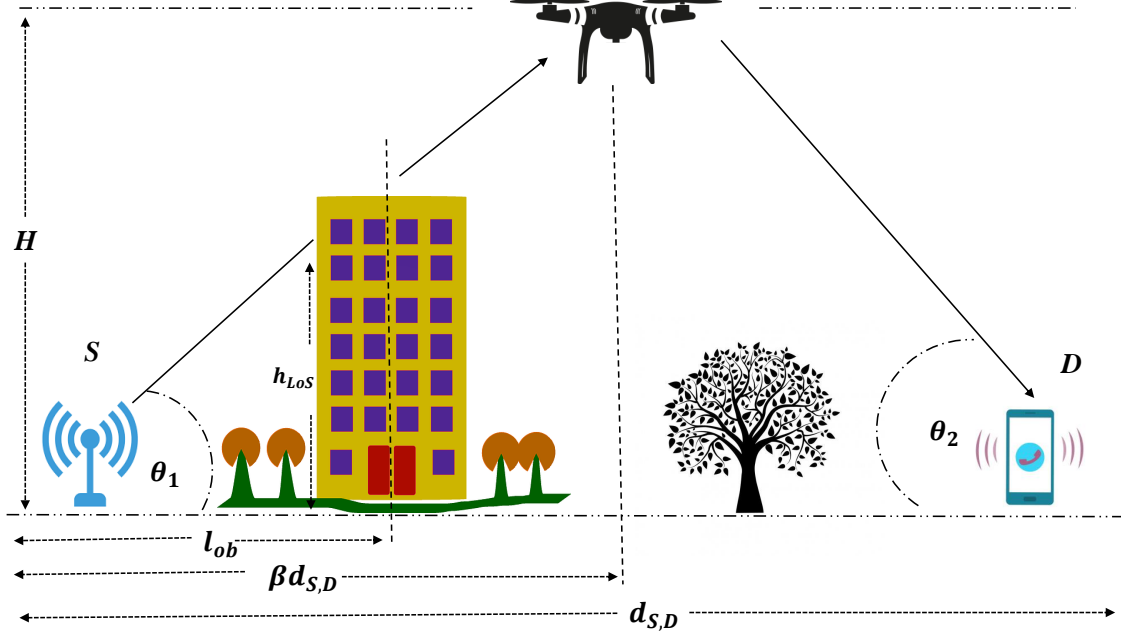
Figure 3.1: System model of UAV communication network

3.1.2   Organization

The chapter is organised as follows: Section 3.2 introduces the URLLC-enabled UAV relay system and a closed-form equation for AAoI is derived. Subsequently, Section 3.3 presents some numerical results and the system performance is analysed. Finally, the work is concluded in Section 3.4.

3.2   System Model

As shown in Figure 3.1, an URLLC-enabled UAV relay network is considered, where the UAV is placed at an altitude of H and acts as a wireless relay between the source (S) node and the destination (D) node. It is assumed that the altitude of the S and the D are negligible as compared to UAV amplitude. The distance between S and D is $d_{S,D}$ and it is expected that UAV aerial wireless relay node can freely move between S and D, while the distance between S and UAV is $d_{S,UAV} = \beta d_{S,D}$ and the distance between UAV relay and D is denoted by $d_{UAV,D} = (1-\beta)d_{S,D}$, where β denotes the distance dividing factor. The elevation angle of UAV is θ and if it is measured from the S, $\theta = \theta_1 = \arctan(\frac{H}{\beta d_{S,D}})$ and from the D, $\theta = \theta_2 = \arctan(\frac{H}{(1-\beta)d_{S,D}})$. In this proposed UAV-assisted wireless communication scheme, each transmission time block is divided into two distinct time slots. In the literature, several cooperative communication techniques have been proposed for the UAV-enabled relay communication networks; among them, decode-and-forward

(DF) is one of the most commonly used techniques, where the DF technique is deployed in this system. The source sends data to the UAV relay during the first time span. During the second time slot, the UAV decodes and re-transmits the received data to the destination. It is assumed that no direct communication exists between the source and the destination. The transmitted signal by the source, the received signal at the UAV realy, the transmitted signal by the UAV and the received signal at the destination are denoted by X_1, Y_1, X_2 and Y_2, respectively. The received signal at each communication node can be written as

$$Y_1 = \sqrt{P_S} H_{S,UAV} X_1 + W_{S,UAV}, \tag{3.1}$$

$$Y_2 = \sqrt{P_{UAV}} H_{UAV,D} X_2 + W_{UAV,D}, \tag{3.2}$$

where H_{ij} is the channel coefficient of the channel between node i to node j where $i \in \{S, UAV\}$ and $j \in \{UAV, D\}$. The W_{ij} denotes the independent and identically distributed AWGN of the channel with zero mean and σ^2 variance.

3.2.1 Aerial Communication Channel Characterisation

It is important to design a new statistical propagation model to predict path loss, shadowing and fading of aerial communication in UAV-enabled communication. It is different from the common propagation model, which are used for terrestrial communication networks. Basically, this is based on environment properties [154, 155]. Normally, UAV communications may provide strong LoS paths between the UAV and transmission nodes in the ground and it strength the received signal level compared to the NLoS condition. Hence, it is important to calculate LoS probability to develop a proper channel model for the UAV communication system. Besides the channel statistics, it is important to consider how UAV is used as an aerial communication node.

3.2.1.1 Line of sight probability

The possibility that a LoS channel exists between each node is determined by adding the probabilities that each building in the propagation pathway is lower than the height of the ray connecting the two nodes. The height of the ray at the obstruction point can be calculated as

$$h_{\text{LoS}} = l_{ob} \tan(\theta), \tag{3.3}$$

where l_{ob} is distance from the S (or D) to the obstacle. If structures in the ground are evenly spaced, number of structures between two nodes can be estimated. Assuming area between two nodes has flat or constant slope, the probability that a LoS ray exists P_{LoS} is can be calculated as follows:

$$P_{\text{LoS}} = \prod_{b=1}^{b_r} \mathbb{P}(h < h_{\text{LoS}}), \tag{3.4}$$

where h is the structure height and b_r is the number of buildings crossed by the ray. The expected number of buildings passed per km b_1 is given by:

$$b_1 = \sqrt{Z_B M_B}, \tag{3.5}$$

where Z_B is the ratio of land area covered by buildings to total land area and M_B is the average number of buildings per unit area (buildings/km^2). Then, b_r is given by:

$$b_r = \text{floor}\left(r_{ij} b_1\right),\tag{3.6}$$

where r_{ij} , (km), $i \in \{S, UAV\}$, $j \in \{UAV, D\}$ is the horizontal distance between the transmitter and the receiver and the floor function guarantee that an integer number of terms (not greater than the arguments of the function) are contained in (3.4). The LoS probability can be expressed as closed form expression as follows [156]:

$$P(\text{LoS}) = \prod_{k=0}^{b_r-1}\left[1 - \exp\left[-\frac{\left(\frac{(k+\frac{1}{2})r_{ij}\tan\theta}{b_r}\right)^2}{2h_d^2}\right]\right],\tag{3.7}$$

where h_d is a scale parameter that describes the buildings' heights distribution that follows Rayleigh probability distribution. Akram et al. [157] approximated (3.7) to a modified Sigmoid function as follows:

$$P_{\text{LoS}}(\theta) = \frac{1}{1 + A_s \exp(-B_s(\theta - A_s))},\tag{3.8}$$

where A_s and B_s are S-curve parameters that totally depend on Z_B, M_B and h_d constants. In this chapter, this approximation is employed for our analysis due to the complexity of (3.7).

3.2.1.2 Large-Scale Fading

In the UAV communication, large-scale channel statistics such as path loss and shadow fading is effected by the LoS probability. Hence, it is important to derive relationship between LoS probability and large-scale channel gain. The additional loss incurred on top of the free space path loss due to the shadowing and scattering caused by buildings and trees is referred to as excessive path loss, which has a Gaussian distribution. However, instead of focusing on its random behaviour, its mean value is considered in this study. Let α_{ij} be the large-scale channel gain of channel between each node and it can be obtained as follows:

$$-10\log(\alpha_{ij}) = 20\log(H\csc(\theta)) + 20\log(\frac{4\pi f_c}{c}) + \eta_{NLOS} + \frac{\eta_{LOS} - \eta_{NLOS}}{1 + A_s \exp(-B_s(\theta - A_s))},\tag{3.9}$$

where f_c and c are the carrier frequency (Hz) and the speed of the light (m/s), respectively. η_{LoS} and η_{NLoS} are the expectation of the additional environment-dependent excessive path loss for the LoS and NLoS components, respectively. In this analysis, it is assumed that all three nodes are stationary when communicating with each other. Hence, the Doppler effect is not taken into account.

3.2.1.3 Small-Scale Fading Statistics

Besides large-scale channel fading characterization, it is essential to investigate the impact of multi-path propagation and small-scale channel characterization of wireless channels. The Rician fading model is often used for UAV communication due to its characteristic nature. The small-scale

channel gain g_{ij} is denoted as $g_{ij} = |H_{ij}^2|$, where H_{ij} denotes the Rician fading channel coefficient and the distribution of g_{ij} follows a non-central chi-square probability distribution. Then, the probability density function (PDF) of the small-scale channel gain is given by:

$$f_{g_{ij}}(z) = \frac{\left(K_f + 1\right)e^{-K_f}}{\bar{g}_{ij}} e^{\frac{-\left(K_f+1\right)z}{\bar{g}_{ij}}} I_0\left(2\sqrt{\frac{K_f\left(K_f + 1\right)z}{\bar{g}_{ij}}}\right), \qquad (3.10)$$

where $z \geq 0$, $\bar{g}_{ij}=1$, $I_0\left(\cdot\right)$ is the zero-order modified Bessel function of the first kind and K_f is the Rician factor that depends on the ratio between the power of the LoS component and NLoS components. Then, Rician factor can be expressed as follows [158, 159]:

$$K_f = \frac{P_{\text{LoS}}\left(\theta\right)}{1 - P_{\text{LoS}}\left(\theta\right)}. \qquad (3.11)$$

3.2.1.4 Instantaneous SNR

In this system, transmission power at each transmission node is fixed as P_i and the noise power at each receiving node is denoted as σ^2. The instantaneous SNR at each receiving node γ_j is given by:

$$\gamma_j = \frac{\alpha_{ij}g_{ij}P_i}{\sigma^2}. \qquad (3.12)$$

3.2.2 Decoding Error Probability Under the Short Packet Communication

In this system, it is assumed that a short packet channel coding scheme is used for encoding. Hence, finite block length information theory was used to evaluate the decoding error probability at the receiving node [90, 160]. The fading coefficients are expected to be constant over the duration of each transmission block in this system and the receiver has perfect channel state information. Then, the expectation of the decoding error probability at the receiving node, ε_j can be calculated as follows, according to the PPV:

$$\varepsilon_j = \mathbb{E}\left[Q\left(\frac{n_{i,j}\left(\log_2(1 + \gamma_j)\right) - k_b}{\sqrt{n_{i,j}\left(\frac{\log_2^2 e}{2}(1 - \frac{1}{(1+\gamma_j)^2})\right)}}\right)\right], \qquad (3.13)$$

where $\mathbb{E}\left[\cdot\right]$ is the expectation operator and $Q(\cdot)$ is the Q-function. It can be defined as $Q(x) = \frac{1}{\sqrt{2\pi}}\int_x^\infty e^{-\frac{t^2}{2}}\,dt$. It is assumed that k_b number of information bits are contained in a $n_{i,j}$ bit length block. Moreover, under the Rician fading block fading conditions, ε_j can be expressed as

$$\varepsilon_j = \int_0^\infty f_{\gamma_j}(z)Q\left(\frac{n_{i,j}\left(\log_2(1 + \gamma_j)\right) - k_b}{\sqrt{n_{i,j}\left(\frac{\log_2^2 e}{2}(1 - \frac{1}{(1+\gamma_j)^2})\right)}}\right)dz, \qquad (3.14)$$

where $f_{\gamma_j}(z)$ denotes the PDF of the γ_j and it is given by:

$$f_{\gamma_j}(z) = \frac{\left(K_f + 1\right)e^{-K_f}}{\bar{\gamma}_j} e^{\frac{-\left(K_f+1\right)z}{\bar{\gamma}_j}} I_0\left(2\sqrt{\frac{K_f\left(K_f + 1\right)z}{\bar{\gamma}_j}}\right), \qquad (3.15)$$

where $\bar{\gamma}_j$ is expectation of SNR at node j and it can be calculated as $\bar{\gamma}_j = \frac{P_i \alpha_{ij}}{\sigma^2}$. Due to the complexity of the Q-function, it is difficult to get a closed-form expression for the overall decoding error probability. Thus, using the approximation technique given in [161] and [94], (3.14) can be approximated as follows:

$$\varepsilon_j \approx \int_0^\infty f_{\gamma_j}(z) \Theta_j(z) dz, \tag{3.16}$$

where $\Theta_j(z)$ denotes the linear approximation of $Q\left(\frac{n_{i,j}\left(\log_2(1+\gamma_j)\right)-k_b}{\sqrt{n_{i,j}\left(\frac{\log_2^2 e}{2}(1-\frac{1}{(1+\gamma_j)^2})\right)}}\right)$, this can be expressed as [94]

$$\Theta_j(\gamma_j) = \begin{cases} 1, & \gamma_j \leq \phi_j, \\ \frac{1}{2} - \beta_j \sqrt{n_{i,j}}(\gamma_j - \psi_j), & \phi_j < \gamma_j < \delta_j, \\ 0, & \gamma_j \geq \delta_j, \end{cases} \tag{3.17}$$

where $\beta_j = \frac{1}{2\pi\sqrt{2^{\frac{k_b}{n_{i,j}}}-1}}, \psi_j = 2^{\frac{k_b}{n_{i,j}}} - 1, \phi_j = \psi_j - \frac{1}{2\beta_j\sqrt{n_{i,j}}}$ and $\delta_j = \psi_j + \frac{1}{2\beta_j\sqrt{n_{ij}}}$. Using approximation in (3.17) and [162] the ε_j is calculated as

$$\varepsilon_j \approx \beta_j \sqrt{n_{i,j}} \int_{\phi_j}^{\delta_j} F_{\gamma_j}(z) dz \simeq F_{\gamma_j}(\psi_j), \tag{3.18}$$

where F_{γ_j} is the cumulative distribution function (CDF) of the γ_j and it can be derived as [163] follows:

$$\begin{aligned} F_{\gamma_j}\left(z, K_f, \bar{\gamma}_j\right) &= \int_0^z f_{\gamma_j}(z) dz \\ &= 1 - Q_1\left(\sqrt{2K_f}, \sqrt{\frac{2\left(K_f+1\right)z}{\bar{\gamma}_j}}\right), \end{aligned} \tag{3.19}$$

where $Q_1(\cdot, \cdot)$ is first order Marcum Q-function. Thus, ε_j can be calculated as

$$\varepsilon_j = 1 - Q_1\left(\sqrt{2K_f}, \sqrt{\frac{2\left(K_f+1\right)\psi_j}{\bar{\gamma}_j}}\right), \tag{3.20}$$

However, due to complexity of Marcum Q-function, semi-linear approximation is used to get closed-form equation for the error probability as follows [164]:

$$\begin{aligned} \varepsilon_j &\simeq \Xi\left(\sqrt{2K_f}, \sqrt{\frac{2\left(K_f+1\right)\psi_j}{\bar{\gamma}_j}}\right) \\ &\simeq \Xi\left(\Phi, \Psi\right), \end{aligned} \tag{3.21}$$

where $\Xi(\cdot, \cdot)$ is the semi-linear approximation of the $1 - Q_1(\cdot, \cdot)$ and it can be calculated as

$$\Xi\left(\Phi, \Psi\right) = \begin{cases} 0, \text{ if } \Psi < c_1, \\ \Psi_0 e^{-\frac{1}{2}(\Phi^2+\Psi_0^2)} I_0\left(\Phi\Psi_0\right)\left(\Psi - \Psi_0\right) + \\ \quad 1 - Q_1\left(\Phi, \Psi_0\right) \text{ if } c_1 \leq \Psi \leq c_2, \\ 1, \text{ if } \Psi > c_2, \end{cases} \tag{3.22}$$

with

$$\Psi_0 = \frac{\Phi + \sqrt{\Phi^2 + 2}}{2},$$

$$c_1(\Phi) = \max\left(0, \Psi_0 + \frac{Q_1(\Phi, \Psi_0) - 1}{\Psi_0 e^{-\frac{1}{2}(\Phi^2 + \Psi_0^2)} I_0(\Phi\Psi_0)}\right),$$

and

$$c_2(\Phi) = \Psi_0 + \frac{Q_1(\Phi, \Psi_0)}{\Psi_0 e^{-\frac{1}{2}(\Phi^2 + \Psi_0^2)} I_0(\Phi\Psi_0)}.$$

When the UAV relay decodes a transmitted block with an error, it may cause transmission failure under the DF relay scheme. Furthermore, even if the UAV correctly decodes the transmitted block, a decoding error at the destination node may cause transmission failure. Then, the overall decoding error probability ε can be written as [94]

$$\varepsilon = \varepsilon_{UAV} + \varepsilon_D(1 - \varepsilon_{UAV}), \tag{3.23}$$

where ε_{UAV} is the block error probability at the UAV and ε_D is the block error probability at the destination.

3.2.3 AAoI of the UAV Communication System

This section estimates the AAoI at the destination (D) of the UAV relay system. The status update packets are generated at the S and transmitted to the D using UAV relay system. It is considered that mean update generate rate at the S is λ_a and UAV relay network transmit update at rate μ. It is assumed that an update in transmission has an error with probability $0 \leq \varepsilon < 1$ and it can be calculated using (3.23). The mean update transmission rate μ is given by inversely propositional to the mean transmission time per update $\mathbb{E}[T]$ in the UAV relay network and it is given by:

$$\frac{1}{\mu} = \mathbb{E}[T] = nT_s \tag{3.24}$$

where T_s and n denotes symbol duration and total block-length, respectively. If the generation time of the freshest update received at time stamp t is $g(t)$, then AoI ($x_0(t)$) can be defined as a random process as

$$x_0(t) = t - g(t). \tag{3.25}$$

As illustrated in the Figure 3.2, it is assumed that at $t = 0$ the measurements of the AoI starts and the AoI at the D is set to $x_0(0) = X_0$. The S generate updates at time stamps $g_1, g_2, ...,$ and the D receive these updates at time stamps $z_1, z_2, ...,$ if update successfully transmitted by the S and decoded by the D. As illustrated in Figure 3.2, data update i is transmitted from the S at time stamp $t = g_i$ and it is successfully delivered to the D at time stamp $z_i = g_i + nT_s$. Therefore, if update packet delivered successfully, at the time z_i, the AoI at the D can be estimated as

$$x(z_i) = nT_s. \tag{3.26}$$

AoI increases linearly until the next update is successfully delivered to the D. As an example, one packet fails to be decoded at time z_2, hence, $x_0(t)$ continues to increase linearly. Similarly, when

31

there is an update (packet) in transmission, new updates that arrive at the S are blocked and cleared, as an example, update generated at the time g_4 is not transmitted since at that time the previous update which is generated at the time g_3 still under the transmission. Hence, the update generated at the time g_4 does not affect the AoI process. For the considered time period T_c, time average AoI can be computed using the area under $x_0(t)$. Similarly, the time average age Δ_{T_c} of the proposed UAV relay system can be estimated as

$$\Delta_{T_c} = \frac{1}{T_c} \int_0^{T_c} x_0(t)dt. \tag{3.27}$$

Similar to the work presented in [29, 55], Δ_{T_c} tends to ensemble average age (AAoI) Δ^{AAoI} when $T_c \to \infty$, i.e., which can be expressed as

$$\Delta^{AAoI} = \mathbb{E}[x_0] = \lim_{t \to \infty} \mathbb{E}[x_0(t)] = \lim_{T_c \to \infty} \Delta_{T_c}. \tag{3.28}$$

In this chapter, SHS techniques are used to evaluate $\mathbb{E}[x_0]$, which is referred to as the AoI at the D. Under the SHS analysis, the AoI process is modeled as combination of continuous states x(t) and discrete states $q(t)$. Where, discrete states capture transmission status of the UAV relay that can be represented using Markov chain and the state space of the Markov chain is $(q(t), x(t))$, where $q(t) \in Q = \{0, 1\}$, $q = 0$ indicates that UAV relay is idle and $q = 1$ indicates that UAV relay is in transmission state. The evaluation of the age process at D is represented using
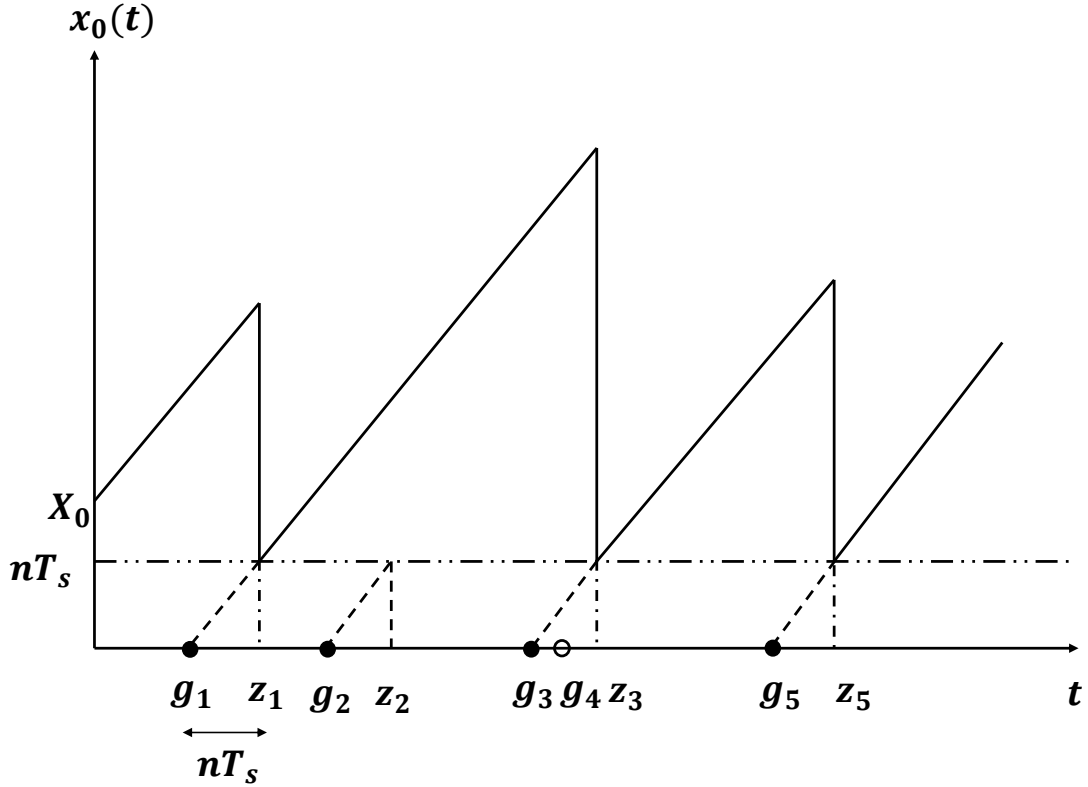
Figure 3.2: Evolution of AoI ($x_0(t)$) with the time

continuous vector $x(t) = [x_1(t), x_0(t)]$ where $x_0(t)$ tracks the age at the D that sees update that complete transmission without error and $x_1(t)$ specifies what $x_0(t)$ would become if the packet-in-transmission is delivered. The SHS model for the AoI process at D the can be illustrated using a graph $(Q, \mathcal{L})$ which contains two discrete states (transmission states) of the UAV relay as nodes of the graph and each transaction between transmission states of the UAV relay is represented as direct edge as in Figure 3.3. The transaction between the discrete states $q_l \rightarrow q'_l, \forall l \in \mathcal{L}$ and their effect on the continuous state $x(t)$ are summarised in Table 3.1 using linear mapping of the form $x' = xA_l$. In addition, $v_{ql}A_l$ included in this table. The transactions presented in Table 3.1 can be explained as follows:

- $l = 1$: An update arrives at the idle system. With the arrival of an update, the S starts transmission of the update, which is received and $x'_0 = x_0$ is unchanged because the arrival of the update to the source does not yield an age reduction at the D until it is successfully delivered to the destination. However, $x'_1 = 0$ since the arriving update is fresh and its age is zero at the instant.

- $l = 2$: An update successfully completes its transmission and is delivered to the D. In this situation, $x'_0 = x_1$, corresponding to the age at the D being reset to the age of the update that just completed transmission. Moreover, $x'_1 = 0$ since x_1 becomes irrelevant when the UAV relay enters the state 0.

- $l = 3$: An update completes its transmission with an error. In this situation, $x'_0 = x_0$ is unchanged because unsuccessful transmissions do not yield an age reduction at the D. Moreover, $x'_1 = 0$ since x_1 becomes irrelevant when UAV relay enters the state 0.
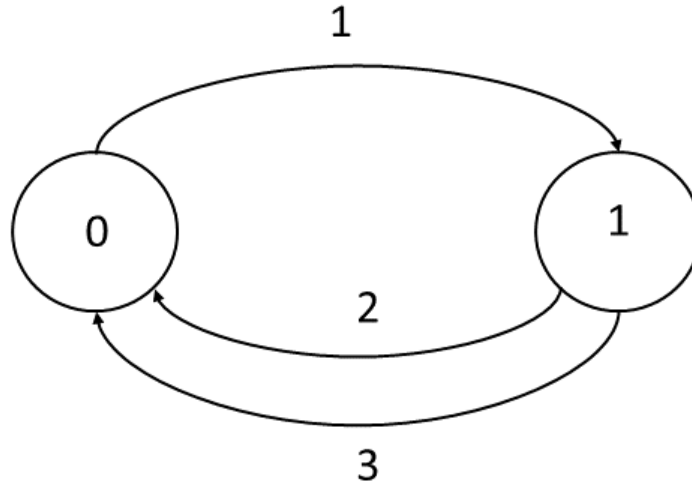
Figure 3.3: The SHS Markov Chain for the UAV relay system

Table 3.1: Transitions Rate for the Markov Chain in UAV Relay System

l	$q_l \rightarrow q'_l$	$\lambda^{(l)}$	$x\mathbf{A}_l$	$v_{q_l}\mathbf{A}_l$
1	$0 \rightarrow 1$	λ_a	$\begin{bmatrix} 0 & x_0 \end{bmatrix}$	$\begin{bmatrix} 0 & v_{00} \end{bmatrix}$
2	$1 \rightarrow 0$	$\mu(1-\varepsilon)$	$\begin{bmatrix} 0 & x_1 \end{bmatrix}$	$\begin{bmatrix} 0 & v_{11} \end{bmatrix}$
3	$1 \rightarrow 0$	$\mu\varepsilon$	$\begin{bmatrix} 0 & x_0 \end{bmatrix}$	$\begin{bmatrix} 0 & v_{10} \end{bmatrix}$

The evolution of $x(t)$ at each discrete state $q(t) = q$ is decided by the b_q as follows:

$$\dot{x}(t) = \frac{\partial x(t)}{\partial t} = b_q = \begin{cases} \begin{bmatrix} 0 & 1 \end{bmatrix} & q = 0, \\[2ex] \begin{bmatrix} 1 & 1 \end{bmatrix} & q = 1. \end{cases} \tag{3.29}$$

To estimate AoI using (2.17), it is necessary to find $\bar{v}_{\bar{q}0}$ using (2.16), in this regards first (2.12) has been employed to find stationary probabilities and it can be shown that the stationary stationary probability vector satisfies $\bar{\pi}\mathbf{D} = \bar{\pi}\mathbf{Q}$ with

$$\mathbf{D} = \text{diag}\begin{bmatrix} \lambda_a & \mu \end{bmatrix}, \quad \mathbf{Q} = \begin{bmatrix} 0 & \lambda_a \\ \mu & 0 \end{bmatrix}$$

Applying (2.13), the stationary probabilities $\bar{\pi}$ are given as

$$\bar{\pi} = \begin{bmatrix} \bar{\pi}_0 & \bar{\pi}_1 \end{bmatrix} = \frac{1}{\lambda_a + \mu}\begin{bmatrix} \mu & \lambda_a \end{bmatrix} \tag{3.30}$$

Using (2.16), the solution can be found for

$$\bar{v} = \begin{bmatrix} \bar{v}_0 & \bar{v}_1 \end{bmatrix} = \begin{bmatrix} \bar{v}_{01} & \bar{v}_{00} & \bar{v}_{11} & \bar{v}_{10} \end{bmatrix}. \tag{3.31}$$

Hence, evaluating (2.13) at $q = 0$ and $q = 1$ and using Table 3.1, the following is obtained:

$$\lambda_a \begin{bmatrix} \bar{v}_{01} & \bar{v}_{00} \end{bmatrix} = \begin{bmatrix} 0 & \bar{\pi}_0 \end{bmatrix} + \mu(1-\varepsilon)\begin{bmatrix} 0 & \bar{v}_{11} \end{bmatrix} + \mu\varepsilon\begin{bmatrix} 0 & \bar{v}_{10} \end{bmatrix} \tag{3.32}$$

$$\mu\begin{bmatrix} \bar{v}_{11} & \bar{v}_{10} \end{bmatrix} = \begin{bmatrix} \bar{\pi}_1 & \bar{\pi}_1 \end{bmatrix} + \lambda_a\begin{bmatrix} 0 & \bar{v}_{00} \end{bmatrix} \tag{3.33}$$

By solving (3.32), (3.33) and (3.30) the values of the $\bar{v}_{\bar{q}0}$ are calculated. Finally, by substituting the result in to (2.17), the AAoI at the D can be obtained as follows:

$$\Delta_D^{AAoI} = \frac{1}{(1-\varepsilon)\lambda_a} + \frac{1}{(1-\varepsilon)\mu} + \frac{\lambda_a}{\mu(\lambda_a+\mu)}. \tag{3.34}$$

Approximated AAoI can be calculated applying semi-linearly approximated decoding error probability for (3.34).

3.3 Simulation Results

In this section, numerical results are presented to validate the theoretical derivations. Unless otherwise specified, the simulation parameters are listed in the Table 3.2.

Table 3.2: Simulation Parameters for UAV-Assisted Communication System [159].

Parameter	Value
Distance between S and D ($d_{S,D}$)	500 m
Distance dividing factor (β)	0.5
Carrier frequency (f_c)	6 GHz
Speed of the light (m/s)	$3 \times 10^8 \mathrm{ms}^{-1}$
η_{LoS} (Suburban)	0.1 dB
η_{NLoS} (Suburban)	21 dB
η_{LoS} (Urban)	1 dB
η_{NLoS} (Urban)	20 dB
η_{LoS} (Dense urban)	1.6 dB
η_{NLoS} (Dense Urban)	23 dB
η_{LoS} (High-rise urban)	2.3 dB
η_{NLoS} (High-rise Urban)	34 dB
Transmission power at source (P_S)	5 mW
Transmission power at UAV (P_{UAV})	5 mW
Symbol duration (T_s)	17 µs
$n_{S,UAV}$	54 bits
$n_{UAV,D}$	54 bits
n	108 bits
k_b	32 bits
λ_a	529 update s^{-1}
Noise power (σ^2)	-100 dBm

In Figure 3.4 plots approximated AAoI as a function of the UAV altitude. The approximated AAoI is calculated using (3.34) with the approximation approach of (3.21).It can be observed from Figure 3.4 that the optimal altitude under all environmental conditions is 500 m. For low altitude, higher AAoI is observed due to the higher error probability caused by the weak LoS. When altitude increases towards its optimal value, AAoI decreases rapidly due to the strong LoS. In this scenario, getting strong LoS channels is more significant than the losses due to the increased length of the communication link. However, beyond optimal altitude, the path loss dominates the other factors, leading to a higher AAoI. In addition, within altitude between 200 m-750 m, approximated AAoI is minimum for all the other environments except high-rise urban. In this scenario, AAoI goes to its minimum value 4.59 ms since error probability is approximated as zero. However, compared to the other environmental conditions, high-rise urban environments have low SNR due to the weak LoS; hence, AAoI can not be approximated to its minimum. The suburban environment has the lowest AAoI for all altitudes due to the strong channel condition.

Figure 3.5a and 3.5b compare the numerically simulated AAoI with the approximated AAoI for the dense urban environment and the high-rise urban environment, respectively. This approximation is tight for moderate values of Ψ and it is improved for small values of Φ as in (3.21). Hence, it can be observed that under dense urban conditions, the AAoI approximation is tight for moderate altitude values. Under high-rise urban conditions, simulated AAoI deviates from the approximations. The main reason for this trend is that under this condition, the Ψ values are not moderate due to the
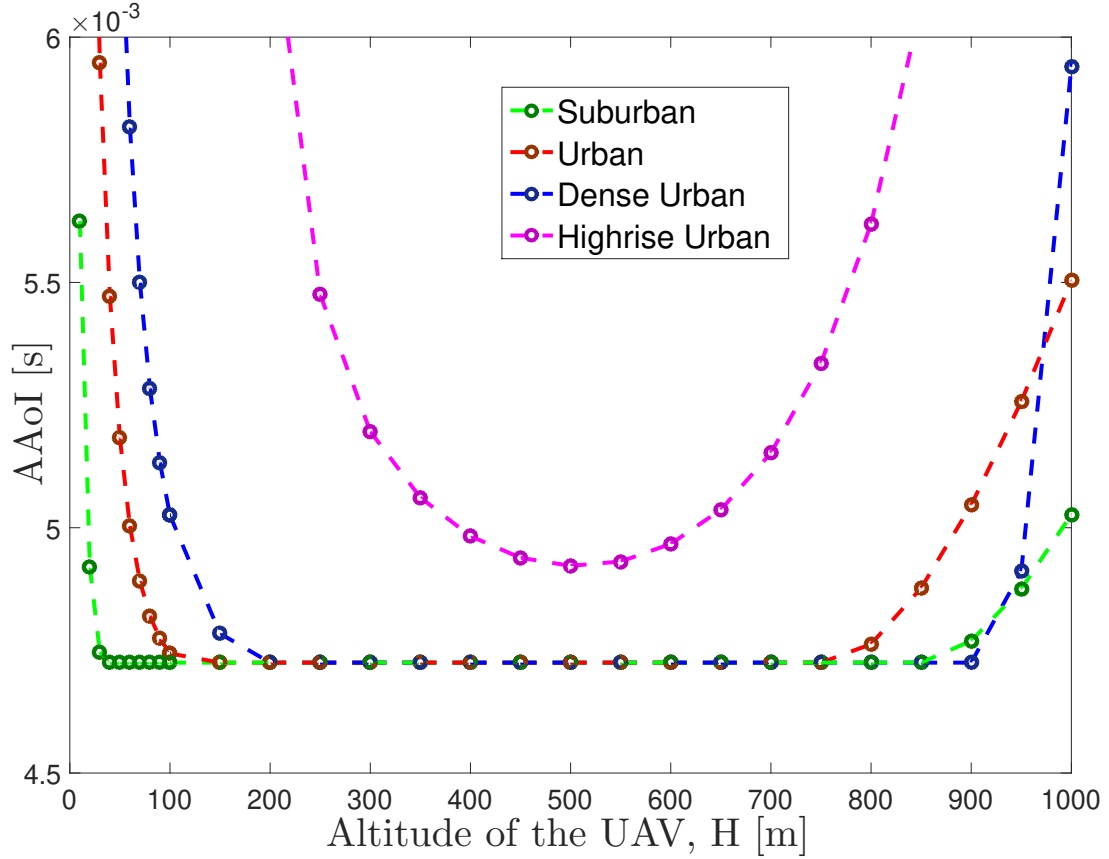
Figure 3.4: Approximated AAoI as a function of UAV Altitude

lower or higher SNR.

Figure 3.6 shows the AAoI versus the transmission power of the UAV and the source under the different environmental conditions. It is assumed that UAV altitude is 500 m. It can be observed that the transmission power significantly affects the AAoI of the proposed UAV communication system. Regardless of the environmental condition, AAoI is continuously decreasing when the transmission power increases. However, since the number of transmission errors in the wireless network is minimal at that time, AAoI seems to saturate at 1.5 mW of transmission power; hence, the system reaches its lowest AAoI 4.59 ms. However, under high-rise, urban environment conditions, more than 1.5 mW transmission power is needed to achieve minimum AAoI compared with the other environments. From Figure 3.6, it can be concluded that transmission power is a more significant factor that changes the AAoI performance of a UAV-assisted wireless communication system. Figure 3.7 illustrate the effect of the block-length on AAoI when the transmission power is equal to 2 mW. In general, the block length is proportional to the transmission time and increasing block length always increases the system delay of the wireless communication networks. From this figure, it can be noted that there is an optimal value for the block length. It is observed that for small values of the block length, the system has a higher AAoI. Note that small block length values increase the number of transmission errors due to the unsuccessful decoding at the receiving nodes. In this scenario, the effect of the decoding error probability on AAoI is more significant
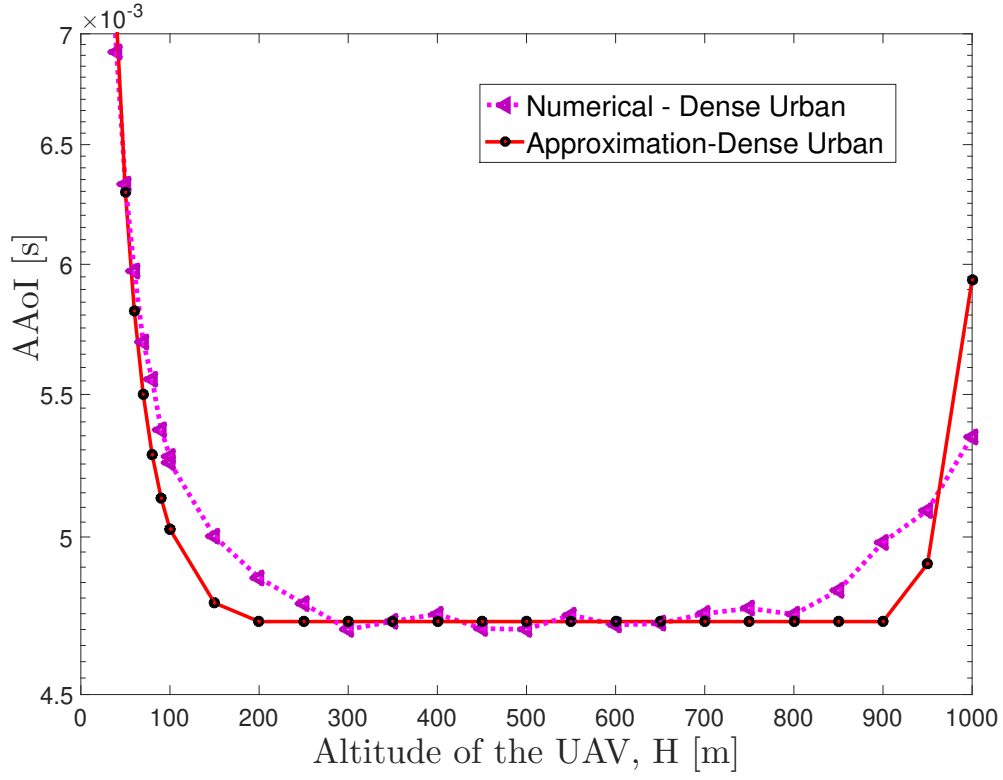
(a) Dense Urban Environment
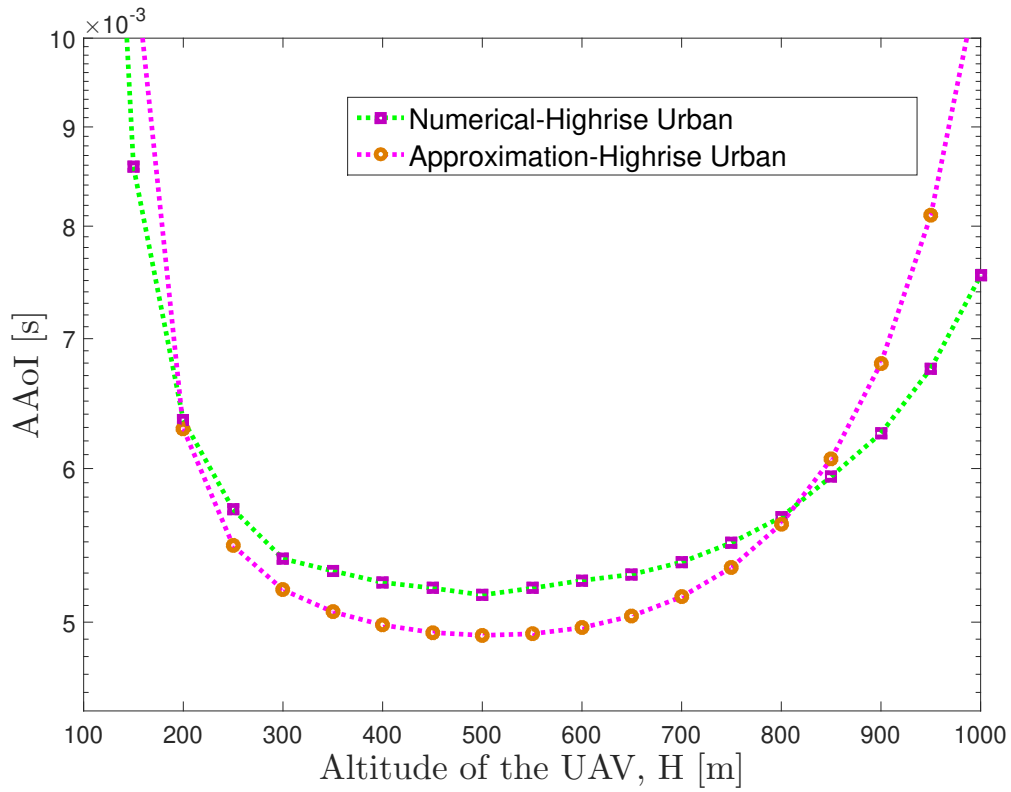
(b) Highrise Urban Environment

Figure 3.5: AAoI as a function of UAV Altitude in different urban environments
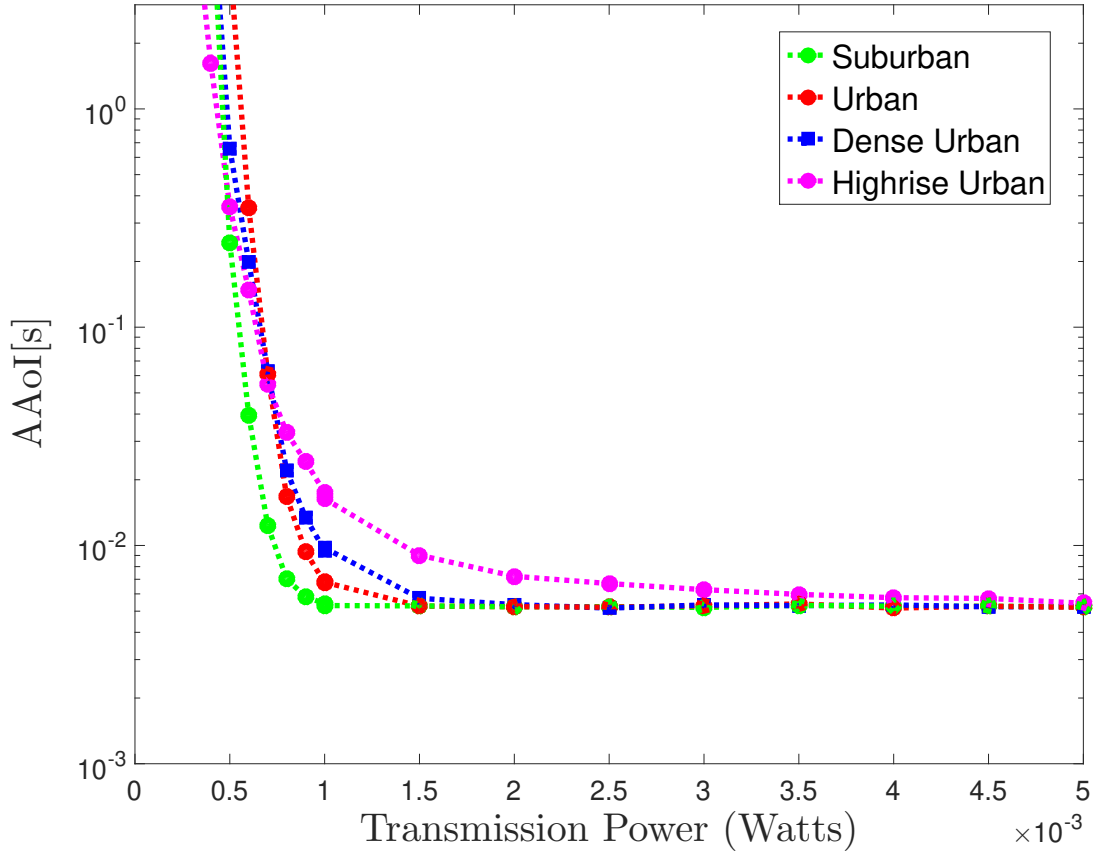
Figure 3.6: AAoI as a function of transmission power at UAV and Source

than the low transmission time. On the other hand, increasing the block length from a small value to the optimal value decreases AAoI due to the small number of decoding errors. In this event, the low error probability effect is more significant than increases in transmission time. However, beyond the optimal value, the effect of the transmission time is more dominant than the decoding error. Thus, from the figure, it can be observed that increasing block length beyond its optimal value rapidly increases the AAoI of the system. The conclusion from Figure 3.7 is that maintaining optimal block length is necessary to achieve better AAoI.

Figure 3.8 plots AAoI as a function of the update generation rate at the source. It is evident that the AAoI of the proposed UAV-assisted communication system is monotonically decreasing with the update generation rate. In this wireless system, no packets are kept in a queue waiting for transmission. Thus, there is no queuing delay in the system and higher update generation rates decrease AAoI. Figure 3.9 compares the AAoI of the UAV-assisted relay system with that of the direct transmission system. For a fair comparison, it is assumed that the transmission power of the direct transmission system at the S is 10 mW which is equal to the total transmission power of the UAV-assisted relay system. UAV altitude is 500 m. It is observed that by employing a UAV-assisted communication system, the AAoI can be reduced. In addition, the performance gap is more significant for long-distance transmission. Specifically, the key findings of this simulation results can be highlighted as follows:
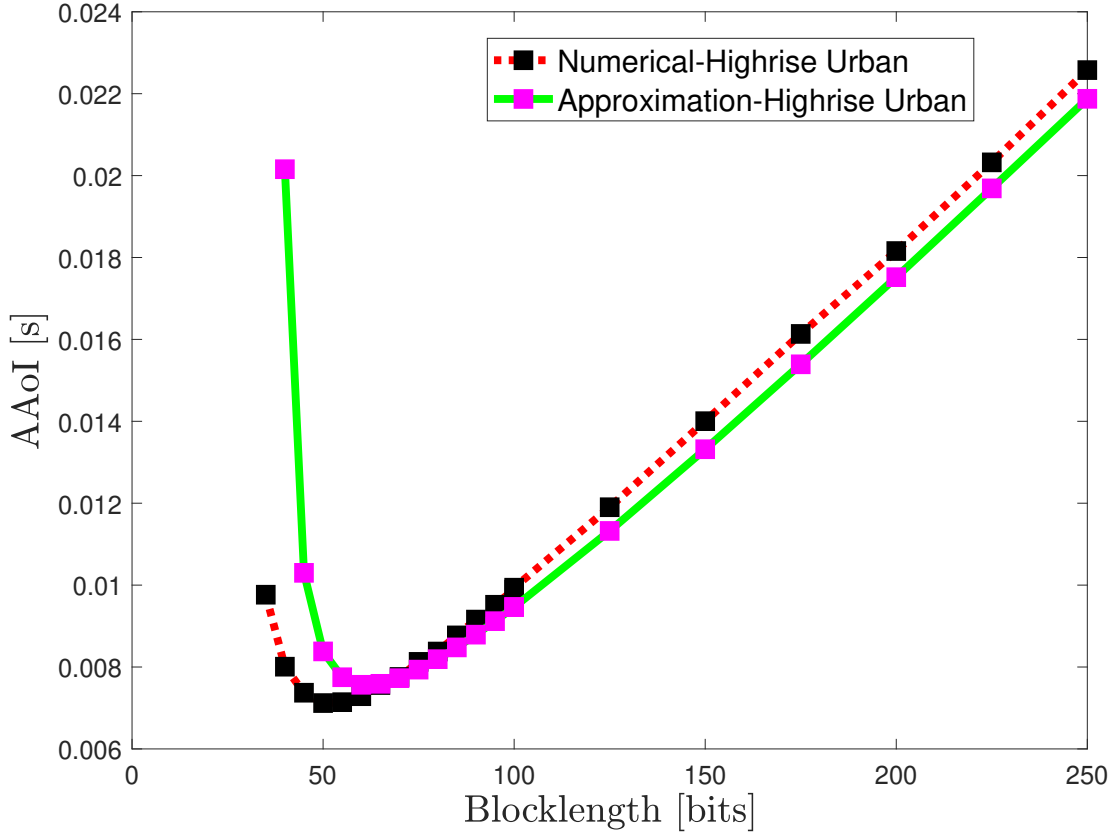
Figure 3.7: AAoI as a function of Blocklength in the Highrise Urban Environment

- AAoI drops initially and then, subsequently, increases as the UAV altitude increases. When UAV altitude is low, increasing UAV altitude enhances the probability of LoS transmission, which improves the connection reliability. As UAV altitude is increased further, a larger path loss is obtained, which dominates the system performance.

- The AAoI of the system decreases monotonically as the update generation rate increases, as there is no queuing delay in the system.

- There is a sub-optimal value of block length that minimises the AAoI. This is mostly due to the trade-off that short block length decreases latency while increasing error probability.

- It has been realised that using a UAV-assisted wireless communication system can reduce the AAoI when compared to terrestrial transmission.

39
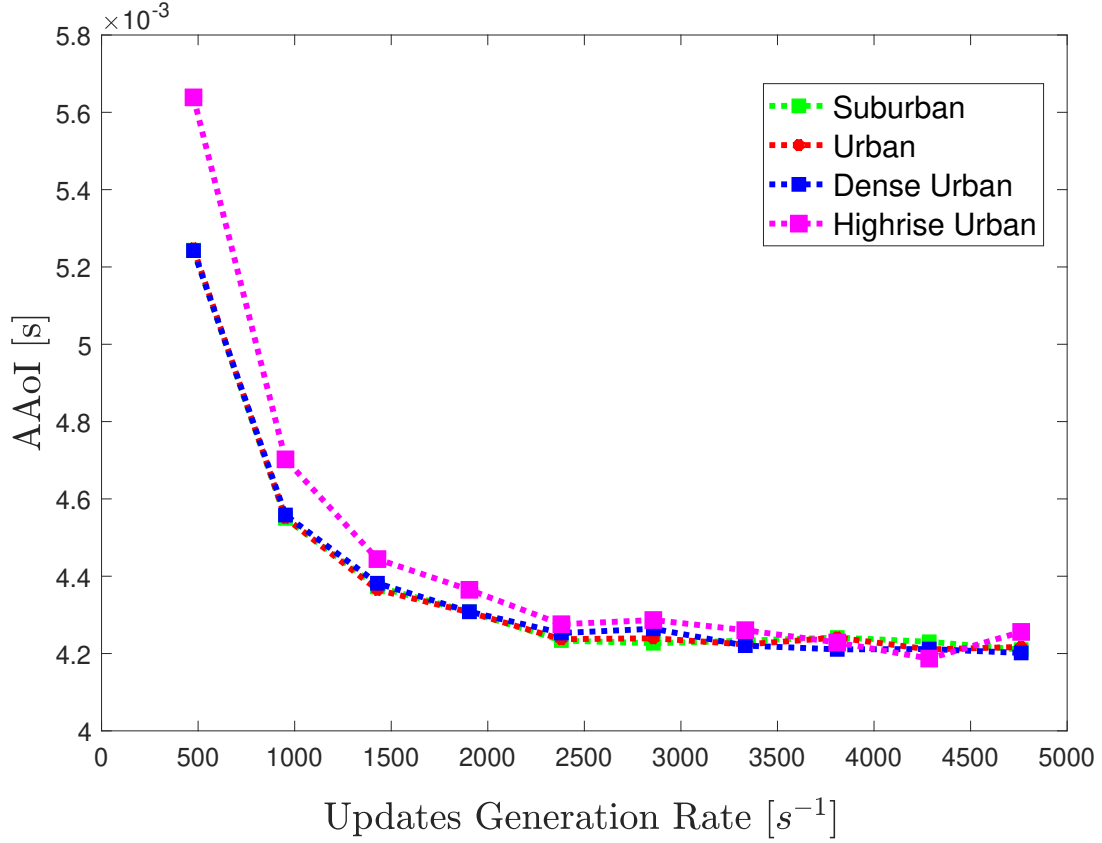
Figure 3.8: AAoI as a function of updates generation rate in the Highrise Urban Environment

3.4 Conclusions

To determine the significance of a UAV-assisted relaying system in terms of information freshness, the AAoI for an URLLC-enabled UAV-assisted communication system was estimated and closed-form expressions for the AAoI were derived. Numerical results were then provided to determine the optimal suitability between UAV-assisted relay and direct transmission systems for mission-critical IoT applications. Furthermore, the study investigated AAoI as a function of block length, UAV altitude, update generation rate, transmission power and distance. More importantly, the numerical results demonstrate that UAV-assisted relayed transmission improves the freshness of information compared to direct transmission.

Publications arising from this Chapter

1. [14] **Basnayaka, C. M. W.**, Jayakody, D. N. K., & Chang, Z. (2021). Age of information-based URLLC-enabled UAV wireless communications system. IEEE Internet of Things Journal, 9(12), 10212-10223.

2. [18] **Basnayaka, C. M. W.**, Jayakody, D. N. K., Perera, T. D. P., & Ribeiro, M. V. (2021, April). Age of information in an URLLC-enabled decode-and-forward wireless
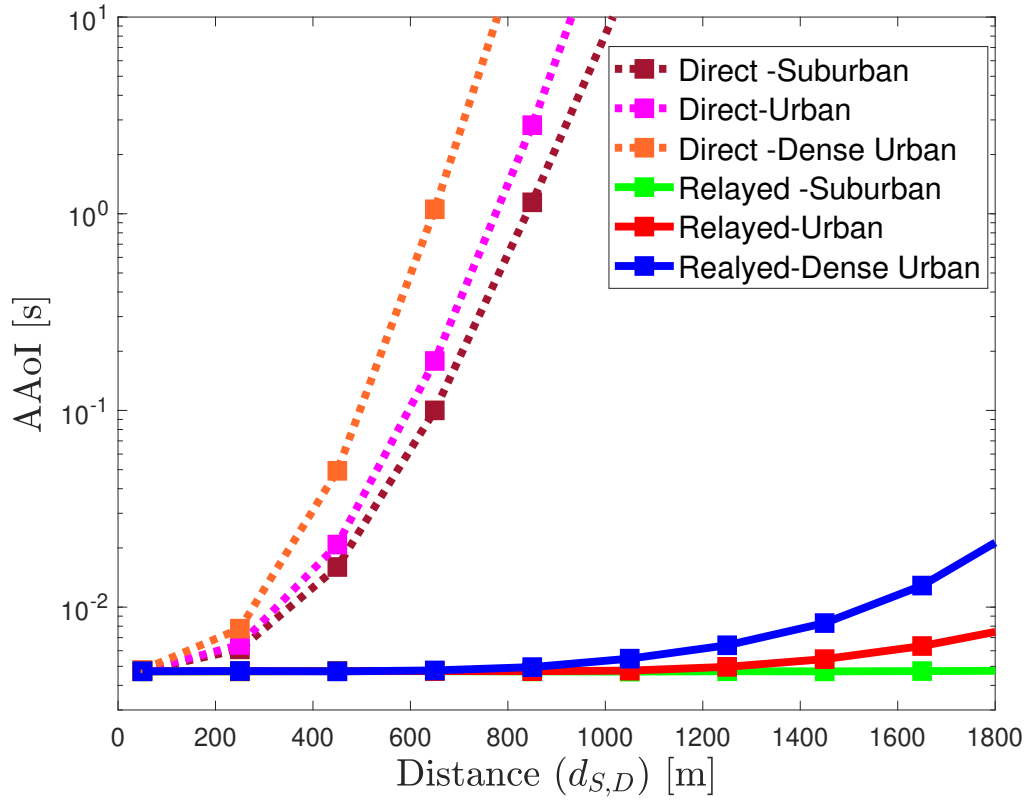
Figure 3.9: AAoI as a function of distance between *S* and D

communication system. In 2021 IEEE 93rd Vehicular Technology Conference (VTC2021-Spring) (pp. 1-6). IEEE.

Chapter 4

AoI in SWIPT-Driven Wireless Communications

4.1 Introduction

SWIPT-enabled wireless cooperative communication systems are an emerging technology for future wireless communication applications. Furthermore, the IoT serves a diverse range of purposes, some of which are mission-critical and require constantly evolving real-time data. Thus, the information received at the destination must be updated in a timely manner to ensure its freshness. The AoI has been introduced to measure the freshness of received information. This study estimates the AoI of a SWIPT assisted decode and forward two-way relay assisted status update system in which two sources attempt to exchange status updates as quickly as possible to the destination. The relay system employs short packet communication to adhere to the latency and reliability requirements of the wireless communication system. The study examines the AAoI at the destination in the proposed relay network and derives approximations for the weighted sum AAoI under two different types of transmission scheduling policies at the relay: *TWW* and *WUC*. Furthermore, the effects of transmission power, packet size, the distance between relay and sources and block-length on the weighted sum AAoI of the proposed SWIPT assisted short packet relay network are extensively investigated. The performance differences of the considered transmission policies are compared and insights are provided. Numerical simulations using the Monte Carlo (MC) method have been employed to validate derived analytical expressions.

4.1.1 Motivations and Contributions

Motivated by the features of SWIPT, short packet communication and cooperative communications, as well as the need for assessing the timeliness of information in modern mission-critical applications, this work analyses the AoI in a SWIPT-enabled wireless cooperative short packet relay system, utilising finite block length information theory and AoI metrics. In summary, this work makes the following contributions:

- First, a theoretical model has been developed to measure the freshness of the information in

a SWIPT-enabled short packet communication two-way cooperative relay scheme under the two type transmission policies at the relay named *TWW* and *WUC*.

- Secondly, expressions were presented for the block error rate (BLER) under each transmission policy separately, using different mathematical approximations. Based on the derived expressions, the BLER performance of the considered system is compared. Several key observations related to the impact of transmission power on the BLER are obtained.

- Thirdly, approximations for the AAoI of the proposed two-way relay scheme under the finite block-length constraint are derived for both transmission policies. Additionally, the accuracy of these approximations has been verified using MC method-based numerical simulations.

- Finally, this chapter analyses how the information freshness of the relay system varies when the transmission scheduling policy at the relay is altered across different transmission power levels. Additionally, this chapter examines the effects of several factors, including block length and packet size, on the weighted sum AAoI. MC-based numerical simulations are provided to verify the accuracy of the theoretical analysis.

4.1.2 Organization

The rest of the chapter is arranged as follows: Section 4.2 presents the system model and the underlying assumptions, evaluating the reliability of the system and freshness of the information at the destination under proposed transmission policies using finite block-length analysis and the AoI analysis, respectively. Section 4.3 compares the proposed policies using extensive simulation results. Section 4.4 concludes the chapter. Several proofs have been added to the appendix to improve readability.

4.2 System Model

As depicted in Figure 4.1, this chapter considers a two-way cooperative status update system where two source nodes, source A (S_A) and source B (S_A) exchange status updates with each other as timely as possible with the help of a bidirectional IoT relay node R. The sources in this system are regarded as energy providers and the relay is equipped with an EH device and is capable of information transmission and harvesting energy simultaneously. The R adopts the dynamic power splitting technique [8]. In this chapter, two types of transmissions and EH policies at R are considered : *TWW* and *WUC*.

- *TWW*: As shown in Figure 4.1, a two-time slot transmission scheme is considered in which S_i sends updates to the R while harvesting energy during the first transmission time slot (T_1). Then, the R exchanges updates received from S_i using harvested energy during the second transmission time slot (T_2). The T_1 and T_2 are constant time slots and $S_i, i \in (A, B)$ transmits status updates, which can be generated at the beginning of any time circle following the generate-at-will updates generation model [165]. Under this policy, the relay uses energy
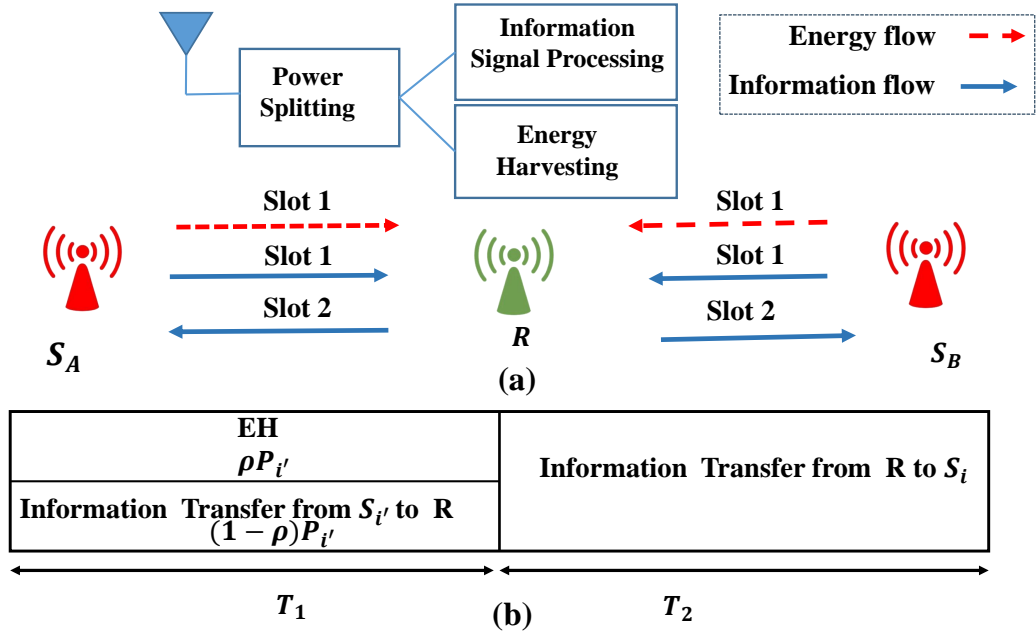
Figure 4.1: (a) In the system model, sources A S_A and B S_B exchange status updates with each other with the help of a single relay R; sources send updates to the R during the first transmission time slot $T1$ while the R is harvesting energy and then the R exchanges updates received from each source using harvested energy during the second transmission time slot T_2. (b) Timing diagram of the proposed cooperative strategies.

harvested within the first transmission time slot for the transmission in the second transmission time slot without waiting. Suppose the harvested energy is less than the minimum required energy for the transmission. In that case, the relay does not transmit the received updates and updates received from both sources are destroyed at the relay. Also, if the update transmission is unsuccessful at the relay or destination nodes within the considered time circle, it is destroyed to keep the information fresh [165].

- *WUC* : Under the WUC policy, $S_i, i \in (A, B)$ generates status updates at the beginning of each transmission circle following the generate-at-will updates generation model and then updates are transmitted to the R while R harvests energy from the sources. However, suppose R is unable to harvest the required energy set by the system within the first time slot. In that case, it waits for the transmission until it harvests the required energy for an update exchange and after it harvests the required energy defined by the system, the R exchanges the latest updates in the second transmission slot (T_2). In this event, $S_i, i \in (A, B)$ sent an update at each transmission slot until R harvested the required power and the R transmits the most recent update received from the sources. Simply, relay will transmit the update received in the final time slot of the waiting time (T_w) to maintain the freshness of the information.

In addition, the following set of assumptions is taken into account throughout this chapter:

1. There is no direct link between the source and the destination (opposite source) node due to intense shadowing or blockage. Therefore, the intermediate relay facilitates the transmission

of messages from the source to the destination (opposite source). This system model considers a single relay node for simplicity.

2. The relay node employs the DF technique as its relaying protocol.

3. The channel gains of each channel in this system are modeled using quasi-static block-fading and non-selective frequency parameters. The channel is independent and identically distributed from one block to the next. All wireless channels are modelled as Rayleigh fading channels and stay constant during each transmission block.

4. The processing power required by the transmit/receive circuitry at the relay is insignificant as compared to the power utilised for signal transmission from the relay to the destination (opposite source)[10].

5. The up-link transmission between the source and the relay are performed in an orthogonal channel.

To facilitate a clear exposition, this chapter concentrates on single-antenna transmission and frequency-flat fading channels. It is worth noting, however, that an extension of the system model to scenarios involving multiple antennas or frequency-selective fading is entirely feasible.

Throughout the chapter, H_{ij} represents the channel coefficient of the channel between node i and node j, where $i, j \in \{A, B, R\}$ and $i \neq j$. The small-scale channel gain g_{ij} is $g_{ij} = |h_{ij}|^2$, where $h_{ij} \sim \mathcal{CN}(0, 1)$ is the fading channel coefficient, where $\mathcal{CN}$ represents complex normal (Gaussian) distribution. The PDF of the small-scale channel gain for the Rayleigh fading can be defined as $f_{g_{ij}}(z) = e^{-z}, z \geq 0$. The large-scale channel gain α_{ij} is given by [92],

$$-10 \log_{10}(\alpha_{ij}) = 20 \log_{10}(d_{ij}) + 20 \log_{10}(\frac{4\pi f_c}{c}), \tag{4.1}$$

where f_c and d_{ij} are the carrier frequency and distance between node i and node j, respectively. c is the speed of light in space. Thus, the channel coefficient can be written as $H_{ij} = \sqrt{\alpha_{ij} g_{ij}}$ and channel gain G_{ij} is written as $G_{ij} = \alpha_{ij} g_{ij}$.

4.2.1 Block error analysis under finite block-length

The AoI is usually recognised as a destination-centric statistic since it measures the time difference between the present time and the generation time of the most recent update received by the destination. It only examines packets that are successfully received and forwarded to the destination. Furthermore, the AoI is greatly influenced by the transmission error rate and the update generation rate at the source. Then, our first objective is to study BLER at each destination (opposite source) in this system. The BLER at the destination under both transmission policies has been derived using different mathematical approximation techniques in this section.

4.2.1.1 Transmission Policy 01 : TWW

To calculate BLER at each node, it is necessary to derive the SNR at each node. The received SNR at the relay from each source node $S_{i'}, i' \in \{A, B\}$, $\gamma_R^{i'}$ is given by,

$$\gamma_R^{i'} = \frac{(1 - \rho)P_{i'}G_{i'R}}{\sigma_R^2}, \tag{4.2}$$

where ρ is the power splitting factor, noise power at the relay is denoted as σ_R^2 and transmit power at the $S_{i'}$ is given by $P_{i'}$. However, the harvested amount of energy at R depends on the EH policy. Thus, the system model is analysed according to the considered EH policy at the R. Under the TWW policy, the energy harvested by the relay from each node is given by,

$$E_R^{i'} = \rho\eta P_{i'}G_{i'R}T_1, \tag{4.3}$$

where η is the EH efficiency and T_1 is the transmission time of the first transmission slot and it can be calculated as $T_1 = n_R^{i'}T_s$, where $n_R^{i'}$ is the allocated block-length for the transmission between i' and R and T_s is the symbol duration. Then, the total energy harvested by the relay within the first transmission slot E_R is given by

$$E_R = \sum_{i'=\{A,B\}} E_R^{i'} = \rho\eta T_1 \left(P_A G_{AR} + P_B G_{BR} \right). \tag{4.4}$$

The available energy harvested by the relay for transmission E_R^T is given by

$$E_R^T = \begin{cases} E_{max}, & E_R \geq E_{max}, \\ E_R, & E_{max} > E_R > E_{min}, \\ 0, & \text{otherwise}, \end{cases} \tag{4.5}$$

where E_{max} is the maximum energy limit that the relay can harvest and E_{min} is the minimum energy required for transmission. E_{min} can be calculated as $E_{min} = P_{min}T_2$, where P_{min} is the minimum required power for the transmission while T_2 is the time of the second transmission slot. T_2 is calculated as

$$T_2 = \sum_{i=\{A,B\}} n_i^R T_s, \tag{4.6}$$

where n_i^R is the allocated block-length for the transmission between R and i. Then, the transmit power of relay P_R is calculated as $P_R = \frac{E_T^R}{T_2}$. During the second time slot, the received SNR at each $S_i \in \{A, B\}$, γ_i is given by

$$\gamma_i = \frac{P_R G_{Ri}}{\sigma_i^2}, \tag{4.7}$$

where σ_i^2 is noise power at the S_i. Then, using (4.4) and (4.5) SNR at the destination is expressed as

$$\gamma_i = \begin{cases} \frac{E_{max}\alpha_{Ri}g_{Ri}}{T_2\sigma_i^2}, & E_R > E_{max} \\ \frac{E_R\alpha_{Ri}g_{Ri}}{T_2\sigma_i^2}, & E_{max} \geq E_R \geq E_{min} \\ 0, & \text{otherwise}. \end{cases} \tag{4.8}$$

An outage happens when the relay or opposite source are unable to decode the received message successfully. Hence, the system overall decoding error probability ε_i at each source node i can be calculated as

$$\varepsilon_i = \varepsilon_R^{i'} + \left(1 - \varepsilon_R^{i'}\right)\varepsilon_i^R, \tag{4.9}$$

where $i \neq i', i, i' \in \{A, B\}$ and ε_j^t is the decoding error probability at receiving node $j \in (i, R)$ for block received from node $t \in (i', R)$. Following PPV´s results on short packet communication [90] and assuming that the receiver has the perfect CSI, the expectation of the block error probability at the receiving node for a given block-length n_j^t can be written as

$$\varepsilon_j^t = \mathbb{E}\left[Q\left(\frac{n_j^t C(\gamma_j^t) - k_j^t}{\sqrt{n_j^t V(\gamma_j^t)}}\right)\right], \tag{4.10}$$

where $\mathbb{E}[\cdot]$ is the expectation operator, $Q(\cdot)$ is the Q-function; it can be defined as $Q(x) = \frac{1}{\sqrt{2\pi}}\int_x^\infty e^{-\frac{t2}{2}}dt$ and $V(\gamma_j^t)$ is the channel dispersion, which can be written $V(\gamma_j^t) = \frac{\log_2^2 e}{2}(1 - \frac{1}{(1+\gamma_j^t)^2})$. The variable $C(\gamma_j^t)$ denotes the channel capacity of a complex AWGN channel and it is given by $C(\gamma_j^t) = \log_2(1 + \gamma_j^t)$. The number of bits per block is k_j^t. Moreover, under the Rayleigh fading channel conditions, ε_j^t can be formulated as

$$\varepsilon_j^t = \int_0^\infty f_{\gamma_j^t}(z)Q\left(\frac{n_j^t C(\gamma_j^t) - k_j^t}{\sqrt{n_j^t V(\gamma_j^t)}}\right)dz, \tag{4.11}$$

where $f_{\gamma_j^t}(z)$ denotes the PDF of the ε_j^t. Due to the complexity of the Q-function, it is challenging to get a closed-form expression for the overall decoding error probability. Thus, using the approximation technique given in [161] and [94], (4.11) can be approximated as

$$\varepsilon_j^t \approx \int_0^\infty f_{\gamma_j^t}(z)\Theta_j^t(z)dz, \tag{4.12}$$

where $\Theta_j^t(z)$ denotes the linear approximation of $Q\left(\frac{n_j^t C(\gamma_j^t) - k_j^t}{\sqrt{n_j^t V(\gamma_j^t)}}\right)$ that can be expressed as in [94]

$$\Theta_j^t(z) = \begin{cases} 1, & \gamma_j^t \leq \phi_j^t, \\ \frac{1}{2} - \beta_j^t\sqrt{n_j^t}(\gamma_j^t - \psi_j^t), & \phi_j^t < \gamma_j^t < \delta_j^t, \\ 0, & \gamma_j^t \geq \delta_j^t, \end{cases} \tag{4.13}$$

where $\tau_j^t = 2^{\frac{2k_j^t}{n_j^t}}, \beta_j^t = \frac{1}{2\pi\sqrt{\tau_j^t - 1}}, \psi_j = 2^{\frac{k_j^t}{n_j^t}} - 1, \phi_j^t = \psi_j^t - \frac{1}{2\beta_j^t\sqrt{n_j^t}}$ and $\delta_j^t = \psi_j^t + \frac{1}{2.\beta_j^t\sqrt{n_j^t}}$. By using above linear approximation, ε_j^t is expressed as

$$\varepsilon_j^t \approx \beta_j^t\sqrt{n_j^t}\int_{\phi_j^t}^{\delta_j^t} F_{\gamma_j^t}(z)\,dz, \tag{4.14}$$

where $F_{\gamma_j^t}(z)$ denotes CDF of the ε_j^t. To calculate error probability at each source i using (4.9), it is necessary to calculate $\varepsilon_R^{i'}$ and ε_i^R. Using (4.13) and (4.14), the BLER at R and each source can be calculated as follows:

$$\varepsilon_R^{i'} \approx \beta_R^{i'} \sqrt{n_R^{i'}} \int_{\phi_R^{i'}}^{\delta_R^{i'}} F_{\gamma_R^{i'}}(z)\, dz, \tag{4.15}$$

$$\varepsilon_i^R \approx \beta_i^R \sqrt{n_i^R} \int_{\phi_i^R}^{\delta_i^R} F_{\gamma_i^R}(z)\, dz, \tag{4.16}$$

Lemma 1. *An approximation expression for the block error probability at the relay can be derived as*

$$\varepsilon_R^{i'} \quad \approx \quad 1 \quad - \quad \left(\frac{(1-\rho)P_{i'}\alpha_{i'R}\beta_R^{i'}\sqrt{n_R^{i'}}}{\sigma_R^2}\right)\left(e^{-\frac{\phi_R^{i'}\sigma_R^2}{(1-\rho)P_{i'}\alpha_{i'R}}} - e^{-\frac{\delta_R^{i'}\sigma_R^2}{(1-\rho)P_{i'}\alpha_{i'R}}}\right). \tag{4.17}$$

Proof. : See Appendix A. $\qquad\qquad\square$

Lemma 2. *Block error probability at the opposite receiving node can be derived as follows:*

$$\varepsilon_i^R \quad \approx \quad \beta_i^R\sqrt{n_i^R}\left(\left(\frac{\delta_i^R + \phi_i^R}{2}\right)\sum_{v=1}^{V_f}\frac{\pi}{V_f}\sqrt{1-\phi_v^2}F_{\gamma_i^R}(q) \quad + \quad R_V\right), \tag{4.18}$$

where $\phi_v = \cos\left(\frac{2v-1}{2v}\pi\right)$, $q = \left(\frac{\delta_i^R - \phi_i^R}{2}\right)\phi_v + \left(\frac{\delta_i^R + \phi_i^R}{2}\right)$, V_f *is the complexity-accuracy trade-off factor, while* R_V *denotes the error term, which is ignored at substantially larger values of* V_f.

Proof. To calculate error probability at S_i, it is necessary to derive the CDF of SNR at the destination node. Using (4.5), $F_{\gamma_j^t}(z)$ can be derived as

$$F_{\gamma_i^R}(z) = \mathbb{P}_r\left(\gamma_i^R < z\right) = 1 - \mathbb{P}_r\left\{E_R \geq E_{min} \cap \gamma_i^R > z\right\}$$
$$F_{\gamma_i^R}(z) = 1 - \underbrace{\mathbb{P}_r\left\{E_{min} \leq E_R \leq E_{max} \cap \gamma_i^R > z\right\}}_{L_1} - \underbrace{\mathbb{P}_r\left\{E_R \geq E_{max} \cap \gamma_i^R > z\right\}}_{L_2}. \tag{4.19}$$

Then, substituting $E_R = \rho\eta T_1\left(P_A\alpha_{AR}g_{AR} + P_B\alpha_{BR}g_{BR}\right)$, L_1 in (4.19) is evaluated as follows:

$$L_1 = \mathbb{P}_r\left\{\Omega_1 < I < \Omega_2 \cap Ig_{Ri} > \Omega_3\right\} \tag{4.20}$$

or

$$L_1 = \begin{cases} 0, & g_{Ri} < \frac{\Omega_3}{\Omega_2} \\ \mathbb{P}_r\left\{\frac{\Omega_3}{g_{Ri}} < I \leqslant \Omega_2\right\}, & \frac{\Omega_3}{\Omega_2} < g_{Ri} < \frac{\Omega_3}{\Omega_1} \\ \mathbb{P}_r\left\{\Omega_1 < I \leqslant \Omega_2\right\}, & g_{Ri} > \frac{\Omega_3}{\Omega_1} \end{cases} \tag{4.21}$$

where $\Omega_1 = \frac{E_{min}}{\rho\eta T_1}$, $\Omega_2 = \frac{E_{max}}{\rho\eta T_1}$, $\Omega_3 = \frac{z\sigma_i^2 T_2}{\rho\eta T_1\alpha_{Ri}}$ and $I = \sum_{i=\{A,B\}}P_i\alpha_{iR}g_{iR}$. To calculate L_1 it is necessary to get PDF and CDF of I and g_{Ri}. Then, to calculate PDF of I, it is considered as summation of two independent random variable as $I = \mu_1 + \mu_2$, where $\mu_1 \sim \exp(\frac{1}{P_A\alpha_{AR}})$ and

$\mu_2 \sim \exp(\frac{1}{P_B \alpha_{BR}})$. Then, using the concepts of convolution of random variables, PDF and CDF of I can be calculated as follows:

$$
\begin{aligned}
f_I(z) &= \int_{-\infty}^{\infty} f_{\mu_1}(x) f_{\mu_2}(z-x) dx \\
&= \int_0^z \frac{1}{P_A \alpha_{AR}} e^{-\frac{1}{P_A \alpha_{AR}} x} \frac{1}{P_B \alpha_{BR}} e^{-\frac{1}{P_B \alpha_{BR}}(z-x)} dx, \\
&= \frac{1}{P_A \alpha_{AR} P_B \alpha_{BR}} e^{-\frac{1}{P_B \alpha_{BR}} z} \int_0^z e^{(\frac{1}{P_B \alpha_{BR}} - \frac{1}{P_A \alpha_{AR}})x} dx, \\
f_I(z) &= \begin{cases} \frac{1}{P_A \alpha_{AR} - P_B \alpha_{BR}}(e^{-\frac{1}{P_A \alpha_{AR}} z} - e^{-\frac{1}{P_B \alpha_{BR}} z}), & \text{if } \frac{1}{P_A \alpha_{AR}} \neq \frac{1}{P_B \alpha_{BR}}, \\ \frac{1}{(P\alpha)^2} z e^{-\frac{1}{P\alpha} z}, & \text{if } \frac{1}{P_A \alpha_{AR}} = \frac{1}{P_B \alpha_{BR}} = \frac{1}{P\alpha}, \end{cases}
\end{aligned}
\tag{4.22}
$$

where $f(\cdot)$ denotes PDF function of a random variable. Then, CDF of I can be calculated as

$$
\begin{aligned}
F_I(z) &= P(Z \leq z) = \int_0^z f(t) dt \\
F_I(z) &= \begin{cases} 1 + \frac{P_B \alpha_{BR}}{P_A \alpha_{AR} - P_B \alpha_{BR}} e^{-\frac{z}{P_B \alpha_{BR}}} - \frac{P_A \alpha_{AR}}{P_A \alpha_{AR} - P_B \alpha_{BR}} e^{-\frac{z}{P_A \alpha_{AR}}}, & \text{if } P_A \alpha_{AR} \neq P_B \alpha_{BR}, \\ 1 - e^{-\frac{1}{P\alpha} z}\left(1 + \frac{1}{P\alpha} z\right), & \text{if } \frac{1}{P_A \alpha_{AR}} = \frac{1}{P_B \alpha_{BR}} = \frac{1}{P\alpha}. \end{cases}
\end{aligned}
\tag{4.23}
$$

Further, approximations for L_1 are derived as follows:

$$
\begin{aligned}
L_1 &= \int_{\frac{\Omega_3}{\Omega_2}}^{\frac{\Omega_3}{\Omega_1}} \left(f_{g_{Ri}}(x) \int_{\frac{\Omega_3}{x}}^{\Omega_2} f_I(y) \, dy \right) dx + \int_{\Omega_1}^{\Omega_2} f_I(x) \, dx \int_{\frac{\Omega_3}{\Omega_1}}^{\infty} f_{g_{Ri}}(x) \, dx, \\
L_1 &= L_3 + (F_I(\Omega_2) - F_I(\Omega_1)) \left(1 - F_{g_{Ri}}\left(\frac{\Omega_3}{\Omega_1}\right) \right),
\end{aligned}
\tag{4.24}
$$

where $F(\cdot)$ denotes CDF function of a random variable and

$$
\begin{aligned}
L_3 &= \int_{\frac{\Omega_3}{\Omega_2}}^{\frac{\Omega_3}{\Omega_1}} \left(f_{g_{Ri}}(x) \int_{\frac{\Omega_3}{x}}^{\Omega_2} f_I(y) \, dy \right) dx \\
&= \int_{\frac{\Omega_3}{\Omega_2}}^{\frac{\Omega_3}{\Omega_1}} f_{g_{Ri}}(x) \left[F_I(\Omega_2) - F_I\left(\frac{\Omega_3}{x}\right) \right] dx, \\
L_3 &= F_I(\Omega_2) \left[F_{g_{Ri}}\left(\frac{\Omega_3}{\Omega_1}\right) - F_{g_{Ri}}\left(\frac{\Omega_3}{\Omega_2}\right) \right] - L_4,
\end{aligned}
\tag{4.25}
$$

where L_4 can be defined as

$$
L_4 = \int_{\frac{\Omega_3}{\Omega_2}}^{\frac{\Omega_3}{\Omega_1}} f_{g_{Ri}}(x) F_I\left(\frac{\Omega_3}{x}\right) dx.
\tag{4.26}
$$

The Gaussian-Chebyshev-quadrature (GCQ) method [166, 167] is used to obtain a closed-form expression for L_4 since it converges much faster than other approximation methods [168]. Then, (4.26) can be approximated as follows:

$$
L_4 \approx \frac{\frac{\Omega_3}{\Omega_1} + \frac{\Omega_3}{\Omega_2}}{2} \sum_{m=1}^{M} \frac{\pi}{M} \sqrt{1 - \phi_m^2} f_{g_{Ri}}(z_1) F_I\left(\frac{\Omega_3}{z_1}\right) + R_M,
\tag{4.27}
$$

where $\phi_m = \cos\left(\frac{2m-1}{2M}\pi\right)$, $z_1 = \frac{\frac{\Omega_3}{\Omega_1} - \frac{\Omega_3}{\Omega_2}}{2}\phi_m + \frac{\frac{\Omega_3}{\Omega_1} + \frac{\Omega_3}{\Omega_2}}{2}$, M is the complexity-accuracy trade-off factor and R_M is the error term that can be ignored at sufficiently high M values. Finally, the closed-form expression for L_1 can be approximated as shown in (4.29). Similarly, L_2 is calculated as

$$
\begin{aligned}
L_2 &= \mathbb{P}_r\left\{I > \Omega_2 \cap g_{Ri} > \Omega_4\right\}, \\
&= \left(1 - F_I\left(\Omega_2\right)\right)\left(1 - F_{g_{Ri}}\left(\Omega_4\right)\right),
\end{aligned}
\tag{4.28}
$$

where $\Omega_4 = \frac{z\sigma_i^2 T_2}{E_{max}\alpha_{Ri}}$. Then, CDF of SNR at each destination ($F_{\gamma_j^t}(z)$) can be obtained by substituting (4.29) and (4.28) in (4.19) as in (4.30). The result can be proved by substituting (4.30) to (4.14) and then applying the GCQ method for the integration of the CDF function. $\qquad\square$

Finally, by substituting (4.17) and (4.18) into (4.9) the overall transmission error probability can be calculated.

4.2.1.2 Transmission Policy 02 : WUC

Under this policy, the relay waits to transmit updates received from the sources until it harvests the required amount of energy E'_{harv} that is defined by the system. The E'_{harv} is calculated as $E_{harv} = P_{req}T_2$, where P_{req} is the required power at R for the transmission. In addition, it also assumes that the maximum energy limit that the relay can harvest under this policy is the same as the required energy. As a result, under this policy, transmission power at the relay is fixed to the P_{req}.

Lemma 3. *An approximation for the overall transmission error probability at each source under the WUC policy can be obtained as*

$$
\varepsilon_i \approx 1 - \left(\frac{\beta_R^{i'}\beta_i^R\sqrt{n_R^{i'}n_i^R}((1-\rho)P_{i'}P_{req})\alpha_{i'R}\alpha_{Ri}}{\sigma_R^2\sigma_i^2}\right)
$$
$$
\left(e^{-\frac{\phi_R^{i'}\sigma_R^2}{\alpha_{i'R}(1-\rho)P_{i'}}} - e^{-\frac{\delta_R^{i'}\sigma_R^2}{\alpha_{iR}(1-\rho)P_{i'}}}\right)\left(e^{-\frac{\phi_i^R\sigma_i^2}{\alpha_{Ri}P_{req}}} - e^{-\frac{\delta_i^R\sigma_i^2}{\alpha_{Ri}P_{req}}}\right). \tag{4.31}
$$

$$
L_1 \approx F_I\left(\Omega_2\right)\left[F_{g_{Ri}}\left(\frac{\Omega_3}{\Omega_1}\right) - F_{g_{Ri}}\left(\frac{\Omega_3}{\Omega_2}\right)\right] - \frac{\frac{\Omega_3}{\Omega_1} + \frac{\Omega_3}{\Omega_2}}{2}\sum_{m=1}^{M}\sqrt{1 - \phi_m^2}f_{g_{Ri}}\left(z_1\right)F_I\left(\frac{\Omega_3}{z_1}\right) + R_M
$$
$$
+ \left(F_I\left(\Omega_2\right) - F_I\left(\Omega_1\right)\right)\left(1 - F_{g_{Ri}}\left(\frac{\Omega_3}{\Omega_1}\right)\right). \tag{4.29}
$$

$$
F_{\gamma_i^R}\left(z\right) \approx 1 - F_I\left(\Omega_2\right)\left[F_{g_{Ri}}\left(\frac{\Omega_3}{\Omega_1}\right) - F_{g_{Ri}}\left(\frac{\Omega_3}{\Omega_2}\right)\right] - \frac{\frac{\Omega_3}{\Omega_1} + \frac{\Omega_3}{\Omega_2}}{2}\sum_{m=1}^{M}\sqrt{1 - \phi_m^2}f_{g_{Ri}}\left(z_1\right)F_I\left(\frac{\Omega_3}{z_1}\right)
$$
$$
+ R_M + \left(F_I\left(\Omega_2\right) - F_I\left(\Omega_1\right)\right)\left(1 - F_{g_{Ri}}\left(\frac{\Omega_3}{\Omega_1}\right)\right) - \left(1 - F_I\left(\Omega_2\right)\right)\left(1 - F_{g_{Ri}}\left(\Omega_4\right)\right). \tag{4.30}
$$

Proof. : See Appendix B. □

4.2.2 AoI Analysis

4.2.2.1 Transmission Policy 01 : TWW

This section calculates the AAoI of the two-way relay system. The S_A and S_B generate new status updates every transmission circle to keep the information at the corresponding destinations as fresh as possible. Then, generated updates are transmitted to its opposite source using relay system. If the generation time of the freshest update received at opposite source time stamp t is $g(t)$, then AoI can be defined as a random process as

$$\Delta(t) = t - g(t). \tag{4.32}$$

As illustrated in Figure 4.2, it is assumed that at $t = 0$ the measurements of the AoI start and the
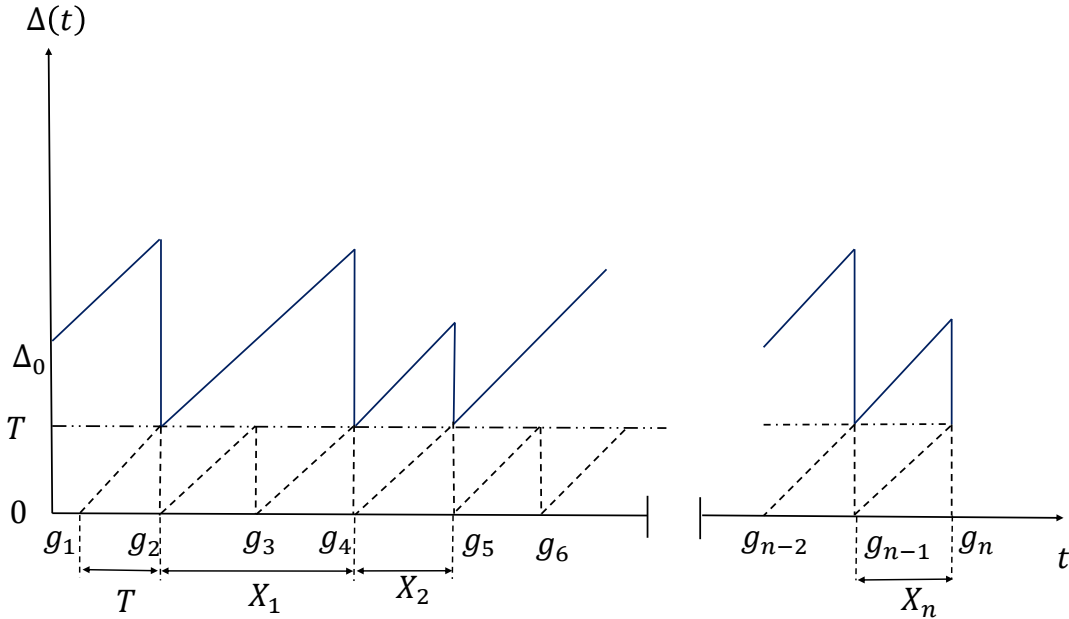
Figure 4.2: Evolution of AoI $\Delta(t)$ at at opposite source (destination) with the time under the *TWW* policy: Each source generate updates at time stamps $g_1, g_2, ..., g_{n-1}$ and the opposite source receive these updates at time stamps $g_2, g_3, ..., g_n$.

AoI at the opposite source (destination) is set to $\Delta(0) = \Delta_0$. Each source generates updates at time stamps $g_1, g_2, ..., g_{n-1}$ and the opposite source receive these updates at time stamps $g_2, g_3, ..., g_n$. As illustrated in Figure 4.2, data update i is transmitted from the source at time stamp $t = g_i$ and it is successfully delivered to its opposite source at time stamp $g_{i+1} = g_i + T$ where T is total time allocated for a transmission circle and $T = T_1 + T_2$. Therefore, if update packet delivered successfully, at the time g_{i+1}, the AoI at the opposite source can be calculated as

$$\Delta(g_{i+1}) = T. \tag{4.33}$$

The AoI increases linearly until the next update is successfully delivered to the opposite source. As an example, since one packet fails to be decoded at time g_3, $\Delta(t)$ continues to increase linearly. Here, X_i is the inter-departure time between two consecutive successfully received status updates at S_i and it is a geometric random variable with mean $E[X_i] = \frac{T}{1-\varepsilon_i}$ and second moment $E\left[X_i^2\right] = \frac{T^2(1+\varepsilon_i)}{(1-\varepsilon_i)^2}$. It assumes that the end-to-end delay of each successfully received update is always a constant given by $E[Y_i] = T_1 + T_2 = T$. Then, applying graphical methods to saw-tooth age waveform in Figure 4.2 and using (2.4) , AAoI at each $S_i, i \in (A, B)$, Δ_i^{AAoI} is computed as follows:

$$\Delta_i^{AAOI} = \frac{E[X_i^2]}{2E[X_i]} + T, \tag{4.34}$$

Lemma 4. *For the two way relay network, the expression of the AAoI at each source Δ_i^{AAoI} can be obtained as follows:*

$$\Delta_i^{AAOI} = \frac{T}{2} + \frac{T}{1 - \varepsilon_i} \tag{4.35}$$

Proof. The result can be proved by substituting $E[X_i] = \frac{T}{1-\varepsilon_i}$ and $E\left[X_i^2\right] = \frac{T^2(1+\varepsilon_i)}{(1-\varepsilon_i)^2}$ into (4.34). □

The expected weighted sum AAoI of the two-way relay system Δ_{Sum}^{AAoI} can be calculated as follows,

$$\Delta_{Sum}^{AAoI} = \sum_{i=\{A,B\}} \omega_i \Delta_i^{AAOI} \tag{4.36}$$

where ω_i is the weighting coefficient at S_i.

4.2.2.2   Transmission Policy 02 : WUC

Under this policy, the delay induced by the energy collection time to harvest the required energy has a significant impact on the AoI. This time period is determined by two factors: the amount of energy necessary for the transmission at the relay and the randomness of harvested energy in each time slot. As a result, the important issue is how long it takes to collect the amount of energy required for the transmission. Under this condition, the end-to-end delay time is not as constant as it was previously and it can be defined as the sum of the waiting and receiving time at the relay T_w and the transmission time between R and the opposite source T_2. The number of time slots in T_w is defined as m_w (one time slot is equal to T_1 amount of time). The probability mass function (PMF) of the m_w defined as $P_w(m)$ gives the probability that m_w is exactly equal to m number of time

slots. Then, $P_w(m)$ obtained as follows:

$$
\begin{aligned}
P_w(m) &= \mathbb{P}_r\left\{\left(\sum_{k=1}^{m-1} E_R^k < E_{harv}\right) \cap \left(\sum_{k=1}^{m} E_R^k \geq E_{harv}\right)\right\}, \\
&= \mathbb{P}_r\left\{\left(\sum_{k=1}^{m-1}\sum_{i\in\{A,B\}} \rho\eta P_i G_{iR}^k T_1 < E_{harv}\right) \cap \left(\sum_{k=1}^{m}\sum_{i\in\{A,B\}} \rho\eta P_i G_{iR}^k T_1 \geq E_{harv}\right)\right\}, \\
&= \mathbb{P}_r\left\{\left(\sum_{k=1}^{m-1}\sum_{i\in\{A,B\}} P_i G_{iR}^k < E'_{harv}\right) \cap \left(\sum_{k=1}^{m}\sum_{i\in\{A,B\}} P_i G_{iR}^k \geq E'_{harv}\right)\right\}, \\
&= \mathbb{P}_r\left\{\left(\sum_{k=1}^{m-1}\sum_{i\in\{A,B\}} P_i \alpha_{iR} g_{iR}^k < E'_{harv}\right) \cap \left(\sum_{k=1}^{m}\sum_{i\in\{A,B\}} P_i \alpha_{iR} g_{iR}^k \geq E'_{harv}\right)\right\}, \\
&= \mathbb{P}_r\left\{(Z < E'_{harv}) \cap (Z + V_c \geq E'_{harv})\right\}, \\
&= \int_{z=0}^{E'_{harv}} \int_{v_c=E'_{harv}-z}^{\infty} f_Z(z) f_{V_c}(v_c)\, dv\, dz, \\
P_w(m) &= \int_{z=0}^{E'_{harv}} f_Z(z)[1 - F_{V_c}(E'_{harv} - z)]\, dz,
\end{aligned}
$$

$$(4.37)$$

where $E'_{harv} = \frac{E_{harv}}{\rho\eta T_1}$, Z and Vc are random variables. The distribution of the Z is the same as the mixture of two mutually independent Erlang distributions. It is known as hyper-Erlang distribution [169, 170]. Therefore, the PDF of Z is given by

$$
\begin{aligned}
f_Z(z) = \frac{(-1)^{m-1} \xi_A^{m-1} \xi_B^{m-1}}{(\xi_B - \xi_A)^{2(m-1)}} &\left[e^{-\xi_A z} \sum_{k=1}^{m-1} \binom{2m-k-3}{m-2} \right. \\
&\frac{(\xi_A - \xi_B)^k z^{k-1}}{(k-1)!} + e^{-\xi_B z} \sum_{k=1}^{m-1} \binom{2m-k-3}{m-2} \\
&\left. \frac{(\xi_B - \xi_A)^k z^{k-1}}{(k-1)!}\right], \quad (4.38)
\end{aligned}
$$

where $\xi_A = \frac{1}{P_A \alpha_{AR}}$, $\xi_B = \frac{1}{P_B \alpha_{BR}}$ and $\xi_A \neq \xi_B$. CDF of Vc is given by

$$
F_{V_c}(t) = \mathbb{P}(V_c \leq t) = 1 + \frac{\xi_A}{\xi_B - \xi_A} e^{-\xi_B t} - \frac{\xi_B}{\xi_B - \xi_A} e^{-\xi_A t}. \quad (4.39)
$$

When $\xi_A \neq \xi_B$, it is challenging to find closed-form expression for $P_w(m)$. However, when $\xi_A = \xi_B = \xi$, the following is obtained:

$$
f_Z(z) = \frac{\xi^{2m-2} e^{-\xi z} z^{2m-3}}{(2m-3)!} \sim \text{Erlang}(2m-2, \xi), \quad (4.40)
$$

$$
F_{V_c}(t) = \mathbb{P}(V_c \leq t) = 1 - e^{-\xi t}\left[1 + \xi t\right], \quad (4.41)
$$

$$
P_w(m) = \frac{e^{-\xi E'_{harv}}\left(\xi E'_{harv}\right)^{2m-2}\left[2m-1+\xi E'_{harv}\right]}{(2m-1)!}. \quad (4.42)
$$

To compare the two transmission policies, it is considered that $\xi_A = \xi_B = \xi$

Lemma 5. *The first and second moments of the number of slots in the sum of the waiting and receiving time at the relay are computed as follows,*

$$E\left[m_w\right] = 1 + \frac{\xi E'_{harv}}{2}, \tag{4.43}$$

$$E\left[m_w^2\right] = 1 + \frac{\left(\xi E'_{harv}\right)^2}{4} + \frac{5\xi E'_{harv}}{4}, \tag{4.44}$$

Proof. : See Appendix C. □

Then, the first and second moments of waiting time are calculated as follows,

$$E\left[T_w\right] = \left(1 + \frac{\xi E'_{harv}}{2}\right) T_1, \tag{4.45}$$

$$E\left[T_w^2\right] = \left(1 + \frac{\left(\xi E'_{harv}\right)^2}{4} + \frac{5\xi E'_{harv}}{4}\right) T_1^2. \tag{4.46}$$

Lemma 6. *The AAoI at each source in a decode and forward two-way relay network under the WUC policy can be derived as*

$$\Delta_i^{AAOI} = \frac{(1 + \varepsilon_i)\left(T_2^2 + 2T_2 E\left[T_w\right] + E\left[T_w^2\right]\right)}{2\left(1 - \varepsilon_i\right)\left(E\left[T_w\right] + 2T_2\right)} + T_2 + E\left[T_w\right]. \tag{4.47}$$

Proof. To calculate AAoI at each source, it is necessary to calculate the overall transmission error probability ε_i at each source. It is assumed that after one successful update received at the opposite source, n_f number of failures occur until the next successful update received, where n_f is geometrically distributed with parameter $1 - \varepsilon_i$. The time span between two consecutive successful update receptions is $X = (n_f + 1)Y$, where Y denotes the time incurred to traverse through the network and it can be defined as $Y = T_w + T_2$. Thus, X is distributed as

$$X \sim \sum_{n_f=0}^{\infty} \left(\varepsilon_i\right)^{n_f} \left(1 - \varepsilon_i\right) \delta\left(X - \left(n_f + 1\right) Y\right), \tag{4.48}$$

where $\delta(X)$ refers to the dirac impulse [171]. The AAoI stated in (2.4) depends on Y and first and second moments of the X. Thus, $E[X]$ can be derived as

$$\begin{aligned}
E\left[X\right] &= \sum_{n_f=0}^{\infty} \left(\varepsilon_i\right)^{n_f} \left(1 - \varepsilon_i\right) \left(n_f + 1\right) E\left[Y\right], \\
&= \frac{E\left[Y\right]}{1 - \varepsilon_i} = \frac{E\left[T_w\right] + T_2}{1 - \varepsilon_i},
\end{aligned} \tag{4.49}$$

and the second-order-moment $E\left[X^2\right]$ can be calculated as

$$\begin{aligned}
E\left[X^2\right] &= \sum_{n=0}^{\infty} E\left[((n + 1) Y)^2 \left(\varepsilon_i\right)^n \left(1 - \varepsilon_i\right) \left(n + 1\right)\right], \\
&= E\left[Y^2\right] \frac{1 + \varepsilon_i}{\left(1 - \varepsilon_i\right)^2}, \\
E\left[X^2\right] &= \frac{1 + \varepsilon_i}{\left(1 - \varepsilon_i\right)^2} \left[T_2^2 + 2T_2 E\left[T_w\right] + E\left[T_w^2\right]\right].
\end{aligned} \tag{4.50}$$

55

Then, using (2.4), Δ_i^{AAoI} under WUC policy is formulated as follows:

$$\Delta_i^{AAOI} = \frac{E\left[X^2\right]}{2E\left[X\right]} + T_2 + \frac{E[T_w X]}{E\left[X\right]}, \tag{4.51}$$

and assuming T_w and X are independent and identically distributed random variables, AAoI Δ_i^{AAoI} is given by (4.51) can be re-formulated as

$$\Delta_i^{AAOI} = \frac{E\left[X^2\right]}{2E\left[X\right]} + T_2 + E\left[T_w\right]. \tag{4.52}$$

Then, the result can be proved by substituting (4.49) and (4.50) into (4.52). □

The expected weighted sum AAoI of the two-way relay system under WUC policy can be calculated using (4.36).

4.3 Simulation results and discussions

This section presents the analytical and simulation results. Unless otherwise mentioned, the simulation parameters are listed in Table 4.1.

Table 4.1: Simulation Parameters for SWIPT-Enabled Two-Way Relay System with Short Packet Communication [172, 173]

Parameter	Value
Distance between S_A and R (d_{AR})	30 m
Distance between S_B and R (d_{BR})	30 m
Carrier frequency (f_c)	900 MHz
Speed of the light (m/s) (c)	$3 \times 10^8 \text{ms}^{-1}$
Transmission power at $S_A(P_A)$	1 W
Transmission power at $S_B(P_B)$	1 W
Symbol duration (T_s)	20 µs
n_R^A, n_R^B	200 bits
n_A^R, n_B^R	200 bits
k_R^A, k_R^B	32 bits
Noise power ($\sigma_R^2, \sigma_A^2, \sigma_B^2$)	-100 dBm
E_{max}	0.001 J
P_{min}	0.0001 mW
P_{req}	0.01 mW
Power spitting factor (ρ)	0.5
ω_A	0.5
ω_B	0.5
EH efficiency (η)	0.9

Figure 4.3 presents the comparison of BLER performance between MC-based simulations and theoretical approximations for both transmissions and EH policies. Theoretical BLER closely matches simulation outcomes for both policies. In the context of the TWW policy, it is observed that the BLER nearly reaches 1 when the transmission power of the sources is low. This is due to the fact that, under the TWW policy, the relay does not wait to harvest enough energy for
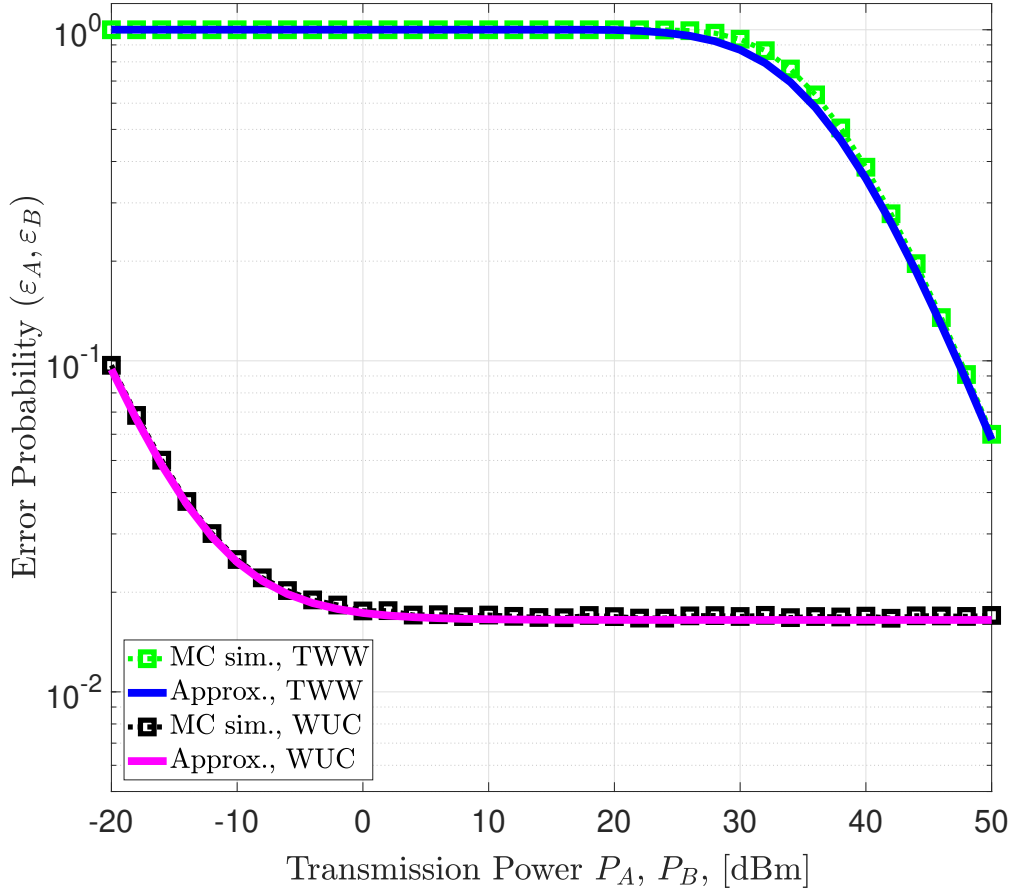
Figure 4.3: BLER as a function of transmission power.

transmission and EH depends solely on the power transmitted during the first transmission slot. Consequently, with low transmission power from the source, the energy available for harvesting remains insufficient. As a result, the received SNR at the receiver is very low, leading to a high level of BLER. In contrast, increasing the transmission power of the sources enhances the EH capacity of the relay, consequently allowing for the maintenance of a substantial level of transmission power at the relay. As a result, this leads to a reduction in BLER when the transmission power of the sources increases. On the contrary, BLER under the WUC policy remains relatively stable despite changes in the transmission power of the sources. The WUC policy allows the relay to wait for sufficient power before transmitting, maintaining a nearly constant relay transmission power. As a result, it maintains a high received SNR at the receiver, leading to a low level of BLER. Therefore, variations in the transmission power of the sources have a minimal impact on BLER, making the WUC policy more suitable for applications requiring a high level of reliability.

In Figure 4.4, the weighted sum of AAoI is plotted as a function of transmission power at the sources. Under both policies, as the transmission power at the sources increases, the weighted sum of AAoI decreases. However, the decrease in the weighted sum of AAoI is more pronounced under the WUC policy when power increases. This is due to, according to Lemma 6, the AAoI under the WUC policy depending on the transmission waiting time T_w and the BLER at the
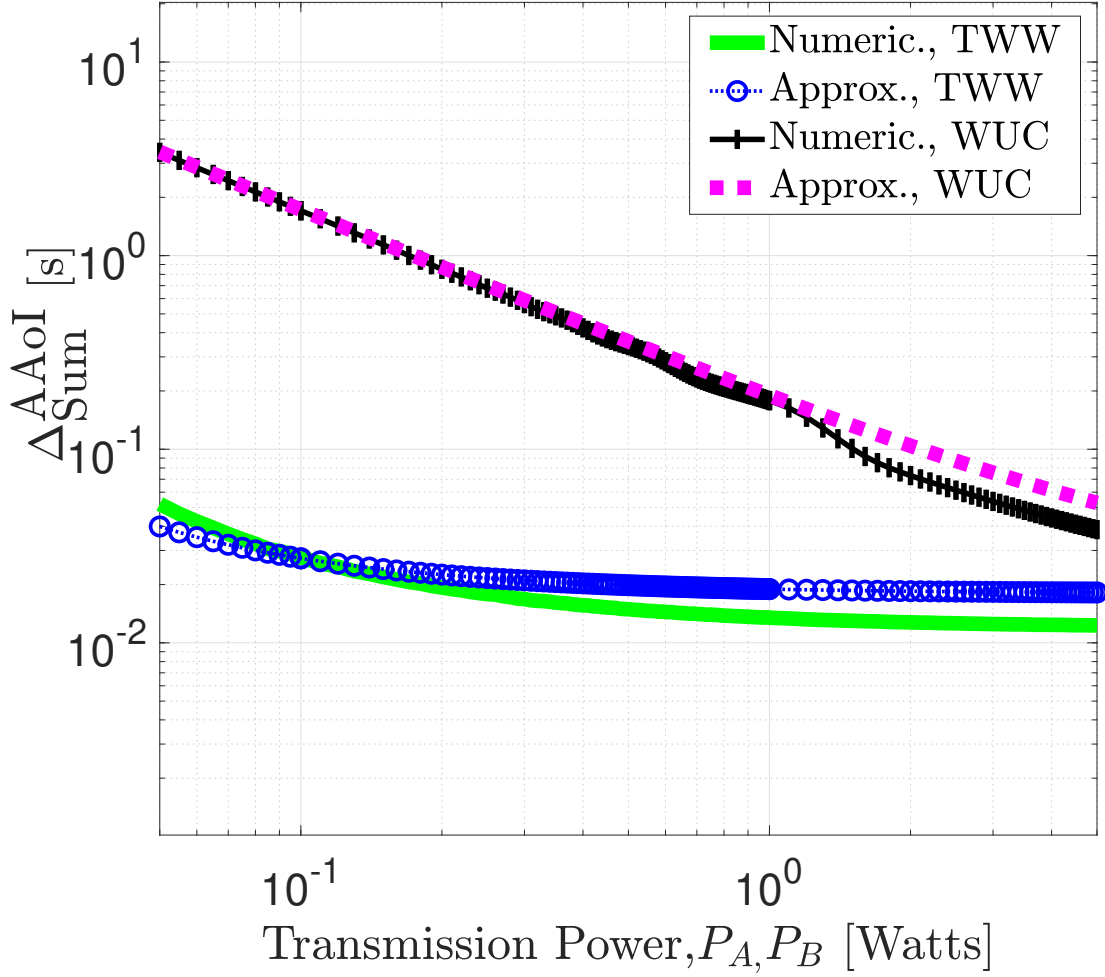
Figure 4.4: Weighed sum AAoI as a function of transmission power.

receiving end. Furthermore, according to Lemma 5, increasing transmission power at the source leads to a reduction in both T_w and BLER. As a result, increasing transmission power leads to a reduction in the weighted sum of AAoI, especially due to the high influence of waiting time reduction. On the other hand, as per Lemma 4, under the TWW policy, if transmission time is fixed, only BLER becomes a main factor influencing the weighted sum of AAoI. From this figure, it can be concluded that, especially under low-level transmission power, the influence of T_w is more significant than BLER on the weighted sum of AAoI. Thus, the TWW policy maintains a low level of the weighted sum of AAoI when the transmission power is low compared to the WUC policy. Consequently, the TWW policy emerges as a suitable choice for low-power IoT applications with stringent requirements for information freshness. On the other hand, the WUC policy proves more suitable for applications where reliability takes precedence over information freshness. These findings highlight the significance of selecting an appropriate policy based on the specific requirements of the application, ensuring optimal performance.

In Figure 4.5, the relationship between the weighted sum of the AAoI and block length for both policies is illustrated. When the transmission power is high, there is a noticeable increase in AAoI
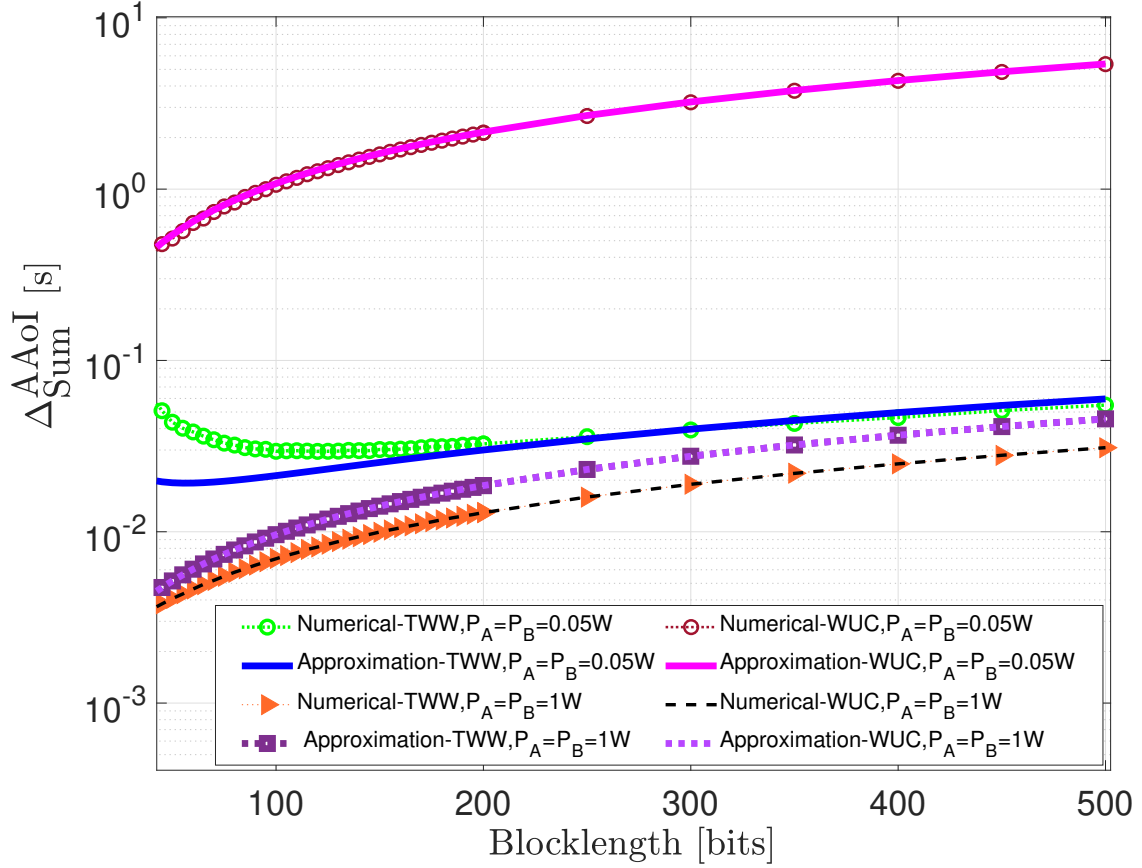
Figure 4.5: Weighed sum AAoI as a function of block-length.

as the block length increases for both policies. Typically, an increase in block length leads to a decrease in BLER [90] and an extension of transmission time. Lemmas 4 and 6 indicate that a reduction in BLER should decrease AAoI, while also suggesting that prolonged transmission time contributes to an increase in AAoI. In particular, in scenarios with high transmission power, the impact of the extended transmission time becomes more pronounced than the reduction in BLER on AAoI. Therefore, under high transmission power conditions, increasing the block length results in an increase in the weighted sum of AAoI for both policies.

Under the TWW policy, when the transmission power is low, increasing the block length from a small value reduces BLER [90]. Consequently, AAoI decreases according to Lemma 4 until it reaches its optimal value. In this scenario, the decrease in BLER has a more significant impact on AAoI compared to the increase in transmission time. However, once the block length surpasses its optimal value, increasing it further only serves to extend the transmission time. Consequently, AAoI starts to increase, especially in high-power scenarios. However, for the WUC policy, under all transmission power scenarios, increasing the block length always increases the AAoI since it maintains a higher received SNR level at the destination using constant transmission power in the relay node. Hence, in the figure, it is observed that, beyond a block length of 200, under all transmission power scenarios, AAoI exhibits the same behaviour. Furthermore, the gap between the AAoI under the two policies decreases as the power level increases. This is due to increasing

block length, which increases both transmission time and waiting time. Both parameters affect AAoI under the WUC policy, while under the TWW policy, only an increase in transmission time affects AAoI.

Additionally, concerning the WUC policy, numerical results closely match the approximated outcomes. However, in the low- SNR regime for the TWW policy, the approximated AAoI results do not align well with the numerically simulated results. This discrepancy arises due to the approximations in (4.17) and (4.18) are accurate only for moderate SNR values [14]. Moreover, this inconsistency is particularly evident when the block length is lower than 200, as finite block length information theory-based approximations fail to reconcile with simulation-based results, especially under low SNR scenarios.
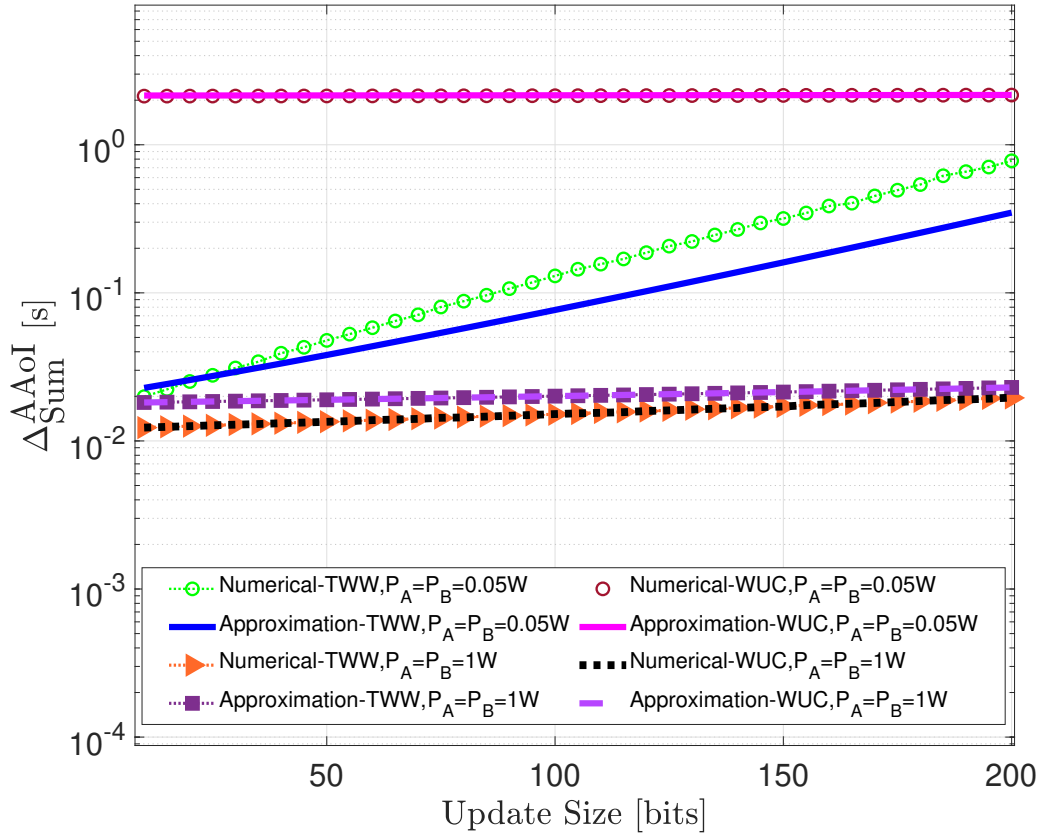
Figure 4.6: Weighed sum AAoI as a function of update size

In Figure 4.6, the weighted sum of AAoI is presented as a function of the update size for both policies. Under low transmission power conditions, if the packet size increases, the AAoI also increases under the TWW policy, while there is no significant change under the WUC policy. This is due to the fact that under the TWW policy, due to low transmission power at the relay, varying update sizes under a fixed block length increases BLER, which affects the AAoI as in Lemma 4. However, under the WUC policy, the transmission power at the relay is maintained at a satisfactory level, resulting in a low BLER. Additionally, there are no changes in the transmission time or waiting time since the block length is fixed. Consequently, the AAoI under the WUC policy

remains relatively unchanged when the block length varies. In a high-transmission power scenario, the packet size does not have a significant impact on the AAoI for either policy. This is due to the fact that with high SNR, the BLER is very small and increasing the update size results in a slight increase in BLER [90]. However, the effect of this small variation in the BLER does not significantly affect the AAoI, since other parameters such as the waiting time and the transmission time are also fixed. Furthermore, it has been observed that the TWW policy outperforms the WUC policy in terms of information freshness under low SNR scenarios for all packet sizes.
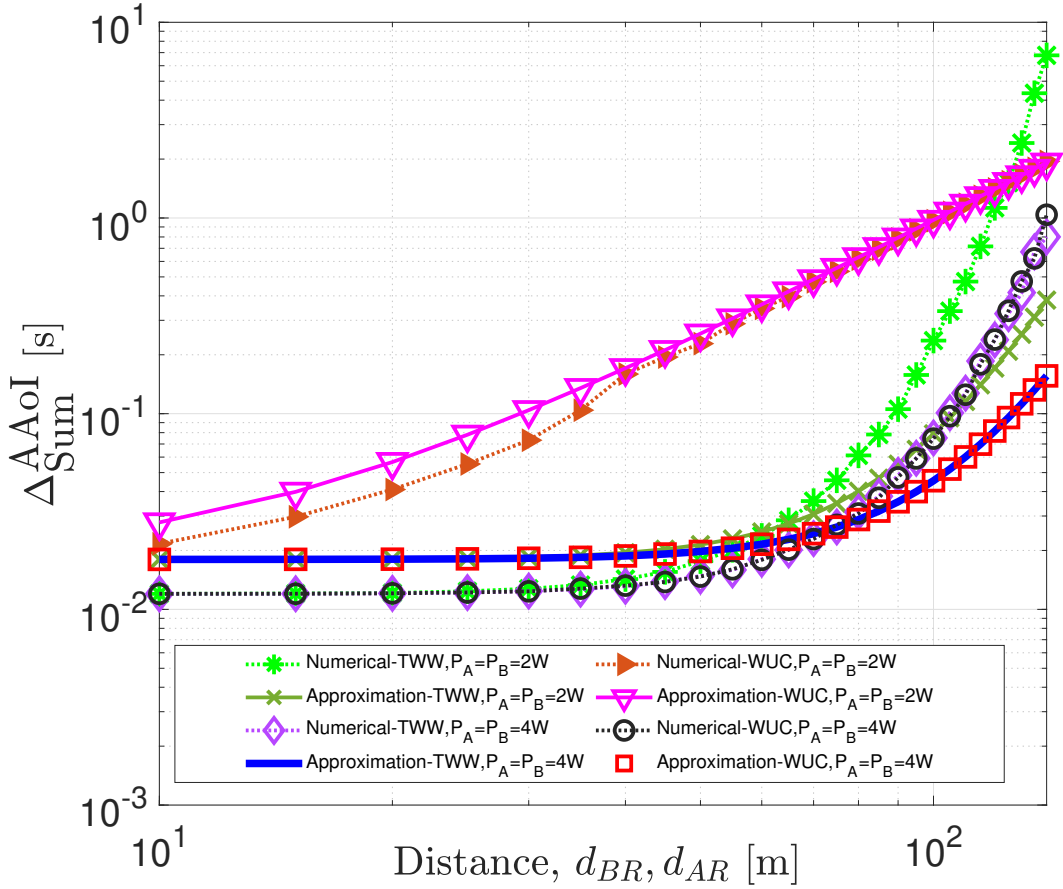
Figure 4.7: Weighed sum AAoI as a function of distance.

Figure 4.7 illustrates the weighted sum AAoI as a function of the distance between the relay and sources, where both sources are located at the same distance from the relay (i.e., $d_{BR} = d_{AR}$). The AAoI grows as the distance between the sources and the relay increases (i.e., the SNR drops). This is due to the fact that decreasing the SNR increases BLER, as well as the waiting time for harvesting under the WUC policy, thereby increasing AAoI according to Lemma 4 and 6. Additionally, when the distance is increased, it increases AAoI under the TWW policy dramatically compared to the linear growth under the WUC policy. This is due to the fact that under the TWW policy, increments in distance increase BLER significantly due to low transmission power at the relay. Moreover, the approximated results coincide with the numerically simulated results under the WUC

policy, even for long distances. However, in relation to the TWW policy, as the distance increases, there is a significant deviation between the approximated and simulated results. This discrepancy is particularly noticeable for low SNR values, where the approximation used in (4.12) does not perform as effectively for low SNR values [94]. Overall, the WUC policy outperforms the TWW policy for long-distance communication since it maintains better freshness of the information at the receiving node, whereas the TWW policy maintains a very high level of AAoI for long distances.
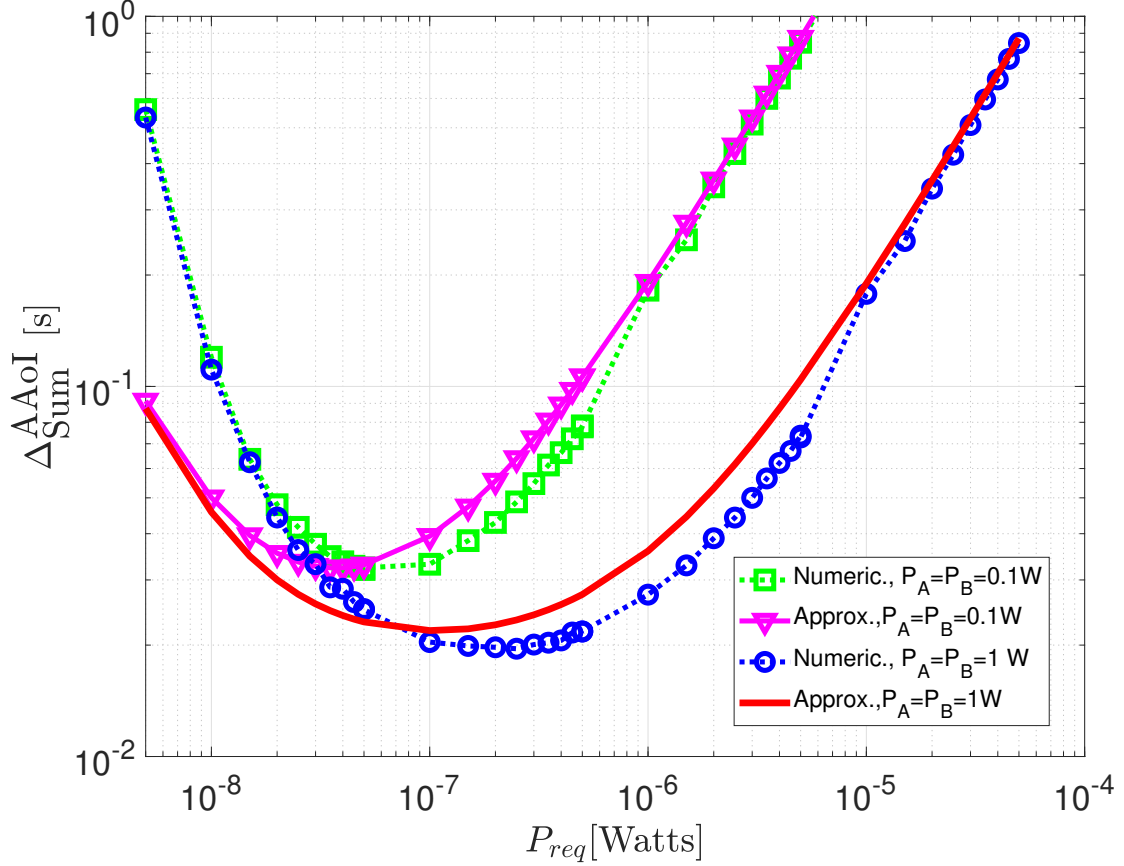
Figure 4.8: Weighed sum AAoI as a function of P_{req} under WUC policy.

Figure 4.8 shows the weighted sum AAoI as a function of P_{req} under the WUC policy. This figure reveals that there is an optimal value for P_{req}. The system exhibits a larger AAoI for small P_{req} values, as this increases the BLER at the receiving node. In such circumstances, the impact of the higher BLER at the opposing receiving source on AAoI becomes more significant than the short waiting time required to harvest small P_{req} values. In contrast, increasing P_{req} from a low value to an optimal value reduces AAoI, due to the reduction in BLER resulting from the higher transmission power. In this scenario, the benefit of a small BLER is more significant than the increased waiting time for harvesting. However, beyond the optimal value, the impact of waiting time for harvesting outweighs the benefits of reduced decoding error. Thus, it can be observed from the figure that increasing P_{req} above its optimal value rapidly increases the AAoI of the system. Additionally, for small P_{req} values, the approximate AAoI deviates from the simulated

value, where the approximation used in (4.12) does not perform as effectively for low SNR values [94]. In summary, maintaining an optimal P_{req} is essential to achieving a better AAoI under the WUC policy.
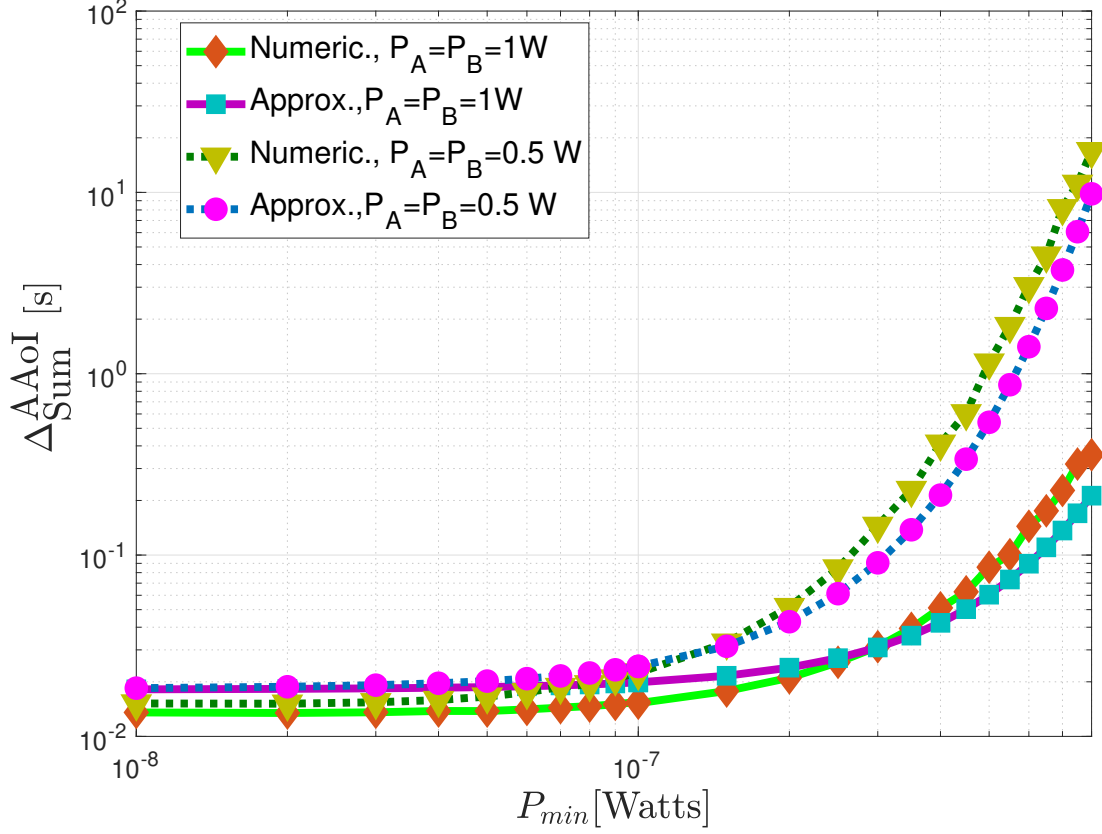
Figure 4.9: Weighed sum AAoI as a function of P_{min} under TWW policy .

Figure 4.9 illustrates the weighted sum AAoI as a function of P_{min} under the TWW policy. It is observed that the weighted sum AAoI of the system monotonically increases with P_{min}, since high P_{min} threshold values increase update loss at the relay. This causes an increase in AAoI due to infrequent updates at the receiving node. This emphasises the importance of the relay being equipped with more efficient communication devices. Based on the simulation results, the following key observations can be identified:

- The WUC policy is the optimal choice for applications with high-reliability requirements, prioritizing reliability over information freshness. On the other hand, the TWW policy is the preferred option for applications focused on achieving better information freshness conditions.

- Under high SNR conditions, a short block length consistently maintains the freshness of information. However, increasing the block length leads to an increase in AAoI. In contrast, in the low SNR regime, short block lengths can increase AAoI due to the higher frequency of erroneous updates, particularly under the TWW policy. Thus, short block-length

communication does not always contribute to maintaining freshness, even though it helps to achieve low latency.

- In high SNR conditions, the size of the update has a minimal impact on AAoI for both policies. However, in low SNR conditions, AAoI increases with the update size, especially under the TWW policy. Therefore, considering the update size is crucial when designing a wireless communication system following the TWW policy.

- For applications with a large distance between the relay and the sources, the WUC policy is the ideal choice. On the other hand, the TWW policy is more suitable for short-distance applications.

- There exists a suboptimal value of P_{req} in terms of minimising AAoI. This is mainly due to the lower P_{req} reducing the time required for EH, while simultaneously increasing the probability of decoding errors.

These observations provide valuable insights into the performance and trade-offs of different policies under varying SNR, block length, update size and distance conditions.

4.4   Conclusions

This chapter estimated the freshness of information in a SWIPT-assisted short-packet two-way relaying wireless communication system for mission-critical applications. Two types of transmission policies at the relay were considered, namely, TWW and WUC. Approximations were derived for the weighted sum of AAoI of the relay system for both policies. Furthermore, the effect of various factors on the weighted sum AAoI of the proposed system was studied, including transmission power, packet size, the distance between the relay and sources and block length. Moreover, it was observed that short block lengths support maintaining the freshness of the information only when the SNR is high. In addition, it is noticed that the TWW policy outperforms in terms of AAoI while WUC policy is best suited when the wireless communication application requires higher reliability. Furthermore, it was discovered that packet size under fixed block length does not influence data freshness in the high SNR regime. However, short packet communication supports maintaining a better AoI in the low SNR regime under fixed block-length. Considering all the numerical simulation results, it is proven that WUC is the optimal transmission policy for applications with high-reliability requirements, while TWW is best for applications with high information freshness requirements. Future work could involve deploying a small-scale prototype to compare the effectiveness of these transmission policies in a more realistic environment.

Publications arising from this Chapter

1. [15] **Basnayaka, C. M. W.**, Jayakody, D. N. K., Perera, T. D. P., & Beko, M. (2024). DataAge: Age of Information in SWIPT-Driven Short Packet IoT Wireless Communications. IEEE Internet of Things Journal, 11(16), 26984-26999.

2. [20] **Basnayaka, C. M. W.**, Jayakody, D. N. K., Perera, T. D. P., Hämäläinen, T. T., & Da Silva, M. M. (2022, December). Age of Information in a SWIPT and URLLC enabled Wireless Communications System. In 2022 IEEE International Conference on Advanced Networks and Telecommunications Systems (ANTS) (pp. 302-307). IEEE.

Chapter 5

AoI-Inspired UAV-Assisted Wireless Sensor Networks

5.1 Introduction

This chapter proposes a theoretical model that utilises the AoI metric and finite block length information theory to estimate information freshness in an UAV-assisted WSN. This network includes multiple sensing nodes and relies on short-packet communication for transmission. In this chapter, closed-form expressions for a AAoI and the BLER are derived. Furthermore, the optimal altitude and block length that ensure the freshness of received information at the destination is determined. The results of the analysis provide valuable insights into the performance characteristics of UAV-assisted WSNs and have important implications for the design and optimisation of such systems.

The chapter addresses the pivotal problem of analysing the average AAoI for UAV-assisted WSNs with multiple sensing nodes. A novel theoretical framework is developed that synergistically combines the AoI metric with finite block-length information theory to estimate information freshness in such multi-source settings under short-packet transmissions. The key motivations are to bridge the gap in existing literature by extending AoI analysis to realistic multi-source scenarios and to leverage finite block-length information theory principles which are better suited for analysing short-packet communications compared to traditional approaches assuming infinitely long block lengths. The main contributions include developing this theoretical model, deriving closed-form expressions for the AAoI and BLER, determining the optimal UAV altitude, block length and sensor activation probability that minimises the AAoI, and formulating a lemma that specifies the optimal sensor activation probability to maintain an optimal AoI at the destination. Through comprehensive simulations, the work validates the lemma's efficacy and demonstrates that the proposed UAV-assisted WSN significantly outperforms traditional fixed base transceiver station (BTS)-based systems in maintaining information freshness, particularly in urban scenarios where the performance gap is substantial.

The remaining sections of this chapter are organised as follows: Section 5.2 presents the system model and evaluates the BLER and the AAoI of the network. Section 5.3 presents numerical
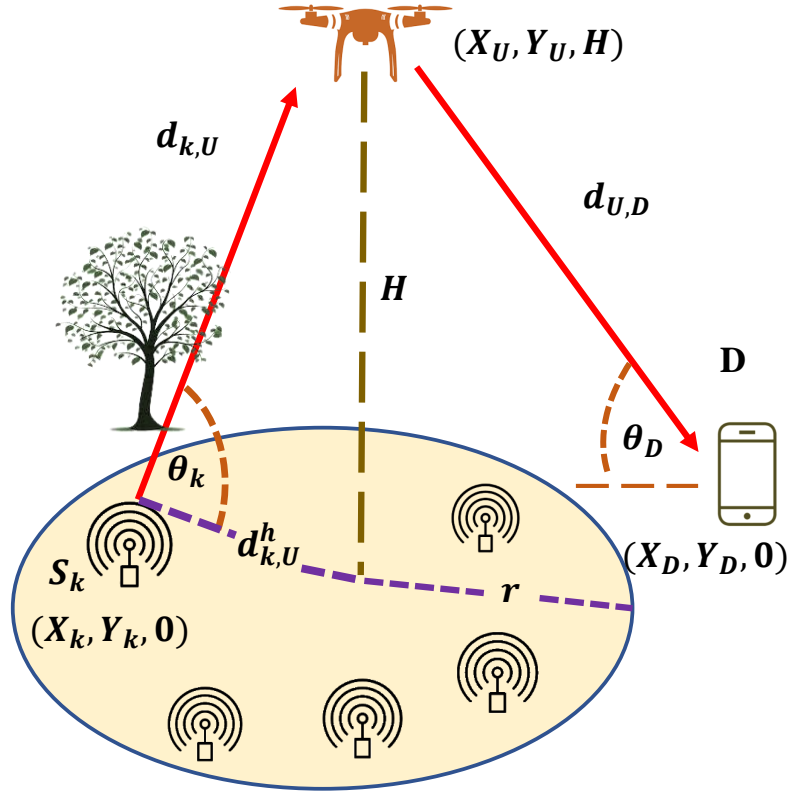
Figure 5.1: System model of UAV-assisted WSN: A UAV at altitude H serving as a DF relay between sensor nodes S_k and the destination node D.

simulation results and evaluates the performance of the system. Finally, Section 5.4 summarises the conclusions drawn in the chapter.

5.2 System Model

As shown in Figure 5.1, a UAV-assisted WSN is considered, where the UAV (U) is placed at an altitude of H and it acts as a wireless DF relay between the sensor nodes ($S_k \forall k \in \{1, ..., K\}$) and the destination ($D$) node. Suppose that each ground node S_k has a fixed location $L_k = (X_k; Y_k; 0)$ the location of the UAV and Destination are denoted as $L_U = (X_U; Y_U; H)$ and $L_D = (X_D; Y_D; 0)$ respectively. The horizontal distance between each node i and j is $l_{i,j} = \sqrt{(X_i - X_j)^2 + (Y_i - Y_j)^2}$ where $i \in (S_k, U)$, $j \in (U, D)$. The S_k is said to be in the coverage of the UAV if their horizontal distance $l_{k,U}$ is less than or equal to r. The elevation angle of UAV is θ_k and if it is measured from the S_k, $\theta_k = \arctan(\frac{H}{l_{k,U}})$ and if it is measured from the D, $\theta_D = \arctan(\frac{H}{l_{U,D}})$. In this wireless communication system, the transmission time is divided into equal intervals known as time blocks. Each time block is further divided into two slots and each slot is used to transmit a single packet. Each sensor node in the network becomes active independently with a probability of $P_{a,j}$ at the beginning of each block and the probability follows a binomial distribution with parameters $(K; P_{a,j})$. The system does not consider any feedback or re-transmission policies, which means

that each update is delivered only once. In the first slot, sensor nodes send data to the UAV relay and all sensor nodes share the same wireless resources. In the second slot, the UAV decodes and transmits the data to the destination. There is no direct communication between the sensor nodes and the destination.

The system considers both LoS and NLoS links between the UAV and the ground stations (sensor nodes or destination). The probability of LoS between the UAV and ground station $l \in (S_k, D)$, P_{LoS} can be expressed as follows [14, 157]:

$$P_{\text{LoS}}(\theta_l) = \frac{1}{1 + A_s \exp(-B_s(\theta_l - A_s))}, \tag{5.1}$$

where A_s and B_s are S-curve parameters that are completely dependent on the environment. The large-scale channel gain α_{ij} for the channel between transmitting node $i \in (S_k, U)$ and receiving node $j \in (U, D)$ is determined as follows [14]:

$$-10 \log(\alpha_{ij}) = 20 \log(d_{i,j}) + 20 \log(\frac{4\pi f_{c_{i,j}}}{c}) + \eta_{NLOS} + \frac{\eta_{LOS} - \eta_{NLOS}}{1 + A_s \exp(-B_s(\theta_l - A_s))}, \tag{5.2}$$

where $f_{c_{i,j}}$ and c are the carrier frequency (Hz) and the speed of the light (m/s), respectively. η_{LoS} and η_{NLoS} are the expectations of the additional environment-dependent excessive path loss for the LoS and NLoS components, respectively. Assuming that the three nodes remain static during transmission and ignoring the Doppler effect, the Rician fading model is employed to investigate the small-scale channel characteristics and multi-path propagation in this system [1]. The probability distribution of g_{ij} follows a non-central chi-square distribution and the PDF [2] for the small-scale channel gain can be expressed as:

$$f_{g_{ij}}(z) = \frac{(K_f + 1) e^{-K_f}}{\bar{g}_{ij}} e^{\frac{-(K_f+1)z}{\bar{g}_{ij}}} I_0 \left(2\sqrt{\frac{K_f (K_f + 1) z}{\bar{g}_{ij}}} \right), \tag{5.3}$$

where $z \geq 0$, $\bar{g}_{ij}=1$, $I_0(\cdot)$ is the zero-order modified Bessel function of the first kind and K_f is the Rician factor, which can be expressed as follows [14, 159]:

$$K_f = \frac{P_{\text{LoS}}(\theta_l)}{1 - P_{\text{LoS}}(\theta_l)} = \frac{1}{A_s \exp(-B_s(\theta_l - A_s))}. \tag{5.4}$$

Then, the instantaneous SNR at each receiving node γ_j can be calculated as follows:

$$\gamma_j = \frac{\alpha_{ij} g_{ij} P_i}{\sigma^2}, \tag{5.5}$$

where P_i is the transmission power at node i and σ^2 is the noise power at the receiver. In addition, the expectation of γ_j as a function of $l_{i,j}$ ($\bar{\gamma}_j(l_{i,j})$) can be derived as follows:

$$\bar{\gamma}_j (l_{i,j}) = \frac{\tilde{D} e^{\frac{\tilde{A}}{1+A_s \exp(-B_s(\arctan\left(\frac{H}{l_{i,j}}\right) - A_s))}}}{\left(l_{i,j}^2 + H^2\right)}, \tag{5.6}$$

---

[1] The small-scale channel gain g_{ij} is denoted as $g_{ij} = |H_{ij}^2|$, where H_{ij} represents the Rician fading channel coefficient.

[2] $F_X(x)$ and $f_X(x)$ represents the CDF and PDF of an arbitrary random variable X, respectively.

where $\tilde{A} = \frac{-(\eta_{LOS} - \eta_{NLOS}) \ln(10)}{10}$ and $\tilde{D} = \frac{P_i 10^{-\frac{\tilde{G}}{10}}}{\sigma^2}$, where $\tilde{G} = 20 \log \left(\frac{4\pi f_{c_{i,j}}}{c} \right) + \eta_{NLOS}$. Furthermore, the conditional PDF of SNR at the UAV ($f_{\gamma_{k,U}}(z \mid l_{k,U})$) is given by:

$$f_{\gamma_{k,U}}(z \mid l_{k,U}) = \frac{(K_f + 1) e^{-K_f}}{\bar{\gamma}_{k,U}} e^{\frac{-(K_f + 1)z}{\bar{\gamma}_{k,U}}} I_0 \left(2 \sqrt{\frac{K_f (K_f + 1) z}{\bar{\gamma}_{k,U}}} \right). \tag{5.7}$$

Thus, $F_{\gamma_{k,U}}(z \mid l_{k,U})$ can be derived as in [163]:

$$F_{\gamma_{k,U}} \left(z, \mid l_{k,U} \right) = 1 - Q_1 \left(\sqrt{2K_f}, \sqrt{\frac{2(K_f + 1)z}{\bar{\gamma}_{k,U}}} \right), \tag{5.8}$$

where $Q_1(\cdot, \cdot)$ is first-order Marcum Q-function. However, due to the intricate complexity of the Marcum Q-function, an approximation is utilised as in [174] at the high SNRs in order to derive a closed-form equation for $F_{\gamma_{k,U}}(z \mid l_{k,U})$ as follows:

$$F_{\gamma_{k,U}} \left(z, \mid l_{k,U} \right) \approx \frac{e^{-K_f} \left(1 + K_f \right) z}{\bar{\gamma}_{k,U}}. \tag{5.9}$$

Furthermore, $F_{\gamma_{k,U}}(z)$ can be formulated as follows:

$$F_{\gamma_{k,U}}(z) = \int_0^\infty F_{\gamma_{k,U}} \left(z \mid l_{k,U} \right) f_{l_{k,U}} \left(l_{k,U} \right) dl_{k,U}, \tag{5.10}$$

where $f_{l_{k,U}} \left(l_{k,U} \right)$ can be calculated as follows, since it is assumed that sensor nodes are uniformly distributed :

$$f_{l_{k,U}} \left(l_{k,U} \right) = \begin{cases} \frac{2l_{k,U}}{r^2}, & l_{k,U} \leq r, \\ 0, & \text{otherwise.} \end{cases} \tag{5.11}$$

Moreover, (5.10) can be reformulated as follows using (5.6), (5.9), (5.10) and (5.11) :

$$F_{\gamma_{k,U}}(z) = \frac{2}{\tilde{D}r^2} \int_0^r \underbrace{\frac{e^{-\frac{W_l}{1-W_l}} z \left(l_{k,U}^2 + H^2 \right) l_{k,U}}{(1 - W_l) e^{\tilde{A}W_l}}}_{q_l(l_{k,U}, z)} dl_{k,U}, \tag{5.12}$$

where $W_l = \frac{1}{1 + A_s \exp(-B_s (\arctan(\frac{H}{l_{k,U}}) - A_s))}$. Then, since the GCQ method converges much faster than other approximation methods, it has been employed for the integration of $q_l(l_{k,U}, z)$ to obtain a closed-form expression for (5.13) as follows [166]:

$$F_{\gamma_{k,U}}(z) \approx \frac{2}{\tilde{D}r} \sum_{m=1}^M \frac{M}{\pi} \sqrt{1 - \phi_m^2} q_l(\alpha_l, z) + R_m, \tag{5.13}$$

where $\phi_m = \cos \left(\frac{2m - 1\pi}{M} \right)$, $\alpha_l = \frac{r}{2} \phi_m + \frac{r}{2}$, M is the complexity-accuracy trade-off factor. R_M is the error term and at high M values, R_M becomes negligible and has little impact on the overall system performance. Furthermore, the CDF of $\gamma_{U,D}$ can be expressed as in [163] :

$$F_{\gamma_{U,D}}(z) = 1 - Q_1 \left(\sqrt{2K_f}, \sqrt{\frac{2(K_f + 1)z}{\bar{\gamma}_{U,D}}} \right), \tag{5.14}$$

where $Q_1 (\cdot, \cdot)$ is the first-order Marcum Q-function, a function that is challenging to manipulate directly [175]. Thus, a semi-linear approximation is employed to derive a closed-form expression for $F_{\gamma_{U,D}} (z)$ as in [14, 175]:

$$F_{\gamma_{U,D}} (z) \simeq \Xi \left(\sqrt{2K_f}, \sqrt{\frac{2 (K_f + 1) z}{\bar{\gamma}_{U,D}}} \right),$$

$$\simeq \Xi (\omega_1, \omega_2), \tag{5.15}$$

where $\Xi(\cdot, \cdot)$ is the semi-linear approximation of the $1-Q_1 (\cdot, \cdot)$ and it can be calculated as in [175].

5.2.1 Block Error Probability

In order to analyse decoding error probability ε_j using finite block length information theory, it is assumed that fading coefficients remain constant throughout each transmission block. In addition, it is assumed that the receiver possesses accurate CSI. Consequently, the expectation of decoding error probability at each receiving node is expressed as follows [89]:

$$\varepsilon_j = \mathbb{E} \left[Q \left(\frac{n_{i,j} \left(\log_2(1 + \gamma_j) \right) - k_b}{\sqrt{n_{i,j} \left(\frac{\log_2^2 e}{2}(1 - \frac{1}{(1+\gamma_j)^2}) \right)}} \right) \right], \tag{5.16}$$

where $\mathbb{E} [\cdot]$ denotes the expectation operator and $Q(x) = \frac{1}{\sqrt{2\pi}} \int_x^\infty e^{-\frac{t^2}{2}} \, dt$. It is assumed that k_b information bits are contained in a $n_{i,j}$ bit length block. Moreover, under the Rician fading block fading conditions, ε_j can be expressed as

$$\varepsilon_j = \int_0^\infty f_{\gamma_j}(z) Q \left(\frac{n_{i,j} \left(\log_2(1 + \gamma_j) \right) - k_b}{\sqrt{n_{i,j} \left(\frac{\log_2^2 e}{2}(1 - \frac{1}{(1+\gamma_j)^2}) \right)}} \right) dz. \tag{5.17}$$

Obtaining a closed-form expression for the overall decoding error probability can be challenging due to the complexity of the Q-function. To address this matter, an approximation technique similar to the approach in [14, 94] has been used as follows:

$$\varepsilon_j \approx \beta_j \sqrt{n_{i,j}} \int_{\phi_j}^{\delta_j} F_{\gamma_j}(z) dz \simeq F_{\gamma_j} (\psi_j). \tag{5.18}$$

where $\beta_j = \frac{1}{2\pi \sqrt{2^{\frac{2k_b}{n_{i,j}}} - 1}}, \psi_j = 2^{\frac{k_b}{n_{i,j}}} - 1, \phi_j = \psi_j - \frac{1}{2\beta_j \sqrt{n_{i,j}}}$ and $\delta_j = \psi_j + \frac{1}{2\beta_j \sqrt{n_{ij}}}$. Then, using (5.13), (5.15) and (5.18) closed form expression for block error at each node can be derived. The probability of a node successfully updating the UAV at the end of the first time slot, denoted by $\tau_{k,U}$, occurs when a node transmits during the slot, no other node transmits and the UAV correctly decodes the packet. Then, $\tau_{k,U}$ can be calculated as follows:

$$\tau_{k,U} = P_{a,k} \left(1 - \varepsilon_{k,U} \right) \prod_{k \neq j} \left(1 - P_{a,j} \right). \tag{5.19}$$

Then, the overall decoding error probability can be expressed as $\varepsilon_{ovr,k} = 1 - \tau_{k,U} + \varepsilon_{U,D} \tau_{k,U}$ [94].

5.2.2 AoI Analysis

The AAoI at the D for updates receiving each node S_k is computed as follows, using [14]:

$$\Delta_k^{AAOI} = \frac{\mathbb{E}[^d X_k^{\,2}]}{2\mathbb{E}[X_k]} + T, \tag{5.20}$$

where $^d X_k$ denotes the inter-departure time between two consecutive successfully received status updates at D. It assumes that the end-to-end delay of each successfully received update is always a constant, this is given by $T = (n_{k,U} + n_{U,D}) T_s$, where T_s is the symbol duration. The inter-departure time $^d X_k$ is a geometric random variable with mean $\mathbb{E}[^d X_k] = \frac{T}{1 - \varepsilon_{ovr,k}}$ and second moment $\mathbb{E}[^d X_k^{\,2}] = \frac{2T^2}{(1 - \varepsilon_{ovr,k})^2} - \frac{T^2}{1 - \varepsilon_{ovr,k}}$. Then, (5.20) can be reformulated as follows:

$$\Delta_k^{AAOI} = T\left(\frac{1}{2} + \frac{1}{1 - \varepsilon_{ovr,k}}\right). \tag{5.21}$$

Finally, the network AAoI Δ_{net}^{AAOI} can be calculated as follows [176]:

$$\Delta_{net}^{AAOI} = \frac{T}{2} + \frac{T}{K} \sum_{k=1}^{K} \frac{1}{1 - \varepsilon_{ovr,k}}. \tag{5.22}$$

Lemma 7. *The optimal value for the active probability of sensors that minimises Δ_{net}^{AAOI} is $P_{a,k}^* \approx \frac{1}{K}$.*

Proof: It is assumed that in networks comprising numerous nodes, node K is likely to have a small optimal active probability $P_{a,k}^*$. Then, using inequality $1 - y \leq e^{-y}$ and $1 - y \approx e^{-y}$ for small y, (5.19) can be reformulated as follows:

$$\tau_{k,U} \leq \frac{P_{a,k}\left(1 - \varepsilon_{k,U}\right)}{\left(1 - P_{a,k}\right)} e^{-\sum_{j=1}^{K} P_{a,j}}. \tag{5.23}$$

Then, $\hat{\Delta}_{net}^{AAOI}$ the lower bound of Δ_{net}^{AAOI} can be calculated as

$$\Delta_{net}^{AAOI} \geq \hat{\Delta}_{net}^{AAOI} = \frac{T}{2} + \frac{T e^{\sum_{j=1}^{K} P_{a,j}}}{K} \sum_{k=1}^{K} \frac{1}{\Phi_k}\left(\frac{1}{P_{a,k}} - 1\right), \tag{5.24}$$

where $\Phi_k = \left(1 - \varepsilon_{k,U}\right)\left(1 - \varepsilon_{U(k),D}\right)$. Then, defining the quantities as

$$A = \sum_{k=1}^{K} \frac{1}{\Phi_k}\left(\frac{1}{P_{a,k}} - 1\right) \text{ and } A' = \sum_{k=1}^{K} \frac{1}{\Phi_k P_{a,k}}, \tag{5.25}$$

the first-order optimality conditions for $\hat{\Delta}_{net}^{AAOI}$ can be calculated as $P_{a,k} = \frac{1}{\sqrt{A\Phi_k}}$. As in (5.25), $A < A'$ and as a result, $P_{a,k}^*$ can be derived as follows:

$$P_{a,k} \geq \frac{1}{A' \Phi_k P_{a,k}} = \frac{\sqrt{A\Phi_k}}{A' \Phi_k} = \frac{1/\sqrt{\Phi_k}}{\sum_{j=1}^{K}\left(1/\sqrt{\Phi_k}\right)} \approx \frac{1}{K} \approx P_{a,k}^*. \tag{5.26}$$

5.3 Simulation Results

In this section, numerical results are presented to validate the theoretical derivations. Unless otherwise specified, the simulation parameters are set as $r = 400$ m, $d_{U,D} = 1000$ m, $H = 500$ m, $f_{c_{S_k,U}} = 900$ MHz, $f_{c_{U,D}} = 2.4$ GHz, $c = 3 \times 10^8$ ms^{-1}, η_{LoS} (Suburban) = 0.1 dB, η_{NLoS} (Suburban) = 21 dB, η_{LoS} (Urban) = 1 dB, η_{NLoS} (Urban) = 20 dB, η_{LoS} (Dense urban) = 1.6 dB, η_{NLoS} (Dense Urban) = 23 dB, η_{LoS} (High-rise urban) = 2.3 dB, η_{NLoS} (High-rise Urban) = 34 dB, P_{S_k} = 90 mW, P_U = 0.2 W, T_s = 17 µs, $n_{k,U}$ = 54 bits, $n_{U,D}$ = 54 bits, k_b = 32 bits, P_a = 0.2, K = 5 nodes and σ^2 = -100 dBm [159].

In Figure 5.2, the network AAoI is plotted against the altitude of the UAV using (5.22). The results indicate that the optimal altitude is 600 m in all environmental conditions. At lower altitudes, the network AAoI is higher due to the high error probability caused by the weak LoS. As altitude increases towards the optimal value, the AAoI decreases rapidly due to a stronger LoS that outweighs the impact of path loss. However, beyond the optimal altitude, the path loss dominates other factors, leading to a higher network AAoI. When the altitude is between 250 m - 700 m, the network AAoI is at its minimum for all environments except for high-rise urban. The network AAoI cannot be reduced to its minimum due to a low SNR caused by weak LoS conditions in high-rise urban areas. The suburban environment has the lowest AAoI for all altitudes due to strong channel conditions.
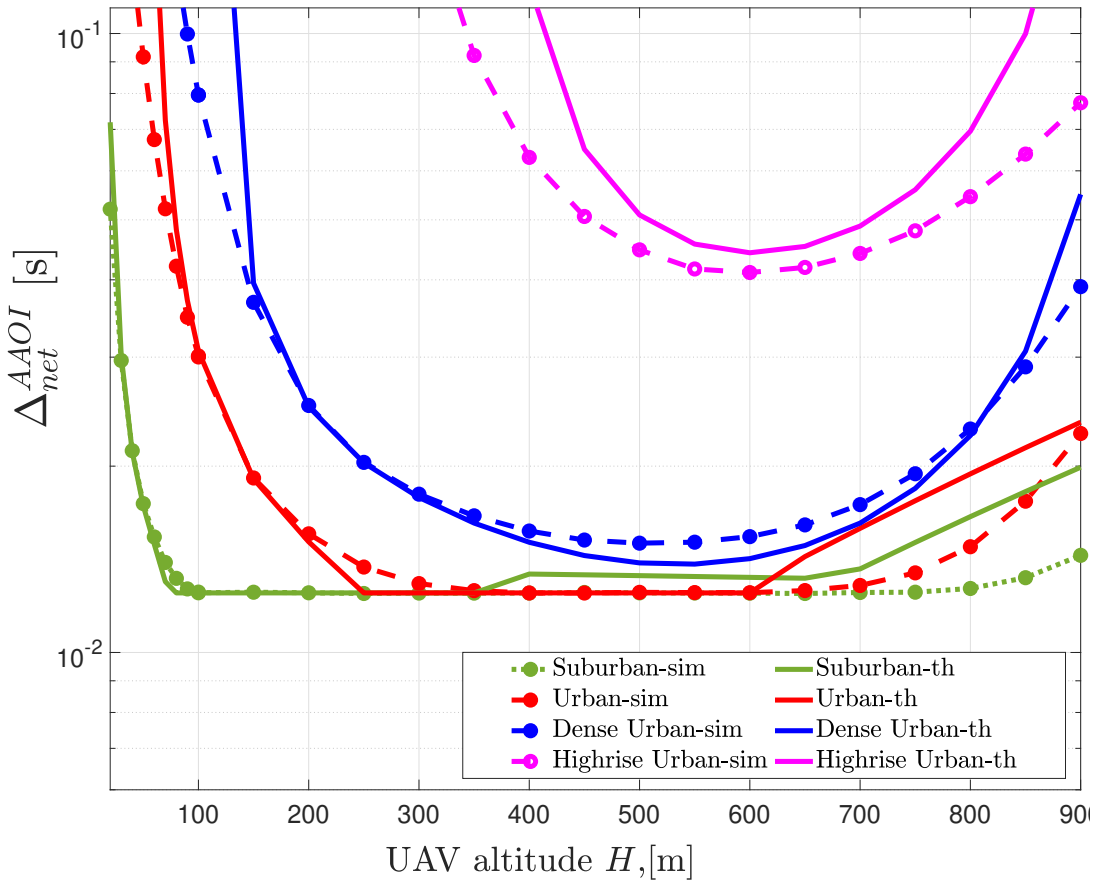
Figure 5.2: Network AAoI as a function of UAV altitude for different environments.

Figure 5.3 shows the impact of block length on network AAoI in this system. Longer block lengths increase system delay, as transmission time directly correlates with block length. Conversely, shorter block lengths result in more decoding errors. For smaller block lengths, decoding error probability significantly affects AAoI compared to transmission time. However, when the block length increases towards its optimal value, AAoI decreases due to fewer decoding errors. Beyond optimal value, the increase in transmission time outweighs the reduction in transmission errors, resulting in a higher AAoI. Therefore, when selecting the block length in a wireless communication system, it is important to balance the trade-offs between transmission time and decoding error to ensure optimal AAoI performance of the system.
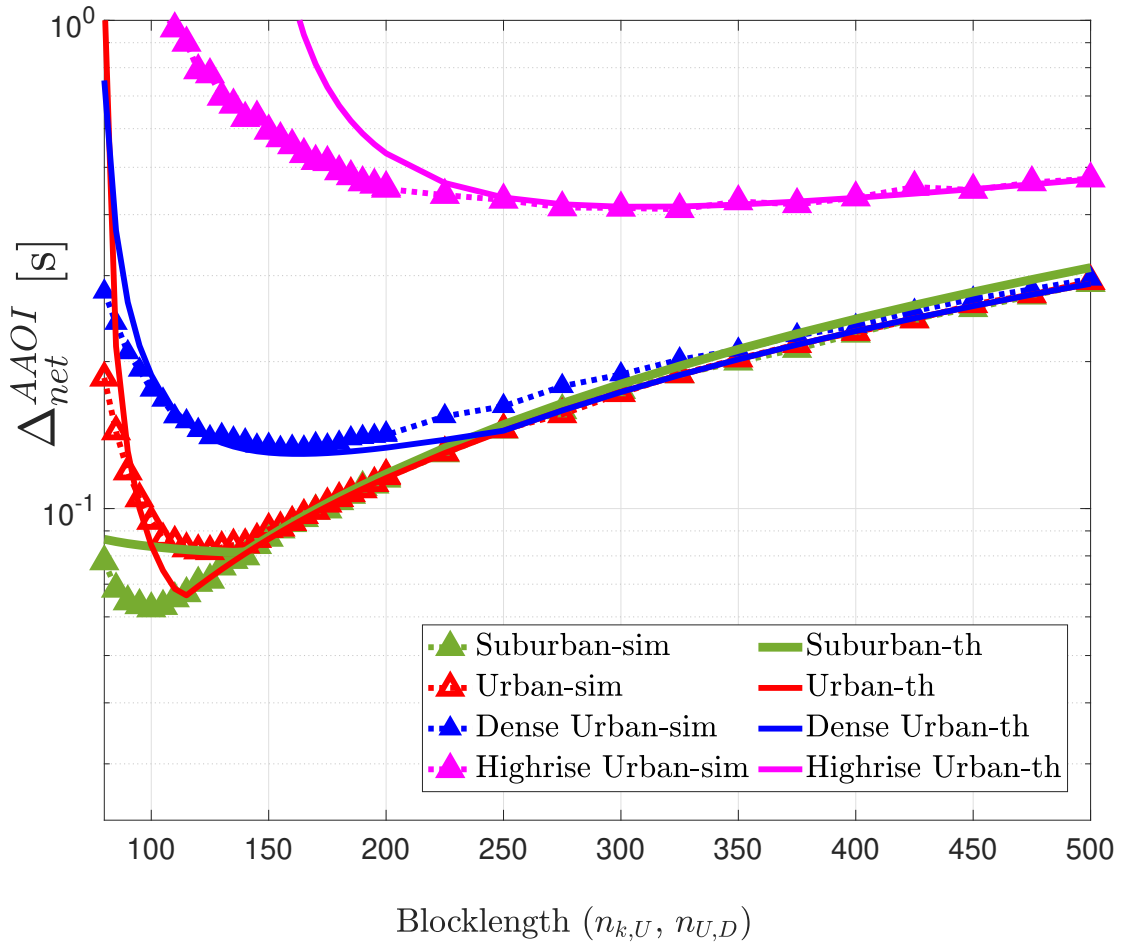
Figure 5.3: Network AAoI as a function of block length for different environments.

Figure 5.4 illustrates the relationship between the network AAoI and the active probability (P_a) for different numbers of nodes. As illustrated in the figure, a small active probability results in a higher network AAoI due to the scarcity of frequent status updates at the destination. As the active probability increases towards its optimal point, the AAoI decreases due to more frequent updates at the destination. However, beyond the optimal value, increasing the active probability increases the network AAoI due to a higher number of transmission collisions. Notably, Figure 5.4 highlights that the system achieves the minimum network AAoI when $P_a \approx 1/K$, as stated in Lemma 7.
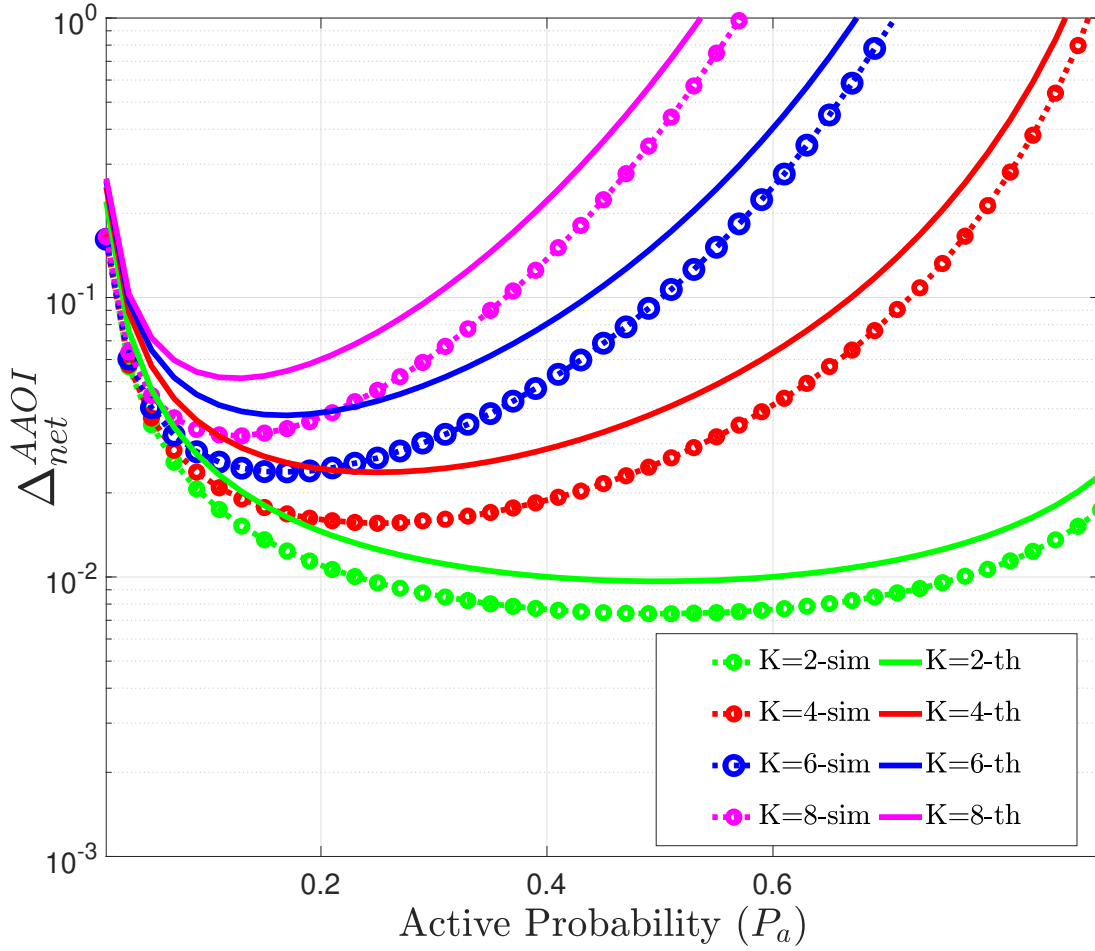
Figure 5.4: Network AAoI as a function of Active Probability (P_a) for different numbers of nodes (K) in a wireless network.

Figure 5.5 illustrates the relationship between network AAoI and total transmission power for the UAV-assisted WSN and traditional fixed BTS-based system under different environmental conditions. As shown, transmission power significantly impacts AAoI, with AAoI decreasing as transmission power increases in both scenarios. However, in the UAV-assisted WSN model, AAoI remains nearly constant beyond 0.1W due to the low transmission error rate at the receiver. The UAV-assisted WSN significantly improves information freshness compared to the traditional fixed terrestrial-based BTS-assisted WSN, with a larger performance gap in urban scenarios. The proposed UAV-assisted WSN model better maintains information freshness in WSNs under various environmental conditions, particularly in dense urban areas where traditional fixed BTS-based systems fail due to poor LoS conditions. This makes the model suitable for real-world urban applications, such as smart city scenarios and disaster management. In smart cities, UAV-assisted WSNs enable efficient monitoring of traffic, air quality, noise levels and energy consumption. In disaster management, the model ensures accurate and up-to-date information collection, enabling informed decision-making and effective resource allocation by emergency responders, ultimately

saving lives in the aftermath of natural disasters or emergencies.
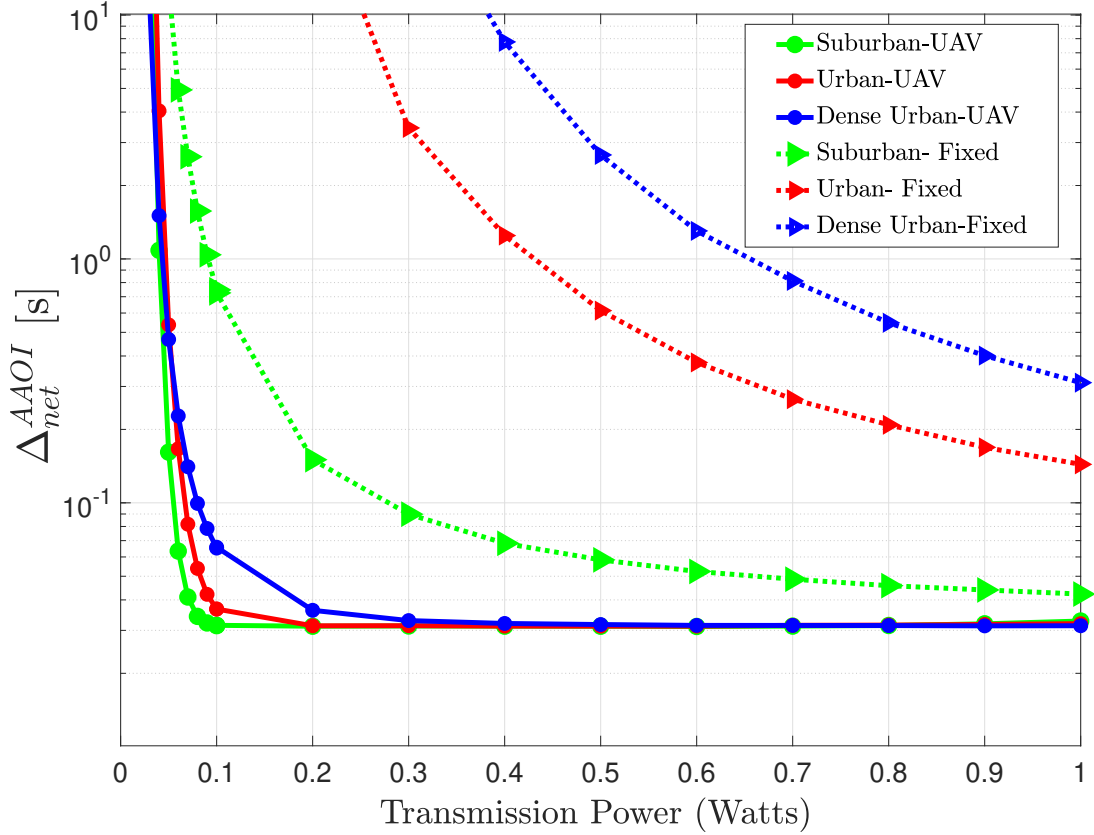
Figure 5.5: Network AAoI vs. total transmission power for UAV − assisted and fixed BTS− based WSNs under different environments.

5.4 Conclusions

This chapter presents a study on the freshness of data in a UAV-assisted WSN with multiple sensors, using AoI as a metric. Closed-form expressions for the network AAoI and block error probability, which depend on the UAV altitude, block length and activation probability of sensors, have been derived. Our numerical analysis reveals the existence of an optimal block length, UAV altitude and activation probability that minimises the network AAoI, thus ensuring the freshness of the sensor network. Both theoretical analysis and simulation results demonstrates that the optimal activation probability minimises the network AAoI. This approximately equals the reciprocal of the number of nodes in the network. Furthermore, the simulation results clearly show that the proposed UAV-assisted WSN system significantly outperforms the traditional fixed-BTS based system in terms of maintaining the freshness of information. The proposed system model guides the system designers in allocating communication resources for UAV-assisted WSNs and designing more reliable and efficient WSN systems in practical applications. While this study focuses specifically on UAV-assisted WSNs, integrating edge servers with WSN systems could also further enhance the freshness of the information. Future research should explore how this type of system enhances the

freshness of the information and conduct a comparative analysis between the UAV-based solution and the edge server-based solution to provide valuable insights into the optimal design of WSN systems.

Publications arising from this Chapter

1. [6] **Basnayaka, C. M. W.**, Jayakody, D. N. K., & Beko, M. (2024). Freshness-in-air: An AoI-inspired UAV-assisted wireless sensor networks. ICT Express, 10(5), 1103-1109.

Chapter 6

Age of Information in Semantic Communications

6.1 Optimizing Real-Time Freshness: Deep Joint Source-Channel Coding-Based AoI in Wireless Networks

6.1.1 Introduction

This section proposes a DJSCC to minimise the AoI for image transmission. A new content-based AoI metric called AoMI is introduced to estimate the freshness of the information in an image classification system. AoMI is a critical metric in timely information delivery, measuring the age of the most recently received and correctly classified image at the receiver. The proposed system leverages a Deep neural network (DNN) at the transmitter to map image pixels directly to channel input symbols, eliminating the need for separate source and channel coding. At the receiver, the channel output is processed to perform image classification. To analyse the AoMI performance of the system, the SHS approach is employed. Closed-form expressions for the average AoMI (AAoMI) are derived, providing insights into the impact of system parameters on the AoMI. Simulation results demonstrate the effectiveness of the proposed DJSCC-based system in achieving lower AoMI compared to traditional separate source and channel coding schemes. The findings highlight the potential of deep learning techniques to maintain the freshness of the information in wireless communication systems.

Whilst AoI provides valuable insights into the timeliness of information delivery, it does not capture the impact of information content on the usefulness of the delivered data. In many applications, such as image classification in surveillance systems, not all information updates are equally important. The successful delivery of key semantic information is more critical than receiving every single update. Motivated by this observation, this section proposes a novel performance metric called AoMI, which measures the age of the most recently received and correctly classified semantic information at the receiver. To minimise AoMI in wireless image classification systems, this section leverages the recent advancements in deep learning and proposes a DJSCC approach. DJSCC utilises a DNN to map the source signal directly to the channel input, eliminating

the need for separate source and channel coding. This approach has shown promising results in improving the efficiency and robustness of wireless communication systems [177].

The main contributions of this section are as follows: (1) introducing a new performance metric, AoMI, to measure the freshness of correctly classified semantic information in wireless communication systems; (2) proposing a DJSCC-based system that minimizes AoMI by using a DNN at the transmitter to map image pixels directly to channel input symbols and a classifier at the receiver for image classification; (3) developing a SHS approach to analyse the AoMI performance, deriving closed-form expressions for AAoMI; and (4) conducting extensive simulations to evaluate the AoMI of the proposed system and compare it with traditional separate source and channel coding schemes using better portable graphics (BPG) [178] compression and LDPC coding [179].

To the best of the authors' knowledge, this is the first work that investigates the use of DJSCC for minimising AoI in wireless communication systems. The rest of this section is organised as follows: Sub-section 6.1.2 describes the system model, the proposed DJSCC-based approach and the AAoMI analysis using SHS. Sub-section 6.1.3 provides the simulation results and discussions. Finally, Sub-section 6.1.4 concludes the section.

6.1.2 System Model

The study introduces a wireless communication system arrangement consisting of transmitter, channel and receiver components, as shown in Figure 6.1, for image transmission. It is assumed that the source image-capture process adheres to a Poisson point process. The transmitter employs the DJSCC technique for wireless image transmission, mapping image pixel values onto complex-valued channel input symbols. These complex-valued channel input symbols are subsequently transmitted through a wireless communication channel between the source and destination. One of the key aspects of this system model is the joint training of both the transmitter and receiver. This collaborative training strategy enables adaptation to changing channel conditions, ensuring robust image transmission despite the inherently dynamic nature of the channel.

In the considered system, the receiver executes classification tasks utilising the channel output. The input image is denoted as $\boldsymbol{I} \in \mathbb{R}^{I_H \times I_W \times I_C}$, where I_H, I_W and I_C represent the height, width and number of colour channels, respectively. The total number of pixels in the image is denoted as $k_P = I_H \times I_W \times I_C$, which is referred to as the source bandwidth. The transmitter employs a DNN encoded by the DJSCC encoder, denoted as $f(\cdot, \boldsymbol{\vartheta})$, where $\boldsymbol{\vartheta}$ represents the learnable parameters of the network. Given an input source signal $\boldsymbol{I}$, the output encoded semantic features S produced by $f(\cdot, \boldsymbol{\vartheta})$ are expressed as $\boldsymbol{s} = f(\boldsymbol{I}, \boldsymbol{\vartheta})$ and S belongs to the real vector space $\mathbb{R}^{2n_T}$, where n_T is the channel bandwidth. The ratio "n_T/k_P" is called the bandwidth ratio [180]. The encoded semantic features S are then reshaped into complex-valued symbols n_T to form the encoded signal $\hat{s}$. After encoding the semantic signal S from the images received from the source $\boldsymbol{I}$, a normalisation step ensures that $\hat{s}$ satisfies the average power constraint as

$$\frac{1}{n_T}\mathbb{E}\|\hat{s}\|^2 \leq P, \tag{6.1}$$
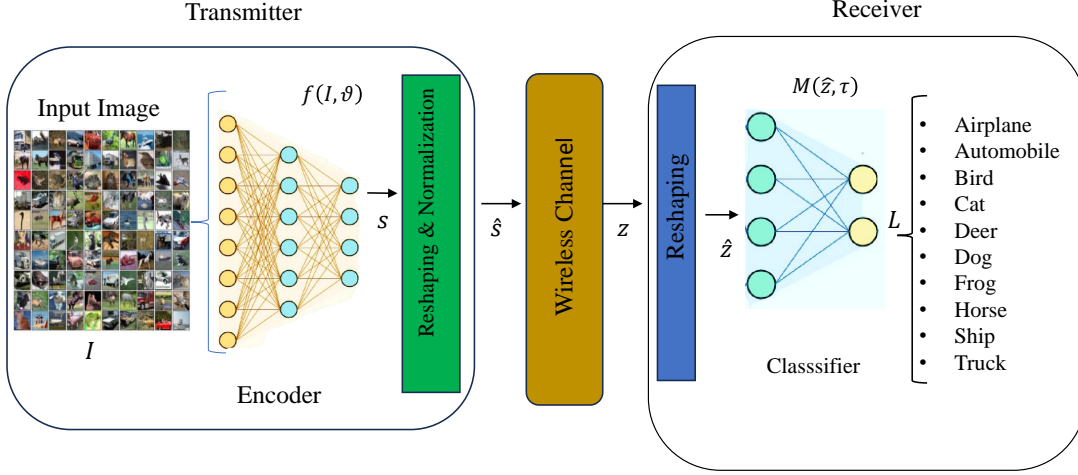
Figure 6.1: Proposed DJSCC-based communication system. The transmitter sends images captured by a source, assuming a Poisson point process for image capture. DJSCC technique is used for wireless image transmission. The receiver processes channel output for classification.

where $\mathbb{E}[\cdot]$ denotes the expectation operator, $\|\cdot\|$ denotes Euclidean norm of for a complex-valued vector x and P denotes the transmission power of the source. Subsequently, the encoded signal $\hat{s}$ is transmitted through the wireless channel between the source and the destination. It is assumed that the channel's characteristics remain stable throughout the transmission of a single symbol; however, they may independently vary when subsequent symbols are transmitted. Consequently, the received signal, represented as $z \in \mathbb{C}^{n_T}$ and can be expressed as follows, where $\mathbb{C}^{x \times y}$ denotes the space of $x \times y$ complex-valued matrices :

$$z = \sqrt{P}\hat{s} + W_n,$$ (6.2)

where $W_n \sim \mathcal{CN}(0, \sigma^2 I_n)$ represents independent and identically distributed (i.i.d.) circularly symmetric complex Gaussian noise with an average noise power of σ^2, where I_n stands for an identity matrix and $\mathcal{CN}$ represents complex normal (Gaussian) distribution. The average SNR is then given by $\bar{\gamma} = 10 \log_{10} \frac{P}{\sigma^2}$ (dB).

At the receiver end, the real and imaginary components of z are reshaped to form $\hat{z} \in \mathbb{R}^{2n_T}$ for further processing. The receiver then performs classification tasks based on $\hat{z}$. This involves feeding the derived features $\hat{z}$ into a classifier $M(\cdot, \tau)$, where τ denotes the learnable parameters of the network. The classifier outputs the classification result $L = M(\hat{z}, \tau)$. The performance of the image classification task is evaluated using classification accuracy. The encoder consists of convolutional neural network (CNN) layers, followed by normalization through Generalized divisive normalization (GND) transformations and a parametric rectified linear unit (PReLU) activation function. This architecture is chosen because CNN layers are effective at extracting salient features from images, GND facilitates local divisive normalization beneficial for density modeling and image compression and non-linear activations allow learning complex mappings from the source signal space to the channel input space. The classifier model uses dense layers with activation

Table 6.1: Encoder-decoder architectures for DJSCC

Layer	Properties
Encoder	
Input	input size: $32 \times 32 \times 3$
SignalConv2D	filter: 16, kernel: $(9, 9)$, activations: [GDN, PReLU]
SignalConv2D	filter: 16, kernel: $(5, 5)$, activations: [GDN, PReLU]
SignalConv2D	filter: 16, kernel: $(5, 5)$, activations: [GDN, PReLU]
SignalConv2D	filter: 16, kernel: $(5, 5)$, activations: [GDN, PReLU]
SignalConv2D	filter: n_{con}, kernel: $(5, 5)$
Channel	
Flatten	output size: $64 n_{\text{con}}$
L2 Normalization	scale factor: $\sqrt{64 n_{\text{con}}}$
AWGN	noise stddev: $\sqrt{10^{-\text{SNR}/10}}$
Reshape	output shape: $(8, 8, n_{\text{con}})$
Decoder	
SignalConv2D	filter: 16, kernel: $(5, 5)$, activations: [IGDN, PReLU]
SignalConv2D	filter: 16, kernel: $(5, 5)$, activations: [IGDN, PReLU]
SignalConv2D	filter: 16, kernel: $(5, 5)$, activations: [IGDN, PReLU]
SignalConv2D	filter: 16, kernel: $(5, 5)$, activations: [IGDN, PReLU]
SignalConv2D	filter: 3, kernel: $(9, 9)$, activation: Sigmoid

functions sigmoid or rectified linear unit (ReLU). It is trained using the Adamax optimiser with sparse categorical cross-entropy as the loss function. The final encoder layer has a depth parameter n_{con}, determining the overall bandwidth ratio across all layers as [180]:

$$\frac{n_T}{k_p} = \frac{\left(\frac{I_H}{4} \times \frac{I_W}{4} \times n_{\text{con}} \right)}{I_H \times I_W \times I_C} = \frac{n_{\text{con}}}{16 \times I_C}. \tag{6.3}$$

Table 6.1 shows the detailed architecture of the proposed DJSCC model.

6.1.2.1 Estimating the AoMI

This section aims to estimate the AAoMI of the deep learning-based wireless communication system. It is assumed that the average image generation rate at the transmitter is denoted by λ_I and the wireless communication system transmits images at a rate of μ. Furthermore, the probability of correct image classification is considered as $0 \leq \rho_{ac} < 1$. The average image transmission rate μ is inversely proportional to the mean transmission time per image, denoted by $\mathbb{E}[T]$, within this wireless network. This relationship is given by the following equation:

$$\frac{1}{\mu} = \mathbb{E}[T] = n_T T_s, \tag{6.4}$$

where T_s represents the symbol duration and n_T denotes the total number of symbol used for the transmission by the transmitter. If the generation time stamp of the received image with the most recently correctly classified image received at timestamp t is represented by $g(t)$, then AoMI can

be defined as a random process $x_0(t)$ as

$$x_0(t) = t - g(t). \tag{6.5}$$

The illustration in Figure 6.2 assumes that AoMI measurements commence at $t = 0$, with the initial
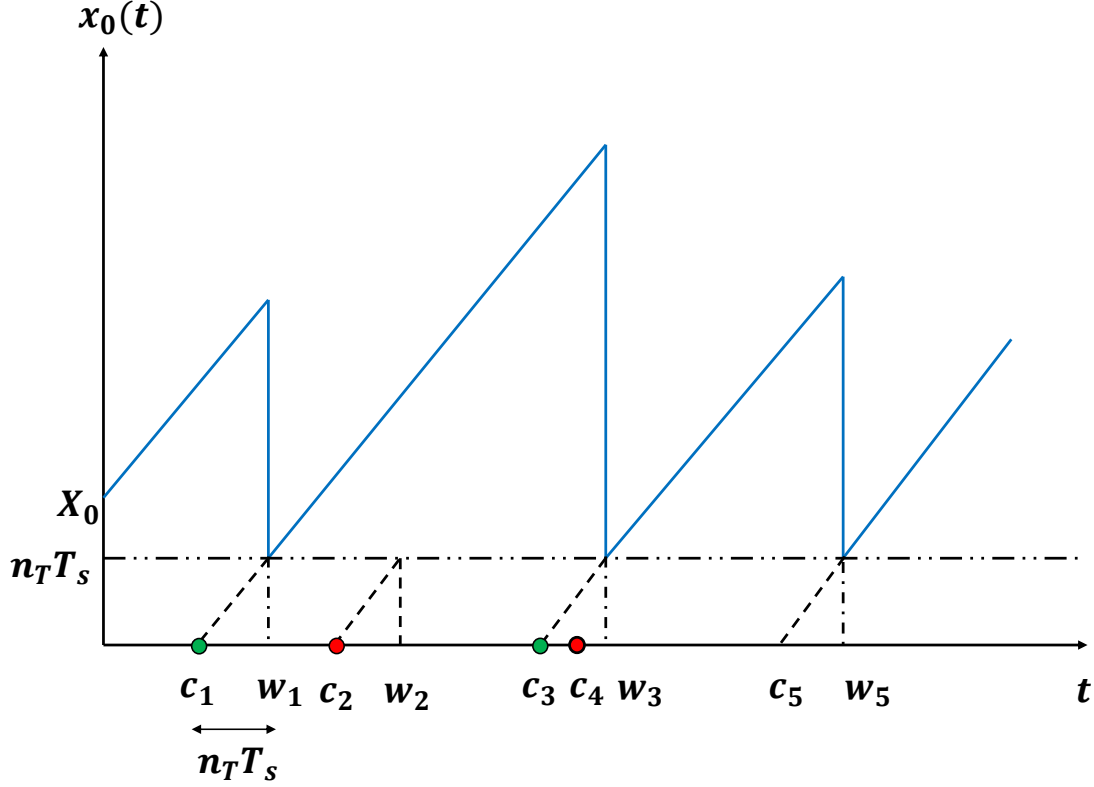
Figure 6.2: Evolution of AoMI $x_0(t)$ with the time at the receiver: Source generate images at time stamps $c_1, c_2, ..$ and the receiver receive and classify these images at time stamps $w_1, w_2, ...$

AoI at the receiver set as $x_0(0) = X_0$. The source generates images at timestamps $\{c_1, c_2, \ldots\}$, while the receiver obtains these images at timestamps $\{w_1, w_2, \ldots\}$. As per Figure 6.2, for an image i captured at $t = c_i$, the receiver classifies it at $w_i = c_i + n_T T_s$. If correctly classified at w_i, the AoMI at the receiver is estimated as:

$$x(w_i) = n_T T_s. \tag{6.6}$$

The AoMI of the receiver grows linearly until a correct classification occurs. For instance, if misclassified at w_2, $x_0(t)$ continues increasing linearly. Moreover, when transmitting an image, newly generated images at the source are blocked and discarded. Specifically, if a new image is captured at c_4 while an earlier image from c_3 is still being transmitted, the c_4 image is not transmitted and does not affect the AoMI process. To calculate the average AoMI over a period T_c, the area under $x_0(t)$ is utilised:

$$\Delta_{T_c} = \frac{1}{T_c} \int_0^{T_c} x_0(t) \, dt. \tag{6.7}$$

The time-averaged AoMI (Δ_{T_c}) converges to the ensemble average AoMI (Δ) as $T_c \to \infty$, expressed as:

$$\Delta = \mathbb{E}[x_0] = \lim_{t \to \infty} \mathbb{E}[x_0(t)] = \lim_{T_c \to \infty} \Delta_{T_c}. \tag{6.8}$$

This study employs SHS techniques to estimate $\mathbb{E}[x_0]$, representing the AoMI at the receiver. Within the SHS framework, the AoMI process is modelled by combining continuous states x(t) and discrete states $q(t)$. These discrete states signify the wireless system's transmission status, effectively described by a Markov chain. The state space is defined as $(q(t), \mathbf{x}(t))$, where $q(t) \in Q = \{0, 1\}$; $q = 0$ indicates an idle system, while $q = 1$ signifies active transmission. The continuous vector $\mathbf{x}(t) = [x_1(t), x_0(t)]$ evaluates the age process, where $x_0(t)$ monitors the age for correctly classified images and $x_1(t)$ represents the projected $x_0(t)$ value for accurate classification. The AoMI process is visually represented as a graph $(q, \mathcal{L})$, with transmission states as nodes and transitions as directed edges. The transition rate from node q_l to q'_l is given by $\lambda^{(l)}\delta_{q_l,q_{(t)}}$, where the Kronecker delta $\delta_{q_l,q_{(t)}}$ ensures transitions occur only for state q_l. Each transition l corresponds to a sudden change in the continuous state, represented by a linear transition reset mapping:

$$\mathbf{x}' = \mathbf{x}\mathbf{A}_l, \tag{6.9}$$

where $\mathbf{A}_l \in \{0, 1\}^{(2) \times (2)}$ is a binary transition reset matrix. For this system, the interactions between discrete states and their impact on continuous states are summarised in Table 6.2 through linear mapping. The transactions described in Table 6.2 can be interpreted as follows: (1) When the wireless system is idle, an image is generated by the source. The system starts transmitting the captured image, but $x'_0 = x_0$ remains unchanged since image capture does not reduce the age at the receiver until correct classification. However, $x'_1 = 0$ since the age of the captured image is initially zero. (2) When the receiver correctly classifies an image transmitted by the source, $x'_0 = x_1$, resetting the age at the receiver to the age of the transmitted image. Moreover, $x'_1 = 0$ since x_1 becomes irrelevant when the source system enters the idle state 0. (3) In the case of the receiver misclassifying an image transmitted by the source, $x'_0 = x_0$ remains unchanged since misclassification does not reduce the age at the receiver. Additionally, $x'_1 = 0$ since x_1 becomes irrelevant when the system enters state 0. (4) If the source captures an image while another image is being transmitted, the new image is discarded and transmission continues with the current image. In this scenario, $x'_0 = x_0$ remains unchanged since this operation does not affect the age at the receiver. Furthermore, $x'_1 = x_1$ is unaffected since the age of the transmitting image remains unchanged. The growth rate of the continuous state at each discrete $q(t) = q$, where $q \in Q$, is given by:

$$\dot{\mathbf{x}}(t) = \frac{\partial \mathbf{x}(t)}{\partial t} = \mathbf{b}_q, \tag{6.10}$$

where $\mathbf{b}_q = [\mathbf{b}_{q,0}, \mathbf{b}_{q,1}]$ is a vector containing binary elements. When $\mathbf{x}_j(t)$ grows at a unit rate as a normal age process in state q, $\mathbf{b}_{q,j} = 1$; and when it is irrelevant to the age process or not tracked in state q, $\mathbf{b}_{q,j} = 0$. Hence, for this system, $\mathbf{b}_q$ can be expressed as:

$$\mathbf{b}_q = \begin{cases} \begin{bmatrix} 1 & 0 \end{bmatrix}, & q = 0, \\[2ex] \begin{bmatrix} 1 & 1 \end{bmatrix}, & q = 1. \end{cases} \tag{6.11}$$

Let $\pi_{\hat{q}}(t)$ denote the discrete state probabilities for all $\hat{q} \in Q$ and $\mathbf{v}\hat{q}(t)$ denote the correlation between the age process and the discrete state $q(t) = \hat{q}$. Accordingly, $\pi\hat{q}(t) = \mathbb{E}[\delta_{\hat{q},q(t)}]$ and the correlation vector function $\mathbf{v}\hat{q}(t) = \begin{bmatrix} \upsilon\hat{q}0(t), \upsilon_{\hat{q}1}(t) \end{bmatrix}$, where $\upsilon_{\hat{q}j}(t) = \mathbb{E}[x_j(t)\delta_{\hat{q},q(t)}]$, $\quad j \in (0,1)$. All transitions $\mathcal{L}$ can be divided into incoming and outgoing transitions. For each state q, incoming transitions are labelled as $\mathcal{L}'q = l \in \mathcal{L} : q'l = q$ and outgoing transitions are labelled as $\mathcal{L}q = l \in \mathcal{L} : ql = q$. To compute the time-averaged age, it is assumed that the Markov chain $q(t)$ is ergodic. Hence, the state probability vector $\pi(t) = [\pi_0(t), \pi_1(t)]$ converges to a unique stationary vector $\bar{\pi} = [\bar{\pi}_0, \bar{\pi}_1]$ satisfying the following:

$$\bar{\pi}_{\bar{q}} \sum_{l \in \mathcal{L}_{\bar{q}}} \lambda^{(l)} = \sum_{l \in \mathcal{L}'_{\bar{q}}} \lambda^{(l)}\bar{\pi}_{ql}, \quad \bar{q} \in Q, \tag{6.12}$$

$$\sum_{\bar{q} \in Q} \bar{\pi}_{\bar{q}} = 1. \tag{6.13}$$

For this system, (6.12) has been used to find the stationary probabilities and it can be shown that the stationary probability vector satisfies $\bar{\pi}\mathbf{A} = \bar{\pi}\mathbf{B}$, where:

$$\mathbf{A} = \text{diag} \begin{bmatrix} \lambda_I & \mu + \lambda_I \end{bmatrix}, \quad \mathbf{B} = \begin{bmatrix} 0 & \lambda_I \\ \mu & \lambda_I \end{bmatrix}.$$

where $\text{diag}(x)$ represents a diagonal matrix, with each diagonal element being the corresponding element in x. Then, applying (6.13), the stationary probabilities $\bar{\pi}$ can be calculated as

$$\bar{\pi} = \begin{bmatrix} \bar{\pi}_0 & \bar{\pi}_1 \end{bmatrix} = \frac{1}{\lambda_I + \mu} \begin{bmatrix} \mu & \lambda_I \end{bmatrix}. \tag{6.14}$$

When $\pi(t) = \bar{\pi}$ and $\mathbf{v}(t) = [\mathbf{v}_0(t), \mathbf{v}_1(t)]$, the system follows first-order differential equations for all $\bar{q} \in Q$ as

$$\dot{\mathbf{v}}_{\bar{q}}(t) = \mathbf{b}_{\bar{q}}\bar{\pi}_{\bar{q}} + \sum_{l \in \mathcal{L}'_{\bar{q}}} \lambda^{(l)}\mathbf{v}_{ql}(t)\mathbf{A}_l - \mathbf{v}_{\bar{q}}(t) \sum_{l \in \mathcal{L}_{\bar{q}}} \lambda^{(l)}, \tag{6.15}$$

Under the ergodicity assumption, this differential equation is stable and $\mathbf{v}_{\bar{q}}(t) = \mathbb{E}[\mathbf{x}(t)\delta_{\bar{q},q(t)}]$ converges to a non-negative limit $\bar{\mathbf{v}}_{\bar{q}}$ as $t \to \infty$. Accordingly:

$$\mathbb{E}[\mathbf{x}] = \lim_{t \to \infty} \mathbb{E}[\mathbf{x}(t)] = \lim_{t \to \infty} \mathbb{E}[\mathbf{x}(t)\delta_{\bar{q},q(t)}] = \sum_{\bar{q} \in Q} \bar{\mathbf{v}}_{\bar{q}}, \tag{6.16}$$

$$\bar{\mathbf{v}}_{\bar{q}} \sum_{l \in \mathcal{L}_{\bar{q}}} \lambda^{(l)} = \mathbf{b}_{\bar{q}}\bar{\pi}_{\bar{q}} + \sum_{l \in \mathcal{L}'_{\bar{q}}} \lambda^{(l)}\bar{\mathbf{v}}_{ql}\mathbf{A}_l, \quad \bar{q} \in Q, \tag{6.17}$$

Here, $x_0(t)$ is the age at the destination and the AAoMI Δ is calculated as:

$$\Delta = \mathbb{E}[x_0] = \lim_{t \to \infty} \mathbb{E}[x_0(t)] = \sum_{\bar{q} \in Q} \bar{\upsilon}_{\bar{q}0}. \tag{6.18}$$

Table 6.2: Transitions Rate for the Markov Chain in DJSCC-based Wireless Image Transmission System

l	$q_l \rightarrow q_l'$	$\lambda^{(l)}$	$\mathbf{x}\mathbf{A}_l$	$\mathbf{v}_{q_l}\mathbf{A}_l$
1	$0 \rightarrow 1$	λ_I	$\begin{bmatrix} x_0 & 0 \end{bmatrix}$	$\begin{bmatrix} v_{00} & 0 \end{bmatrix}$
2	$1 \rightarrow 0$	$\mu\rho_{ac}$	$\begin{bmatrix} x_1 & 0 \end{bmatrix}$	$\begin{bmatrix} v_{11} & 0 \end{bmatrix}$
3	$1 \rightarrow 0$	$\mu(1 - \rho_{ac})$	$\begin{bmatrix} x_0 & 0 \end{bmatrix}$	$\begin{bmatrix} v_{10} & 0 \end{bmatrix}$
4	$1 \rightarrow 1$	λ_I	$\begin{bmatrix} x_0 & x_1 \end{bmatrix}$	$\begin{bmatrix} v_{10} & v_{11} \end{bmatrix}$

To estimate Δ using (6.18), it is necessary to find $\bar{v}_{\bar{q}0}$ from (6.17). First, a solution for $\bar{\mathbf{v}} = [\bar{\mathbf{v}}_0, \bar{\mathbf{v}}_1] = [\bar{v}_{00}, \bar{v}_{01}, \bar{v}_{10}, \bar{v}_{11}]$ can be found using (6.17). Evaluating this equation at $q = 0$ and $q = 1$ and using Table 6.2, the following is obtained:

$$\lambda_I \begin{bmatrix} \bar{v}_{00} & \bar{v}_{01} \end{bmatrix} = \begin{bmatrix} \bar{\pi}_0 & 0 \end{bmatrix} + \mu\rho_{ac} \begin{bmatrix} \bar{v}_{11} & 0 \end{bmatrix} + \mu(1 - \rho_{ac}) \begin{bmatrix} \bar{v}_{10} & 0 \end{bmatrix} \quad (6.19)$$

$$(\mu + \lambda_I) \begin{bmatrix} \bar{v}_{10} & \bar{v}_{11} \end{bmatrix} = \begin{bmatrix} \bar{\pi}_1 & \bar{\pi}_1 \end{bmatrix} + \lambda_I \begin{bmatrix} \bar{v}_{00} & 0 \end{bmatrix} + \lambda_I \begin{bmatrix} \bar{v}_{10} & \bar{v}_{11} \end{bmatrix}. \quad (6.20)$$

Next, the aforementioned expressions can be expressed as system equations in the following manner:

$$\lambda_I \bar{v}_{00} = \bar{\pi}_0 + \mu\rho_{ac}\bar{v}_{11} + \mu(1 - \rho_{ac})\bar{v}_{10}, \quad (6.21)$$

$$\mu\bar{v}_{10} = \bar{\pi}_1 + \lambda_I \bar{v}_{00}, \quad (6.22)$$

$$\mu\bar{v}_{11} = \bar{\pi}_1. \quad (6.23)$$

By solving these equations and using (6.14), the values of $\bar{v}_{\bar{q}0}$ can be calculated. Then, by substituting the result into (6.18), the AAoMI Δ at the destination can be obtained as follows:

$$\Delta = \frac{1}{\lambda_I \rho_{ac}} + \frac{1}{\mu\rho_{ac}} + \frac{\lambda_I}{\mu(\lambda_I + \mu)}. \quad (6.24)$$

Finally, the AAoMI of the wireless communication system is calculated using Algorithm 1.

6.1.3 Simulation Results

The DJSCC is evaluated using the CIFAR-10 [181] image dataset, which consists of 60,000 32x32 colour images, divided into 50,000 training images and 10,000 test images. The training data is combined with random channel realisations to train the DJSCC model. The model is trained using a fixed SNR and its performance is investigated over a range of SNR values and bandwidth ratios. The proposed DJSCC is compared with a separate source and channel coding scheme that uses the BPG compression algorithm for source coding and the LDPC code for channel coding as the digital baseline. In this scheme, the source node compresses the image using BPG, which employs advanced coding techniques such as intra-frame prediction and context-adaptive binary arithmetic coding. The BPG encoder uses a quality parameter to control the trade-off between compression ratio and image quality, determined by a rate-distortion optimisation algorithm. The compressed bitstream is encoded using an LDPC code compliant with the 5G New Radio standard [182]. The

---

Algorithm 1 Algorithm for Train DJSCC and Calculating AAoMI

    Training Phase

1: **Require:** A batch of images I for training from the CIFAR-10 [181] image dataset.

2: **Ensure:** Trained encoder $f(\cdot, \boldsymbol{\vartheta})$ and classifier $M(\cdot, \boldsymbol{\tau})$.

3: **Initialize:** Initialise the weights of $f(\cdot, \boldsymbol{\vartheta})$ and $M(\cdot, \boldsymbol{\tau})$ using a standard initialisation method.

4: **for** each epoch **do**

      Transmitter:

5:       Extract semantic features using $f(\cdot, \boldsymbol{\vartheta})$.

6:       Apply power normalisation as in (6.1).

7:       Set the wireless channel average SNR as $\bar{\gamma}_{train}$ and transmit the symbols through wireless channels.

      Receiver:

8:       Perform reshaping on the received signal z.

9:       Conduct image classification with $M(\hat{z}, \boldsymbol{\tau})$.

10: **end for**

    Deployment and AAoMI Calculation Phase

11: **Require:** A batch of images I_{test} for testing from the CIFAR-10 image dataset.

12: **Ensure:** Calculate AAoMI.

13: **Initialize:** Image generation process parameters λ_I and image transmission rate μ.

    Transmitter:

14:     Deploy the learned $f(\cdot, \boldsymbol{\vartheta})$. Extract semantic features S.

15:     Apply power normalisation as in (6.1).

16:     Set the wireless channel parameters. Then, the symbols are transmitted through the wireless channel.

    Receiver:

17:     Perform reshaping on the received signal z and deploy the learned $M(\cdot, \boldsymbol{\tau})$.

18:     Conduct image classification using $M(\hat{z}, \boldsymbol{\tau})$.

19:     **Compute Classification Accuracy:**

20:     Compare the predicted class L with the true class of I_{test}.

21:     Calculate the classification accuracy ρ_{ac}.

22:     **Compute AAoMI:**

23:     Calculate AAoMI using

$$\Delta = \frac{1}{\lambda_I \rho_{ac}} + \frac{1}{\mu \rho_{ac}} + \frac{\lambda_I}{\mu(\lambda_I + \mu)}.$$

Table 6.3: Simulation Parameters for DJSCC-Based Wireless Network

Parameter	Symbol	Value
System Parameters		
Symbol Duration	T_s	20 μs
Number of Convolutional Filters	n_{con}	16
Bandwidth Ratio	n_T/k_p	1/3
Image Generation to Transmission Rate	λ_I/μ	1
Training SNR	γ_{train}	5 dB
LDPC Code Rate	–	2/3 (3072, 4608)
Modulation Scheme	–	4-QAM
Training Parameters		
Optimizer	–	Adam
Learning Rate	–	0.001
Loss Function	–	MSE
Batch Size	–	128
Dataset Parameters		
Dataset	–	CIFAR-10
Training Set Size	–	50,000
Test Set Size	–	10,000
Image Preprocessing	–	Normalization to [0,1]

LDPC encoder performs rate-matching, including puncturing and shortening, to achieve the desired codeword length. At the receiver, the LDPC decoder employs the iterative belief propagation decoding algorithm. The decoded bitstream is decompressed using the BPG decompression algorithm to obtain the reconstructed image. In the traditional model, these reconstructed images will be used for a classification task which is trained using the original images, compared to the DJSCC approach. The flexibility and configurability of both the BPG compression algorithm and the LDPC code and decoder provide a strong baseline for comparison with the DJSCC approach. Unless otherwise specified, the simulation parameters and system configuration used in this study are summarised in Table 6.3.

In Figure 6.3, the relationship between AAoMI and channel SNR for different bandwidth ratios is illustrated. In these simulations, the DJSCC models were trained at a fixed SNR $\bar{\gamma}_{train}$, after which the AAoMI was evaluated across various channel SNRs. The AAoMI of the DJSCC-based approach was compared with that of a digital baseline system whilst considering different bandwidth ratios. The digital baseline system, consisting of LDPC + BPG, adapts its compression ratio based on the specified code rate and overall bandwidth ratio. The LDPC code, corresponding to a 2/3 code rate and 4-Quadrature amplitude modulation were evaluated as the digital baseline. The experimental results reveal that the DJSCC approach exhibits superior AoI performance compared to the digital baseline transmission schemes in low channel bandwidth and low SNR scenarios. Conversely, in high bandwidth ratios and high SNR environments, the traditional system performs better. Importantly, the DJSCC approach does not suffer from the 'cliff effect' commonly observed in digital transmission schemes. This limitation of digital schemes stems from the fact that once the channel code and modulation scheme are chosen for a specific target SNR, the number of bits
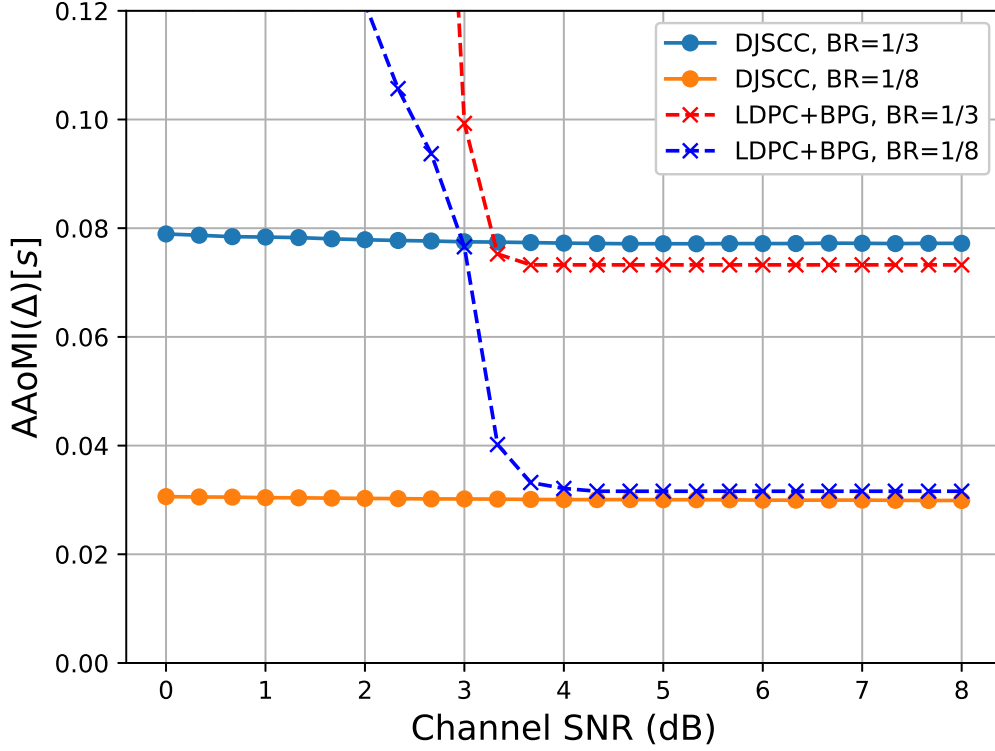
Figure 6.3: AAoMI vs. channel SNR for different bandwidth ratios (BR).

available for compression remains constant. Consequently, the AAoMI does not improve even when the SNR increases. In addition, when channel quality deteriorates below the target SNR, the channel code struggles to handle the escalating error rate, resulting in a substantial increase in AAoMI at very low SNR levels. On the other hand, for traditional systems, lower SNR and lower bandwidth ratios lead to a higher AAoMI compared with the DJSCC system. This is due to the reduction in image quality, caused by high compression levels at lower bandwidth ratios, reduces classification accuracy, especially under lower SNR levels, as the traditional system classifies images at the receiver using a model that is not trained to adapt to the reduction of image quality due to noise or high compression levels. In addition, for both DJSCC-based systems and traditional systems, when the bandwidth ratio is reduced, the AAoMI also reduces since the reduction in transmission time becomes more prominent compared to the reduction in classification accuracy. This adaptability and resilience exhibited by the DJSCC scheme make it an attractive solution for efficient communication in low SNR channel environments, offering potential for improved freshness performance and robustness compared to traditional approaches. Moreover, while the AoI performance of the DJSCC system falls behind traditional schemes in high SNR conditions, it is suggested that adopting a more complex neural network structure and leveraging advanced activation and loss functions could lead to enhancements in the freshness capabilities of the DJSCC model. Figure 6.4 presents the inverse relationship between the AAoMI and the image generation rate (λ_I) in the evaluated wireless communication system. As the figure illustrates, there is a notable
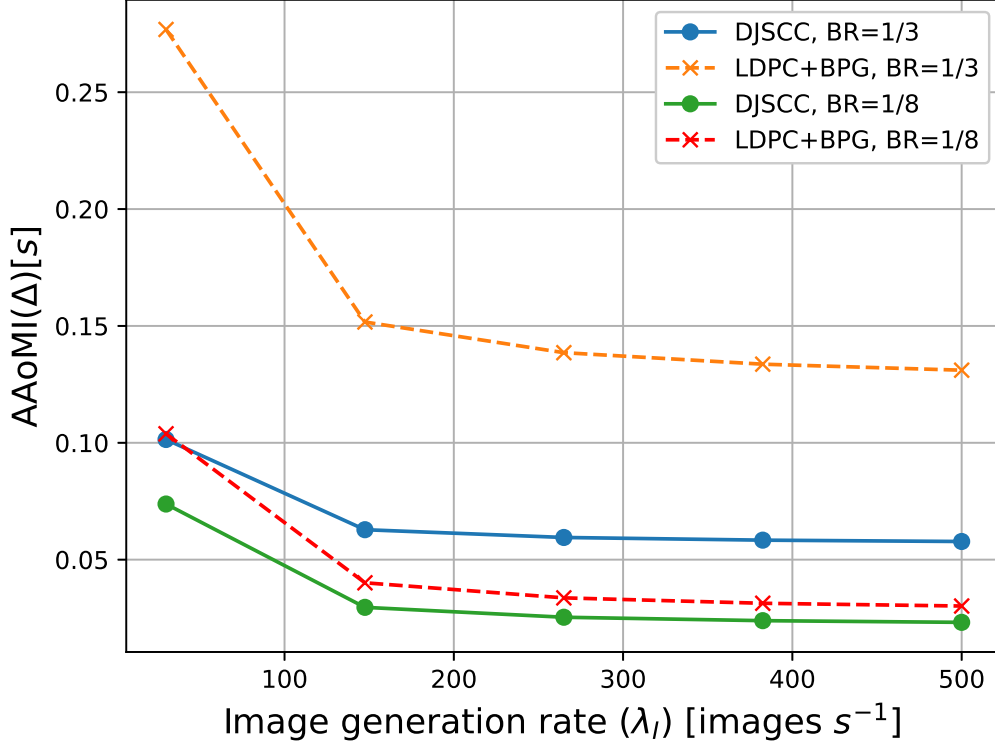
Figure 6.4: Comparison of AAoMI against image generation (capturing) rate (λ_I) for different bandwidth ratios (BR).

decline in AAoMI with an upsurge in the image capture rate. This system is characterised by the absence of a transmission queue, thus eliminating any queuing delay. The enhanced image capture rate correlates with a more frequent update of images at the destination node. Thus, the decrease in AAoMI can be directly attributed to the increase in temporal density of the image updates received by the receiver, which emphasises the efficiency of the system in maintaining the freshness of the information.

6.1.4 Conclusion

This section introduces a novel wireless communication system that employs DJSCC to minimise the AoMI for image transmission. The proposed system leverages a DNN at the transmitter and a classifier at the receiver to enable end-to-end optimisation of the age of information. By introducing AoMI as a new metric, this work captures the freshness of correctly classified semantic information -this is crucial for time-critical wireless applications that rely on timely delivery of information. Simulations confirmed that the proposed DJSCC system significantly reduces the AoMI compared to traditional schemes. These results underscore the capability of deep learning techniques to enhance the timeliness of information delivery over wireless channels, especially in environments characterised by limited bandwidth and low SNR.

6.2 Sky Sentinels: UAV-Powered Semantics Wireless Communications for Dynamic Wildfire Detection

6.2.1 Introduction

This section introduces a technique for wildfire detection by integrating UAVs with the DJSCC scheme. This extracts semantic information efficiently from the data while subsequently transmitting it using a reduced number of symbols to maintain freshness. The primary objective is to enhance the accuracy and efficiency of wildfire detection while ensuring the freshness of transmitted information. The system serves a dual purpose by facilitating both image reconstruction and wildfire image classification. To quantify the freshness of information at the receiver, a new performance metric called the AoMI is introduced. This deploys the concept of AoI in image classification systems. The AAoMI is estimated using the SHS model. Furthermore, an expression is derived for the AAoMI of the UAV wireless communication system. This facilitates the estimation of ideal system parameters such as UAV altitude, transmission power, image generation rate and bandwidth ratio to maintain optimal freshness of the information. In particular, this work is one of the first comprehensive analyses of information freshness in a DJSCC-based wireless communications system.

In recent years, the frequency, size and severity of wildfires worldwide have seen a significant increase, impacting economies, ecosystems and local communities [183, 184]. Approximately 23 million acres of land are lost due to wildfires annually around the world and experts predict a further rise in fire risks in the near future [185]. Effectively managing wildfires poses a considerable challenge, with early detection being crucial [186]. However, current methods, such as satellite imagery and infrared cameras, have limitations, especially in adverse weather conditions such as cloudy environments. Thus, to address the uncontrolled spread of wildfires, the use of IoT networks has emerged as a promising solution [187]. These networks can connect various cost-effective self-powered IoT sensors known for their simplicity. Projections suggest that by the end of 2023, IoT networks could support up to 100,000 IoT devices per square kilometre [188]. However, shortcomings in infrastructure in forested areas and inherent limitations of IoT devices include power and computational constraints. Thus, the traditional IoT networks are unsuitable for efficient data gathering. To overcome this, UAVs are a viable option [17, 189, 190]. UAVs offer advantages such as flexibility and reduced costs, making them well suited for reaching dangerous and remote disaster-stricken areas [191]. Recent studies propose the use of UAV-added communication networks in managing natural disasters such as wildfires [192].

This section presents an innovative approach to identifying wildfires using UAVs along with a deep learning-based semantic wireless communications system. The main objective of this study is to evaluate how to maintain the freshness of the information in a UAV-assisted semantic wireless communication network for wildfire detection. This enhancement aims to enable the rapid and accurate identification of wildfires.

6.2.1.1 Contributions

Significant theoretical research work has been dedicated to DJSCC and semantic communication. However, its practical implementation in UAV-based wireless communication has received limited attention. Furthermore, there is a notable gap in understanding how semantic wireless communication schemes contribute to reducing AoI while preserving the freshness of information.

This section presents pioneering work in applying AoI metrics to a DJSCC-based semantic communication system used for UAV-assisted communication systems. The primary contribution of this work lies in the introduction of context-based AoI metrics for UAV communication, specifically designed for wireless end-to-end image classification systems, denoted as AoMI. This metric extends beyond wildfire detection and can be adapted for a broader range of classification systems. Notably, to the best of the author's knowledge, no prior study has focused on a semantic wireless communication-based wildfire detection system using UAV communication, making this study one of the first in this domain.

The study proposes a DJSCC framework that includes an encoder, decoder and classifier, enabling seamless end-to-end training for image classification in the context of wildfire detection. The wireless communication channel is modeled as a Rician fading channel, effectively simulating the communication conditions in a UAV network. In addition, the receiver decoder plays a crucial role in image recovery, ensuring an accurate assessment of the scale of wildfires in critical scenarios.

One of the key outcomes of this study is the development of an expression for AAoMI using the SHS approach in a UAV-assisted semantic classification system. This expression can be utilised to determine the optimal altitude, block length and update generation rate needed to uphold the freshness of received information at the destination, thereby pushing forward the state-of-the-art in this emerging field.

The rest of this section is organised as follows: Sub-section 6.2.2 introduces the system model and presents the proposed workflow algorithm and AAoMI estimation algorithm for a semantic communication system. Sub-section 6.2.3 provides simulation results to evaluate the performance of the proposed system. Finally, the section is concluded in sub-section 6.2.4.

6.2.2 System Model

Figure 6.5 examines a wildfire detection system utilising a UAV. The UAV (U) is positioned at an altitude H and equipped with cameras for image capture. The UAV and GCS (G_c) have coordinates $D_U = (X_U; Y_U; H)$ and $D_{G_c} = (X_{G_c}; Y_{G_c}; 0)$, respectively. The horizontal distance is $d_{U,G_c} = \sqrt{(X_U - X_{G_c})^2 + (Y_U - Y_{G_c})^2}$. The angle of elevation is $\theta = \arctan\left(\frac{H}{d_{U,G_c}}\right)$. Communication involves LoS and NLoS channels between UAV and GCS.

This study introduces a wireless communication system arrangement consisting of transmitter, channel and receiver components, as shown in Figure 6.6. It is assumed that the UAV image-capture process adheres to a Poisson point process, thus introducing a stochastic and random nature to the image-capturing process. The transmitter employs the DJSCC technique for wireless image transmission. In contrast to traditional methods that rely on separate source coding and channel
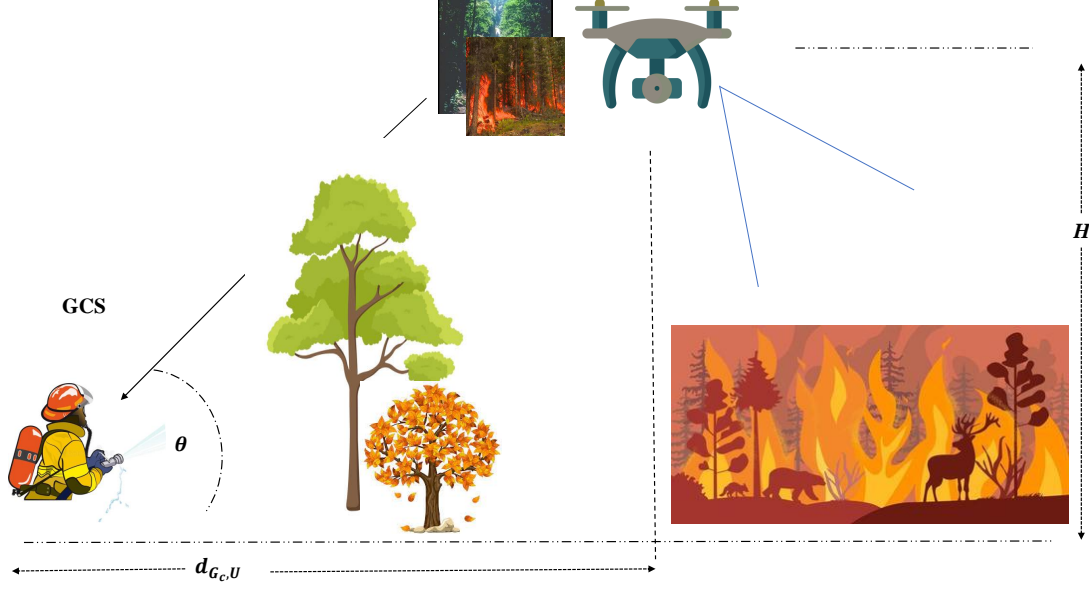
Figure 6.5: Illustration of the UAV-based wildfire detection system. The UAV is positioned at altitude H and equipped with cameras for image capture.

coding, DJSCC takes a more direct approach by mapping image pixel values onto complex-valued channel input symbols. This eliminates the necessity for distinct coding mechanisms [145, 146].

These complex-valued channel input symbols are subsequently transmitted through a wireless communication channel between the UAV and GCS. Channel characteristics are modeled using the Rician fading model, which effectively captures small-scale fading in UAV-assisted wireless channels. In addition, one of the key aspects of this system model is the joint training of both the transmitter and receiver. This collaborative training strategy enables adaptation to changing channel conditions, ensuring robust image transmission despite the inherently dynamic nature of the channel.

In the considered system, the receiver fulfils both classification and image reconstruction tasks, utilising the channel output in accordance with the GCS requirements. The input image is denoted as $I \in \mathbb{R}^{I_H \times I_W \times I_C}$, where I_H, I_W and I_C represent the height, width and number of colour channels, respectively. The total number of pixels in the image is denoted as $k_P = I_H \times I_W \times I_C$, which is referred to as the source bandwidth. The wireless transmission of the image source is then considered. The transmitter employs a DNN encoded by the DJSCC encoder, denoted as $f(\cdot, \boldsymbol{\vartheta})$, where $\boldsymbol{\vartheta}$ represents the learnable parameters of the network. Given an input source signal I, the output encoded semantic features S produced by $f(\cdot, \boldsymbol{\vartheta})$ are expressed as $s = f(I, \vartheta)$ and S belongs to the real vector space $\mathbb{R}^{2n_T}$, where n_T is the channel bandwidth. The ratio "n_T/k_P" is called the bandwidth ratio [180]. Then, encoded semantic features S are reshaped into complex-valued symbols n_T to form the encoded signal $\hat{s}$. After encoding the semantic signal S from the images received from the UAV I, a normalization process is applied to ensure that $\hat{s}$ adheres to the average power constraint as
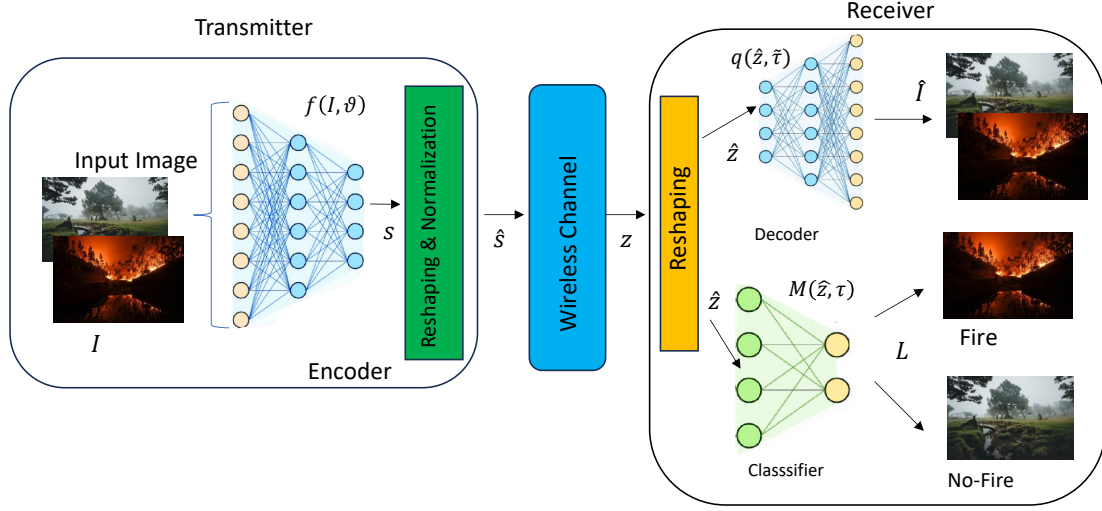
Figure 6.6: Proposed DJSCC-based communication system. The transmitter sends images captured by a UAV, assuming a Poisson point process for image capture. DJSCC technique is used for wireless image transmission. The Rician fading model is used to characterise the wireless channel. The receiver processes channel output for classification and image reconstruction tasks.

$$\frac{1}{n_T}\mathbb{E}\|\hat{\boldsymbol{s}}\|^2 \le P, \tag{6.25}$$

where P denotes the transmission power of the UAV. Subsequently, the encoded signal denoted $\hat{\boldsymbol{s}}$ is transmitted through the wireless channel between the UAV and the GCS. In the context of this wireless communication system, the wireless channel is characterized as a frequency-flat block fading channel. It is assumed that the channel's characteristics remain stable throughout the transmission of a single symbol however may independently vary when subsequent symbols are transmitted. Consequently, the received signal, represented as $\boldsymbol{z} \in \mathbb{C}^{n_T}$, can be expressed as follows:

$$\boldsymbol{z} = \sqrt{GP}\hat{\boldsymbol{s}} + \boldsymbol{W_n}, \tag{6.26}$$

where $\boldsymbol{W_n} \sim \mathcal{CN}(0, \sigma^2 \boldsymbol{I_n})$ represents independent and identically distributed (i.i.d.) circularly symmetric complex Gaussian noise with an average noise power of σ^2, where $\boldsymbol{I_n}$ stands for an identity matrix and $\mathcal{CN}$ represents complex normal (Gaussian) distribution. The parameter G is the channel gain. In this UAV communication configuration, the channel gain G is considered the product of the large-scale channel gain and the small-scale channel gain. Both the small-scale and large-scale channel gains are influenced by both LoS and NLoS channels. Consequently, it is essential to compute the LoS probability between the transmitter and the receiver. The LoS probability between the UAV and GCS, P_{LoS} can be expressed as in [157],

$$P_{\text{LoS}}(\theta) = \frac{1}{1 + A_s \exp\left(-B_s(\theta - A_s)\right)}, \tag{6.27}$$

where A_s and B_s are parameters characterizing the S-curve and are environment-dependent. The large-scale channel gain α for the channel between the UAV and GCS is determined as follows [193]:

$$-10\log\alpha = 20\log\left(H\csc\theta\right) + 20\log\left(\frac{4\pi f_c}{c}\right) + \eta_{\text{NLOS}} + \frac{\eta_{\text{LOS}} - \eta_{\text{NLOS}}}{1 + A_s\exp\left(-B_s(\theta - A_s)\right)}, \qquad (6.28)$$

where f_c and c are the carrier frequency (Hz) and the speed of light (m/s), respectively. glsetalos and η_{NLoS} represent the expectations of additional environmental-dependent excess path loss for the LoS and NLoS components, respectively. Assuming that the UAV and GCS remain static during the transmission of a block and ignoring the Doppler effect, the Rician fading model is employed to investigate the small-scale channel characteristics and multi-path propagation in this system. The probability distribution of the small-scale channel gain g follows a non-central chi-square distribution and the PDF for the small-scale channel gain can be expressed as:

$$f_{g(z)} = \frac{(K_f + 1)e^{-K_f}}{\bar{g}}e^{\frac{-(K_f+1)z}{\bar{g}}}I_0\left(2\sqrt{\frac{K_f(K_f + 1)z}{\bar{g}}}\right), \qquad (6.29)$$

where $z \geq 0$, $\bar{g} = 1$, $I_0(\cdot)$ is the zero-order modified Bessel function of the first kind and K_f is the Rician factor, which can be expressed as follows [159]:

$$K_f = \frac{P_{\text{LoS}}(\theta)}{1 - P_{\text{LoS}}(\theta)} = \frac{1}{A_s\exp(-Bs(\theta - A_s))}. \qquad (6.30)$$

Then, the channel gain and average SNR at the receiver can be calculated as $G = \alpha g$ and $\bar{\gamma} = \frac{\alpha P}{\sigma^2}$ respectively. Additionally, receiver processing has been incorporated to facilitate image recovery and execution of classification tasks, thereby enabling the detection of wildfire occurrence. Then, at the receiver end, the real and imaginary components of z are reshaped to form $\hat{z} \in \mathbb{R}^{2b}$ for further processing. Following this step, the receiver performs data recovery and classification tasks based on $\hat{z}$. One approach the receiver takes is to conduct the classification task directly within the feature space. This involves feeding the derived features $\hat{z}$ into a classifier $M(\cdot, \tau)$, where τ represents the learnable parameters of the network. The classifier produces the classification outcome denoted as $L = M(\hat{z}, \tau)$.

Alternatively, the decoder at the receiver maps the acquired $\hat{z}$ to an estimated reconstruction of the original transmitted image, denoted as $\hat{I} \in \mathbb{R}^{k_P}$. This decoding process involves a neural network represented as $q(\cdot, \tilde{\tau})$, which is parameterized by $\tilde{\tau}$. The image reconstruction is achieved through the function $\hat{I} = q(\bar{z}, \tilde{\tau})$. Our objective is to extract and transmit pertinent semantic information $\hat{s}$ from the original image I, with the aim of minimising communication overhead, quantified in terms of the number of symbols n_T that need to be transmitted. This goal is pursued while ensuring the effectiveness of image recovery and classification tasks, specifically for the detection of wildfires. To assess the performance of the image recovery task, the peak signal-to-noise ratio (PSNR) is used, which quantitatively measures the similarity between two images. The PSNR is calculated as follows for an original image I and its corresponding reconstructed image at the receiver end $\hat{I}$:

$$\text{PSNR}(I, \hat{I}) = 10 \cdot \log_{10}\left(\frac{\text{MAX}^2}{\frac{1}{k_P}||I - \hat{I}||^2}\right) \qquad (6.31)$$
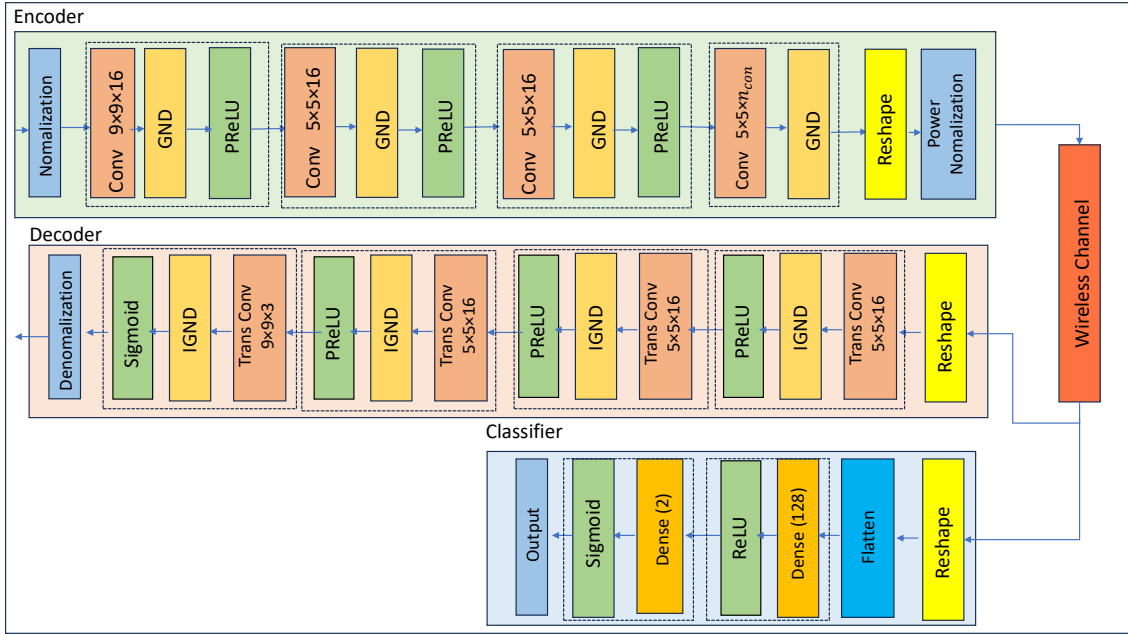
Figure 6.7: Encoder and decoder architecture with CNN layers, GDN/IGDN normalization and PReLU/Sigmoid activations. The classifier employs Dense Layers with Sigmd/ReLU for wildfire classification.

where MAX denotes the maximum potential value of the image pixels and k_P is a constant. The performance of the image classification task is assessed through the classification accuracy.

The specific architecture of each component in the transmitter and the receiver is illustrated in Figure 6.7. Both the encoder and decoder are composed of CNN layers. These convolution layers are followed by normalization achieved through the use of GND or inverse inverse generalized divisive normalization (IGDN) transformations. After normalisation, a PReLU activation function is applied, except for the final blocks of the decoder, where a sigmoid activation function is used.

The rationale behind this chosen architecture is as follows: convolutional layers are adept at extracting crucial features from the image. The application of GND facilitates local divisive normalization, a technique demonstrated to be effective for density modelling and image compression [194]. Simultaneously, the non-linear activations permit the learning of intricate mappings from the source signal space to the channel input space and vice versa. The classifier model employs dense layers with appropriate activation functions, such as sigmoid or rectified linear unit, to discern between instances of fire and non-fire. During the training process of both the encoder and decoder, the model employs the Adam optimiser with the objective of minimizing the mean squared error between the reconstructed image and the initial input image. Conversely, the classifier is trained using the Adam optimiser in conjunction with sparse categorical cross-entropy as the loss function. In addition, the final layer of the encoder is characterised by its depth parameter, denoted as n_{con}, determining the aggregate bandwidth ratio across all layers as follows:

$$\frac{n_T}{k_p} = \frac{\left(\frac{I_H}{4} \times \frac{I_W}{4} \times n_{con}\right)}{I_H \times I_W \times I_C} = \frac{n_{con}}{16 \times I_C}. \tag{6.32}$$

6.2.2.1 Estimating the AoMI

This section aims to estimate the AAoMI of the deep learning-based UAV-assisted wildfire detection system. It is assumed that the average image capture rate at the UAV is denoted by λ_I and the UAV-based wireless communication system transmits images at a rate of μ. Furthermore, the probability of correct image classification is considered as $0 \leq \rho_{ac} < 1$.

The average image transmission rate μ is inversely proportional to the mean transmission time per image, denoted by $\mathbb{E}[T]$, within this wireless network. This relationship is given by the following equation:

$$\frac{1}{\mu} = \mathbb{E}[T] = n_T T_s \tag{6.33}$$

where T_s represents the symbol duration and n_T denotes the total number of symbol used for the transmission by the transmitter at the UAV. If the capturing time stamp of the most recently correctly classified image received at timestamp t is represented by $g(t)$, then AoMI can be defined as a random process as

$$x_0(t) = t - g(t). \tag{6.34}$$
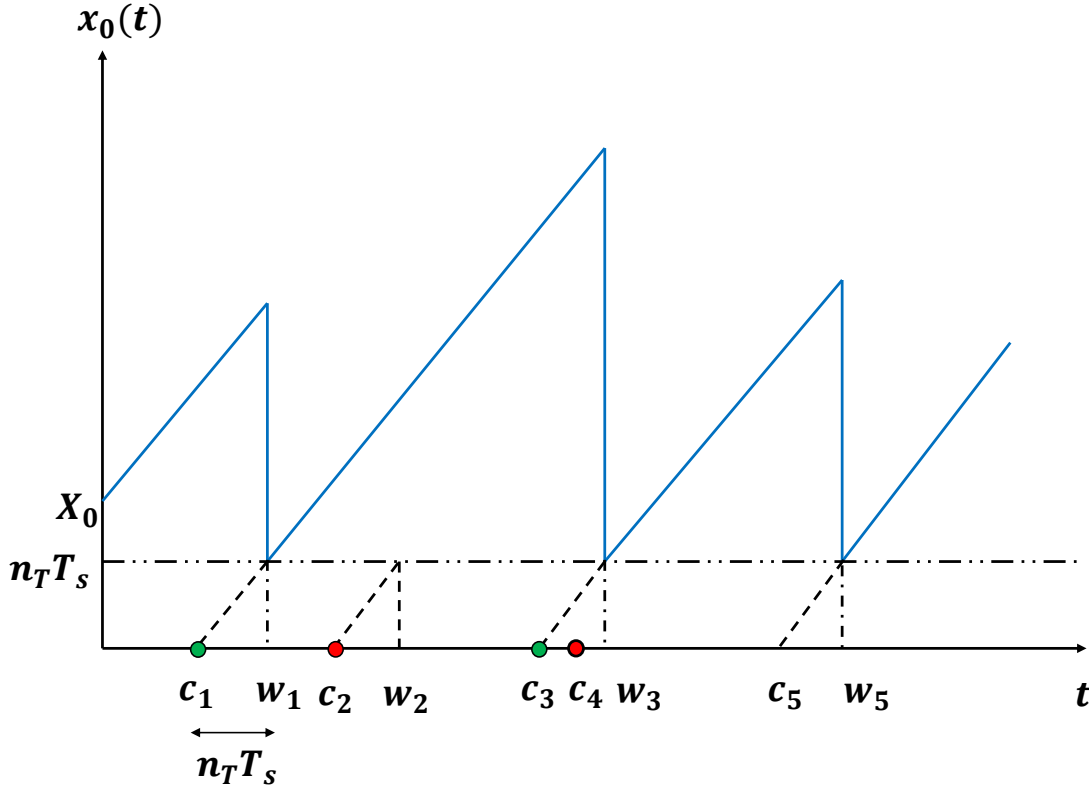
Figure 6.8: Evolution of AoMI $x_0(t)$ with the time at the GCS: UAV capture images at time stamps $c_1, c_2, ..$ and the GCS receive and classify these images at time stamps $w_1, w_2, ...$

As illustrated in Figure 6.8, it is assumed that at $t = 0$ the measurements of the AoMI begin and the AoI at G_c is set to $x_0(0) = X_0$. The UAV captures images on time stamps $c_1, c_2, \ldots$ and the G_c receives these images on time stamps $w_1, w_2, \ldots$. As shown in Figure 6.8, the captured

image i is transmitted from the UAV at timestamp $t = c_i$ and is classified by the G_c at time stamp $w_i = c_i + nT_s$. Therefore, if the image is classified correctly at time w_i, the AoMI at G_c can be estimated as

$$x(w_i) = n_T T_s. \tag{6.35}$$

AoMI at G_c increases linearly until it classifies an image correctly. For example, if one image received by the G_c is misclassified at time w_2, then $x_0(t)$ continues to increase linearly. Similarly, when an image is in transmission, new images captured on the UAV are blocked and cleared. For instance, an image generated at the time c_4 is not transmitted since at that time the previous image captured at the time c_3 is still under transmission. Hence, the image captured at the time c_4 does not affect the AoMI process. For the time period considered T_c, the average AoMI time can be calculated using the area under $x_0(t)$. Similarly, the time average AoMI of the proposed wildfire detection system can be estimated as

$$\Delta_{T_c} = \frac{1}{T_c} \int_0^{T_c} x_0(t)\, dt. \tag{6.36}$$

Then, the time average AoMI Δ_{T_c} tends to the ensemble average AoMI when $T_c \to \infty$, i.e., which can be expressed as

$$\Delta = \mathbb{E}[x_0] = \lim_{t \to \infty} \mathbb{E}[x_0(t)] = \lim_{T_c \to \infty} \Delta_{T_c}. \tag{6.37}$$

In this study, SHS techniques are employed to estimate $\mathbb{E}[x_0]$, which represents the AoMI at the G_c. Within the SHS framework, the AoMI process is modelled by combining continuous states $x(t)$ and discrete states $q(t)$. These discrete states signify the transmission status of the wireless communication system in the UAV-based wildfire detection system, which can be effectively described using a Markov chain. The state space of this Markov chain is defined as $(q(t), x(t))$, where $q(t) \in Q = \{0, 1\}$; where $q = 0$ indicates an idle wireless communication system, while $q = 1$ signifies an active transmission state. The evaluation of the age process in G_c is represented by the continuous vector $x(t) = [x_1(t), x_0(t)]$, where $x_0(t)$ monitors the age in G_c corresponding to correctly classified images and $x_1(t)$ represents the projected value of $x_0(t)$ in accurate image classification. The AoMI process at G_c, under the SHS framework, is visually depicted by a graph $(Q, \mathcal{L})$. This graphical representation incorporates transmission states of the wireless communication system as nodes and the transitions between these states are illustrated as directed edges. The transition rate from node q_l to q_l' is indicated by $\lambda^{(l)} \delta_{q_l, q_{(t)}}$, where the Kronecker delta function $\delta_{\hat{q}, q_{(t)}}$ ensures that transitions occur only for the state q_l. Each transition l typically corresponds to a sudden change in the continuous state, which can be represented using a linear transition reset mapping:

$$x' = x\mathbf{A}_l, \tag{6.38}$$

where $\mathbf{A}_l \in \{0, 1\}^{(2) \times (2)}$ is a binary transition reset map matrix. For this system, the interactions between discrete states and their impact on continuous states are summarised in Table 6.4 through linear mapping. Additionally, the transactions described in Table 6.4 can be interpreted as follows:

- $l = 1$: An image captured by the UAV when the wireless communication system is in an idle state. With the capture of the image, the wireless communication system in the UAV

starts transmission of the captured image and $x'_0 = x_0$ remains unchanged since capturing an image by the UAV does not reduce the age at the G_c until it is correctly classified by the G_c. However, $x'_1 = 0$ since the captured image is fresh and its age is zero at the instant.

- $l = 2$: An image transmitted by the UAV correctly classified by the G_c. In this situation, $x'_0 = x_1$, corresponding to the age at the G_c being reset to the age of the image that just completed transmission. Moreover, $x'_1 = 0$ since x_1 becomes irrelevant when the wireless communication system of the UAV enters state 0.

- $l = 3$: An image transmitted by the UAV misclassified by the G_c. In this situation, $x'_0 = x_0$ remains unchanged since misclassification does not lead to an age reduction in G_c. Moreover, $x'_1 = 0$ since x_1 becomes irrelevant when the wireless communication system enters the state 0.

- $l = 4$: A UAV captured an image while another image was being transmitted. Consequently, the new image will be discarded and the transmission will continue with the current image. In this scenario, $x'_0 = x_0$ remains unchanged since this operation does not result in an age reduction at the G_c. Furthermore, $x'_1 = x_1$ remains unaffected since the age of the current transmitting image will also remain unchanged.

The growth rate of the continuous state at each discrete $q(t) = q$ where $q \in Q$ is given by:

$$\dot{\mathbf{x}}(t) = \frac{\partial \mathbf{x}(t)}{\partial t} = \mathbf{b}_q, \tag{6.39}$$

where $\mathbf{b}_q = [\mathbf{b}_{q,0}, \mathbf{b}_{q,1}]$ is a vector containing only binary elements. When $\mathbf{x}_j(t), j \in 1, 0$ grows at a unit rate as a normal age process in state q, $\mathbf{b}_{q,j} = 1$; and when it is irrelevant to the age process or does not need to be tracked in state q, $\mathbf{b}_{q,j} = 0$. Hence, for this system, $\mathbf{b}_q$ can be expressed as follows:

$$\mathbf{b}_q = \begin{cases} \begin{bmatrix} 1 & 0 \end{bmatrix}, & q = 0, \\ \\ \begin{bmatrix} 1 & 1 \end{bmatrix}, & q = 1. \end{cases} \tag{6.40}$$

Let $\pi_{\hat{q}}(t)$ denote the discrete state probabilities for all $\hat{q} \in Q$ and $\mathbf{v}_{\hat{q}}(t)$ denote the correlation between the age process and the discrete state of the system $q(t) = \hat{q}$. Accordingly, the following is obtained:

$$\pi_{\hat{q}}(t) = \mathbb{E}[\delta_{\hat{q},q(t)}], \tag{6.41}$$

and the correlation vector function:

$$\mathbf{v}_{\hat{q}}(t) = \begin{bmatrix} \upsilon_{\hat{q}0}(t), \upsilon_{\hat{q}1}(t) \end{bmatrix}, \tag{6.42}$$

where:

$$\upsilon_{\hat{q}j}(t) = \mathbb{E}[x_j(t)\delta_{\hat{q},q(t)}], \quad j \in (0, 1). \tag{6.43}$$

99

All transactions $\mathcal{L}$ can be divided into two categories: incoming transitions and outbound transitions. For each state q, all incoming transitions are labelled as:

$$\mathcal{L}'_q = \{l \in \mathcal{L} : q'_l = q\}, \tag{6.44}$$

and all outgoing transitions are labelled as:

$$\mathcal{L}_q = \{l \in \mathcal{L} : q_l = q\}. \tag{6.45}$$

To compute the time-averaged age, it is assumed that the Markov chain $q(t)$ is ergodic. Hence, the state probability vector $\pi(t) = [\pi_0(t), \pi_1(t)]$ always converges to a unique stationary vector $\bar{\pi} = [\bar{\pi}_0, \bar{\pi}_1]$ satisfying:

$$\bar{\pi}_{\bar{q}} \sum_{l \in \mathcal{L}_{\bar{q}}} \lambda^{(l)} = \sum_{l \in \mathcal{L}'_{\bar{q}}} \lambda^{(l)} \bar{\pi}_{q_l}, \quad \bar{q} \in Q, \tag{6.46}$$

$$\sum_{\bar{q} \in Q} \bar{\pi}_{\bar{q}} = 1. \tag{6.47}$$

For this system, (6.46) has been employed to find stationary probabilities and it can be shown that the stationary probability vector satisfies $\bar{\pi}\mathbf{A} = \bar{\pi}\mathbf{B}$, with:

$$\mathbf{A} = \text{diag}\begin{bmatrix} \lambda_I & \mu + \lambda_I \end{bmatrix}, \quad \mathbf{B} = \begin{bmatrix} 0 & \lambda_I \\ \mu & \lambda_I \end{bmatrix}.$$

Applying (6.47), the stationary probabilities $\bar{\pi}$ can be calculated as:

$$\bar{\pi} = \begin{bmatrix} \bar{\pi}_0 & \bar{\pi}_1 \end{bmatrix} = \frac{1}{\lambda_I + \mu} \begin{bmatrix} \mu & \lambda_I \end{bmatrix}. \tag{6.48}$$

As shown in [55], when $\pi(t) = \bar{\pi}$, $v(t) = [v_0(t), v_1(t)]$, the system follows first-order differential equations for all $\bar{q} \in Q$:

$$\dot{v}_{\bar{q}}(t) = b_{\bar{q}} \bar{\pi}_{\bar{q}} + \sum_{l \in \mathcal{L}'_{\bar{q}}} \lambda^{(l)} v_{q_l}(t) \mathbf{A}_l - v_{\bar{q}}(t) \sum_{l \in \mathcal{L}_{\bar{q}}} \lambda^{(l)}, \tag{6.49}$$

Under the ergodicity assumption, the differential equation (6.49) is stable and each $v_{\bar{q}}(t) = \mathbb{E}[x(t)\delta_{\bar{q},q(t)}]$ converges to a non-negative limit $\bar{v}_{\bar{q}}$ as $t \to \infty$. Accordingly, the following is obtained:

$$\mathbb{E}[x] = \lim_{t \to \infty} \mathbb{E}[x(t)] = \lim_{t \to \infty} \mathbb{E}[x(t)\delta_{\bar{q},q(t)}] = \sum_{\bar{q} \in Q} \bar{v}_{\bar{q}}, \tag{6.50}$$

$$\bar{v}_{\bar{q}} \sum_{l \in \mathcal{L}_{\bar{q}}} \lambda^{(l)} = b_{\bar{q}} \bar{\pi}_{\bar{q}} + \sum_{l \in \mathcal{L}'_{\bar{q}}} \lambda^{(l)} \bar{v}_{q_l} \mathbf{A}_l, \quad \bar{q} \in Q, \tag{6.51}$$

where $x_0(t)$ is the age at the destination and AAoMI at the destination is calculated as follows [61]:

$$\Delta = \mathbb{E}[x_0] = \lim_{t \to \infty} \mathbb{E}[x_0(t)] = \sum_{\bar{q} \in Q} \bar{v}_{\bar{q}0}. \tag{6.52}$$

To estimate AAoMI using (6.52), it is necessary to find $\bar{v}_{\bar{q}0}$ using (6.51). First, a solution can be found for $\bar{v} = \begin{bmatrix} \bar{v}0 & \bar{v}1 \end{bmatrix} = \begin{bmatrix} \bar{v}_{00} & \bar{v}_{01} & \bar{v}_{10} & \bar{v}_{11} \end{bmatrix}$ using (6.51). Hence, evaluating (6.51) at $q = 0$ and $q = 1$ and using Table 6.4, the following is obtained:

$$\lambda_I \begin{bmatrix} \bar{v}_{00} & \bar{v}_{01} \end{bmatrix} = \begin{bmatrix} \bar{\pi}_0 & 0 \end{bmatrix} + \mu \rho_{ac} \begin{bmatrix} \bar{v}_{11} & 0 \end{bmatrix} + \mu(1 - \rho_{ac}) \begin{bmatrix} \bar{v}_{10} & 0 \end{bmatrix}, \tag{6.53}$$

Table 6.4: Transitions Rate for the Markov Chain in UAV-Assisted Wildfire Detection System

l	$q_l \rightarrow q'_l$	$\lambda^{(l)}$	$\mathbf{xA}_l$	$\mathbf{v}_{q_l}\mathbf{A}_l$
1	$0 \rightarrow 1$	λ_I	$\begin{bmatrix} x_0 & 0 \end{bmatrix}$	$\begin{bmatrix} v_{00} & 0 \end{bmatrix}$
2	$1 \rightarrow 0$	$\mu\rho_{ac}$	$\begin{bmatrix} x_1 & 0 \end{bmatrix}$	$\begin{bmatrix} v_{11} & 0 \end{bmatrix}$
3	$1 \rightarrow 0$	$\mu(1-\rho_{ac})$	$\begin{bmatrix} x_0 & 0 \end{bmatrix}$	$\begin{bmatrix} v_{10} & 0 \end{bmatrix}$
4	$1 \rightarrow 1$	λ_I	$\begin{bmatrix} x_0 & x_1 \end{bmatrix}$	$\begin{bmatrix} v_{10} & v_{11} \end{bmatrix}$

$$(\mu + \lambda_I) \begin{bmatrix} \bar{v}_{10} & \bar{v}_{11} \end{bmatrix} = \begin{bmatrix} \bar{\pi}_1 & \bar{\pi}_1 \end{bmatrix} + \lambda_I \begin{bmatrix} \bar{v}_{00} & 0 \end{bmatrix} + \lambda_I \begin{bmatrix} \bar{v}_{10} & \bar{v}_{11} \end{bmatrix}. \tag{6.54}$$

Then, the above expressions can be written as the following system of equations:

$$\lambda_I \bar{v}_{00} = \bar{\pi}_0 + \mu\rho_{ac}\bar{v}_{11} + \mu(1 - \rho_{ac})\bar{v}_{10}, \tag{6.55}$$

$$\mu\bar{v}_{10} = \bar{\pi}_1 + \lambda_I \bar{v}_{00}, \tag{6.56}$$

$$\mu\bar{v}_{11} = \bar{\pi}_1. \tag{6.57}$$

By solving these equations and using (6.48), the values of $\bar{v}_{\bar{q}0}$ can be calculated. Finally, by substituting the result into (6.52), the AAoMI Δ at the G_c can be obtained as follows:

$$\Delta = \frac{1}{\lambda_I \rho_{ac}} + \frac{1}{\mu\rho_{ac}} + \frac{\lambda_I}{\mu(\lambda_I + \mu)}. \tag{6.58}$$

Finally, the AAoMI Δ of the wildfire detection system is calculated using Algorithm 2.

6.2.3 Simulation Results

In this section, the simulation results are presented to validate the functionality of the system model in terms of image recovery and classification for the detection of wildfires. Specifically, experiments are conducted using a wildfire detection image dataset [195]. This dataset comprises colourful images with dimensions of 250 × 250 × 3 pixels, depicting various real-world wildfire scenarios as well as non-fire scenarios in forest environments. Unless mentioned, the simulation parameters are listed in Table 6.5.

Figure 6.9 depicts the relationship between average SNR ($\bar{\gamma}$) and UAV altitude for varying levels of transmission power and distances. The findings suggest that the most favourable altitude for achieving the highest average SNR is approximately 300 m. The SNR remains lower at lower altitudes due to a weak LoS signal. As the altitude approaches the optimal value, the average SNR experiences rapid improvement owing to a more robust LoS component, which outweighs the effects of signal attenuation due to the increase in distance between the transmitter and the receiver. However, exceeding this optimal altitude leads to a path loss effect dominant over the effect of the LoS, ultimately resulting in a decrease in the average SNR. Furthermore, reducing the distance and increasing transmission power substantially elevates the average SNR level, as depicted in the graph. In addition, it is noticed that the effect of the transmission power plays a major role in the average SNR level for high altitude compared to the distance between the transmitter and receiver.

Figure 6.10 illustrates the relationship between the average SNR, denoted as $\bar{\gamma}$ and the distance between the transmitter and receiver. The figure presents two scenarios: one with UAV support for

---

Algorithm 2 Algorithm for Training DJSCC and Calculating AAoMI in UAV-Assisted Wildfire Detection

---

    Training Phase

1: **Require:**A batch of images I for training from the wildfire detection image dataset [195].

2: **Ensure:**Trained encoder $f(\cdot, \boldsymbol{\vartheta})$ and classifier $M(\cdot, \boldsymbol{\tau})$.

3: **Initialize:** Initialise the weights of $f(\cdot, \boldsymbol{\vartheta})$ and $M(\cdot, \boldsymbol{\tau})$ using a standard initialisation method.

4: **for** each epoch **do**

      Transmitter:

5:       Extract semantic features using $f(\cdot, \boldsymbol{\vartheta})$.

6:       Apply power normalisation as in (6.25).

7:       Set the wireless channel average SNR as $\bar{\gamma}_{\text{train}}$ and transmit the symbols through wireless channels.

      Receiver:

8:       Perform reshaping on the received signal z.

9:       Conduct image classification with $M(\hat{z}, \boldsymbol{\tau})$.

10: **end for**

    Deployment and AAoMI Calculation Phase

11: **Require:**A batch of images I_{test} for testing from the wildfire detection image dataset [195].

12: **Ensure:**Calculate AAoMI.

13: **Initialise:** Image generation process parameters λ_I and image transmission rate μ.

    Transmitter:

14:    Deploy the learned $f(\cdot, \boldsymbol{\vartheta})$. Extract semantic features S.

15:    Apply power normalisation as in (6.25).

16:    Set the wireless channel parameter of UAV communication channel following (6.28), (6.29) and (6.30). Then, the symbols are transmitted through the wireless channel.

    Receiver:

17:    Perform reshaping on the received signal z and deploy the learned $M(\cdot, \boldsymbol{\tau})$.

18:    Conduct image classification using $M(\hat{z}, \boldsymbol{\tau})$.

19:    **Compute Classification Accuracy:**

20:    Compare the predicted class L with the true class of I_{test}.

21:    Calculate the classification accuracy ρ_{ac}.

22:    **Compute AAoMI:**

23:    Calculate AAoMI using

$$\Delta = \frac{1}{\lambda_I \rho_{ac}} + \frac{1}{\mu \rho_{ac}} + \frac{\lambda_I}{\mu(\lambda_I + \mu)}.$$

Table 6.5: Simulation Parameters for UAV-Assisted Semantic Wireless Communication System in Wildfire Detection [159].

Parameter	Value
Distance between UAV and GCS (d_{UG})	1500 m
UAV altitude (d_{UG})	150 m
Carrier frequency (f_c)	2.4 GHz
Speed of the light (m/s) (c)	$3 \times 10^8 \text{ms}^{-1}$
Transmission power at UAV(P)	30 dBm
η_{LoS}	0.1 dB
η_{NLoS}	21 dB
Symbol duration (T_s)	20 μs
n_{con}	16
Bandwidth ratio n_T/k_p	1/3
Noise power (σ^2)	-100 dBm
S-curve parameter A	4.87
S-curve parameters B	0.429
Image generation rate λ_I	3 images s^{-1}

Figure 6.9: Average SNR vs. UAV altitude for different transmission power levels at the UAV and different distances between the UAV and GCU.
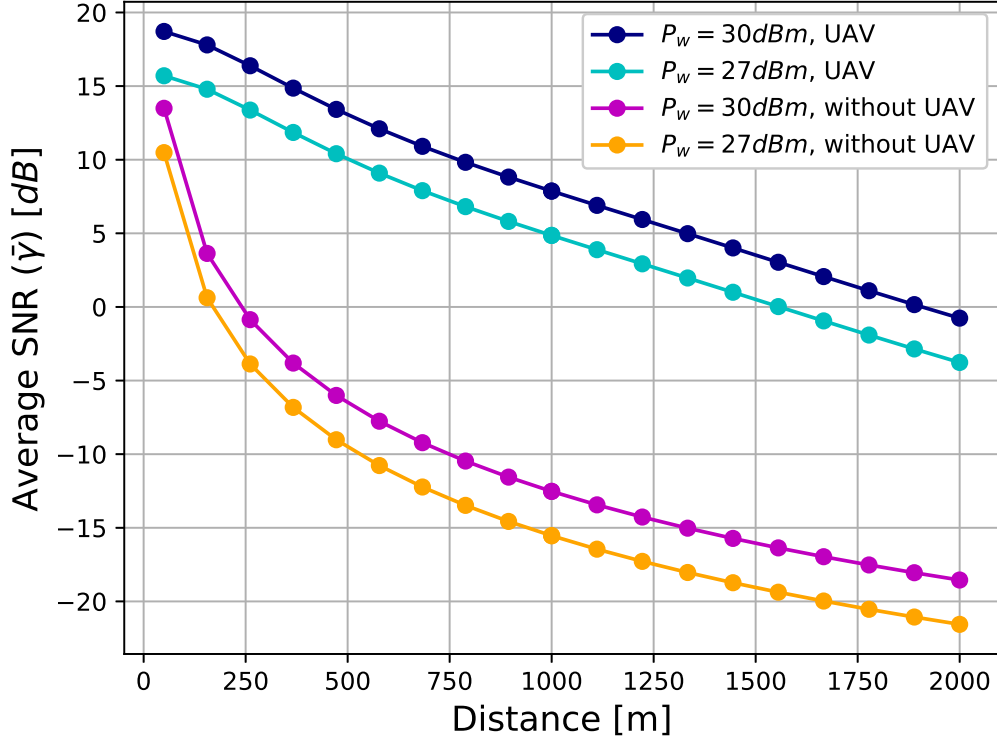
Figure 6.10: Comparison of average SNR at different distances: With UAV deployment and without UAV deployment.

transmission and the other without UAV deployment. When examining the graph, it becomes evident that as the distance between the transmitter and receiver increases, the average SNR experiences a dramatic decrease when no UAV support is available. On the contrary, when a UAV is deployed to assist in transmission, there is a notable increase in the average SNR across all distances. From this graph, a clear conclusion can be drawn: the UAV-assisted communication system outperforms the terrestrial-based communication system in terms of maintaining a consistently higher average SNR. This indicates that UAV-assisted communication is more reliable and effective, particularly when dealing with longer transmission distances.

In Figure 6.11, the relationship between UAV altitude and classification accuracy is illustrated. Initial training of DJSCC involves setting $\bar{\gamma}_{\text{train}} = 20\,\text{dB}$ and $K_f = 2$. It is important to note that the performance of the DJSCC relies heavily on the SNR level. Consequently, when the UAV operates at lower altitudes, the classification accuracy tends to decrease due to weaker LoS channel conditions. However, as depicted in Figure 6.11, the classification accuracy gradually improves as the altitude of the UAV increases, eventually reaching its optimal point. This trend observed in Figure 6.11 is in line with what was noticed in Figure 6.9, where the average SNR value rises towards its optimum levels owing to the presence of strong LoS conditions. Consequently, mirroring the average SNR variation pattern, the classification accuracy starts to decline. This reduction is attributed to the growing impact of path loss, which becomes more pronounced under robust LoS
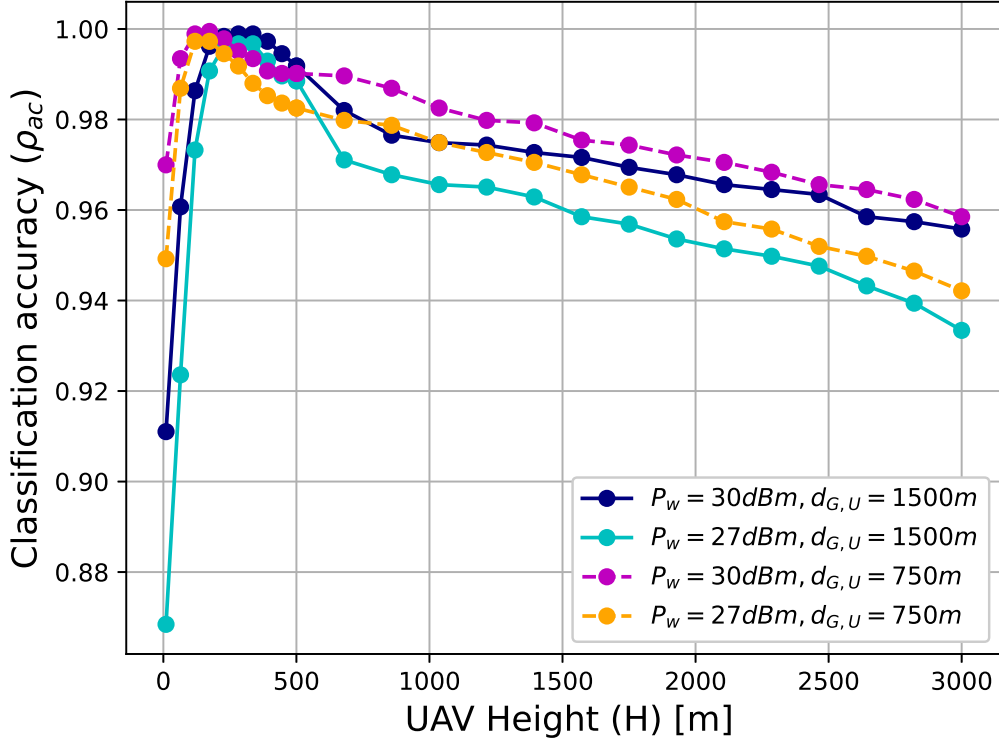
Figure 6.11: Classification accuracy vs. UAV altitude for different transmission power levels at the UAV and different distances between the UAV and GCU.

channel conditions.

In Figure 6.12, the relationship between UAV altitude and AAoMI is depicted. It is essential to note that, as indicated by equation (6.58), AAoMI depends solely on classification accuracy when both λ_I and μ are constant. Consequently, at lower UAV altitudes, AAoMI is high due to the lower classification accuracy caused by the weaker LoS channel conditions and, hence, the reduced average SNR. However, as shown in Figure 6.12, AAoMI gradually decreases as UAV altitude increases, eventually reaching its optimal point. This trend, observed in Figure 6.12, aligns with what was noticed in Figure 6.11, where average classification accuracy rises towards its optimum levels owing to the high SNR levels resulting from strong LoS conditions. Subsequently, beyond this optimal altitude point, AAoMI starts to increase. This increase is attributed to the reduction in classification accuracy due to low SNR, amplified by the pronounced effects of path loss. Figure 6.13 shows the relationship between AAoMI and transmission power of the UAV-assisted communication system. The findings highlight the substantial impact of varying transmission power levels at the UAV on AAoMI. The graph shows a consistent pattern: as transmission power increases, AAoMI consistently decreases. Notably, at a transmission power of 1 mW (0 dBm), AAoMI reaches a saturation point, resulting in minimal classification accuracy at this point and the system achieves its lowest AAoMI within approximately 0.8 seconds. Beyond this saturation point, increasing transmission power does not further enhance the freshness of information. However,
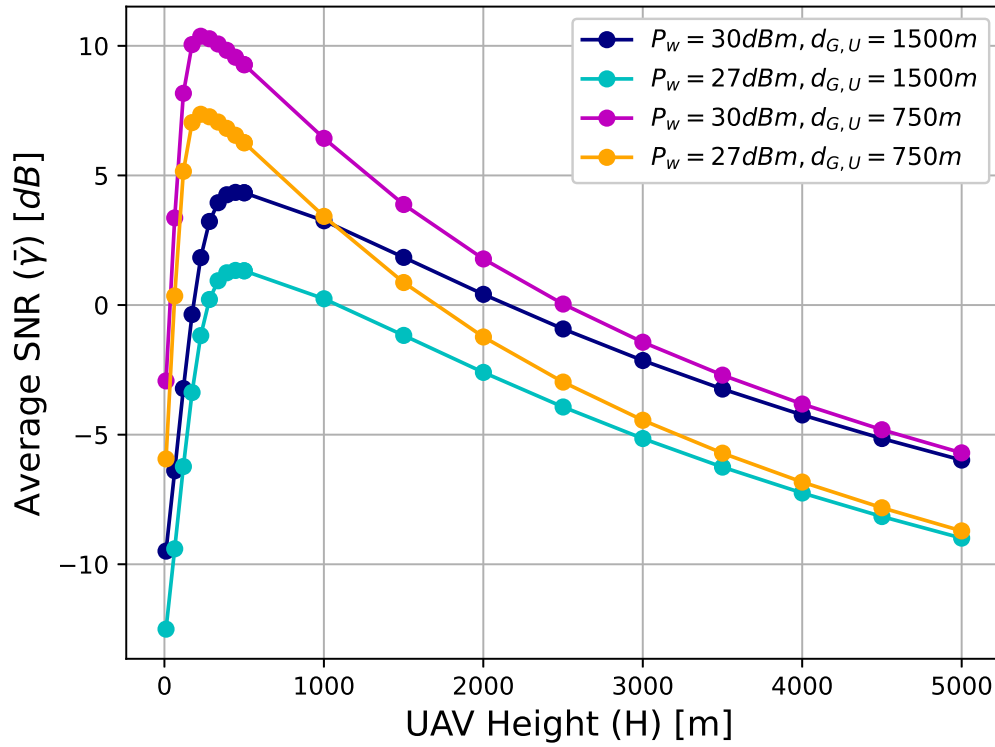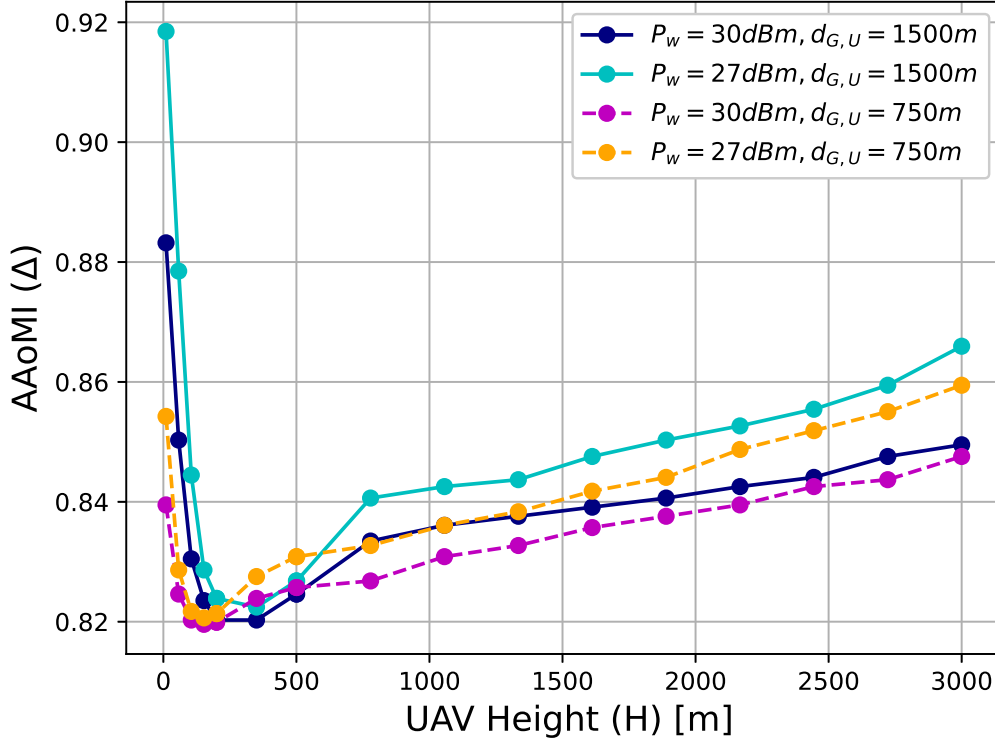
Figure 6.12: AAoMI vs. UAV altitude for different transmission power levels at the UAV and different distances between the UAV and GCU.

in the absence of UAV deployment, AAoMI significantly increases compared to UAV-assisted communication, particularly for low transmission power scenarios. Furthermore, AAoMI saturates at a higher transmission power, approximately 10 mW (10 dBm), when UAV assistance is not employed. This observation underscores the substantial improvements in information freshness and power efficiency attainable through UAV integration, particularly for low-level transmission power applications. In summary, the findings depicted in Figure 6.13 highlight the crucial role of UAV-assisted communication in shaping the AAoI performance of the semantic-based communication system.

Figure 6.14 illustrates the relationship between AAoMI and the image capture rate of the UAV. It demonstrates a consistent decrease in AAoMI for the proposed wireless communication system as the image capture rate increases. It is worth noting that in this wireless system, there is no queue waiting for transmission. Consequently, there is no queuing delay within the system. The higher image capture rate results in more frequent reception of images at the GCS. To put it plainly, this reduction in AAoMI is a direct outcome of the increased frequency of image reception at the GCS. In Figure 6.15, the graphs illustrate how classification accuracy varies with the bandwidth ratio (n_T/k_p), taking into account different transmission power levels and distances. In particular, as the bandwidth ratio increases, there is an improvement in classification accuracy. This enhancement can be attributed to the adoption of larger block lengths during transmission, particularly when
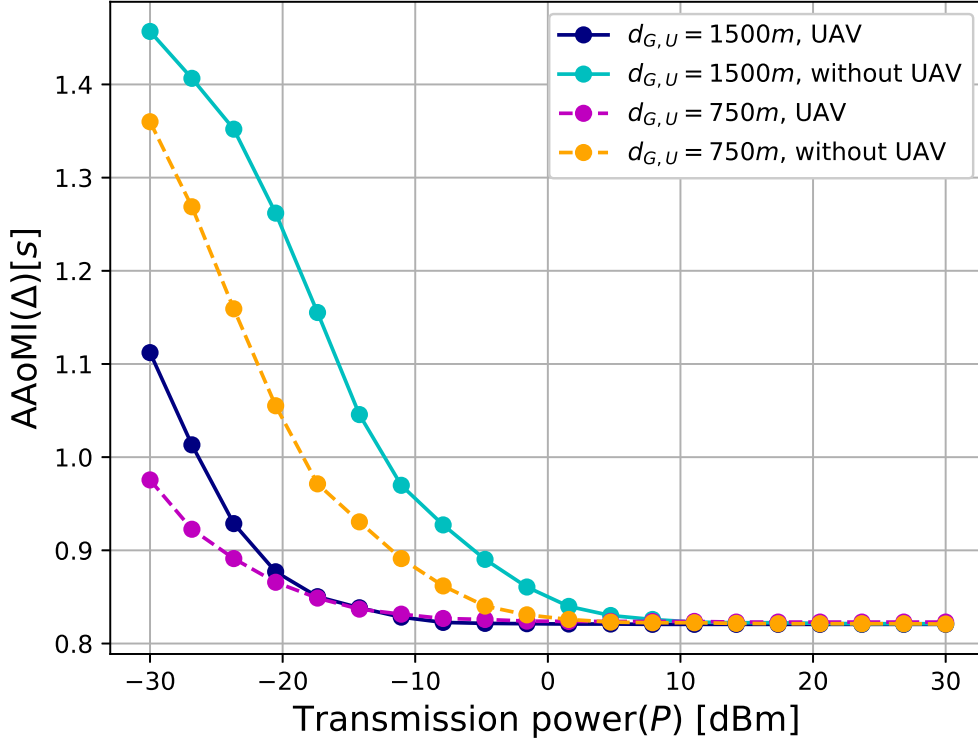
Figure 6.13: AAoMI vs. transmission power for different distances between the transmitter and receiver, both with UAV deployment and without UAV deployment.

the bandwidth ratio is increasing. Furthermore, this boost in accuracy becomes more pronounced when the distance between the transmitter and receiver is substantial. This is primarily due to the longer block length assisting in transmitting information accurately even when the SNR at the receiver is poor, which often occurs in long-distance scenarios. In Figure 6.16, the graphs depict how AAoMI changes with respect to the bandwidth ratio (n_T/k_p), taking into consideration different transmission power levels and distances. It is important to note that increasing the bandwidth ratio leads to longer transmission times, given that k_P remains constant. As observed in Figure 6.15, increasing the bandwidth ratio results in higher classification accuracy. According to equation (6.58), it would be expected that AAoMI decreases with an increase in the bandwidth ratio. However, contrary to this expectation, the graphs in Figure 6.16 show that AAoMI increases as the bandwidth ratio rises. This phenomenon can be attributed to the dominant influence of the extended transmission time compared to the gains in classification accuracy. It is worth mentioning that traditional communication systems typically exhibit higher AAoI with shorter block lengths due to the strong impact of a lower error rate on AAoI[18]. In contrast, deep learning-based systems demonstrate a lower AAoMI even with short block lengths, as they excel at extracting semantic information efficiently without compromising accuracy. In Figure 6.17, the relationship between UAV altitude and PSNR for image recovery is depicted. In this particular scenario, the DJSCC is initially trained with a fixed $\bar{\gamma}_{train}$ value of 20 dB and $K_f = 2$. Subsequently, the trained DJSCC
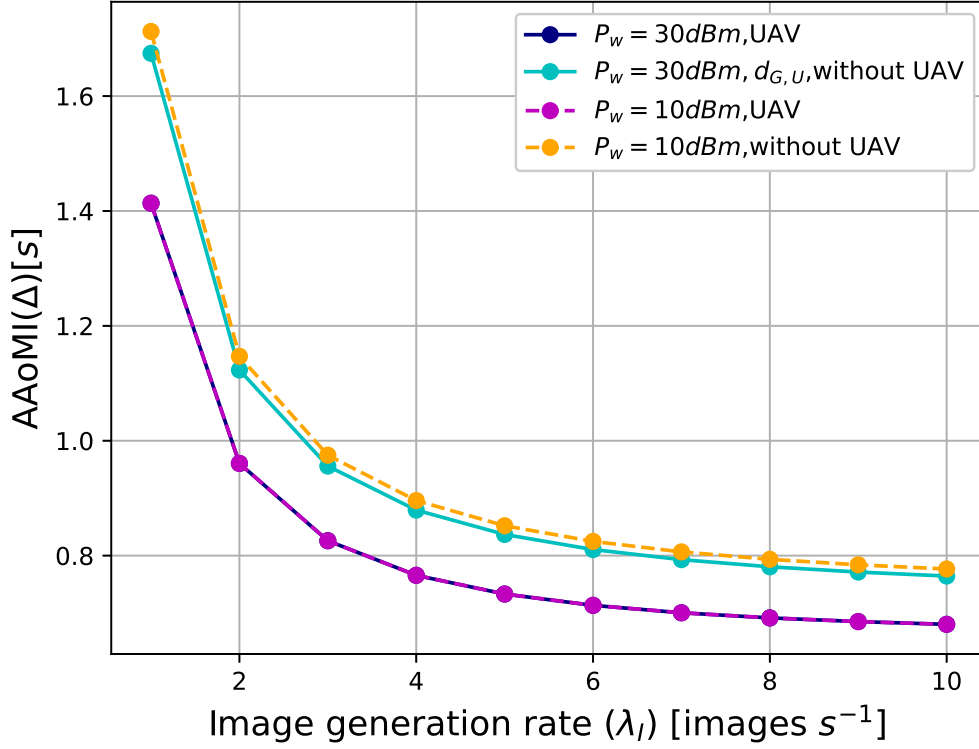
Figure 6.14: Comparison of AAoMI against image generation (capturing) rate (λ_I) for various transmission power levels and distances, both with UAV deployment and without UAV deployment.

model is applied for image transmission, where the transmitted image is reconstructed using the received signal and the resulting PSNR is evaluated.

In the graph shown in Figure 6.17, the PSNR is measured under various UAV altitudes, which represent different channel conditions. It is important to note that the performance of DJSCC is closely tied to the average SNR. Hence, at lower UAV altitudes, where LoS channels are weaker, the PSNR tends to be lower due to the diminished average SNR levels. However, as the UAV altitude increases and the channel conditions improve, the PSNR experiences a significant boost, approaching its optimal point.

This trend aligns with the observations made in Figure 6.9, where the average SNR values increase as the altitude of the UAV increases and the LoS conditions strengthen. Similarly, when the average SNR varies, the PSNR also exhibits a sharp decrease after reaching its peak performance. It is worth noting that this decrease in PSNR is more pronounced compared to the reduction in classification accuracy in Figure 6.11. This discrepancy arises since image reconstruction demands a higher SNR than classification tasks.

Figure 6.18 shows the relationship between the PSNR and the number of training epochs in the training phase of the DJSCC. Initially, there is a pronounced upward trend in PSNR, indicative of enhanced performance of the system. However, as training progresses beyond approximately 40 epochs, PSNR will not improve much. This suggests that additional training beyond this point
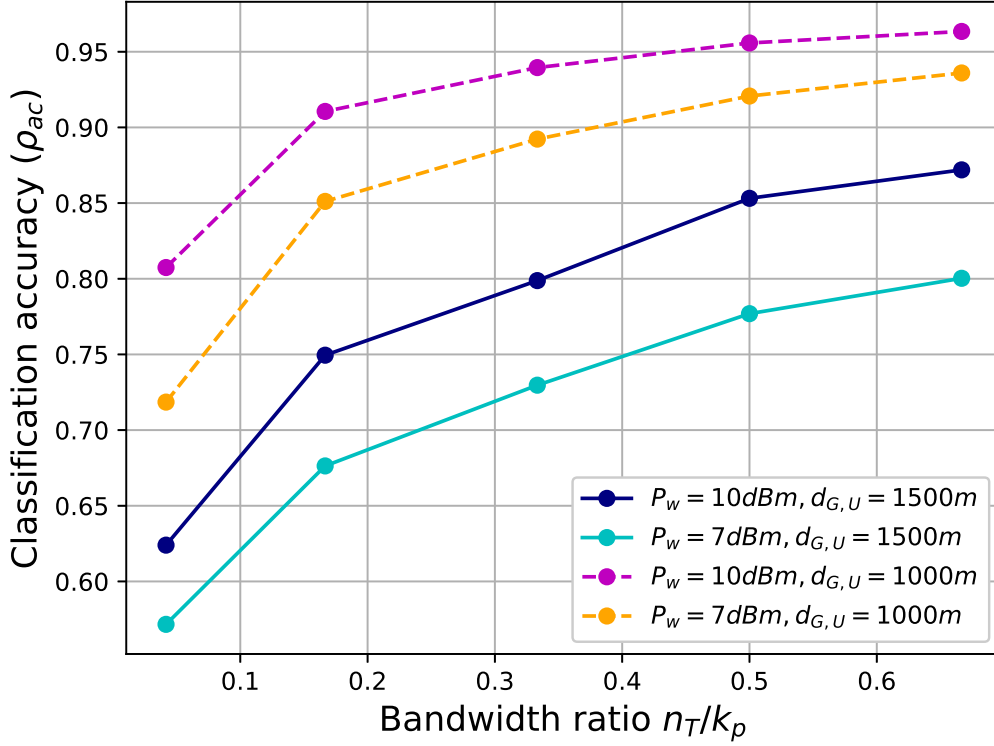
Figure 6.15: Classification Accuracy vs. bandwidth ratio (n_T/k_p) for different transmission power levels at the UAV and different distances between the UAV and GCU.

may yield diminishing returns in terms of PSNR. Furthermore, based on the simulation results, the following key observations can be identified:

1. The average SNR exhibits a clear pattern with changes in UAV altitude. As the UAV's altitude approaches the optimal level, the average SNR undergoes a sharp rise, primarily attributed to the reinforcement of LoS components. Conversely, once the altitude surpasses this optimal point, the average SNR begins to decrease, mainly due to the increasing impact of path loss, ultimately compromising signal quality.

2. The accuracy of classification is strongly tied to the SNR. Lower UAV altitudes, which result in weaker LoS conditions, result in diminished accuracy. On the other hand, higher altitudes enhance accuracy; nevertheless, surpassing the optimal altitude point leads to a decrease in accuracy due to path loss.

3. AAoMI is highly dependent on classification accuracy when the image generation rate and transmission time are fixed; it is also optimal at an optimal UAV altitude.

4. Transmission power has a significant impact on AAoMI, with a saturation point beyond which increasing power does not contribute to freshness maintenance.
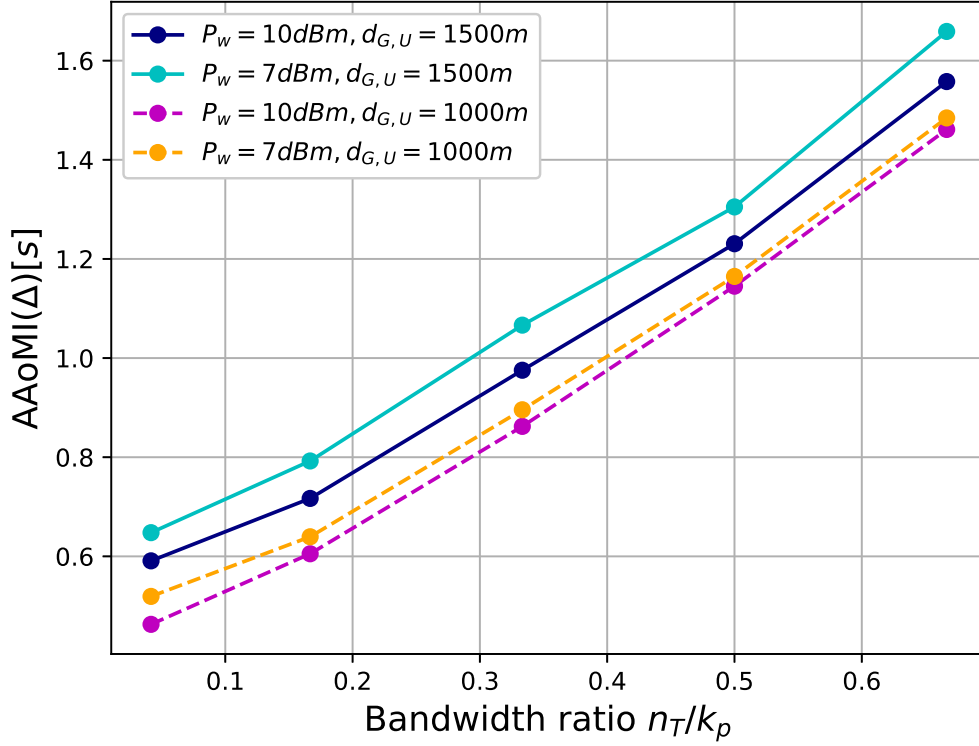
Figure 6.16: AAoMI vs. bandwidth ratio (n_T/k_p) for different transmission power levels at the UAV and different distances between the UAV and GCU.

5. UAV-assisted communication significantly improves information freshness and power efficiency of semantic-based communication systems, especially for low-transmission power scenarios, compared to non-UAV deployment.

6. AAoMI decreases as the image capture rate at the UAV increases since this system does not consider any queue for the transmission while new image updates are cleared by the UAV while it is in the transmission of another image.

7. PSNR for image reconstruction is closely related to average SNR, emphasising the importance of signal quality for image reconstruction.

8. Increasing the bandwidth ratio (n_T/k_p) leads to a rise in the AAoMI indicating that extended transmission time has a stronger influence than gains in classification accuracy.
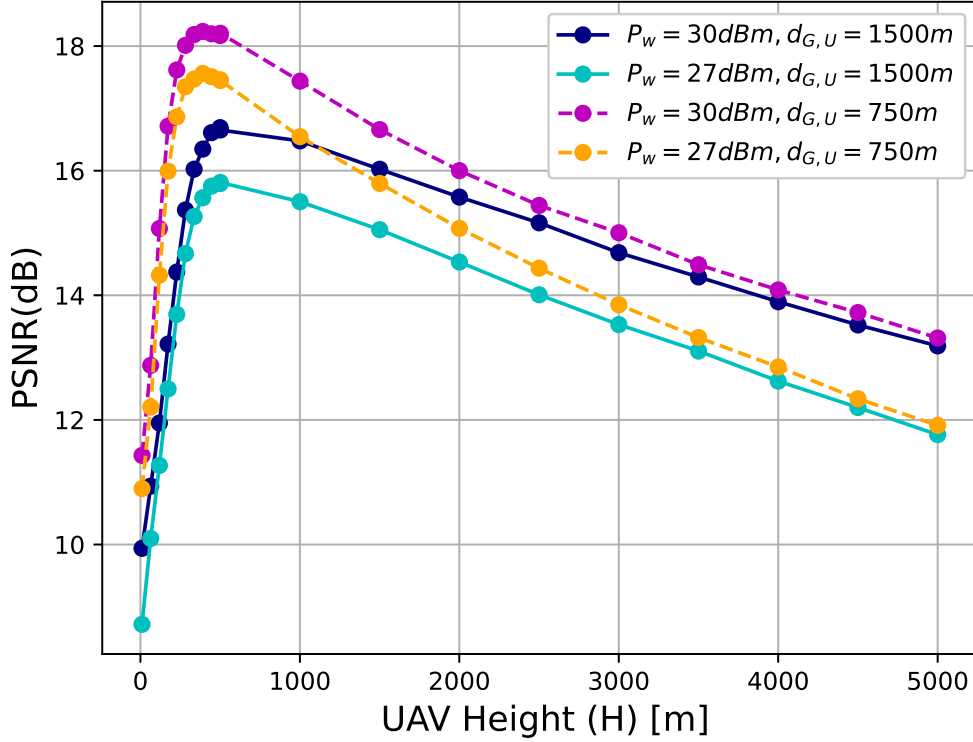
Figure 6.17: PSNR of the image reconstruction process vs. UAV altitude.

6.2.4 Conclusion

This section presented a novel approach to wildfire detection by employing UAV-assisted communication and deep learning-based JSCC. The wireless communication system model introduced in this work effectively extracts and transmits semantic information while minimising the transmission of redundant data to ensure the freshness of the information at the receiver. This pioneering approach significantly improves the accuracy and efficiency of wildfire detection. In addition, the introduction of the AoMI metric and the estimation of the AAoMI through the utilization of an SHS model have allowed us to quantitatively assess the information freshness at the receiver, which is critical for wildfire detection. Our study highlights the substantial advantages of employing UAV-assisted communication, particularly in scenarios with constrained transmission power, in maintaining the freshness of information within the semantic communication system. This research not only contributes to the field of wildfire detection but also underscores the potential of deep learning-based UAV-assisted communication systems to enhance communication in challenging environments, effectively transforming UAV into vigilant "Sky Sentinels."

Publications arising from this Chapter

1. **Basnayaka, C. M. W.**, Jayakody, D. N. K., & Beko, M. (2024). Sky Sentinels: UAV-Powered Semantics Wireless Communications for Dynamic Wildfire Detection. (Revision
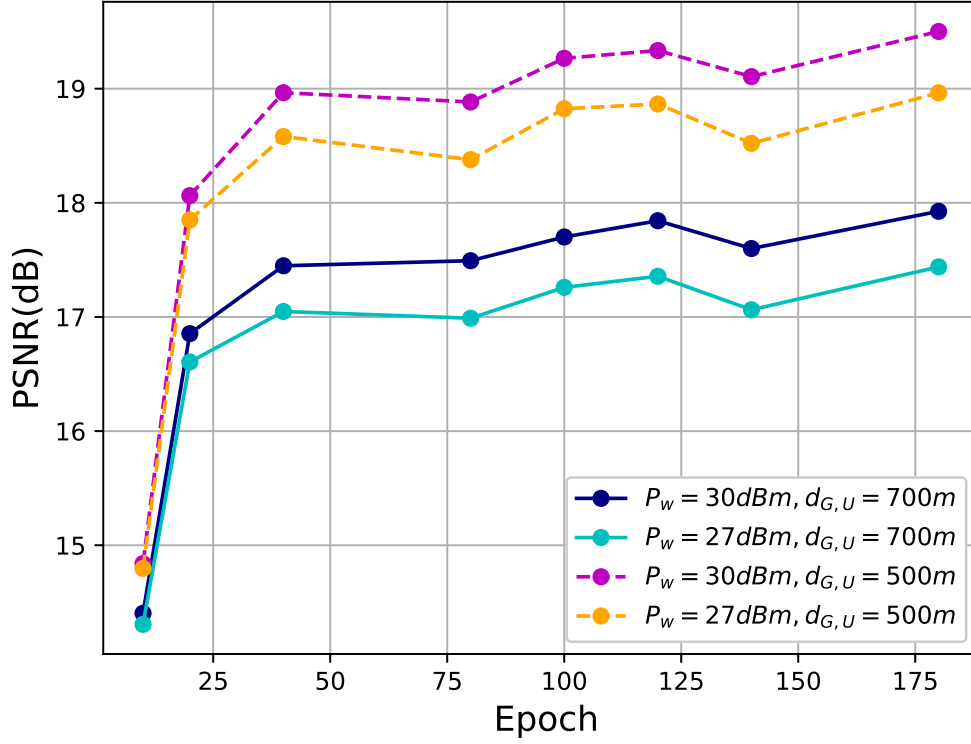
Figure 6.18: PSNR of the image reconstruction process as a function of epoch during the training phase.

stage).

2. [19] **Basnayaka, C. M. W.**, Jayakody, D. N. K., & Beko, M. (2023, November). Semantics-Empowered UAV-assisted Wireless Communication System for Wildfire Detection. In 2023 IEEE 28th International Workshop on Computer Aided Modeling and Design of Communication Links and Networks (CAMAD) (pp. 152-157). IEEE.

3. **Basnayaka, C. M. W.**, Jayakody, D. N. K., & Beko, M. (2024, December). Optimizing Real-Time Freshness: Deep Joint Source–Channel Coding Based AoI in Wireless Networks. In 2024 IEEE Global Communications Conference (GLOBECOM). IEEE. (Accepted)

Chapter 7

Conclusions and Recommendations for Future Studies

7.1 Conclusions

This dissertation analysed AoI in various wireless communication scenarios, focusing on UAV-assisted networks, SWIPT-based communication systems, and DJSCC-based semantic communications. The thesis provides valuable analytical frameworks and insights to guide the design and optimisation of mission-critical wireless networks that prioritise timely information delivery.

The work on URLLC-enabled UAV wireless communications estimated the AoI in URLLC-enabled UAV relay networks. Closed-form expressions were derived for the AAoI in UAV relay networks using finite block length information theory and SHS analysis. One of the significant findings was the existence of an optimal UAV altitude that minimises AAoI by balancing the trade-off between LoS probability and path loss effects of the UAV communication link. The simulation results showed that UAV-assisted relay communication maintains a lower AAoI compared to direct transmission, with the performance gap widening at longer distances. This is due to the ability of the UAV to establish stronger LoS links, particularly in environments with significant obstacles, compared to traditional terrestrial base stations.

As this UAV-assisted communication system operates with transmission errors, SHS analysis was employed to calculate AAoI, since conventional graphical-based analyses fail to analyse such a system. The derived closed-form equations indicate that AAoI depends mainly on the transmission error, transmission time and update generation rate at the source. The integration of short packet communication was crucial to calculate transmission error at the receiver. The analysis incorporated finite block length theory to accurately model the performance of short packet transmissions in UAV-assisted networks, especially when calculating the BLER. This analysis allowed for a more realistic assessment of AoI in scenarios where traditional asymptotic information theory assumptions are invalid. In summary, this work introduces parameters such as an optimal block length that balances transmission errors and latency to minimise AoI, providing important design guidelines for URLLC-enabled UAV communication systems.

For SWIPT-driven wireless communications, AoI in SWIPT-enabled two-way cooperative relay

networks was estimated. This made significant contributions to understanding how the freshness of information affects the complex interplay between EH and information transfer in SWIPT systems. The focus was on estimating the AAoI under two different transmission policies at the relay: TWW and WUC. In the TWW policy, the relay transmits immediately after receiving an update from the source, using the energy harvested during the reception time of the update without waiting. In contrast, in the WUC policy, the relay waits until it reaches sufficient energy before transmitting an update to the destination. A key contribution was the development of an analytical framework that derived closed-form expressions for the weighted sum AAoI at the destinations under both policies. These expressions incorporated factors such as EH efficiency, power splitting ratio, and transmission time. The simulation results showed that TWW outperforms WUC in terms of AAoI when transmission power is low, while WUC achieves better reliability, especially in high-power scenarios. These findings highlight the importance of selecting appropriate transmission policies based on specific application requirements and energy constraints.

In addition, finite block length theory-based analysis was extended to calculate BLER in SWIPT systems, providing a more accurate assessment of system performance under practical constraints. This approach offered valuable insights into the trade-offs between block length, error probability, and AoI. The impact of various factors on AAoI was evaluated, including transmission power, packet size, and block length. This comprehensive study led to the identification of optimal power allocation strategies for minimising AAoI under different channel conditions and transmission policies at the relay.

A framework to estimate AoI in UAV-assisted WSNs, focusing on multi-source scenarios was developed. This made significant contributions to understanding the dynamics of information freshness in complex WSN deployments supported by aerial platforms. It also developed a comprehensive theoretical framework for analysing AoI in these systems, providing valuable insights for the design and optimisation of UAV-assisted WSNs that prioritise timely information delivery.

A key technical contribution was the derivation of closed-form expressions for network AAoI and BLER in multi-source scenarios. These expressions incorporate critical system parameters such as UAV altitude, transmission power, sensor activation probability and channel conditions. The analysis revealed an optimal UAV altitude that minimises network AAoI by balancing the trade-off between LoS probability and path loss effects. This finding provides important guidance for UAV deployment strategies in WSN applications.

This work determined an optimal sensor activation probability that minimises network AAoI, given by the inverse of the number of sensor nodes. This result offers valuable insights for the design of energy-efficient WSNs that maintain information freshness. By optimising the sensor activation probability, the system can achieve a balance between network lifetime and timely data delivery, addressing a critical challenge in WSN deployments.

The analysis was extended to short packet communication scenarios, acknowledging the prevalence of small data payloads in many WSN applications. The study incorporated finite block length theory to accurately model the performance of short packet transmissions in UAV-assisted WSNs. This approach allowed for a more realistic assessment of AoI in scenarios where

traditional asymptotic information theory assumptions do not hold. An optimal block length that balances transmission errors and latency to minimise AoI was identified, providing important design guidelines for WSNs with stringent latency requirements.

A comparative analysis between UAV-assisted WSNs and traditional fixed base station systems was presented. The results demonstrated that UAV-assisted WSNs significantly outperform fixed base station systems in maintaining information freshness, especially in urban environments with complex propagation characteristics. This finding underscores the potential of UAV technology to enhance the performance of WSNs in challenging deployment scenarios.

For semantic communications, a novel content-based AoI metric called AoMI was introduced, addressing the limitations of conventional AoI metrics. The AoMI captured both the timeliness and semantic accuracy of the received information at the destination in a wireless communication system. This metric was designed to estimate the freshness of information in image classification systems, extending beyond the temporal aspects captured by traditional AoI. AoMI considers not only the time elapsed since the generation of an update but also the correctness of the received information.

A DJSCC approach was proposed to minimise AoMI in wireless communication systems. The DJSCC framework employed a deep neural network to map source signals directly to channel inputs, eliminating the need for separate source and channel coding. This end-to-end approach allows for more efficient transmission of semantic information, particularly in challenging channel conditions and low bandwidth scenarios. A detailed analysis of the DJSCC architecture was presented, including the design of the encoder, decoder and classifier components. An SHS model was developed to analyse the AoMI performance of the proposed system. This analytical framework provided insights into the impact of various system parameters on information freshness and classification accuracy. Closed-form expressions for average AoMI were derived, offering a theoretical foundation for optimising the freshness of information in semantic communication systems.

Extensive simulations were conducted to evaluate the AoMI performance of the DJSCC-based system compared to traditional separate source and channel coding schemes. The LDPC code was used as the channel coding baseline, while the BPG code was used as the source coding baseline since both coding schemes are extensively adapted in image transmission in modern wireless communication networks. The results demonstrated that DJSCC outperforms traditional separate source and channel coding schemes, especially at low SNR and bandwidth ratios. This finding highlights the potential of deep learning techniques in enhancing the freshness of the received information in wireless communication systems for time-sensitive and semantically critical applications.

Furthermore, the concepts of AoMI and DJSCC were extended to a practical application by adapting these two concepts to a UAV-based wildfire detection system. The system was designed to ensure accurate and timely transmission of critical information in challenging environments, demonstrating the potential of semantic communication principles in mission-critical applications.

The impact of various factors on AoMI performance was investigated, including UAV altitude, transmission power, image capture rate and channel conditions. These analyses provided insights

into design trade-offs in UAV-assisted semantic communication systems and offered guidelines for optimising system parameters to maintain information freshness in dynamic scenarios.

This thesis has demonstrated the critical role of AoI in ensuring information freshness across diverse wireless communication scenarios, from UAV-assisted networks to semantic communications. Through rigorous theoretical analysis and extensive simulations, the work has provided comprehensive frameworks for optimising information timeliness in mission-critical applications. However, it is important to acknowledge a fundamental limitation identified through this research: the effectiveness of AoI diminishes in systems with low latency, high transmission rates, and high transmission power. In such scenarios, where rapid update delivery naturally minimises delays, the need for detailed AoI optimisation becomes less important. Nevertheless, the research has clearly established the significant value of AoI in resource-constrained environments, particularly those characterised by limited energy, restricted bandwidth, or challenging propagation conditions. Thus, its applicability extends to interdisciplinary fields such as healthcare, industrial automation, and environmental monitoring, where timely data delivery is critical. For example, in UAV-assisted wildfire detection or IoT-driven industrial processes, AoI facilitates timely decision-making by ensuring the availability of fresh and actionable information.

7.2 Recommendations for Future Studies

Based on the findings and insights gained from this thesis, the following key recommendations are proposed for future research in the areas of AoI in wireless communication systems.

For AoI in URLLC-enabled UAV wireless communications, future work should focus on extending AAoI analysis in Chapter 3 to multi-UAV scenarios. This extension will need to address inter-UAV interference and more complex aerial communication network architecture and transmission scheduling between UAVs. In addition, when AAoI is calculated in Chapter 3, it is assumed that perfect CSI is at the receiver. However, as future work, this AAoI analysis can be extended under imperfect CSI at the receiver. To calculate BLER in finite block length transmission with imperfect CSI, analysis in [196] can be adapted since AAoI is a function of the BLER. Furthermore, investigating the AAoI performance under sophisticated UAV trajectory patterns, especially in urban environments with varying LoS probabilities, will provide valuable insights. In addition, in this chapter for the numerical simulations, block error is calculated using approximation used in finite block length information theory; however, it can be compared with practical short packet channel coding such as polar code [197] as further work.

In the domain of AoI estimation in SWIPT-driven wireless communications, Chapter 4 analysed freshness of information in the communication system under two types of transmission policies: TWW and WUC. Future work should focus on hybrid strategies that can switch between these two policies based on instantaneous network conditions and user requirements, whether for low-latency data or low-AoI data. A detailed study into the impact of imperfect CSI on AoI in SWIPT systems is necessary. Furthermore, exploring AoI performance for different models of EH, such as fully nonlinear EH models, will increase the practical applicability of theoretical results, since this chapter focused on the piecewise nonlinear EH model. Moreover, the theoretical AoI analysis in

Chapter 4 considered a single-antenna system; extending this work to multiple-antenna systems will facilitate broader applicability of this analysis. Ref. [198] can be used as a base architecture for this extension. Moreover, this chapter considers a generate-at-will update generation model; however, sometimes the update generation model at the source can be random. As a future study, the proposed model can be redesigned for random update generation models.

For AoI in UAV-assisted WSNs discussed in Chapter 5, future studies must consider the challenges introduced by mobile sensors and their impact on network AAoI. Furthermore, developing sophisticated sensor activation strategies that can jointly optimize energy efficiency and information freshness is critical for practical deployments. Investigating the application of advanced multiple access techniques, such as non-orthogonal multiple access, for improving AoI performance in multi-source scenarios is also recommended. Moreover, the AoI analysis in Chapter 5 limited our analysis to the physical layer parameters. However, the impact of MAC protocols on AoI is still unclear in this system. Thus, future studies can focus on how medium access protocols work with AoI in these types of massive IoT networks. For such studies, system models discussed in [86, 199, 200] can be used as a foundation. In addition, further studies are needed at the implementation level to adapt the proposed model in industrial-level WSNs.

The DJSCC-based semantic communication framework proposed in this thesis for AoI minimization in image transmission shows great promise. Future research should focus on extending AoMI and other content-based AoI metrics to diverse data types, such as text and audio. Investigating more efficient semantic communication systems through advanced deep learning architectures, such as transformers, in DJSCC encoding and decoding is recommended. Furthermore, exploring hybrid transmission models involving both DJSCC and conventional source-channel coding schemes could yield interesting results since DJSCC-based models outperform only for the low SNR levels compared to traditional separate source channel coding schemes.

For the UAV-based wildfire detection system design presented in this thesis, future studies should focus on developing adaptive bandwidth ratio schemes to further optimize AoMI in dynamic channel conditions. Integrating multiple sensor modalities, such as thermal imaging and gas sensors, into the semantic communication framework would enhance the system's capabilities. Investigating how well this proposed system could scale up for large-scale environmental monitoring applications, considering factors such as coordination between UAV swarms and distributed semantic processing, is also crucial.

Across all areas of wireless communication, developing unified analytical frameworks that can combine traditional timeliness metrics such as latency with semantic-aware AoI-based freshness measures is recommended. In addition, developing a complete cross-layer optimization framework that considers physical layer parameters and MAC protocols to minimize AoI in these semantic communication networks is also proposed. This could provide valuable insights into the complex interplay between different network layers and their impact on information freshness.

The application of machine learning techniques, particularly reinforcement learning, in developing adaptive transmission policies for AoI minimization in dynamic UAV-assisted networks is a promising research direction. These learning-based methods may outperform traditional optimization techniques under highly uncertain and time-varying channel conditions.

Furthermore, all of the semantic communication systems described in Chapter 6, particularly DJSCC-based systems, are incompatible with the existing digital communication infrastructure. To support real-world applications and information freshness, further studies are necessary to ensure their compatibility with current digital hardware. Furthermore, the proposal for semantic communication in wireless communication systems lacks a comprehensive theoretical foundation. To properly design semantic-aware AoI metrics, future research should aim to develop a unified semantic-aware channel capacity for the various communication contexts.

The research community can further enhance the AoI-aware state-of-the-art in wireless communication systems by using the theoretical bases and analytic frameworks outlined in this thesis, as well as following the recommendations in this chapter. This will contribute to the development of future wireless networks that prioritise information timeliness and semantic relevance for a variety of mission-critical applications in a highly interconnected world.

Bibliography

[1] L. Romeo et al. "Internet of robotic things in smart domains: Applications and challenges". In: *Sensors* 20.12 (2020), p. 3355 (cit. on pp. 1, 9).

[2] J. Shi et al. "A survey of cyber-physical systems". In: *2011 Int. Conf. Wirel. Commun. Signal Process. Netw. (WCSP)*. IEEE. 2011, pp. 1–6 (cit. on pp. 1, 9).

[3] S. Shue and J. M. Conrad. "A survey of robotic applications in wireless sensor networks". In: *2013 Proc. IEEE Southeastcon*. IEEE. 2013, pp. 1–5 (cit. on pp. 1, 9).

[4] R. D. Yates et al. "Age of information: An introduction and survey". In: *IEEE J. Sel. Areas Commun.* 39.5 (2021), pp. 1183–1210 (cit. on pp. 1, 2, 9, 10, 12).

[5] Y. Sun et al. "Update or wait: How to keep your data fresh". In: *IEEE Trans. Inf. Theory* 63.11 (2017), pp. 7492–7508 (cit. on pp. 1, 2, 9).

[6] C. M. W. Basnayaka, D. N. K. Jayakody, and M. Beko. "Freshness-in-air: An AoI-inspired UAV-assisted wireless sensor networks". In: *ICT Express* 10.5 (2024), pp. 1103–1109 (cit. on pp. 1, 6, 77).

[7] L. Zhang and Y.-C. Liang. "Average throughput analysis and optimization in cooperative IoT networks with short packet communication". In: *IEEE Trans. Veh. Technol.* 67.12 (2018), pp. 11549–11562 (cit. on pp. 1, 16, 17).

[8] T. D. P. Perera et al. "Simultaneous wireless information and power transfer (SWIPT): Recent advances and future challenges". In: *IEEE Commun. Surv. Tutor.* 20.1 (2017), pp. 264–302 (cit. on pp. 1, 19, 44).

[9] R. Jiang et al. "Outage performance of SWIPT-enabled two-way relay networks". In: *Proc. IEEE Int. Workshop High Mobility Wireless Commun.* 2015, pp. 106–110 (cit. on pp. 1, 19).

[10] A. A. Nasir et al. "Relaying protocols for wireless energy harvesting and information processing". In: *IEEE Trans. Wirel. Commun.* 12.7 (2013), pp. 3622–3636 (cit. on pp. 1, 19, 20, 46).

[11] A. A. Laghari et al. "Unmanned aerial vehicles: A review". In: *Cogn. Robot.* 3 (2023), pp. 8–22. ISSN: 2667-2413. DOI: https://doi.org/10.1016/j.cogr.2022.12.004 (cit. on pp. 1, 15, 16).

[12] H. Nawaz, H. M. Ali, and A. A. Laghari. "UAV communication networks issues: A review". In: *Arch. Comput. Methods Eng.* 28.3 (2021), pp. 1349–1369 (cit. on pp. 1, 15, 16).

[13] A. A. Khan et al. "A drone-based data management and optimization using metaheuristic algorithms and blockchain smart contracts in a secure fog environment". In: *Comput. Electr. Eng.* 102.C (2022-09). ISSN: 0045-7906. DOI: 10.1016/j.compeleceng.2022.108234 (cit. on pp. 1, 15, 16).

[14] C. M. W. Basnayaka, D. N. K. Jayakody, and Z. Chang. "Age of Information Based URLLC-enabled UAV Wireless Communications System". In: *IEEE Internet Things J.* (2021) (cit. on pp. 6, 9, 16, 40, 60, 69, 71, 72).

[15] C. M. W. Basnayaka et al. "DataAge: Age of Information in SWIPT-Driven Short Packet IoT Wireless Communications". In: *IEEE Internet of Things Journal* 11.16 (2024), pp. 26984–26999. DOI: 10.1109/JIOT.2024.3397032 (cit. on pp. 6, 9, 64).

[16] A. Sharma et al. "Communication and networking technologies for UAVs: A survey". In: *J. Netw. Comput. Appl.* (2020), p. 102739 (cit. on pp. 7, 15, 17, 22).

[17] A. Sharma et al. "Recent Trends in AI-Based Intelligent Sensing". In: *Electronics* 11.10 (2022). ISSN: 2079-9292. DOI: 10.3390/electronics11101661. URL: https://www.mdpi.com/2079-9292/11/10/1661 (cit. on pp. 7, 91).

[18] C. M. Wijerathna Basnayaka et al. "Age of Information in an URLLC-enabled Decode-and-Forward Wireless Communication System". In: *IEEE Veh. Technol. Conf. (VTC2021-Spring)*. 2021, pp. 1–6. DOI: 10.1109/VTC2021-Spring51267.2021.9449007 (cit. on pp. 7, 25, 40, 107).

[19] C. M. Wijerathna Basnayaka, D. N. K. Jayakody, and M. Beko. "Semantics-Empowered UAV-assisted Wireless Communication System for Wildfire Detection". In: *Proc. IEEE Int. Workshop Comput. Aided Model. Des. Commun. Links Netw.* 2023 (cit. on pp. 7, 22, 112).

[20] C. M. W. Basnayaka et al. "Age of Information in a SWIPT and URLLC enabled Wireless Communications System". In: *Proc. IEEE Int. Conf. Adv. Netw. and Tele. Syst.* 2022, pp. 1–6 (cit. on pp. 7, 9, 20, 65).

[21] P. M. P. Payagalage et al. "Network Virtualization and Slicing in UAV-enabled Future Networks". In: *Proc. Conf. Cloud Internet Things (CIoT)*. 2023, pp. 98–103. DOI: 10.1109/CIoT57267.2023.10084908 (cit. on pp. 7, 14).

[22] S. Liyanaarachchi and S. Ulukus. "The Role of Early Sampling in Age of Information Minimization in the Presence of ACK Delays". In: *IEEE Trans. Inf. Theory* (2024), pp. 1–1. DOI: 10.1109/TIT.2024.3394321 (cit. on p. 9).

[23] S. Kaul et al. "Minimizing age of information in vehicular networks". In: *Proc. IEEE Int. Conf. Sensor, Mesh Ad Hoc Commun. Netw.* 2011, pp. 350–358. DOI: 10.1109/SAHCN.2011.5984917 (cit. on p. 9).

[24] I. Kadota, A. Sinha, and E. Modiano. "Optimizing Age of Information in Wireless Networks with Throughput Constraints". In: *Proc. IEEE Int. Conf. Comput. Commun. (INFOCOM)*. 2018, pp. 1844–1852. DOI: `10.1109/INFOCOM.2018.8486307` (cit. on p. 9).

[25] T. D. P. Perera et al. "Age of Information in SWIPT-Enabled Wireless Communication System for 5GB". In: *IEEE Wirel. Commun.* 27.5 (2020), pp. 162–167 (cit. on pp. 9, 16, 20–22).

[26] O. T. Yavascan and E. Uysal. "Analysis of slotted aloha with an age threshold". In: *IEEE J. Sel. Areas Commun.* 39.5 (2021), pp. 1456–1470 (cit. on p. 9).

[27] I. Kadota et al. "Scheduling policies for minimizing age of information in broadcast wireless networks". In: *IEEE ACM Trans. Netw.* 26.6 (2018), pp. 2637–2650 (cit. on p. 9).

[28] L. Hu et al. "Status Update in IoT Networks: Age-of-Information Violation Probability and Optimal Update Rate". In: *IEEE Internet of Things J.* 8.14 (2021), pp. 11329–11344. DOI: `10.1109/JIOT.2021.3051722` (cit. on p. 9).

[29] A. Kosta, N. Pappas, V. Angelakis, et al. "Age of information: A new concept, metric, and tool". In: *Found. Trends Netw.* 12.3 (2017), pp. 162–259 (cit. on pp. 11, 23, 32).

[30] R. D. Yates. "The age of information in networks: Moments, distributions, and sampling". In: *IEEE Trans. Inf. Theory* 66.9 (2020), pp. 5712–5728 (cit. on p. 12).

[31] R. Talak and E. Modiano. "Age-delay tradeoffs in single server systems". In: *Proc. IEEE Int. Symp. Inf. Theory (ISIT)*. IEEE. 2019, pp. 340–344 (cit. on p. 12).

[32] S. Kaul, R. Yates, and M. Gruteser. "Real-time status: How often should one update?" In: *Proc. IEEE Int. Conf. Comput. Commun. (INFOCOM)*. IEEE. 2012, pp. 2731–2735 (cit. on p. 12).

[33] S. K. Kaul, R. D. Yates, and M. Gruteser. "Status updates through queues". In: *Proc. Annu. Conf. Inf. Sci. Syst. (CISS)*. IEEE. 2012, pp. 1–6 (cit. on p. 12).

[34] L. Huang and E. Modiano. "Optimizing age-of-information in a multi-class queueing system". In: *Proc. IEEE Int. Symp. Inf. Theory (ISIT)*. IEEE. 2015, pp. 1681–1685 (cit. on p. 12).

[35] A. M. Bedewy, Y. Sun, and N. B. Shroff. "Optimizing data freshness, throughput, and delay in multi-server information-update systems". In: *Proc. IEEE Int. Symp. Inf. Theory (ISIT)*. 2016, pp. 2569–2573. DOI: `10.1109/ISIT.2016.7541763` (cit. on p. 12).

[36] E. Najm and E. Telatar. "Status updates in a multi-stream M/G/1/1 preemptive queue". In: *Proc. IEEE Conf. Comput. Commun. Workshops*. IEEE. 2018, pp. 124–129 (cit. on p. 12).

[37] A. Soysal and S. Ulukus. "Age of Information in G/G/1/1 Systems: Age Expressions, Bounds, Special Cases, and Optimization". In: *IEEE Trans. Inf. Theory* 67.11 (2021), pp. 7477–7489. DOI: `10.1109/TIT.2021.3095823` (cit. on p. 12).

[38] J. P. Champati, H. Al-Zubaidy, and J. Gross. "On the Distribution of AoI for the GI/GI/1/1 and GI/GI/1/2 Systems: Exact Expressions and Bounds". In: *Proc. IEEE Conf. Comput. Commun. (INFOCOM)*. 2019, pp. 37–45. DOI: `10.1109/INFOCOM.2019.8737474` (cit. on p. 12).

[39] Y. Sun et al. *Age of information: A new metric for information freshness*. Springer Nature, 2022 (cit. on p. 12).

[40] M. Costa, M. Codreanu, and A. Ephremides. "Age of information with packet management". In: *Proc. IEEE Int. Symp. Inf. Theory (ISIT)*. 2014, pp. 1583–1587. DOI: `10.1109/ISIT.2014.6875100` (cit. on p. 12).

[41] N. Pappas et al. "Age of information of multiple sources with queue management". In: *Proc. IEEE Int. Conf. Commun. (ICC)*. 2015, pp. 5935–5940. DOI: `10.1109/ICC.2015.7249268` (cit. on p. 12).

[42] C. Kam et al. "Controlling the age of information: Buffer size, deadline, and packet replacement". In: *Proc. IEEE Mil. Commun. Conf. (MILCOM)*. 2016, pp. 301–306. DOI: `10.1109/MILCOM.2016.7795343` (cit. on p. 12).

[43] A. M. Bedewy, Y. Sun, and N. B. Shroff. "The Age of Information in Multihop Networks". In: *IEEE/ACM Trans. Netw.* 27.3 (2019), pp. 1248–1257. DOI: `10.1109/TNET.2019.2915521` (cit. on p. 12).

[44] C. Kam et al. "Effect of Message Transmission Path Diversity on Status Age". In: *IEEE Trans. Inf. Theory* 62.3 (2016), pp. 1360–1374. DOI: `10.1109/TIT.2015.2511791` (cit. on p. 12).

[45] M. Costa, M. Codreanu, and A. Ephremides. "Age of information with packet management". In: *Proc. IEEE Int. Symp. Inf. Theory (ISIT)*. IEEE. 2014, pp. 1583–1587 (cit. on p. 12).

[46] K. Chen and L. Huang. "Age-of-information in the presence of error". In: *Proc. IEEE Int. Symp. Inf. Theory (ISIT)*. 2016, pp. 2579–2583. DOI: `10.1109/ISIT.2016.7541765` (cit. on p. 12).

[47] S. S. Raikar and R. Bhat. "Optimizing Reported Age of Information with Short Error Correction and Detection Codes". In: *Proc. IEEE Wirel. Commun. Netw. Conf. (WCNC)*. 2024, pp. 1–6. DOI: `10.1109/WCNC57260.2024.10570652` (cit. on p. 12).

[48] R. Talak, S. Karaman, and E. Modiano. "When a Heavy Tailed Service Minimizes Age of Information". In: *Proc. IEEE Int. Symp. Inf. Theory (ISIT)*. 2019, pp. 345–349. DOI: `10.1109/ISIT.2019.8849697` (cit. on p. 12).

[49] A. O. Al-Abbasi et al. "On the Information Freshness and Tail Latency Trade-Off in Mobile Networks". In: *Proc. IEEE Global Commun. Conf. (GLOBECOM)*. 2019, pp. 1–6. DOI: `10.1109/GLOBECOM38437.2019.9013174` (cit. on p. 12).

[50] S. K. Kaul and R. D. Yates. "Age of Information: Updates with Priority". In: *Proc. IEEE Int. Symp. Inf. Theory (ISIT)*. 2018, pp. 2644–2648. DOI: `10.1109/ISIT.2018.8437591` (cit. on p. 12).

[51] Y. Inoue et al. "A general formula for the stationary distribution of the age of information and its application to single-server queues". In: *IEEE Trans. Inf. Theory* 65.12 (2019), pp. 8305–8324 (cit. on p. 12).

[52] S. Farazi, A. G. Klein, and D. R. Brown. "Average age of information in multi-source self-preemptive status update systems with packet delivery errors". In: *Conf. Rec. Asilomar Conf. Signals Syst. Comput.* IEEE. 2019, pp. 396–400 (cit. on p. 12).

[53] Z. Chen et al. "Age of Information of a Dual Queue Status Update System: A Stochastic Hybrid Systems Method". In: *IEEE Commun. Lett.* 27.7 (2023), pp. 1714–1718. DOI: `10.1109/LCOMM.2023.3274348` (cit. on p. 12).

[54] S. Farazi, A. G. Klein, and D. R. Brown. "Average Age of Information in Update Systems With Active Sources and Packet Delivery Errors". In: *IEEE Wirel. Commun. Lett.* 9.8 (2020), pp. 1164–1168. DOI: `10.1109/LWC.2020.2983397` (cit. on p. 12).

[55] R. D. Yates and S. K. Kaul. "The age of information: Real-time status updating by multiple sources". In: *IEEE Trans. Inf. Theory* 65.3 (2018), pp. 1807–1827 (cit. on pp. 12, 14, 25, 32, 100).

[56] M. Moltafet, M. Leinonen, and M. Codreanu. "Average AoI in multi-source systems with source-aware packet management". In: *IEEE Trans. Commun* 69.2 (2020), pp. 1121–1133 (cit. on p. 12).

[57] S. K. Kaul and R. D. Yates. "Age of information: Updates with priority". In: *Proc. IEEE Int. Symp. Inf. Theory (ISIT)*. IEEE. 2018, pp. 2644–2648 (cit. on p. 12).

[58] A. Maatouk, M. Assaad, and A. Ephremides. "Age-Aware Stochastic Hybrid Systems: Stability, Solutions, and Applications". In: *arXiv preprint arXiv:2109.03919* (2021) (cit. on p. 12).

[59] R. D. Yates and S. K. Kaul. "Age of Information in Uncoordinated Unslotted Updating". In: *Proc. IEEE Int. Symp. Inf. Theory*. 2020, pp. 1759–1764. DOI: `10.1109/ISIT44484.2020.9174098` (cit. on p. 12).

[60] A. Maatouk, M. Assaad, and A. Ephremides. "Analysis of an Age-Dependent Stochastic Hybrid System". In: *Proc. IEEE Int. Symp. Inf. Theory*. 2022, pp. 150–155. DOI: `10.1109/ISIT50566.2022.9834502` (cit. on p. 12).

[61] R. D. Yates and S. K. Kaul. "Timely updates by multiple sources: The M/M/1 queue revisited". In: *Proc. Annu. Conf. Inf. Sci. Syst. (CISS)*. IEEE. 2020, pp. 1–6 (cit. on pp. 14, 100).

[62] A. Fouda et al. "UAV-Based in-band Integrated Access and Backhaul for 5G Communications". In: *Proc. IEEE Veh. Technol. Conf. (VTC-Fall)*. IEEE. 2018, pp. 1–5 (cit. on p. 14).

[63] M. Mozaffari et al. "Mobile unmanned aerial vehicles (UAVs) for energy-efficient Internet of Things communications". In: *IEEE Trans. Wirel. Commun.* 16.11 (2017), pp. 7574–7589 (cit. on p. 14).

[64] M. Chen et al. "Caching in the sky: Proactive deployment of cache-enabled unmanned aerial vehicles for optimized quality-of-experience". In: *IEEE J. Sel. Areas Commun.* 35.5 (2017), pp. 1046–1061 (cit. on p. 14).

[65] M. Wzorek, D. Landén, and P. Doherty. "GSM technology as a communication media for an autonomous unmanned aerial vehicle". In: *Proc. Int. Conf. UAV Syst.* Citeseer. 2006 (cit. on p. 14).

[66] Y. Zeng, J. Lyu, and R. Zhang. "Cellular-connected UAV: Potential, challenges, and promising technologies". In: *IEEE Wirel. Commun.* 26.1 (2018), pp. 120–127 (cit. on p. 14).

[67] G. Yang et al. "A telecom perspective on the Internet of drones: From LTE-advanced to 5G". In: *arXiv preprint arXiv:1803.11048* (2018) (cit. on p. 14).

[68] S. D. Muruganathan et al. "An Overview of 3GPP Release-15 Study on Enhanced LTE Support for Connected Drones". In: *IEEE Commun. Stand. Mag.* 5.4 (2021), pp. 140–146. DOI: 10.1109/MCOMSTD.0001.1900021 (cit. on p. 14).

[69] J. Korhonen. *Enhanced LTE support for aerial vehicles*. Tech. rep. 3rd Generation Partnership Project (3GPP), 2018, pp. 1–89. URL: https://www.3gpp.org/ftp/Specs/archive/36_series/36.777/ (cit. on p. 15).

[70] P. S. Bithas et al. "UAV-to-Ground communications: Channel modeling and UAV selection". In: *IEEE Trans. Commun.* 68.8 (2020), pp. 5135–5144 (cit. on p. 15).

[71] L. Sboui et al. "Achievable rates of UAV-relayed cooperative cognitive radio MIMO systems". In: *IEEE Access* 5 (2017), pp. 5190–5204 (cit. on p. 15).

[72] H. Wang et al. "Secure Short-Packet Communications for Mission-Critical IoT Applications". In: *IEEE Trans. Wirel. Commun.* 18.5 (2019), pp. 2565–2578. DOI: 10.1109/TWC.2019.2904968 (cit. on p. 15).

[73] M. A. Abd-Elmagid and H. S. Dhillon. "Average peak age-of-information minimization in UAV-assisted IoT networks". In: *IEEE Trans. Veh. Technol.* 68.2 (2018), pp. 2003–2008 (cit. on p. 15).

[74] C. Mao, J. Liu, and L. Xie. "Multi-UAV Aided Data Collection for Age Minimization in Wireless Sensor Networks". In: *Proc. Int. Conf. Wirel. Commun. Signal Process. (WCSP).* IEEE. 2020, pp. 80–85 (cit. on p. 15).

[75] J. Liu et al. "Age-optimal trajectory planning for UAV-assisted data collection". In: *IEEE Conf. Comput. Commun. Workshops (INFOCOM WKSHPS).* IEEE. 2018, pp. 553–558 (cit. on p. 15).

[76] G. Ahani, D. Yuan, and Y. Zhao. "Age-optimal UAV scheduling for data collection with battery recharging". In: *IEEE Commun. Lett.* 25.4 (2020), pp. 1254–1258 (cit. on p. 15).

[77] A. Ranjha and G. Kaddoum. "URLLC facilitated by mobile UAV relay and RIS: A joint design of passive beamforming, blocklength, and UAV positioning". In: *IEEE Internet Things J.* 8.6 (2020), pp. 4618–4627 (cit. on p. 15).

[78] B. Yu, X. Guan, and Y. Cai. "Joint Blocklength and Power Optimization for Half Duplex Unmanned Aerial Vehicle Relay System with Short Packet Communications". In: *Proc. Int. Conf. Wirel. Commun. Signal Process. (WCSP)*. IEEE. 2020, pp. 981–986 (cit. on p. 15).

[79] C. She et al. "UAV-assisted uplink transmission for ultra-reliable and low-latency communications". In: *Proc. IEEE Int. Conf. Commun. Workshops (ICC Workshops)*. IEEE. 2018, pp. 1–6 (cit. on p. 15).

[80] K. Wang et al. "Packet error probability and effective throughput for ultra-reliable and low-latency UAV communications". In: *IEEE Trans. Commun.* 69.1 (2020), pp. 73–84 (cit. on p. 15).

[81] H. Ren et al. "Joint transmit power and placement optimization for URLLC-enabled UAV relay systems". In: *IEEE Trans. Veh. Technol.* 69.7 (2020), pp. 8003–8007 (cit. on p. 15).

[82] J. Wang et al. "Age of Information Based URLLC Transmission for UAVs on Pylon Turn". In: *IEEE Trans. Veh. Technol.* (2024), pp. 1–14. DOI: `10.1109/TVT.2024.3358844` (cit. on p. 16).

[83] X. Gao, X. Zhu, and L. Zhai. "AoI-Sensitive Data Collection in Multi-UAV-Assisted Wireless Sensor Networks". In: *IEEE Trans. Wirel. Commun.* (2023), pp. 1–1. DOI: `10.1109/TWC.2022.3232366` (cit. on p. 16).

[84] Y. Emami et al. "Age of Information Minimization using Multi-agent UAVs based on AI-Enhanced Mean Field Resource Allocation". In: *IEEE Trans. Veh. Technol.* (2024), pp. 1–14. DOI: `10.1109/TVT.2024.3394235` (cit. on p. 16).

[85] X. Zhang, J. Wang, and H. V. Poor. "AoI-Driven Statistical Delay and Error-Rate Bounded QoS Provisioning for mURLLC Over UAV-Multimedia 6G Mobile Networks Using FBC". In: *IEEE J. Sel. Areas Commun.* 39.11 (2021), pp. 3425–3443. DOI: `10.1109/JSAC.2021.3088625` (cit. on p. 16).

[86] A. Munari. "Modern Random Access: An Age of Information Perspective on Irregular Repetition Slotted ALOHA". In: *IEEE Trans. Commun.* 69.6 (2021), pp. 3572–3585. DOI: `10.1109/TCOMM.2021.3060429` (cit. on pp. 16, 117).

[87] T. N. Weerasinghe, I. A. Balapuwaduge, and F. Y. Li. "Priority-based initial access for URLLC traffic in massive IoT networks: Schemes and performance analysis". In: *Comput. Netw.* 178 (2020), p. 107360 (cit. on pp. 16, 24).

[88] C. Feng and H.-M. Wang. "Secure Short-Packet Communications at the Physical Layer for 5G and Beyond". In: *IEEE Commun. Mag.* 5.3 (2021), pp. 96–102 (cit. on p. 16).

[89] G. Durisi et al. "Short-packet communications over multiple-antenna Rayleigh-fading channels". In: *IEEE Trans. Commun.* 64.2 (2015), pp. 618–629 (cit. on pp. 16, 17, 71).

[90] Y. Polyanskiy, H. V. Poor, and S. Verdu. "Channel Coding Rate in the Finite Blocklength Regime". In: *IEEE Trans. Inf. Theory* 56.5 (2010), pp. 2307–2359. DOI: `10.1109/TIT.2010.2043769` (cit. on pp. 17, 18, 29, 48, 59, 61).

[91] J. Östman et al. "URLLC with Massive MIMO: Analysis and Design at Finite Blocklength". In: *IEEE Trans. Wirel. Commun* (2021) (cit. on p. 17).

[92] C. M. W. Basnayaka et al. "Age of Information in an URLLC-enabled Decode-and-Forward Wireless Communication System". In: *2021 IEEE 93rd Veh. Technol. Conf.(VTC2021-Spring)*. IEEE. 2021, pp. 1–6 (cit. on pp. 17, 46).

[93] C. K. Kourtellaris, C. Psomas, and I. Krikidis. "Finite Blocklength Analysis of Multiple Access Channels With/Without Cooperation". In: *IEEE Trans. Commun.* 68.10 (2020), pp. 6317–6330 (cit. on p. 17).

[94] Y. Gu et al. "Ultra-reliable short-packet communications: Half-duplex or full-duplex relaying?" In: *IEEE Wirel. Commun.* 7.3 (2017), pp. 348–351 (cit. on pp. 17, 30, 31, 48, 62, 63, 71).

[95] G. Durisi, T. Koch, and P. Popovski. "Toward massive, ultrareliable, and low-latency wireless communication with short packets". In: *Proc. of the IEEE* 104.9 (2016), pp. 1711–1726 (cit. on pp. 17, 18).

[96] B. Makki, T. Svensson, and M. Zorzi. "Wireless energy and information transmission using feedback: Infinite and finite block-length analysis". In: *IEEE Trans. Commun.* 64.12 (2016), pp. 5304–5318 (cit. on p. 17).

[97] S. Schiessl. "Performance trade-offs for ultra-reliable low-latency communication systems". PhD thesis. KTH Royal Institute of Technology, 2019 (cit. on pp. 18, 19).

[98] W. Yang et al. "Quasi-Static Multiple-Antenna Fading Channels at Finite Blocklength". In: *IEEE Trans. Inf. Theory* 60.7 (2014), pp. 4232–4265. DOI: `10.1109/TIT.2014.2318726` (cit. on p. 19).

[99] Z. Tang et al. "The Age of Information of Short-Packet Communications: Joint or Distributed Encoding?" In: *Proc. IEEE Int. Conf. Commun. (ICC)*. 2022, pp. 2175–2180. DOI: `10.1109/ICC45855.2022.9838286` (cit. on p. 19).

[100] R. Wang et al. "On the Age of Information of Short-Packet Communications with Packet Management". In: *Proc. IEEE Global Commun. Conf. (GLOBECOM)*. 2019, pp. 1–6. DOI: `10.1109/GLOBECOM38437.2019.9014267` (cit. on p. 19).

[101] W. Yang et al. "Age of Information for Short-Packet Covert Communication". In: *IEEE Wirel. Commun. Lett.* 10.9 (2021), pp. 1890–1894. DOI: `10.1109/LWC.2021.3085025` (cit. on p. 19).

[102] B. Yu et al. "Average Age of Information in Short Packet Based Machine Type Communication". In: *IEEE Trans. Veh. Technol.* 69.9 (2020), pp. 10306–10319. DOI: `10.1109/TVT.2020.3004828` (cit. on p. 19).

[103] J. Cao et al. "Information Age-Delay Correlation and Optimization With Finite Block Length". In: *IEEE Trans. Commun.* 69.11 (2021), pp. 7236–7250. DOI: `10.1109/TCOMM.2021.3102624` (cit. on p. 19).

[104] Z. Wei et al. "Resource Allocation for Simultaneous Wireless Information and Power Transfer Systems: A Tutorial Overview". In: *Proc. of the IEEE* 110.1 (2022), pp. 127–149. DOI: 10.1109/JPROC.2021.3120888 (cit. on p. 19).

[105] D. N. K. Jayakody et al. *Wireless information and power transfer: A new paradigm for green communications*. Springer, 2017 (cit. on p. 19).

[106] A. Rajaram et al. "Novel SWIPT schemes for 5G wireless networks". In: *Sensors* 19.5 (2019), p. 1169 (cit. on p. 20).

[107] D. Wang et al. "Capacity-Enhancing Full-Duplex Relay Networks based on Power-Splitting (PS-)SWIPT". In: *IEEE Trans. Veh. Technol.* 66.6 (2017), pp. 5445–5450. DOI: 10.1109 /TVT.2016.2616147 (cit. on p. 20).

[108] A. Rajaram et al. "Opportunistic-Harvesting: RF Wireless Power Transfer Scheme for Multiple Access Relays System". In: *IEEE Access* 5 (2017), pp. 16084–16099. DOI: 10.1109/ACCESS.2017.2734852 (cit. on p. 20).

[109] A. Rajaram et al. "Optimum Performance Analysis and Receiver Design for OFDM-Based Frequency-Splitting SWIPT With Strong Nonlinear Effects". In: *IEEE Internet of Things J.* 10.23 (2023), pp. 20928–20940. DOI: 10.1109/JIOT.2023.3284350 (cit. on p. 20).

[110] P. Popovski, A. M. Fouladgar, and O. Simeone. "Interactive Joint Transfer of Energy and Information". In: *IEEE Trans. Commun.* 61.5 (2013), pp. 2086–2097. DOI: 10.1109 /TCOMM.2013.031213.120723 (cit. on p. 20).

[111] Q. Li, Q. Zhang, and J. Qin. "Beamforming in Non-Regenerative Two-Way Multi-Antenna Relay Networks for Simultaneous Wireless Information and Power Transfer". In: *IEEE Trans. Wirel. Commun.* 13.10 (2014), pp. 5509–5520. DOI: 10.1109/TWC.2014.23217 63 (cit. on p. 20).

[112] T. N. Nguyen et al. "Security–Reliability Tradeoff Analysis for SWIPT- and AF-Based IoT Networks With Friendly Jammers". In: *IEEE Internet of Things J.* 9.21 (2022), pp. 21662–21675. DOI: 10.1109/JIOT.2022.3182755 (cit. on p. 20).

[113] P. Liu et al. "Energy Harvesting Noncoherent Cooperative Communications". In: *IEEE Trans. on Wirel. Commun.* 14.12 (2015), pp. 6722–6737. DOI: 10.1109/TWC.2015.245 8969 (cit. on p. 20).

[114] I.-M. Kim, D. I. Kim, and J.-M. Kang. "Rate-Energy Tradeoff and Decoding Error Probability-Energy Tradeoff for SWIPT in Finite Code Length". In: *IEEE Trans. on Wirel. Commun.* 16.12 (2017), pp. 8220–8234. DOI: 10.1109/TWC.2017.2759200 (cit. on p. 20).

[115] Y. Khorsandmanesh, M. J. Emadi, and I. Krikidis. "Average Peak Age of Information Analysis for Wireless Powered Cooperative Networks". In: *IEEE Trans. Cogn. Commun. Netw.* 7.4 (2021), pp. 1291–1303. DOI: 10.1109/TCCN.2021.3085593 (cit. on p. 21).

[116] Y. Zheng, J. Hu, and K. Yang. "Average Age of Information in Wireless Powered Relay Aided Communication Network". In: *IEEE Internet of Things J.* (2021), pp. 1–1. DOI: 10.1109/JIOT.2021.3128358 (cit. on p. 21).

[117] R. Devassy et al. "Reliable Transmission of Short Packets Through Queues and Noisy Channels Under Latency and Peak-Age Violation Guarantees". In: *IEEE J. Sel. Areas Commun.* 37.4 (2019), pp. 721–734. DOI: 10.1109/JSAC.2019.2898760 (cit. on p. 21).

[118] R. Devassy et al. "Delay and Peak-Age Violation Probability in Short-Packet Transmissions". In: *Proc. IEEE Int. Symp. Inf. Theory (ISIT)*. 2018, pp. 2471–2475. DOI: 10.1109/ISIT.2018.8437671 (cit. on p. 21).

[119] D. Kumar et al. "Latency-Aware Multi-Antenna SWIPT System With Battery-Constrained Receivers". In: *IEEE Trans. Wirel. Commun.* 22.5 (2023), pp. 3022–3037. DOI: 10.1109/TWC.2022.3215864 (cit. on p. 21).

[120] W. Lyu et al. "Optimizing the Age of Information in RIS-Aided SWIPT Networks". In: *IEEE Trans. Veh. Technol.* 72.2 (2023), pp. 2615–2619. DOI: 10.1109/TVT.2022.3208612 (cit. on p. 21).

[121] I. Krikidis. "Average age of information in wireless powered sensor networks". In: *IEEE Wirel. Commun. Lett.* 8.2 (2019), pp. 628–631 (cit. on p. 21).

[122] M. A. Abd-Elmagid, H. S. Dhillon, and N. Pappas. "A reinforcement learning framework for optimizing age of information in RF-powered communication systems". In: *IEEE Trans. Commun.* 68.8 (2020), pp. 4747–4760 (cit. on p. 21).

[123] Y. Hu et al. "SWIPT-enabled relaying in IoT networks operating with finite blocklength codes". In: *IEEE J. Sel. Areas Commun.* 37.1 (2018), pp. 74–88 (cit. on p. 21).

[124] A. Agarwal, A. K. Jagannatham, and L. Hanzo. "Finite Blocklength Non-Orthogonal Cooperative Communication Relying on SWIPT-Enabled Energy Harvesting Relays". In: *IEEE Trans. Commun.* 68.6 (2020), pp. 3326–3341. DOI: 10.1109/TCOMM.2020.2976005 (cit. on p. 21).

[125] O. L. Alcaraz López et al. "Ultra reliable short message relaying with wireless power transfer". In: *2017 IEEE Int. Conf. Commun.* 2017, pp. 1–6. DOI: 10.1109/ICC.2017.7997203 (cit. on p. 21).

[126] Z. Qin et al. "Semantic communications: Principles and challenges". In: *arXiv preprint arXiv:2201.01389* (2021) (cit. on p. 22).

[127] J. Bao et al. "Towards a theory of semantic communication". In: *Proc. IEEE Netw. Sci. Workshop*. 2011, pp. 110–117. DOI: 10.1109/NSW.2011.6004632 (cit. on p. 22).

[128] G. Shi et al. "From Semantic Communication to Semantic-Aware Networking: Model, Architecture, and Open Problems". In: *IEEE Commun. Mag.* 59.8 (2021), pp. 44–50. DOI: 10.1109/MCOM.001.2001239 (cit. on p. 22).

[129] H. Xie et al. "Deep Learning Enabled Semantic Communication Systems". In: *IEEE Trans. Signal Process.* 69 (2021), pp. 2663–2675. DOI: `10.1109/TSP.2021.3071210` (cit. on p. 22).

[130] Y. Liu et al. "A survey on semantic communications: technologies, solutions, applications and challenges". In: *Digit. Commun. Netw* (2023) (cit. on p. 22).

[131] S. Ma et al. "A Theory for Semantic Communications". In: *arXiv preprint arXiv:2303.05181* (2023) (cit. on p. 22).

[132] C. Shannon and W. Weaver. *The Mathematical Theory of Communication*. University of Illinois Press, 1998. ISBN: 9780252098031. URL: `https://books.google.pt/books?id=IZ77BwAAQBAJ` (cit. on p. 22).

[133] C. E. Shannon. "A mathematical theory of communication". In: *Bell Syst. Tech. J.* 27.3 (1948), pp. 379–423 (cit. on p. 22).

[134] E. C. Strinati and S. Barbarossa. "6G networks: Beyond Shannon towards semantic and goal-oriented communications". In: *Comput. Netw.* 190 (2021), p. 107930 (cit. on p. 22).

[135] R. Carnap, Y. Bar-Hillel, et al. "An outline of a theory of semantic information". In: *TECHNICAL REPORT NO. 247* (1952) (cit. on p. 22).

[136] K. Lu et al. "Rethinking Modern Communication from Semantic Coding to Semantic Communication". In: *IEEE Wirel. Commun.* 30.1 (2023), pp. 158–164. DOI: `10.1109/MWC.013.2100642` (cit. on p. 22).

[137] V. Guruswami, A. Riazanov, and M. Ye. "Arikan meets Shannon: Polar codes with near-optimal convergence to channel capacity". In: *Proc. Annu. ACM Symp. Theory Comput.* 2020, pp. 552–564 (cit. on p. 22).

[138] I. Djordjevic and B. Vasic. "Approaching Shannon's capacity limits of fiber optics communications channels using short LDPC codes". In: *Proc. Conf. Lasers Electro-Opt. (CLEO)*. Vol. 1. 2004 (cit. on p. 22).

[139] C.-H. Hsu and A. Anastasopoulos. "Capacity Achieving LDPC Codes Through Puncturing". In: *IEEE Trans. Inf. Theory.* 54.10 (2008), pp. 4698–4706. DOI: `10.1109/TIT.2008.928274` (cit. on p. 22).

[140] N. C. Luong et al. "Data collection and wireless communication in Internet of Things (IoT) using economic analysis and pricing models: A survey". In: *IEEE Commun. Surv. Tutor.* 18.4 (2016), pp. 2546–2590 (cit. on p. 22).

[141] H.-N. Dai et al. "Big data analytics for large-scale wireless networks: Challenges and opportunities". In: *ACM Comput. Surv.* 52.5 (2019), pp. 1–36 (cit. on p. 22).

[142] J. Xu et al. "Deep Joint Source-Channel Coding for Semantic Communications". In: *arXiv preprint arXiv:2211.08747* (2022) (cit. on p. 22).

[143] P. Jiang et al. "Deep Source-Channel Coding for Sentence Semantic Transmission With HARQ". In: *IEEE Trans. Commun.* 70.8 (2022), pp. 5225–5240. DOI: `10.1109/TCOMM.2022.3180997` (cit. on p. 22).

[144] D. Gündüz et al. "Beyond Transmitting Bits: Context, Semantics, and Task-Oriented Communications". In: *IEEE J. Sel. Areas Commun.* 41.1 (2023), pp. 5–41. DOI: 10.1109/JSAC.2022.3223408 (cit. on p. 22).

[145] E. Bourtsoulatze, D. B. Kurka, and D. Gündüz. "Deep Joint Source-channel Coding for Wireless Image Transmission". In: *Proc. IEEE Int. Conf. Acoust. Speech Signal Process.* 2019, pp. 4774–4778. DOI: 10.1109/ICASSP.2019.8683463 (cit. on pp. 22, 93).

[146] D. B. Kurka and D. Gündüz. "DeepJSCC-f: Deep Joint Source-Channel Coding of Images With Feedback". In: *IEEE J. Sel. Areas Inf. Theory* 1.1 (2020), pp. 178–193. DOI: 10.1109/JSAIT.2020.2987203 (cit. on pp. 22, 93).

[147] N. Farsad, M. Rao, and A. Goldsmith. "Deep learning for joint source-channel coding of text". In: *Proc. IEEE Int. Conf. Acoust. Speech Signal Process.* IEEE. 2018, pp. 2326–2330 (cit. on p. 22).

[148] Z. Lyu et al. "Semantic Communications for Image Recovery and Classification via Deep Joint Source and Channel Coding". In: *arXiv preprint arXiv:2304.02317* (2023) (cit. on p. 22).

[149] N. Pappas et al. *Age of Information: Foundations and Applications*. Cambridge University Press, 2022 (cit. on p. 22).

[150] A. Maatouk et al. "The Age of Incorrect Information: A New Performance Metric for Status Updates". In: *IEEE/ACM Trans. Netw.* 28.5 (2020), pp. 2215–2228. DOI: 10.1109/TNET.2020.3005549 (cit. on p. 23).

[151] X. Zheng, S. Zhou, and Z. Niu. "Beyond age: Urgency of information for timeliness guarantee in status update systems". In: *Proc. 6G Wirel. Summit (6G SUMMIT)*. IEEE. 2020, pp. 1–5 (cit. on p. 23).

[152] A. Maatouk, M. Assaad, and A. Ephremides. "Semantics-Empowered Communications Through the Age of Incorrect Information". In: *Proc. IEEE Int. Conf. Commun.* 2022, pp. 3995–4000. DOI: 10.1109/ICC45855.2022.9838737 (cit. on p. 23).

[153] Y. E. Sagduyu, S. Ulukus, and A. Yener. "Age of information in deep learning-driven task-oriented communications". In: *arXiv preprint arXiv:2301.04298* (2023) (cit. on p. 23).

[154] A. Al-Hourani, S. Kandeepan, and A. Jamalipour. "Modeling air-to-ground path loss for low altitude platforms in urban environments". In: *Proc. IEEE Glob. Commun. Conf.* IEEE. 2014, pp. 2898–2904 (cit. on p. 27).

[155] H. Hydher et al. "Intelligent UAV deployment for a disaster-resilient wireless network". In: *Sensors* 20.21 (2020), p. 6140 (cit. on p. 27).

[156] P. Data. "Prediction methods required for the design of terrestrial broadband millimetric radio access systems operating in a frequency range of about 20-50 ghz". In: *Draft New Recommendation ITU-R P.[DOC. 3/47], Working Party K* 3 (2003) (cit. on p. 28).

[157] A. Al-Hourani, S. Kandeepan, and S. Lardner. "Optimal LAP altitude for maximum coverage". In: *IEEE Commun. Lett.* 3.6 (2014), pp. 569–572 (cit. on pp. 28, 69, 94).

[158] M. M. Azari et al. "Optimal UAV positioning for terrestrial-aerial communication in presence of fading". In: *Proc. IEEE Glob. Commun. Conf.* IEEE. 2016, pp. 1–7 (cit. on p. 29).

[159] B. Wang et al. "Optimal Altitude of UAV-BS for Minimum Boundary Outage Probability with Imperfect Channel State Information". In: *Proc. IEEE/CIC Int. Conf. Commun. China (ICCC).* IEEE. 2019, pp. 607–611 (cit. on pp. 29, 35, 69, 73, 95, 103).

[160] J. Chen et al. "Resource Allocation for Wireless-Powered IoT Networks With Short Packet Communication". In: *IEEE Trans. Wirel. Commun.* 18.2 (2019), pp. 1447–1461. DOI: 10.1109/TWC.2019.2893335 (cit. on p. 29).

[161] B. Makki, T. Svensson, and M. Zorzi. "Finite block-length analysis of the incremental redundancy HARQ". In: *IEEE Wirel. Commun. Lett.* 3.5 (2014), pp. 529–532 (cit. on pp. 30, 48).

[162] H. Guo, B. Makki, and T. Svensson. "Predictor Antennas for Moving Relays: Finite Block-length Analysis". In: *Proc. Int. Conf. Adv. Commun. Technol. Netw. CommNet (CommNet).* IEEE. 2020, pp. 1–8 (cit. on p. 30).

[163] D. Mishra, S. De, and D. Krishnaswamy. "Dilemma at RF energy harvesting relay: Downlink energy relaying or uplink information transfer?" In: *IEEE Trans. Wirel. Commun.* 16.8 (2017), pp. 4939–4955 (cit. on pp. 30, 70).

[164] H. Guo et al. "A semi-linear approximation of the first-order Marcum Q-function with application to predictor antenna systems". In: *IEEE open J. Commun. Soc.* 2 (2021), pp. 273–286 (cit. on p. 30).

[165] E. T. Ceran, D. Gündüz, and A. György. "Average age of information with hybrid ARQ under a resource constraint". In: *IEEE Trans. Wirel. Commun* 18.3 (2019), pp. 1900–1913 (cit. on pp. 44, 45).

[166] M. Abramowitz, I. A. Stegun, and R. H. Romer. *Handbook of mathematical functions with formulas, graphs, and mathematical tables.* 1988 (cit. on pp. 50, 70).

[167] S. Dhok et al. "Non-Linear Energy Harvesting in RIS-assisted URLLC Networks for Industry Automation". In: *IEEE Trans. Commun.* 69.11 (2021), pp. 7761–7774 (cit. on p. 50).

[168] F. Zhu et al. "Chebyshev-Gauss Approximation Analysis for Mobile Edge Computing-Aided IoT Networks". In: *Wirel. Commun. Mob. Comput.* 2022 (2022) (cit. on p. 50).

[169] T. Kadri and K. Smaili. "Convolutions of hyper-erlang and of erlang distributions". In: *Int. J. Pure Appl. Math.* 98.1 (2015), pp. 81–98 (cit. on p. 54).

[170] C. S. You, J. S. Yeom, and B. C. Jung. "Performance Analysis of Cooperative Low-Power Wide-Area Network for Energy-Efficient B5G Systems". In: *Electronics* 9.4 (2020), p. 680 (cit. on p. 54).

[171]   S. Roth et al. "Remote short blocklength process monitoring: Trade-off between resolution and data freshness". In: *IEEE Int. Conf. Commun. 2020 -Proc.* IEEE. 2020, pp. 1–6 (cit. on p. 55).

[172]   B. Li et al. "Optimizing information freshness in two-way relay networks". In: *2020 IEEE/CIC Int. Conf Commun. in China (ICCC)*. IEEE. 2020, pp. 893–898 (cit. on p. 56).

[173]   P. Mary et al. "Finite Blocklength Information Theory: What Is the Practical Impact on Wireless Communications?" In: *2016 IEEE Glob. Commun. Conf.* 2016, pp. 1–6. DOI: `10.1109/GLOCOMW.2016.7848909` (cit. on p. 56).

[174]   A. Gil, J. Segura, and N. M. Temme. "Algorithm 939: Computation of the Marcum Q-function". In: *ACM Trans. Math. Softw.* 40.3 (2014), pp. 1–21 (cit. on p. 70).

[175]   H. Guo et al. "A Semi-Linear Approximation of the First-Order Marcum Q-Function With Application to Predictor Antenna Systems". In: *IEEE Open J. Commun. Soc.* 2 (2021), pp. 273–286. DOI: `10.1109/OJCOMS.2021.3056393` (cit. on p. 71).

[176]   R. D. Yates and S. K. Kaul. "Status updates over unreliable multiaccess channels". In: *Proc. IEEE Int. Symp. Inf. Theory*. 2017, pp. 331–335. DOI: `10.1109/ISIT.2017.8006544` (cit. on p. 72).

[177]   C. M. W. Basnayaka, D. N. K. Jayakody, and M. Beko. "Semantics-Empowered UAV-assisted Wireless Communication System for Wildfire Detection". In: *IEEE 28th Int. Workshop Comput. Aided Model. Design Commun. Links Netw.* 2023, pp. 152–157. DOI: `10.1109/CAMAD59638.2023.10478404` (cit. on p. 80).

[178]   F. Bellard. *BPG Image Format*. `https://bellard.org/bpg/`. Accessed: Apr. 10, 2024. 2014 (cit. on p. 80).

[179]   *Low-Density Parity-Check (LDPC) — Sionna 0.16.2 documentation*. `https://nvlabs.github.io/sionna/api/fec.ldpc.html`. Accessed: Apr. 2, 2024 (cit. on p. 80).

[180]   D. B. Kurka and D. Gündüz. "Bandwidth-Agile Image Transmission With Deep Joint Source-Channel Coding". In: *IEEE Trans. Wirel. Commun.* 20.12 (2021), pp. 8081–8095. DOI: `10.1109/TWC.2021.3090048` (cit. on pp. 80, 82, 93).

[181]   A. Krizhevsky. *Learning Multiple Layers of Features from Tiny Images*. `https://www.cs.toronto.edu/~kriz/cifar.html`. Accessed: Mar. 10, 2024. 2009 (cit. on pp. 86, 87).

[182]   3GPP. *5G NR; Multiplexing and channel coding*. Tech. rep. TS 38.212. Version 15.2.0. 3rd Generation Partnership Project (3GPP), 2018-06 (cit. on p. 86).

[183]   M. A. Moritz et al. "Learning to coexist with wildfire". In: *Nature* 515.7525 (2014), pp. 58–66 (cit. on p. 91).

[184]   J.-l. Dupuy et al. "Climate change impact on future wildfire danger and activity in southern Europe: a review". In: *Annals of Forest Science* 77.2 (2020), pp. 1–24 (cit. on p. 91).

[185] J. Jacobo. "Forest Fires Destroyed Nearly 23 Million Acres of Land in 2021, and It's Expected to Get Worse, Experts Say". In: *ABC News* (2022-08). URL: https://abcnews.go.com/International/forest-fires-destroyed-23-million-acres-land-2021/story?id=88400813 (cit. on p. 91).

[186] F. Carta et al. "Advancements in Forest Fire Prevention: A Comprehensive Survey". In: *Sensors* 23.14 (2023). ISSN: 1424-8220. DOI: 10.3390/s23146635. URL: https://www.mdpi.com/1424-8220/23/14/6635 (cit. on p. 91).

[187] O. M. Bushnaq, A. Chaaban, and T. Y. Al-Naffouri. "The Role of UAV-IoT Networks in Future Wildfire Detection". In: *IEEE Internet Things J.* 8.23 (2021), pp. 16984–16999. DOI: 10.1109/JIOT.2021.3077593 (cit. on p. 91).

[188] D. Crnjac Milić, I. Dujmenović, and M. Peko. "An approach to the application of the internet of things in logistics". In: *Tehnički glasnik* 17.1 (2023), pp. 134–140 (cit. on p. 91).

[189] J. C. Hodgson et al. "Precision wildlife monitoring using unmanned aerial vehicles". In: *Scientific reports* 6.1 (2016), p. 22574 (cit. on p. 91).

[190] C. Basnayake, K. O. Lakmal, and D. N. K. Jayakody. "The era of the 5G drone is ahead, are we ready?" In: *Vidurava* 36.4 (2019), pp. 19–21 (cit. on p. 91).

[191] M. Erdelj et al. "Help from the sky: Leveraging UAVs for disaster management". In: *IEEE Pervasive Comput.* 16.1 (2017), pp. 24–32 (cit. on p. 91).

[192] A. Bouguettaya et al. "A review on early wildfire detection from unmanned aerial vehicles using deep learning-based computer vision algorithms". In: *Signal Process.* 190 (2022), p. 108309. ISSN: 0165-1684. DOI: https://doi.org/10.1016/j.sigpro.2021.108309. URL: https://www.sciencedirect.com/science/article/pii/S016516842100 3467 (cit. on p. 91).

[193] C. M. W. Basnayaka, D. N. K. Jayakody, and Z. Chang. "Age-of-Information-Based URLLC-Enabled UAV Wireless Communications System". In: *IEEE Internet Things J.* 9.12 (2022), pp. 10212–10223. DOI: 10.1109/JIOT.2021.3123431 (cit. on p. 95).

[194] J. Ballé, V. Laparra, and E. P. Simoncelli. "Density modeling of images using a generalized normalization transformation". In: *arXiv preprint arXiv:1511.06281* (2015) (cit. on p. 96).

[195] B. Dincer. *Wildfire Detection Image Data*. Accessed: July 01, 2023. Kaggle. 2021. URL: https://www.kaggle.com/datasets/brsdincer/wildfire-detection-image-data (cit. on pp. 101, 102).

[196] S. Schiessl, M. Skoglund, and J. Gross. "NOMA in the Uplink: Delay Analysis With Imperfect CSI and Finite-Length Coding". In: *IEEE Trans. Wirel. Commun.* 19.6 (2020), pp. 3879–3893. DOI: 10.1109/TWC.2020.2979114 (cit. on p. 116).

[197] I. Tal and A. Vardy. "How to Construct Polar Codes". In: *IEEE Trans. Inf. Theory* 59.10 (2013), pp. 6562–6582. DOI: 10.1109/TIT.2013.2272694 (cit. on p. 116).

[198] V. Khodamoradi et al. "Energy-Efficient Massive MIMO SWIPT-Enabled Systems". In: *IEEE Trans. Veh. Technol.* 71.5 (2022), pp. 5111–5127. DOI: `10.1109/TVT.2022.3153 323` (cit. on p. 117).

[199] I. Kadota and E. Modiano. "Age of Information in Random Access Networks with Stochastic Arrivals". In: *Proc. IEEE Int. Conf. Comput. Commun.* 2021, pp. 1–10. DOI: `10.1109/INFOCOM42981.2021.9488897` (cit. on p. 117).

[200] M. Berioli et al. "Modern random access protocols". In: *Foundations and Trends® in Networking* 10.4 (2016), pp. 317–446 (cit. on p. 117).

Appendix A

PROOF OF LEMMA 1

The PDF of SNR at relay from each source can be calculated using (4.2) as follows,

$$f_{\gamma_R^{i'}}(x) = \frac{\sigma_R^2}{(1-\rho)P_{i'}\alpha_{i'R}} e^{-\frac{x\sigma_R^2}{(1-\rho)P_{i'}\alpha_{i'R}}} \tag{A.1}$$

Then, the CDF is calculated as

$$F_{\gamma_R^{i'}}(z) = \mathbb{P}_r\left(\gamma_R^{i'} \leq z\right) = \int_{-\infty}^{z} f_{\gamma_R^{i'}}(t)\, dt$$
$$= 1 - e^{-\frac{z\sigma_R^2}{(1-\rho)P_{i'}\alpha_{i'R}}}. \tag{A.2}$$

From (4.15) block error probability at the relay is calculated as follows,

$$\varepsilon_R^{i'} \approx \beta_R^{i'}\sqrt{n_R^{i'}} \int_{\phi_R^{i'}}^{\delta_R^{i'}} F_{\gamma_R^{i'}}(z)\, dz$$

$$\approx \beta_R^{i'}\sqrt{n_R^{i'}} \int_{\phi_R^{i'}}^{\delta_R^{i'}} 1 - e^{-\frac{z\sigma_R^2}{(1-\rho)P_{i'}\alpha_{i'R}}}\, dz,$$

$$\approx \beta_R^{i'}\sqrt{n_R^{i'}} \left(\left(\delta_R^{i'} - \phi_R^{i'}\right) - \int_{\phi_R^{i'}}^{\delta_R^{i'}} e^{-\frac{z\sigma_R^2}{(1-\rho)P_{i'}\alpha_{i'R}}}\, dz\right),$$

$$\approx \beta_R^{i'}\sqrt{n_R^{i'}} \left(\psi_R^{i'} + \frac{1}{2.\beta_R^{i'}\sqrt{n_R^{i'}}} - \left(\psi_R^{i'} - \frac{1}{2\beta_R^{i'}\sqrt{n_R^{i'}}}\right)\right) \tag{A.3}$$

$$- \left(\frac{(1-\rho)P_{i'}\alpha_{i'R}\beta_R^{i}\sqrt{n_R^{i'}}}{\sigma_R^2}\right)\left(e^{-\frac{\phi_R^{i'}\sigma_R^2}{(1-\rho)P_{i'}\alpha_{i'R}}} - e^{-\frac{\delta_R^{i'}\sigma_R^2}{(1-\rho)P_{i'}\alpha_{i'R}}}\right),$$

$$\varepsilon_R^{i'} \approx 1 - \left(\frac{(1-\rho)P_{i'}\alpha_{iR}\beta_R^{i'}\sqrt{n_R^{i'}}}{\sigma_R^2}\right)\left(e^{-\frac{\phi_R^{i'}\sigma_R^2}{(1-\rho)P_{i'}\alpha_{i'R}}} - e^{-\frac{\delta_R^{i'}\sigma_R^2}{(1-\rho)P_{i'}\alpha_{i'R}}}\right).$$

Appendix B

PROOF OF LEMMA 3

The system overall transmission error probability ε_i at each source can be calculated using (4.9) and $\varepsilon_R^{i'}$ and ε_i^R can be calculated as follows:

$$\varepsilon_R^{i'} \approx 1 - \left(\frac{(1-\rho)P_{i'}\alpha_{i'R}\beta_R^{i'}\sqrt{n_R^{i'}}}{\sigma_R^2} \right) \left(e^{-\frac{\phi_R^{i'}\sigma_R^2}{(1-\rho)P_{i'}\alpha_{i'R}}} - e^{-\frac{\delta_R^{i'}\sigma_R^2}{(1-\rho)P_{i'}\alpha_{i'R}}} \right), \tag{B.1}$$

$$\varepsilon_i^R \approx 1 - \left(\frac{P_{req}\alpha_{Ri}\beta_i^R\sqrt{n_i^R}}{\sigma_i^2} \right) \left(e^{-\frac{\phi_i^R\sigma_i^2}{P_{req}\alpha_{Ri}}} - e^{-\frac{\delta_i^R\sigma_i^2}{P_{req}\alpha_{Ri}}} \right). \tag{B.2}$$

Then, using equation (4.9),ε_i is calculated as follows:

$$\varepsilon_i = \varepsilon_R^{i'} + \left(1 - \varepsilon_R^{i'}\right)\varepsilon_i^R \tag{B.3a}$$

$$\varepsilon_i \approx 1 - \left(\frac{\beta_R^{i'}\beta_i^R\sqrt{n_R^{i'}n_i^R}((1-\rho)P_{i'}P_{\text{req}})\alpha_{i'R}\alpha_{Ri}}{\sigma_R^2\sigma_i^2} \right) \times \left(e^{-\frac{\phi_R^{i'}\sigma_R^2}{(1-\rho)P_{i'}\alpha_{i'R}}} - e^{-\frac{\delta_R^{i'}\sigma_R^2}{(1-\rho)P_{i'}\alpha_iR}} \right)$$

$$\times \left(e^{-\frac{\phi_i^R\sigma_i^2}{P_{\text{req}}\alpha_{Ri}}} - e^{-\frac{\delta_i^R\sigma_i^2}{P_{\text{req}}\alpha_{Ri}}} \right) \tag{B.3b}$$

Appendix C

PROOF OF LEMMA 5

By using the PMF given in (4.42), the first moments of m_w is computed as follows:

$$E\left[m_w\right] = e^{-\xi E'_{harv}} \sum_{m=1}^{\infty} \frac{\left(\xi E'_{harv}\right)^{2m-2} \left[2m - 1 + \xi E'_{harv}\right]}{(2m-1)!}, \tag{C.1a}$$

$$= e^{-\xi E'_{harv}} \left(\sum_{m=1}^{\infty} \frac{m\left(\xi E'_{harv}\right)^{2m-2}}{(2m-2)!} + \sum_{m=1}^{\infty} \frac{m\left(\xi E'_{harv}\right)^{2m-1}}{(2m-1)!} \right), \tag{C.1b}$$

$$= e^{-\xi E'_{harv}} \left(\sum_{T=0}^{\infty} \frac{(T+1)\left(\xi E'_{harv}\right)^{2T}}{(2T)!} + \sum_{T=0}^{\infty} \frac{(T+1)\left(\xi E'_{harv}\right)^{2T+1}}{(2T+1)!} \right), \tag{C.1c}$$

$$= e^{-\xi E'_{harv}} \left(\sum_{T=0}^{\infty} \frac{\left(\xi E'_{harv}\right)^{2T}}{(2T)!} + \sum_{T=0}^{\infty} \frac{\left(\xi E'_{harv}\right)^{2T+1}}{(2T+1)!} + \sum_{T=0}^{\infty} \frac{T\left(\xi E'_{harv}\right)^{2T}}{(2T)!} \right.$$
$$\left. + \sum_{T=0}^{\infty} \frac{T\left(\xi E'_{harv}\right)^{2T+1}}{(2T+1)!} \right), \tag{C.1d}$$

$$= e^{-\xi E'_{harv}} \left(\cosh\left(\xi E'_{harv}\right) + \sinh\left(\xi E'_{harv}\right) + \frac{\sinh\left(\xi E'_{harv}\right)\xi E'_{harv}}{2} \right.$$
$$\left. + \frac{\cosh\left(\xi E'_{harv}\right)\xi E'_{harv}}{2} \right), \tag{C.1e}$$

$$= e^{-\xi E'_{harv}} \left(e^{\xi E'_{harv}} + \frac{e^{\xi E'_{harv}}\xi E'_{harv}}{2} \right) \tag{C.1f}$$

$$E\left[m_w\right] = 1 + \frac{\xi E'_{harv}}{2}. \tag{C.1g}$$

Then, second moments of m_w is computed as follows:

$$E\left[m_w^2\right] = e^{-\xi E'_{harv}} \sum_{m=1}^{\infty} \frac{m^2 \left(\xi E'_{harv}\right)^{2m-2} \left[2m - 1 + \xi E'_{harv}\right]}{(2m-1)!}, \tag{C.2a}$$

$$= e^{-\xi E'_{harv}} \left(\sum_{m=1}^{\infty} \frac{m^2 \left(\xi E'_{harv}\right)^{2m-2}}{(2m-2)!} + \sum_{m=1}^{\infty} \frac{m^2 \left(\xi E'_{harv}\right)^{2m-1}}{(2m-1)!} \right), \tag{C.2b}$$

$$= e^{-\xi E'_{harv}} \left(\sum_{T=0}^{\infty} \frac{(T+1)^2 \left(\xi E'_{harv}\right)^{2T}}{(2T)!} + \sum_{T=0}^{\infty} \frac{(T+1)^2 \left(\xi E'_{harv}\right)^{2T+1}}{(2T+1)!} \right), \tag{C.2c}$$

$$= e^{-\xi E'_{harv}} \left(\sum_{T=0}^{\infty} \frac{\left(\xi E'_{harv}\right)^{2T}}{(2T)!} + \sum_{T=0}^{\infty} \frac{\left(\xi E'_{harv}\right)^{2T+1}}{(2T+1)!} + 2\left(\sum_{T=0}^{\infty} \frac{T \left(\xi E'_{harv}\right)^{2T}}{(2T)!} \right. \right.$$
$$\left. \left. + \sum_{T=0}^{\infty} \frac{T \left(\xi E'_{harv}\right)^{2T+1}}{(2T+1)!} \right) + \sum_{T=0}^{\infty} \frac{T^2 \left(\xi E'_{harv}\right)^{2T}}{(2T)!} + \sum_{T=0}^{\infty} \frac{T^2 \left(\xi E'_{harv}\right)^{2T+1}}{(2T+1)!} \right), \tag{C.2d}$$

$$= e^{-\xi E'_{harv}} \left(\cosh\left(\xi E'_{harv}\right) + \sinh\left(\xi E'_{harv}\right) + \sinh\left(\xi E'_{harv}\right) \xi E'_{harv} \right.$$
$$+ \cosh\left(\xi E'_{harv}\right) \xi E'_{harv} + \frac{\xi E'_{harv} \left(\sinh\left(\xi E'_{harv}\right) + \xi E'_{harv} \cosh\left(\xi E'_{harv}\right)\right)}{4} +$$
$$\left. \frac{\xi E'_{harv} \left(\cosh\left(\xi E'_{harv}\right) + \xi E'_{harv} \sinh\left(\xi E'_{harv}\right)\right)}{4} \right), \tag{C.2e}$$

$$= e^{-\xi E'_{harv}} \left(e^{-\xi E'_{harv}} + e^{-\xi E'_{harv}} \xi E'_{harv} + \right.$$
$$\left. \frac{\xi E'_{harv} \left(e^{-\xi E'_{harv}} + e^{-\xi E'_{harv}} \xi E'_{harv} \right)}{4} \right), \tag{C.2f}$$

$$= e^{-\xi E'_{harv}} \left(e^{-\xi E'_{harv}} + \frac{5 e^{-\xi E'_{harv}} \xi E'_{harv}}{4} + \frac{\left(\xi E'_{harv}\right)^2 \left(e^{-\xi E'_{harv}} \right)}{4} \right), \tag{C.2g}$$

$$E\left[m_w^2\right] = 1 + \frac{\left(\xi E'_{harv}\right)^2}{4} + \frac{5 \xi E'_{harv}}{4}. \tag{C.2h}$$